



HAL
open science

**Simulation aux Grandes Echelles de Feux de Batteries
Lithium-ion pour le Diagnostic de l'Emballlement
Thermique**
Antony Cellier

► **To cite this version:**

Antony Cellier. Simulation aux Grandes Echelles de Feux de Batteries Lithium-ion pour le Diagnostic de l'Emballlement Thermique. Mécanique des fluides [physics.class-ph]. Institut National Polytechnique de Toulouse - INPT, 2023. Français. NNT : 2023INPT0072 . tel-04258393

HAL Id: tel-04258393

<https://theses.hal.science/tel-04258393v1>

Submitted on 25 Oct 2023

HAL is a multi-disciplinary open access archive for the deposit and dissemination of scientific research documents, whether they are published or not. The documents may come from teaching and research institutions in France or abroad, or from public or private research centers.

L'archive ouverte pluridisciplinaire **HAL**, est destinée au dépôt et à la diffusion de documents scientifiques de niveau recherche, publiés ou non, émanant des établissements d'enseignement et de recherche français ou étrangers, des laboratoires publics ou privés.



Université
de Toulouse

THÈSE

En vue de l'obtention du

DOCTORAT DE L'UNIVERSITÉ DE TOULOUSE

Délivré par :

Institut National Polytechnique de Toulouse (Toulouse INP)

Discipline ou spécialité :

Dynamique des fluides

Présentée et soutenue par :

M. ANTONY CELLIER

le vendredi 22 septembre 2023

Titre :

Simulation aux Grandes Échelles de Feux de Batteries Lithium-ion pour le
Diagnostic de l'Emballage Thermique

Ecole doctorale :

Mécanique, Energétique, Génie civil, Procédés (MEGeP)

Unité de recherche :

Centre Européen de Recherche et Formation Avancées en Calcul Scientifique (CERFACS)

Directeurs de Thèse :

M. FLORENT DUCHAINE

M. THIERRY POINSOT

Rapporteurs :

M. EPAMINONDAS MASTORAKOS, UNIVERSITE DE CAMBRIDGE

Membres du jury :

M. NICOLAS NOIRAY, ECOLE POLYTECHNIQUE FEDERALE DE ZURICH, Président

M. FLORENT DUCHAINE, CERFACS, Membre

M. FRÉDÉRIC RAVET, RENAULT GUYANCOURT, Membre

M. MARC BELLENOUE, ENSMA POITIERS, Membre

MME GIZEM OKYAY, SAFT, Membre

M. RONAN VICQUELIN, CENTRALESUPELEC GIF SUR YVETTE, Membre

M. THIERRY POINSOT, TOULOUSE INP, Membre

Abstract

The development of more sustainable energy supply chains is accompanied by an evolution of the demand for safe and efficient storage solutions. Among them, Lithium-ion batteries benefit from the maturity of a technology developed and applied for more than three decades. However, when misused or in case of manufacturing defects, Lithium-ion batteries may uncontrollably trigger decomposition reactions: the so-called Thermal Runaway process. The reactions produce heat and flammable gases, leading to fires when the battery vents out these gases.

During a typical Thermal Runaway course, three main flow scenarios are identified: 1. Under-expanded jets at opening due to the high pressure inside the battery, 2. Jet fires in case of ignition, 3. Explosions in case of delayed ignition. Being able to simulate these events can help to target safer battery designs at a minimal prototyping cost.

This study thus aims at proposing a methodology to simulate failing Lithium-ion batteries-related combustion scenarios, using 3D reactive Large Eddy Simulation. The setup of such a simulation framework begins with the identification of the vent gases, their source and the way they can be modeled efficiently. An Analytically Reduced Chemistry kinetic scheme is then proposed to ensure the representativeness of the combustion processes at optimal costs when targeting 3D scenarios. After a setup phase in 1D, the validation of the 3D Large Eddy Simulation framework is performed on dedicated experimental setups developed and operated at the P' institute for jets and fires and obtained from the literature concerning explosions. Once validated, applications help to evaluate the capability of the simulation setup to target a variety of problems related to Lithium-ion, including effects of simple design choices on each phase of the Thermal Runaway.

This work identifies the difficulties encountered when simulating Lithium-ion related accidents. Propositions are made to alleviate them, helping to advocate for the use of simulations during prototyping phases, to assert venting, fires or explosions of batteries.

Résumé

La mise en place d'un approvisionnement en énergies plus durables amène une évolution de la demande en systèmes de stockage performants et sûrs. Parmi les solutions souvent citées, les batteries Lithium-ion héritent d'une certaine maturité, due à trois décennies de développement et de mises sur le marché. Cependant, mal utilisées ou dans l'éventualité d'un défaut de fabrication, une batterie peut déclencher des réactions de décomposition, aussi appelées un emballement thermique. Ces réactions produisent de la chaleur et des gaz inflammables pouvant causer un feu lorsque la batterie dégaze.

Lors d'un emballement thermique typique, trois événements mettant en scène un écoulement critique sont observés : 1. Un jet sous-détendu dû à la forte pression interne des batteries au moment du dégazage, 2. Des flammes jets en présence d'une source d'allumage, 3. Une explosion si l'allumage est retardé et les gaz ont le temps de se mélanger à l'air ambiant. Être capable de simuler ces événements permettrait de sélectionner des designs sûrs à un coût de prototypage faible.

Cette étude propose une méthodologie pour la simulation de scénarios de combustion liés aux batteries, grâce à la Simulation aux Grandes Échelles réactive. Tout d'abord, l'identification des gaz émis par une batterie en défaut est faite, permettant la production d'un schéma cinétique réduit dédié aux feux de batteries. Suivant l'évaluation des modèles à utiliser en 1D, une validation complète du setup 3D est faite sur des résultats expérimentaux préparés à l'institut P' pour les jets et feux, et tirés de la littérature pour les explosions. Une fois le setup validé, des cas d'application sont donnés, permettant de souligner l'effet de certains choix de design sur le déroulement des phases de l'emballement.

Ce travail soulève les points durs nécessairement rencontrés lorsque des accidents liés aux feux de batteries sont à reproduire par la simulation. Des propositions sont faites pour les supprimer, motivant une utilisation plus répandue de la simulation 3D d'écoulements réactifs durant les phases de prototypage. Cela prend en compte l'ouverture, les feux et explosions liées aux batteries Lithium-ion.

Acknowledgements

Je souhaite tout d'abord remercier les rapporteurs Nicolas Noiray et Epaminondas Mastorakos d'avoir pris le temps d'évaluer mes travaux avec attention, apportant éclairages et conseils pour continuer à développer le sujet. Je remercie aussi Ronan Vicquelin et Frédéric Ravet pour leurs contributions à la correction ainsi que Marc Bellenoue et Gizem Okayay pour leur aide essentielle pendant la thèse, ainsi que leurs retours sur le manuscrit.

Je remercie ensuite Matthieu Leyko pour l'impulsion initiale et le suivi enthousiaste et sans faille des évolutions du projet, je te souhaite le meilleur pour la nouvelle aventure dans laquelle tu t'es lancé. J'ajoute un grand merci à Maxime Pallud pour son soutien et son investissement pendant la thèse.

Je suis aussi reconnaissant envers mes encadrants Florent Duchaine et Thierry Poinot pour leur confiance en moi, leur temps et leurs précieux conseils. Nos échanges ont construit mon goût pour la recherche, et j'espère un jour pouvoir emprunter de votre rigueur, de votre précision et de votre humanité. Je vous dois beaucoup.

Je remercie évidemment mes collègues et désormais amis (le piège se referme) qui m'ont suivi et supporté depuis mon arrivée au CERFACS il y a 4 ans. Que de grands noms dont les âges se souviendront, Étienne, Thomas (la machine), Antoine, Jon, Nico, Thomas, Guillaume, Thomas, Thomas, Arthur, Victor, Quentin, Thomas, Omar, Quentin, Alex, Jean, Nat, Thomas, Jean-Jacques, Benjamin, Francis, Paul, Minh, Jessica, Hector, Justin, Félicia, Thomas et bien sûr Thomas, il y a beaucoup de Thomas. Je tiens à remercier plus généralement l'équipe CFD, la meilleure du monde, de l'univers, pour une atmosphère de travail et une émulation qui permet une recherche innovante, de qualité. Je remercie aussi l'équipe informatique du laboratoire, l'administration, dont Chantal, Brigitte, Michèle, Fabrice, Gérard, Fred, Isabelle, Nicolas ... pour leur aide, rendant le monstre doctoral bien moins combattif !

Je remercie mes amis de Tarbes, Toulouse, Paris, ... de m'avoir supporté jusqu'ici, des amis d'enfance et pour la vie, Robin, Lila, Sarra, Mathieu, Issa, Mel, Alex, Lulu, Ludo, Hugo, Amine, Théo, Olive, Vince, Victor, Mathieu, Étienne, Lise,

Laeti, Emma, Mathis, Elsa, Ali, Célé, Laurie, Romain, Yohann, Stef, et tous ceux auxquels je pense ! On ne se voit pas assez, vous me manquez il faut qu'on se fasse des trucs !

J'ajouterai un merci plus particulier à ceux qui m'ont patiemment accompagné en montagne, en m'apprenant beaucoup (tout), qui m'ont suivi sur le vélo ou en courant. Je sais que vous supportez beaucoup de mes penchants maniaques, merci encore Étienne, Victor, Mathieu, Lise, Paloma, Thomas, ... Désolé mais ça ne s'arrêtera pas, et il y aura plein d'autres raisons de vous embêter !

Et enfin, je remercie ma famille qui représente 99.9% de tout ce qui est dans le manuscrit, et 99.9% de tout ce que je suis, sans qui rien n'aurait été possible. Merci à ces grandes brutes Angelo et Jeanny avec lesquels c'est *vers l'infini et l'au-delà* et dont je suis le premier supporter ! Merci Maman et Laurent pour ce que vous avez construit, sacrifié, pour nous, regardez ce que ça donne aujourd'hui. J'espère que vous mesurerez un jour ce que cela représente pour nous ! Merci Papa et Fabienne de m'avoir soutenu et pour les moments passés ensemble, pour ce que vous m'avez donné. Le temps que l'on ne passe malheureusement pas réunis est aussi investi dans ce projet. Je remercie aussi mes grands-parents, Papi et Mamie pour votre aide, votre culture, les voyages, et un peu de mon côté Suisse, qui complète mon côté Gersois, que je dois à la générosité et la bienveillance de Mamou. Je remercie aussi plus largement ma belle-famille, les cousins-cousines, ... J'ai pour finir une pensée particulière pour ceux que j'aurais voulu rendre fiers, auxquels je pense tous les jours !

Et elle croit que je l'ai oubliée, mais non, elle a la place d'honneur dans ces remerciements ! Je remercie Melle Caroline Martin, a.k.a. el monstro, a.k.a Choumi, pour 3012 jours de soutien, de défis ensemble, le compteur court toujours pour bien plus d'aventures encore ! 54% du diplôme finalement obtenu sont à toi ! J'ai conscience de ce que tu sacrifies pour moi, tu mérites d'être heureuse, et je donnerai tout pour ça. Je t'aime.

"Boboboboooooriing"
(Pas à propos de ma thèse, hein ? Non hein ? Si ?)
- Caroline 'El Monstro' Martin - 2020 -

"On aura eu le temps de prendre le temps"
- Jeanny 'Bouge pas j'arrive' Cellier - 2022 -

"Ça s'grimpe ça"
- Angelo 'T'inquiète' Cellier - 2022 -

"Lailailai laaaaai"
- Raymond 'Paquette' Cellier - 8000 av. J. C. -

"Tu peux le mettre à l'école ça non ?"
(pointant des chaussures de skis ou vélo)
- Susanne 'Suzie' Egli-Vasse - 2010 -

"Où sont mes chaussettes ?"
- Laurent 'el Professor' Vasse - 2012 -

"Et à la fin ils se marient ?"
- Johanna 'Mamie' Egli - 2023 -

"Oh c'est rien à faire !"
(présentant un dessert digne d'un MOF)
- Yvette 'Mamou' Cellier - ca 2005 -

"Ça fait bonne mine !"
(présentant un plat digne d'un étoilé Michelin)
- Hermann 'Papi' Egli - ca 2008 -

... et enfin, une pensée va à Papou

Contents

Nomenclature	xix
1 Introduction and Context	1
1.1 Li-ion batteries in the context of the energy mix transformation . . .	1
1.2 Accidentology around Li-ion batteries	4
1.3 Description of Li-ion batteries	6
1.3.1 The Li-ion cell	6
1.3.2 Battery pack designs	8
1.4 Thermal Runaway	9
1.4.1 Thermal Runaway triggers	10
1.4.2 Course of Thermal Runaway	11
1.5 Li-ion batteries and CFD	12
1.6 Objective definition	13
I Towards the simulation of failing Li-ion battery flows	15
2 Reactive compressible flows governing equations	17
2.1 Multi-species reactive Navier-Stokes	17
2.2 Transport properties	19

2.2.1	Multi-component transport	19
2.2.2	Mixture-averaged transport	19
2.2.3	Simplified transport	21
2.3	Chemical kinetics modelling	22
2.4	Governing equations and canonical flow structures	24
3	Theoretical concepts for reactive compressible flows	25
3.1	Turbulent flows	26
3.2	Theoretical aspects of combustion	26
3.2.1	Mixing in combustion	27
3.2.2	Laminar flame structures	28
3.2.3	Turbulent combustion	31
3.3	Theoretical aspects of shocks and expansions	33
3.3.1	Shocks/expansions and failing batteries	33
3.3.2	Normal shocks jump relations	33
3.3.3	Oblique shocks relations	34
3.3.4	Prandtl-Meyer expansion	35
3.3.5	Moving shocks relations	35
3.4	Preparing a simulation setup	37
4	From theory to simulation	39
4.1	Numerical simulations and inherent constraints	40
4.1.1	Numerical schemes	40
4.1.2	The challenge of turbulent flow simulation	41
4.1.3	The challenge of turbulent combustion simulation	42
4.1.4	The challenge of shock simulation	43

4.2	A framework to unite LES and dedicated models	43
4.2.1	Governing equations for reactive Large Eddy Simulations	43
4.2.2	Dynamically Thickened Flame for LES	46
4.2.3	Shock handling methods	48
4.3	Solvers	50
4.3.1	Cantera	50
4.3.2	AVBP	50
4.3.3	Setting up the solvers for Li-ion specific cases	51
 II Chemical kinetics for the combustion of Lithium-Ion cells vent gases		53
5	Origin of the vented gaseous mixtures	55
5.1	Gas production during Thermal Runaway	55
5.1.1	Cell components and gas production	56
5.1.2	Gas production mechanisms	60
5.2	Electrolyte oxidation and combustion	64
5.2.1	Chemical kinetic schemes to assert electrolyte oxidation and combustion	64
5.2.2	Oxidation products in 0D isochoric reactors	65
5.2.3	Electrolyte species and 1D premixed laminar flames	67
5.2.4	Concluding remarks on electrolyte oxidation	70
6	A representative reduced kinetic scheme	71
6.1	Analytically reduced kinetic framework	72
6.1.1	Cost problem in multispecies environment	72
6.1.2	ARCANE	74

6.2	Vented gaseous mixtures	75
6.2.1	Selection of gaseous mixtures	75
6.2.2	Comparisons using detailed kinetic schemes	75
6.3	Derivation of the reduced scheme	78
6.4	Validation of the reduced kinetic scheme	81
6.4.1	0D isochoric auto-ignition validation	81
6.4.2	1D premixed laminar flame validation	81
6.4.3	1D counter-flow diffusion flame validation	82
6.4.4	Summary of the reduction process	82
6.5	Reduced scheme generalization test	84
6.5.1	Generalization to untested Li-ion vent gases	84
6.5.2	Generalization to pure fuels	86
6.6	Conclusion on kinetic scheme reduction	87
7	Canonical cases and model setup for 3D simulations	89
7.1	Phases of TR and reduced canonical cases	90
7.2	Shock simulation	91
7.2.1	Theoretical 1D shock-tube profiles	92
7.2.2	Simulation of 1D shock propagation	93
7.3	Laminar premixed flame simulation	97
7.3.1	1D laminar premixed flames	97
7.3.2	Setting up the DTFLES approach	101
7.4	Diffusion flame simulation	104
7.4.1	Laminar diffusion flame profiles	105
7.4.2	Mixture fraction for Li-ion vent gases	106

7.4.3	Flame indexes	108
7.4.4	Summary of the strategies for 3D simulations	110
7.5	Selection of 3D scenarios to target	112
III Experimental characterization of Li-ion vent gases jets and fires		115
8	Experimental and simulation setups and objectives	117
8.1	The BTR test bed	118
8.1.1	Targeted TR events	118
8.1.2	Description of the setup	118
8.1.3	Diagnostics	120
8.2	Test bed operation	121
8.3	Experimental/simulation validation process	122
8.4	Simulation setup	123
9	Li-ion vent gas under-expanded jets	127
9.1	Under-expanded jet simulation	128
9.2	Case-specific numerical setup	128
9.3	Selection of validation operating points	128
9.3.1	Inert surrogates	129
9.3.2	Conditions expected theoretically	130
9.3.3	Initialization of the flow	131
9.3.4	Diagnostics to compare	132
9.4	Comparison of simulation frameworks	132
9.4.1	Shock handling methods	132

9.4.2 Numerical schemes	135
9.5 Validation versus experimental	137
9.6 Conclusion on under-expanded jet simulation	142
10 Li-ion vent gas jet ignition	143
10.1 Jet flame simulation	144
10.2 Selection of a validation operating point	144
10.3 Simulation objectives	146
10.4 Case-specific numerical setup	147
10.5 Cold flow simulation	148
10.5.1 Flow initialization process	148
10.5.2 Numerical scheme comparison	148
10.6 Ignition procedure	151
10.6.1 Modelling spark ignition	151
10.6.2 Selection of a flame index	152
10.6.3 Overview of the numerical procedure versus experimental	156
10.7 Ignition to electrode anchoring	158
10.8 Timing of the electrodes crossing	159
10.9 Electrode to lip anchoring	161
10.9.1 Experimental versus simulation	161
10.9.2 Reduced Modelling	163
10.10 Conclusion on jet flame ignition simulations	165
IV Simulations of failing 18650 cells	167
11 Cell opening and initial venting	169

11.1 Cell opening experiments and CFD simulations	170
11.2 Case definition	170
11.2.1 Structure presentation	170
11.2.2 Opening conditions	172
11.2.3 Numerical setup	174
11.3 Simulation of the opening	175
11.4 Effect of confinement on the flow topology	179
11.4.1 Outline of the case	179
11.4.2 Comparison of the venting behavior	180
11.5 Conclusion on cell opening simulation	182
12 Sustained venting and flame dynamics	183
12.1 Cell fire experiments and CFD simulations	184
12.2 Case definition	184
12.2.1 Targeted fire	184
12.2.2 Presentation of the structure	185
12.2.3 Numerical setup	186
12.3 Non-reactive flow characterization	188
12.4 Forced ignition	188
12.5 Effect of design choices	190
12.5.1 Vent design	190
12.5.2 Cell internal chemistry	191
12.5.3 Summary of the effect of design choices	192
12.6 Comparison to experimental observations	193
12.7 Conclusion on sustained venting simulation	193

V	Flame acceleration and explosions for Li-ion vent gases in confined environments	195
13	Flame acceleration in a rectangular channel	197
13.1	The challenge of explosion simulations and batteries	198
13.2	Tulip flame simulation	199
13.3	Experimental and numerical setup	199
13.3.1	Source of the experimental data	199
13.3.2	Simulation framework and models	200
13.4	Validation of the simulation framework	203
13.4.1	A problem of wall boundary conditions	203
13.4.2	A procedure to better define boundary conditions	207
13.4.3	Effect of mesh refinement	211
13.4.4	Final experimental/simulation validation	214
13.5	Concluding remarks	218
14	Towards more realistic explosion simulation applied to Li-ion	219
14.1	Turbulent explosion simulation	219
14.2	Experimental and numerical setup	220
14.2.1	Experimental setup	220
14.2.2	Numerical setup	221
14.3	Results and discussions	223
14.3.1	Profiles for the entire event	223
14.3.2	Laminar phase	225
14.3.3	Obstacle crossing	227
14.4	Perspectives for explosion scenarios	229

15 Conclusions and Perspectives	231
Appendix A Reduced kinetic scheme for Li-ion vent gases	235
Appendix B Models for spark ignition procedures	241
B.1 Energy Deposition model	241
B.2 Soft Ignition with Relaxed Temperature	243
B.3 Conclusion on ignition models	244
Appendix C Under-expanded jet of pure N_2	245
Appendix D Heat release rate visualization	251
Appendix E Jet ignition using TTGC	253
Appendix F 18650 venting cell: internal details and turbulence	257
References	284

Nomenclature

Roman Symbols

C_p	Specific heat capacity of the mixture at constant pressure	$\text{J.K}^{-1}.\text{kg}^{-1}$
Da	Damköhler number	-
Ea_m	Activation energy of reaction m	$\text{mol.m}^{-3}.\text{s}^{-1}$
Ka	Karlovitz number	-
Le_n	Lewis number of species n	-
Pr	Prandtl number of the mixture	-
Re	Reynolds number	-
Sc_n	Schmidt number of species n	-
c_s	Sound speed	m.s^{-1}
D_{nm}	Binary diffusion coefficient of species n in species m	$\text{m}^{-2}.\text{s}^{-1}$
D_n	Diffusion coefficient of species n in the mixture	$\text{m}^{-2}.\text{s}^{-1}$
D_{th}	Thermal diffusivity	$\text{m}^2.\text{s}$
E	Total energy	J.kg^{-1}
G_n	Gibbs free energy of species n	J.mol^{-1}
H_n	Standard enthalpy of species n	J.mol^{-1}
$h_{s,n}$	Sensible enthalpy of species n	J.kg^{-1}
L_t	Turbulence integral length scale	m
M	Mach number	-
p	Pressure	Pa

Q_m	Reaction rate of progress of reaction m	$\text{mol.m}^{-3}.\text{s}^{-1}$
R	Universal gas constant	$\text{J.K}^{-1}.\text{mol}^{-1}$
r	Specific gas constant	$\text{J.K}^{-1}.\text{kg}^{-1}$
s	Stoichiometric ratio	-
s_c	Consumption speed	m.s^{-1}
s_L	Laminar premixed flame speed	m.s^{-1}
S_n	Standard entropy of species n	$\text{J.mol}^{-1}.\text{K}^{-1}$
S_{ij}	Symmetric strain rate tensor	s^{-1}
T	Temperature	K
t	Time	s
u_i	Velocity component associated to direction i	m.s^{-1}
u_p	Moving shock contact surface speed	m.s^{-1}
$V_{i,n}$	Diffusion velocity of species n associated to direction i	m.s^{-1}
$V_{i,n}^a$	Approximated diffusion velocity of species n associated to direction i	m.s^{-1}
$V_{i,n}^c$	Correction diffusion velocity of species n associated to direction i	m.s^{-1}
W	Molecular weight of the mixture	kg.mol^{-1}
w	Shock speed	m.s^{-1}
W_n	Molecular weight of species n	kg.mol^{-1}
x_i	Component of the position associated to direction i	m
X_n	Molar fraction of species n	-
Y_n	Mass fraction of species n	-
Z	Mixture fraction	-
a	Strain rate	s^{-1}

Greek Symbols

Δt	Time step	s
Δx	Space step	m
Δ	LES Filter characteristic length - grid scale	m

δ_L	Laminar flame thickness (superscript \cdot^{prem} or \cdot^{diff} when the combustion mode is to be specified)	m
δ_{ij}	Kronecker delta	-
$\dot{\omega}_n$	Production rate of species n	$\text{kg.m}^{-3}.\text{s}^{-1}$
$\dot{\omega}_T$	Heat release rate	$\text{J.m}^{-3}.\text{s}^{-1}$
η_K	Kolmogorov length scale	m
γ	Isentropic expansion ratio	-
λ	Thermal conductivity	$\text{W.K}^{-1}.\text{m}^{-1}$
λ_n	Pure species thermal conductivity of species n	$\text{W.K}^{-1}.\text{m}^{-1}$
μ	Laminar dynamic viscosity	Pa.s
μ_n	Pure species laminar dynamic viscosity of species n	Pa.s
ν	Kinematic viscosity	$\text{m}^2.\text{s}^{-1}$
ϕ	Equivalence ratio	-
ρ	Gas density	kg.m^{-3}
τ_C	Combustion time scale	s
τ_I	Turbulence integral time scale	s
τ_K	Kolmogorov time scale	s
τ_{ij}	Viscous stress tensor	$\text{kg.m}^{-1}.\text{s}^{-2}$
ε_i	Total deposited energy (Energy Deposition model)	
Ξ	Thickened flame efficiency function	-

Superscripts

\cdot'	Referring to fluctuations
\cdot^t	Refers to the modelled turbulent contribution (LES)
\cdot^-	Refers to the classical Reynolds spatial filtering
$\cdot\tilde{\cdot}$	Refers to the Favre mass-weighted spatial filtering

Subscripts

\cdot_L	Referring to a laminar flow structure
-----------	---------------------------------------

.*t* Referring to turbulence

.*st* Referring to stoichiometric conditions

Acronyms / Abbreviations

ARC Analytically Reduced Chemistry

CMC Carboxymethyl Cellulose

DRGEP Direct Relation Graph with Error Propagation

DEC Di-Ethyl Carbonate

DMC Di-Methyl Carbonate

EC Ethyl Carbonate

EMC Ethyl-Methyl Carbonate

PC Propylene Carbonate

HC Hydrocarbon

LCO Lithium Cobalt Oxide cathode active material

LFL Lower Flammability Limit

LFP Lithium Iron Phosphate cathode active material

LHV Lower Heating Value

$J.m^{-3}$

LMO Lithium Manganese Oxide cathode active material

LNMO Lithium Nickel Manganese Oxide cathode active material

NCA Lithium Nickel Cobalt Aluminum Oxide cathode active material

NMC Lithium Nickel Manganese Cobalt Oxide cathode active material

PE Poly-Ethylene

PP Poly-Propylene

PVDF Polyvinylidene Fluoride

QSS Quasi-Steady State

SEI Solid Electrolyte Interphase/Interphase

SoC State of Charge

1D One-Dimensional

2D	Two-Dimensional	
3D	Three-Dimensional	
CAD	Computer Assisted Design	
CC	Cook and Cabot shock handling method	
CFD	Computational Fluid Dynamics	
CPU	Central Processing Unit	
DNS	Direct Numerical Simulation	
DTF	Dynamically Thickened Flame	
DTFLES	Dynamically Thickened Flame for LES	
ED	Energy Deposition ignition model	
HRR	Heat Release Rate	$\text{J.m}^{-3}.\text{s}^{-1}$
HRR_{int}	Integral Heat Release (1D)	$\text{J.m}^{-2}.\text{s}^{-1}$
LAD	Localized Artificial Diffusion	
LES	Large Eddy Simulation	
LW	Lax Wendroff numerical scheme	
MRE	Mean Relative Error	
NRMSE	Normalized Root Mean Square Error	
NSCBC	Navier-Stokes Characteristic Boundary Conditions	
PM	Creck modelling group kinetic scheme	
RANS	Reynolds Averaged Navier-Stokes	
SD	San Diego kinetic scheme	
SGS	Sub-Grid Scale	
SIRT	Soft Ignition with Relaxed Temperature ignition model	
TF	Thickened Flame	
TR	Thermal Runaway	
TTG	Two-step Taylor Galerkin numerical scheme family	
WALE	Wall Adapting Local Eddy-viscosity	

Chapter 1

Introduction and Context

Contents

1.1 Li-ion batteries in the context of the energy mix transformation	1
1.2 Accidentology around Li-ion batteries	4
1.3 Description of Li-ion batteries	6
1.3.1 The Li-ion cell	6
1.3.2 Battery pack designs	8
1.4 Thermal Runaway	9
1.4.1 Thermal Runaway triggers	10
1.4.2 Course of Thermal Runaway	11
1.5 Li-ion batteries and CFD	12
1.6 Objective definition	13

1.1 Li-ion batteries in the context of the energy mix transformation

The growing collective awareness on questions of energy production and distribution is built on two centuries of research, controversy and breakthroughs. Starting from observations made in the early 1800s by Fourier, and regularly enhanced until the beginning of the XXth century by Foote, Tyndall and Arrhenius, the notion of greenhouse effect slowly raised concerns. The massive use of fossil sources of energy [122] emitting greenhouse gases (CO_2 , H_2O ¹, CH_4 , N_2O , ...) modifies the radiative property of the atmosphere leading to warming runaway.

¹The share from human activities adds to the share naturally present in the atmosphere

In 1979, the first World Climate Conference² reported the rapid course of global warming and set milestones to fight the impending environmental and social crisis. Demands for action flourished and updated reports listed the consequences of driving the global mean temperature to an elevation exceeding 1.5°C [114, 119, 120]³, fueling political decisions to make in the years to come⁴. Massive droughts [258, 270], drastic modifications of weather [211, 275], increase in sea-level due to ice-cap melting [61], biodiversity depletion [217, 170, 82] will impact societal constructions in the very near future [134, 4, 106].

The energy industry must change and adapt a new calendar where sustainable production and distribution chains are prioritized [121], while reducing inequality in access to energy [28]. The energy mix started to evolve towards less carbonated fuels, and sustainable forms take a greater share, intended to grow rapidly [58] (see Fig. 1.1.1).

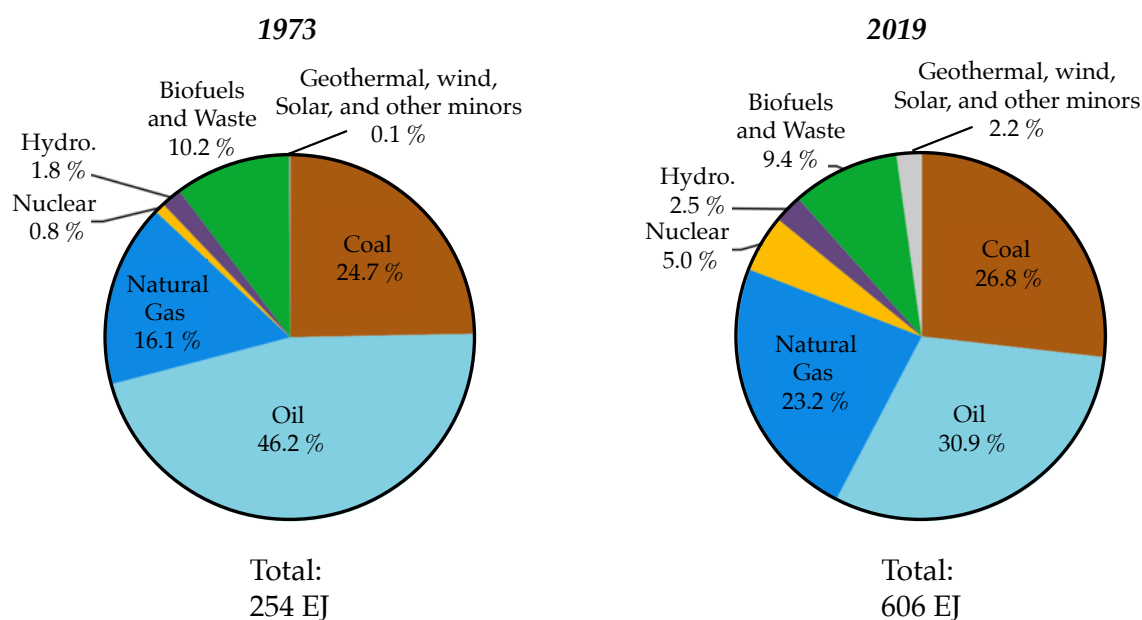


Figure 1.1.1: Energy distribution in 1973 and 2019, reproduced from [122].

With an increase of sustainable energy sources (often under the form of electricity), efficient storage systems become the kingpin in multiple domains. Energy production-consumption suffer from seasonal variability [123], demanding long-term storage systems. In addition to this, renewable energy can be submitted to day-to-day/hour-to-hour cycle variations (solar panels, wind turbines, ...) adding the problem of short-term storage. Producing safe and reliable storage to smooth production versus demand is essential. In conjunction of the energy sector, portable

²Held in Geneva, February 12 to 23, 1979

³Funded in 1988, the Intergovernmental Panel on Climate Change (IPCC) delivered their most recent full reports during the 2021-2023 period

⁴Such as the Paris Agreement under the United Nations Framework Convention on Climate Change, held in Le Bourget, November 30 to December 12, 2015

solutions for transportation or personal devices drive a rapid increase in the development of affordable storage strategies [107]. Realistic solutions include the use of carbon-free fuels (mainly hydrogen and ammonia) to feed the next generation of combustion devices, and hydrogen fuel cells or Lithium-ion (Li-ion) batteries to supply electrical systems. Technological breakthroughs are expected to fill the gap between low-carbon and conventional fossil sources of energy [235, 14, 71, 70] (see Fig. 1.1.2). Recent findings motivate the use of hydrogen as a preferred source of energy for the future, with increases in specific energy and energy density of recent and coming technical solutions [204, 8, 266], shifting hydrogen storage closer to the liquid hydrogen physical limits ($2.3 \text{ kWh}\cdot\text{L}^{-1}$, $33.3 \text{ kWh}\cdot\text{kg}^{-1}$). During the technological revolution to come, Lithium-ion is expected to play a crucial transitioning role [304].

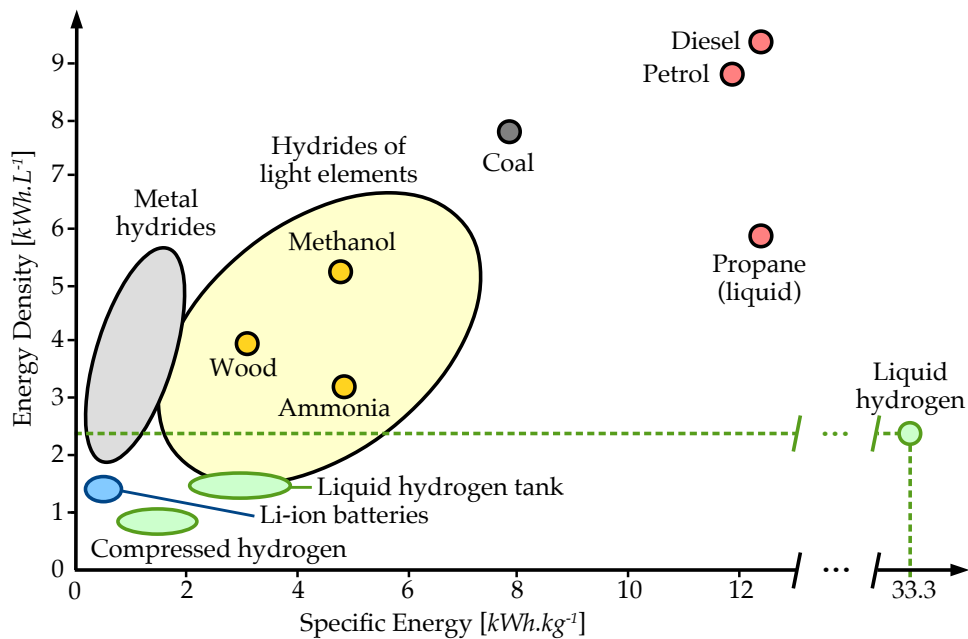


Figure 1.1.2: Energy density versus specific density of energy storage systems and materials, reproduced from [235].

Already widespread, Li-ion benefits from its maturity to solve successfully a variety of storage, and conversion questions [9, 239, 289, 158, 224]. Li-ion batteries are the preferred storage system for wind and solar energy production-demand management [68, 234, 156, 295], and are the center of attention concerning personal vehicles [25, 177, 124, 300, 66]. The sudden increase in battery production in recent years [123] due to the promotion of greener mobility and consumption drives the necessity to improve production processes [69] and mitigate safety flaws. This latter concern is the object of study in this work. Li-ion batteries are prone to specific accidents leading to fires and explosions. The following section summarizes the past decade's accidentology around Li-ion batteries, setting the bigger picture for a numerical study of battery-related combustion scenarios.

1.2 Accidentology around Li-ion batteries

The acceleration of the Li-ion market increased the occurrence of statistically rare events called Thermal Runaway (TR). A certain propensity to become thermally unstable has been observed, leading to critical fires and explosions. Before elaborating on the triggers of such events, a list of incidents widely covered in the media is proposed. The list is divided into two parts, making a distinction between 'fires' and 'explosions'. 'Fires' refers to overall steady long-lasting flames, where no blast is heard, while 'explosions' is reserved for rapid expanding free flames accompanied by overpressures. Table 1.2.1 summarizes recent fires events and Table 1.2.2 lists explosions.

Table 1.2.1: Fire accidentology summary concerning large scale Li-ion storage systems or facility and transportation applications.

Year	Location	Description	Source
2013	Boston (USA)	Boeing 787 Dreamliner grounded during investigation of battery induced fires.	https://bit.ly/3zHphX2
2014	-	Sony recalls a recently released computer due to battery malfunction and risks of fires.	https://bit.ly/3UkdYh4
2016	-	Samsung compelled to recall phones due to multiple battery fires.	https://bit.ly/3nYbM2E
2017	Drogenbos (Belgium)	A large fire destroys an Energy Storage System (ESS).	https://bit.ly/3Yl7kZV
2018	- (S. Korea)	Several ESS catch fire, raising concerns about their widespread use in solar panel farms.	http://bit.ly/43ksk5e
2021	Morris (USA)	Large fire and toxic smoke due to the defect of cells in a large unprotected storage facility for Li-ion batteries.	http://bit.ly/3TW28rr
2022	Azores (Portugal)	A fire in a cargo ship, fueled by burning electric vehicles, is difficultly put out by maritime authorities.	https://bit.ly/41aAwD5
2022	Paris (France)	Two electric buses rapidly burn down after a battery malfunction.	http://bit.ly/3OxuTtv

Continued on next page

Table 1.2.1 – *Continued from previous page*

Year	Location	Description	Source
2023	Sacramento (USA)	Electric vehicles fires are regularly broadcasted, feeding the reluctance of the public to transition towards full electric.	https://bit.ly/3zK5je9
2023	Poitiers (France)	A battery module catches fire under the seat of a wagon from an attraction in an amusement park, two people are injured.	https://bit.ly/41kdJ7W

Table 1.2.2: Explosion accidentology summary concerning large scale Li-ion storage systems or facility and transportation applications.

Year	Location	Description	Source
2017	Houston (USA)	Train car catches fire and a container of Li-ion cells explodes.	http://bit.ly/3gAJ58q
2019	Surprise (USA)	TR led to gas accumulation concluded by the explosion of an ESS.	http://bit.ly/3U8Fo80
2019	Montreal (Canada)	An electric vehicle caught fire and vented flammable gases inside the garage that eventually blew up.	http://bit.ly/3OvO9rx
2019	Boulouparis (France)	Two ESS catch fire in a solar panel station, one container explodes after the intervention of firefighters.	https://bit.ly/3HBeHWH
2019	Bergen (Norway)	An hybrid ferry is hit by a fire. Hours after extinction, an explosion occurs in an adjacent room.	http://bit.ly/3Vf9Ei8
2020	Sanming (China)	An electric car explodes due to charging malfunction, despite water cooling	http://bit.ly/3FnEnDG
2021	Ningxiang (China)	An explosion occurs at a battery recycling factory.	http://bit.ly/3i4p22H
2021	Beijing (China)	A large battery in fire explodes during the intervention of firefighters.	http://bit.ly/3EoOo2Q
2022	Cheongju (S. Korea)	Blasts are heard before fire and smoke destroys a cathode production factory.	http://bit.ly/3EXYoBL

Continued on next page

Table 1.2.2 – *Continued from previous page*

Year	Location	Description	Source
2022	Althengstett (Germany)	An explosion destroys an apartment building after a solar panel battery fails.	http://bit.ly/3OyqSVW
2022	Fuzhou (China)	A blast destroys an electric car after battery enter thermal runaway due to summer heat.	https://yhoo.it/3YkSClm

The storage and transportation of batteries raise concerns at the highest levels [73]. Studying the triggers and mitigation opportunities to Li-ion-related combustion events forms the thread of the study proposed in this manuscript. The description of canonical Li-ion batteries follows, and explanations on the origin of battery decomposition and the definition of scenarios to focus on complete this introduction chapter.

1.3 Description of Li-ion batteries

Before defining Thermal Runaway, it is necessary to describe the main components and formats available in the Li-ion family, showing the diversity of scales to consider.

1.3.1 The Li-ion cell

The Lithium-Ion battery technology is adapted to various formats depending on the targeted application. The fundamental brick of Li-ion battery packs is the cell, where the critical chemical events occur. Four distinct cell categories are commonly used: 1. Pouch cells, 2. Prismatic cells, 3. Cylindrical cells, 4. Coin cells (see Fig. 1.3.1) [238]. For pouch cells, internal components are put into a soft bag. The bag is drained from gases. Aluminum foils are commonly used for their strength and isolating properties but polymer based bags are also considered. The softness and thinness of the material is a direct limitation to bending resistance and increases cell-to-cell thermal transfers, stiff spacers and hard-shell casings are used when mounting the final battery. Prismatic and cylindrical cells are of common use in large battery packs, and stainless-steel is preferred offering structural resistance, and accessibility to the raw material. Coin cells apply to small systems where volume and weight is limiting, and where the power demand is low. The casing is usually made of stainless-steel [283].



Figure 1.3.1: List of the most common cell housing types with illustrating examples [231].

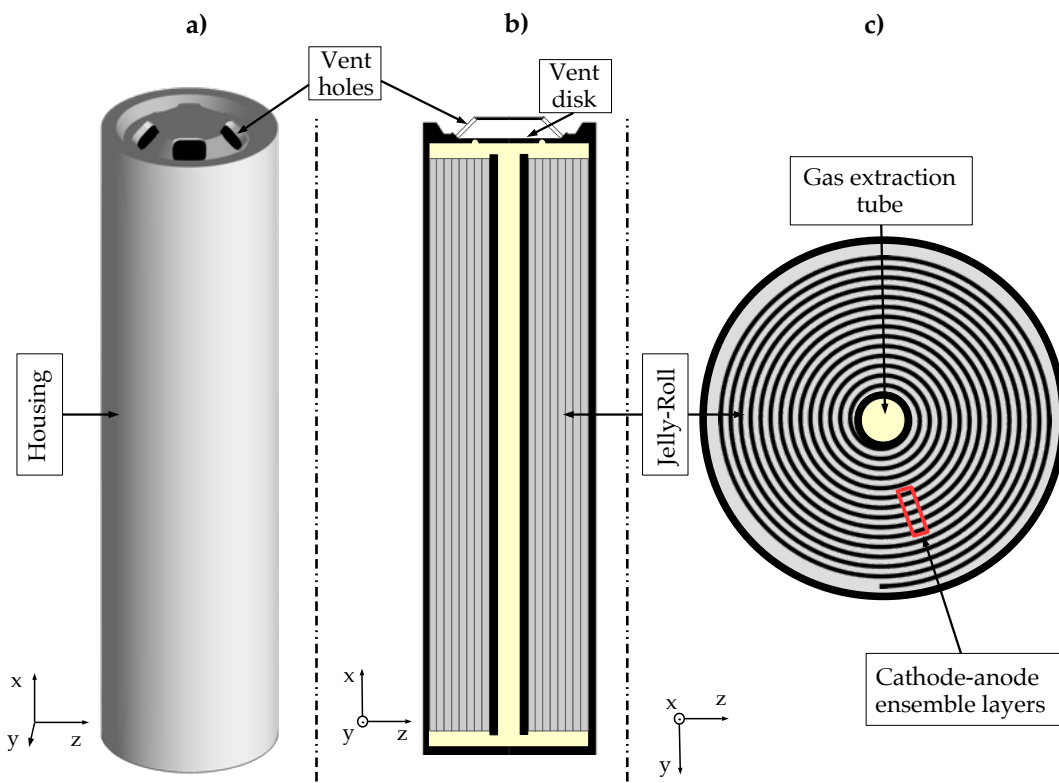


Figure 1.3.2: Description of the components of a generic Lithium-ion cell (here the 18650 cylindrical cell is chosen) [79]: a) External aspect of the cell, b) Longitudinal cut of the cell, c) Transverse cut of the cell with the depiction of the many layers composing the cathode-anode ensemble.

A general representation of a 18650 Lithium-ion cell is given in Figure 1.3.2. The 18650 format representing a cylindrical cell of 18 mm in diameter and 65 mm in length is prevalent in the industry [192], and will be taken as the object of study when an example is needed. A closer look on one layer of anode-cathode ensemble is given in Fig. 1.3.3. Battery charging and discharging phases consist in the migration of Li^+ ions between anode and cathode. While the anode is often made of a copper sheet coated with graphite, a larger diversity exists for the cathode, depending on the use case (power demand, current demand, endurance, ...). In general, the order of magnitude of the energy available for one cell ranges from 0.1 Wh to 100 Wh, which is perfectly fitted for small scale applications (portable devices). When larger applications are targeted, cells can be packed to form modules (0.1-10 kWh), or containers (up to a few MWh). More information on battery pack designs is proposed in the next section.

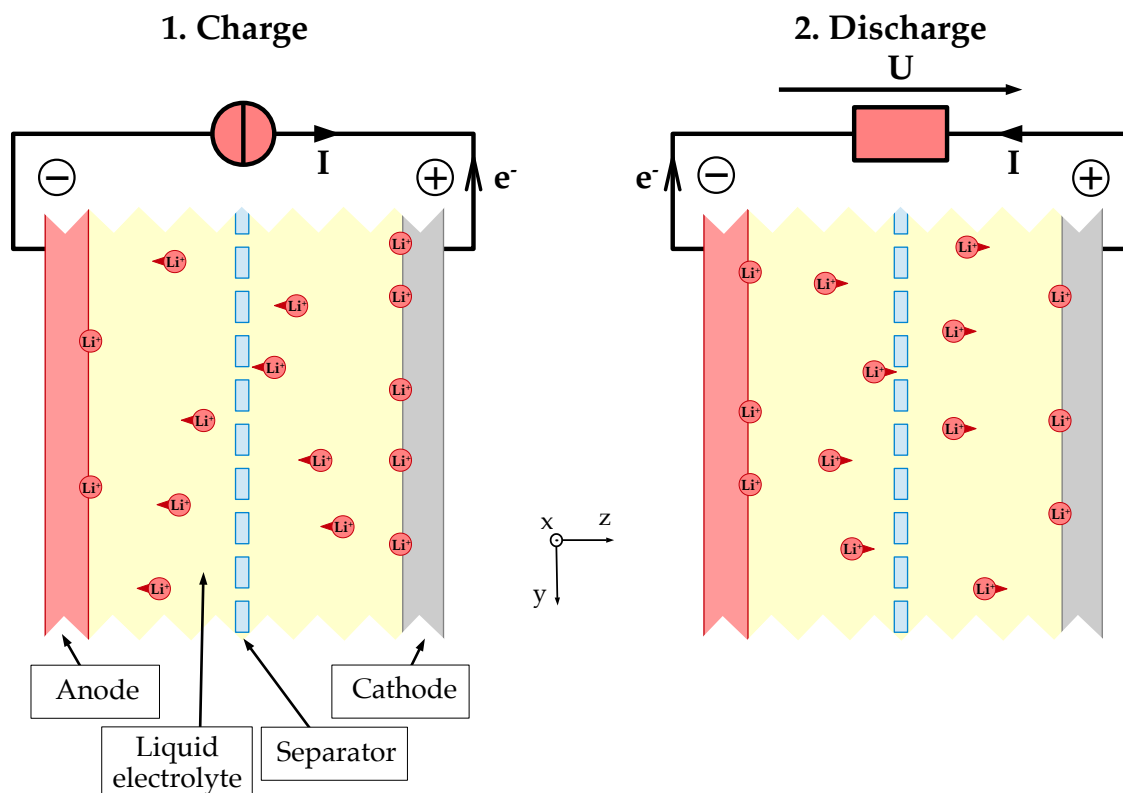


Figure 1.3.3: Schematic representation of one cathode-anode layer [233, 283], with charging and discharging phases.

1.3.2 Battery pack designs

For large applications requiring higher energy/power levels, cells are integrated into modules or into packs, and wired through power electronics, along with a Battery Management System (BMS), to fit performance and safety requirements (see

Fig. 1.3.4). In case of a single cell failure, heat could propagate from cell to cell, resulting in the triggering of TR in adjacent cells, multiplying the problem of heat generation and fire by the size of the system. Three characteristic rule-of-thumb dimensions can be introduced for the problem of failing batteries:

1. **Cell level:** The characteristic dimension is the cubic centimeter. The energy scale is the Wh (ex. portable devices such as phones).
2. **Module level:** For modules containing the equivalent of 10 000 individual cells, characteristic dimensions reach 0.1-1.0 cubic meter, scaling to the kWh (ex. individual electric vehicle).
3. **Container level:** Selected to store from large scale energy production facility, containers are filled with the equivalent of several hundreds modules, in several cubic meters, reaching the MWh scale (ex. solar power-plant storage system).

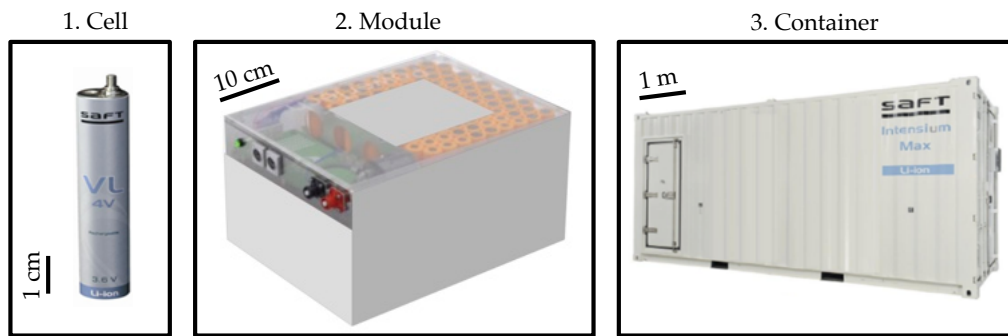


Figure 1.3.4: Representative scales of battery packaging [231].

While most critical issues with batteries are linked to the higher scales (large fires, explosions), an important part of the work implies to understand the physics at the smallest scale. The origin of large battery failures is often identified to be caused by a fault at the smallest scale, propagating from scale to scale due to heat transfers [248, 150, 74, 51]. The key phenomenon at the source of most failing batteries that leads to fire is the Thermal Runaway of one cell. A description of the chain of events triggered when cells enter in Thermal Runaway mode is the subject of the next section.

1.4 Thermal Runaway

When misused or malfunctioning, lithium-ion batteries are submitted to a critical self-heating accompanied by a production of hot flammable and toxic gases, that can lead to fire: it is called a Thermal Runaway (TR) [164, 75, 144, 86, 26, 44]. A familiarization to TR triggers and chain of key events is proposed in this section.

1.4.1 Thermal Runaway triggers

At the source of TR events, there are self-heating reactions in a medium where a large amount of chemical energy is stored [78, 76]. The trigger for these reactions are classified into three main categories [44]:

1. **Mechanical abuse:** When the cell is punctured, bent, crushed or cracked open, layers of anode and cathode made to be isolated using the separator are forced in contact, creating a local short circuit, often the source of an electrical arc releasing suddenly heat into the medium. It locally vaporizes the components, and initiates the reactions between components originally isolated [75].
2. **Electrical abuse:** A first type of electrical abuse is the external short-circuit of the cell which generates a sudden heat release at electrodes collectors. The energy released is sufficient to initiate the exothermic reactions of decomposition of the electrolyte material, starting TR [139, 249]. A second type of electrical abuse is the overcharge due to a malfunction of the battery management system. The excess current flowing into the battery produces heat due to internal resistance which triggers reactions homogeneously [249]. It is a critical abuse condition as TR is violent and no internal propagation phase is needed.
3. **Overheating:** Overheating-to-TR experiments are typical safety tests to perform in order to validate the capability of the cell to resist to its surrounding constraints. When the temperature overshoots the electrolyte ebullition temperature, bubbles form, and the separator shrinks giving way to short-circuits, leading to TR [75, 164].

One or more abuse conditions may occur at the same time, speeding up the first steps of TR, jumping rapidly to reactions at the cell level. Also, aggravating factors have been identified. For example, the State of Charge (SoC) of the battery is used to evaluate the level in % of ions intercalation inside each side. If the SoC is maintained over 100 %, the resistance to mild abuses (shocks, mild overheating, ...) is reduced and the cell may become prone to switch violently to TR mode [249]. Also, aging or initial small production defects move batteries closer to instability.

Overall, once reactions are triggered, the chain of events is similar for all abuse conditions. The thermal runaway rapidly extends to the entire cell due to the heat produced [301, 78]. The typical course of events in the minutes following the trigger is further outlined in the next section.

1.4.2 Course of Thermal Runaway

The course of Thermal Runaway, from one failing cell to the propagation to higher scales is depicted in Fig. 1.4.1.

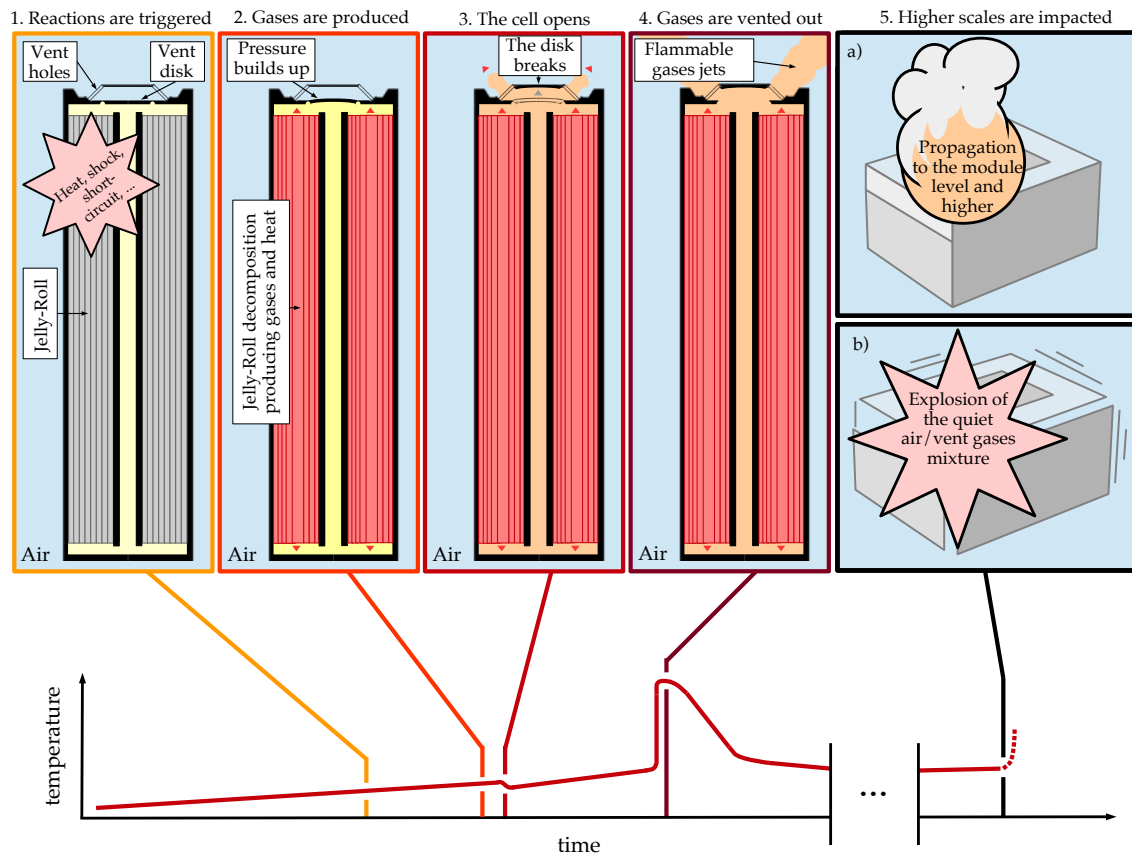


Figure 1.4.1: Usual course of the thermal runaway using a cut-view of a 18650 cell [75]; the different phases refer to the temperature at the cell surface [96].

After TR is triggered (1. in Fig. 1.4.1), the reactivity increases exponentially inside the cell, self sustained by the exothermic reactions. Flammable gases are produced which increases the pressure inside the cell (2. in Fig. 1.4.1). To avoid a complete rupture of the cell structure, the over-pressure must be managed. For prismatic and pouch cells, the corners and joints are structural weak points, and they tend to brake first. For cylindrical cells, the strength of the structure makes mandatory to add breaking disks, calibrated to open under a certain pressure (3. in Fig. 1.4.1). The opening pressure of both types of cell is strongly depending on the manufacturer, but for example, Mier *et al.* [11, 188] obtained experimentally the opening pressure for two types of 18650 cells. The mean value reaches 2.03 MPa. For a battery venting into the atmosphere, a ratio of 20 exists between the internal pressure and the atmospheric pressure. The sudden expansion lowers the temperature of the cell and slows down the decomposition reactions. However, reactions are still running and temperature increases again along with the mass-flow of the gases

vented out by the opened cell, leading to the formation of a sustained jet or, in case of ignition, a jet flame (4. in Fig. 1.4.1). The heat produced by the failing cell and eventual flames propagates inside the module until TR is triggered generally (5. in Fig. 1.4.1). Three potential conclusions come in the picture: 1. the entire battery burns down, 2. unburnt gases accumulate in the free space and mix with air, leaving the explosive mixture for a potential delayed ignition, 3. countermeasures are in place to slow down the propagation from cell to cell (cooling circuit, inert gases injection, ...).

All the phases identified during TR are critical from a design point of view. Being able to assert them properly helps to reduce the consequences of a cell failure. The simulation of a selection of critical events based on design choices becomes an interesting tool to avoid additional costs during prototyping phases, and difficulties during tests for badly designed batteries, by selecting *a priori* promising designs.

1.5 Li-ion batteries and CFD

In view of the consequences of a badly managed TR, multiple studies have been focused on the reproduction of Li-ion accidents, experimentally and numerically. Compilations of results have been proposed [75, 252, 44, 227] which are essential to feed simulation frameworks with operating conditions and geometries of interest. The access to operating conditions is key, and may be complex for such safety processes. Venting following cell opening is explored in [151, 79, 96, 97] with a special focus on the opening process in [11]. Cell fire is characterized in [85, 164, 150, 88] which leads to the documentation of its impact on the process of heat propagation into larger batteries [157, 87, 282, 242, 280]. More rarely, explosions due to vent gases begin to be documented opening the perspectives to high fidelity simulations of such critical events [62, 111, 112]. Once operating conditions are selected, scenarios using simulation can be proposed, for example by computing the influence of TR on cell structure [80, 160, 159], or reproducing internal processes [135, 281]. In that direction, the use of Computational Fluid Dynamics (CFD) becomes essential to observe and predict flows induced by TR, including venting, fires and explosions. In recent studies, CFD has been applied to cell venting [161, 136] and cell fire [143] showing the feasibility and potential of such simulations. Also, applications to heat propagation for the design of cooling systems is discussed in [162, 250, 278]. Eventually, the topic of CFD simulations of TR vent gases induced explosions is a growing subject [111, 112, 205] where mitigation solutions have to be prepared.

In the work presented here, approaches to perform CFD simulations of battery accidents are proposed using the platform AVBP [37, 237], serving as a laboratory for the development of tools, and procedures applied to Li-ion accidents. Steps to take in order to ensure a level of fidelity of the scenarios reproduced is at the center of the discussions.

1.6 Objective definition

In order to treat generic scenarios related to failing Li-ion batteries and enhance applicability, reference to the widely used 18650 design will be preferred (see Fig. 1.3.2). As mentioned in the previous section, typical events can be isolated during TR, where critical flow structures can be observed, reproduced experimentally, and numerically. Studying them separately help to assert how design and flow interact, depending on the phase and scale represented. For this study, and in particular for 18650 cells, three main events are part of the objectives:

1. **Opening:** The simulation of the sudden opening of a 18650 cell is proposed, along with the impact of confinement on the venting process.
2. **Sustained venting:** The simulation of flames igniting on top of a 18650 cell is then given, asserting the effect of vent cap design and cell internal chemistry.
3. **Explosion:** The simulation of the delayed explosion of unburnt gases mixed with air in different configurations concludes the objective, helping to scale up from a one-cell-problem to a many-cells-problem. Explosion is identified as the most critical issue at the scale of a module. Cell-to-cell propagation is part of the perspectives of this study.

When considering the multitude of potential failures leading to combustion for Lithium-ion applications, it is necessary to assert where simulation could help to 1. predict incidents and 2. help to design the next generations of batteries in terms of thermal management, composition, or safety add-ons. The three critical events targeted give way to multiple questioning where methods from the existing must be verified or adapted. To obtain qualitative and quantitative results for these events, it is necessary to set and adapt simulation backgrounds for Li-ion vent gases under typical TR conditions, and propose validations and applications of the methodology to assert Li-ion related safety issues. It demands several actions addressed in this manuscript:

1. **Part I:** An introduction to the background concepts used for the simulation of critical events during TR is given, including governing equations (**Chapter 2**), theoretical aspects of flow structures observed around failing batteries (**Chapter 3**), the choice of a simulation framework to alleviate constraints posed by the listed flow structures (**Chapter 4**).
2. **Part II:** It is followed by the description of the gases vented-out by a failing battery (**Chapter 5**) and a kinetic modelling of these gases that generalizes well under the range of combustion phenomena targeted (**Chapter 6**). It is completed by the study of canonical 1D scenarios with Li-ion vent gases,

helping to prepare 3D simulation setups, in terms of flame modelling and shock handling for such mixtures (**Chapter 7**).

3. **Part III**: A first experimental/simulation validation is performed, for a laboratory scale configuration mimicking conditions of venting around a single cell (**Chapter 8**). Cases targeted are: 1. turbulent inert jets at high mach numbers to reproduce opening (**Chapter 9**), 2. ignition and stabilization of turbulent diffusion jet flames close to conditions of sustained venting of hot vent gases (**Chapter 10**).
4. **Part IV**: The focus is then on applications to the design of cells, for cases representative of real TR situations with the focus on cell opening (**Chapter 11**), and sustained venting and fire (**Chapter 12**).
5. **Part V**: To go beyond the scale of one cell, it is proposed to assert the feasibility of Li-ion related explosion simulations. Explosions in open tubes of vent gases premixed with air, without obstacles (**Chapter 13**), and with obstacles (**Chapter 14**) are targeted based on literature experimental results, giving perspectives for the design of modules using simulation, including explosion scenarios predictions.

The study is supported by SAFT batteries⁵ and TotalEnergies-OneTech⁶ both inputting industrial aspects, and funding experimental investigations conducted at the Pprime institute⁷. Part of the work also benefitted from HPC resources from GENCI-IDRIS⁸. The complementary contribution of modelling, experimental validation and demonstration of potential applications must help to ensure a certain level of confidence when applying simulation methodologies to solve the three critical events observed when Li-ion batteries become thermally unstable. It is proposed to take a step towards a larger use of simulation at prototyping phases when targeting new safer battery designs.

⁵111 Bd. Alfred Daney, 33074 Bordeaux, France [231]

⁶92400 Courbevoie, France [263]

⁷2 Bd. des Frères Lumière, 86360 Chasseneuil-du-Poitou, France [218]

⁸Rue John Von Neumann, 91403 Orsay, France [90, 117]

Part I

Towards the simulation of failing Li-ion battery flows

Chapter 2

Reactive compressible flows governing equations

Contents

2.1	Multi-species reactive Navier-Stokes	17
2.2	Transport properties	19
2.2.1	Multi-component transport	19
2.2.2	Mixture-averaged transport	19
2.2.3	Simplified transport	21
2.3	Chemical kinetics modelling	22
2.4	Governing equations and canonical flow structures	24

In this chapter, general equations describing compressible reactive flows are introduced. The equations set the grounds for theoretical details specific to turbulent flows, combustion, shocks and expansions.

2.1 Multi-species reactive Navier-Stokes

Modern fluid dynamics mathematical descriptions inherited from three centuries of evolution. From Euler's equations in 1757, and theoretical inviscid fluid dynamics, to the addition of viscosity notions by Navier and Stokes during the XIXth century. When considering reacting flows, several species composing a mixture must be linked through reactions. To describe a mixture, the molar (resp. mass) fraction of the species $n \in \llbracket 1, N \rrbracket$ in the global mixture X_n (resp. Y_n) is defined as the ratio between the number of moles of species n divided by the total number of moles of the mixture

(resp. the mass of species n divided by the total mass). Both descriptions are linked by the molecular weight of species n , W_n :

$$Y_n = \frac{X_n W_n}{\sum_{m=1}^N X_m W_m} \quad (2.1)$$

Both fractions conveniently sum to one. Then, an extension of the conservation laws for multi-species compressible newtonian fluids can be written as follows [213]:

Mass conservation:

$$\frac{\partial \rho}{\partial t} + \frac{\partial \rho u_i}{\partial x_i} = 0 \quad (2.2)$$

Momentum conservation:

$$\frac{\partial \rho u_j}{\partial t} + \frac{\partial \rho u_i u_j}{\partial x_i} = -\frac{\partial}{\partial x_i} \left(p \delta_{ij} + \mu \left(\frac{2}{3} \frac{\partial u_k}{\partial x_k} \delta_{ij} - \left(\frac{\partial u_j}{\partial x_i} + \frac{\partial u_i}{\partial x_j} \right) \right) \right) \quad (2.3)$$

Species conservation:

$$\frac{\partial \rho Y_n}{\partial t} + \frac{\partial \rho Y_n u_i}{\partial x_i} = -\frac{\partial \rho Y_n V_{i,n}}{\partial x_i} + \dot{\omega}_n(Y_n, T) \quad (2.4)$$

Energy conservation:

$$\begin{aligned} \frac{\partial \rho E}{\partial t} + \frac{\partial \rho u_i E}{\partial x_i} = & -\frac{\partial}{\partial x_i} \left(p u_j \delta_{ij} + \mu u_j \left(\frac{2}{3} \frac{\partial u_k}{\partial x_k} \delta_{ij} - \left(\frac{\partial u_j}{\partial x_i} + \frac{\partial u_i}{\partial x_j} \right) \right) \right) \\ & + \frac{\partial}{\partial x_i} \left(\lambda \frac{\partial T}{\partial x_i} \right) + \frac{\partial}{\partial x_i} \left(\sum_{n=1}^N \rho Y_n V_{i,n} h_{s,n} \right) + \dot{\omega}_T(Y_n, T) \end{aligned} \quad (2.5)$$

where ρ is the density, p the pressure, T the temperature. $(u_i)_{i \in \{1,2,3\}}$ are the velocity components, and E the total energy ($E = e_s + \frac{u_i u_i}{2}$). The mass fractions, mole fractions, molecular weights, Schmidt numbers, production rates and sensible enthalpies of the n^{th} species ($n \in \llbracket 1, N \rrbracket$) are written as Y_n , X_n , W_n , Sc_n , $\dot{\omega}_n$ and $h_{s,n}$ respectively. $(\delta_{ij})_{i,j \in \{1,2,3\}}$ is the Kronecker delta, $\dot{\omega}_T$ is the heat release rate, C_p is the mixture specific heat capacity, μ is the laminar dynamic viscosity, and λ is the mixture conductivity. The perfect gas law closes the set of equation:

$$p = \rho r T \quad (2.6)$$

where r is the specific gas constant of the mixture.

For simplification purposes, the two reciprocal Dufour effect (variations of temperature due to species gradients) and Soret effect (diffusion induced by temperature

gradients) are discarded in these equations and in the rest of this work. Those effects are negligible in most applications targeted here [93], except for hydrogen combustion where future works will focus on closing this modelling gap.

In conclusion, for these expressions, the reactive multi-species framework introduces two mechanisms which influence flow properties. The first one (transport processes) includes diffusion velocities, viscosity and conductivity. The second one concerns chemical reactions between species. The following sections emphasize the most common solutions chosen to assert those problems.

2.2 Transport properties

Strategies to compute diffusion velocities $V_{i,n}$, mixture dynamic viscosity μ , and mixture thermal conductivity λ in CFD can be gathered into three categories. They are introduced, following a descending computational cost order.

2.2.1 Multi-component transport

Solving for exact diffusion velocities $V_{i,n}$ is done by searching the solution of the $N \times N$ -sized linear system for each of the three directions ($i \in 1, 2, 3$) [286]:

$$\frac{\partial X_m}{\partial x_i} = \sum_{n=1}^N \frac{X_n X_m}{D_{nm}} (V_{i,n} - V_{i,m}) \quad (2.7)$$

for $m \in [1, N]$. $D_{nm} = D_{mn}$ corresponds to the binary diffusion coefficient of species n into species m . Pressure forces, gravity and electro-magnetism are neglected.

This type of transport is adapted to chemical solvers under very simple cases [99]. In practice, due to the number of species, the mesh refinement, and mesh total number of cells necessary to simulate complex 3D combustion phenomena precisely, the computation of the diffusion velocities at each mesh node, each time step, for three directions is generally too intensive for CFD solvers. Therefore, simplifying assumptions are to be made.

2.2.2 Mixture-averaged transport

A first order approximation of the system given in Eq. 2.7 is proposed by Hirschfelder and Curtiss [113, 92]:

$$V_{i,n}^a = -\frac{D_n}{X_n} \frac{\partial X_n}{\partial x_i} \quad (2.8)$$

where D_n is the diffusion coefficient of species n into the mixture:

$$D_n = \frac{1 - Y_n}{\sum_{m=1, m \neq n}^N \frac{X_m}{D_{mn}}} \quad (2.9)$$

To render a mass conservative version of this first order approximation, correction velocities V_i^c must be added so that $\sum_{m=1}^N Y_m (V_{i,m}^a + V_i^c) = 1$:

$$V_i^c = \sum_{m=1}^N D_m \frac{W_m}{W} \frac{\partial X_m}{\partial x_i} \quad (2.10)$$

Eventually, the diffusion velocities write as:

$$V_{i,n} = V_{i,n}^a + V_i^c = -\left(\frac{D_n}{X_n} \frac{\partial X_n}{\partial x_i} - \sum_{m=1}^N D_m \frac{W_m}{W} \frac{\partial X_m}{\partial x_i} \right) \quad (2.11)$$

In addition, mixture dynamic viscosity is obtained using the modified Wilke formula [285, 181]:

$$\mu = \sum_{n=1}^N \frac{\mu_n X_n}{\sum_{m=1}^N X_m \Phi_{nm}} \quad (2.12)$$

with

$$\Phi_{nm} = \frac{1}{2\sqrt{2}} \left(1 + \frac{W_n}{W_m} \right)^{-\frac{1}{2}} \left(1 + \left(\frac{\mu_n}{\mu_m} \right)^{\frac{1}{2}} \left(\frac{W_m}{W_n} \right)^{\frac{1}{4}} \right)^2 \quad (2.13)$$

and for mixture thermal conductivity, a simpler combination averaging formula [183] generally substitutes to the counterpart of Eq. 2.12 [182]:

$$\lambda = \frac{1}{2} \left(\sum_{n=1}^N X_n \lambda_n + \frac{1}{\sum_{n=1}^N X_n \lambda_n^{-1}} \right) \quad (2.14)$$

In the case of large CFD simulations, the computation of the diffusion coefficients, the mixture dynamic viscosity, and mixture thermal conductivity can remain costly, which motivates even further simplifications.

2.2.3 Simplified transport

In addition to the Hirschfelder and Curtiss approximation, simpler strategies are given here for the computation of the species diffusion coefficients D_n , the mixture dynamic viscosity μ , and the mixture thermal conductivity λ . For the combustion of mixtures in air, temperature-dependant empiric laws are often used such as the Sutherland law:

$$\mu = A \left(\frac{T}{T_{ref}} \right)^{\frac{3}{2}} \frac{T_{ref} + B}{T + B} \quad (2.15)$$

or the Power law:

$$\mu = A \left(\frac{T}{T_{ref}} \right)^B \quad (2.16)$$

where A and B are parameters that can be optimized to better fit the specifications of the mixture, under the design operating conditions of the combustion process. T_{ref} is the reference temperature (usually $T_{ref} = 300$ K).

For the computation of D_n and λ , the species Schmidt numbers Sc_n and the Prandtl number Pr are defined as:

$$Sc_n = \frac{\mu}{\rho D_n} \quad (2.17)$$

$$Pr = \frac{\mu C_p}{\lambda} \quad (2.18)$$

to which can be added the species Lewis number Le_n depicting the ratio between thermal diffusion and species diffusion:

$$Le_n = \frac{Sc_n}{Pr} \quad (2.19)$$

In most combustion applications, the species Lewis numbers show little to no variation across the flame front [213]. The assumption of constant Lewis number is therefore often used, and extended to constant Lewis and constant Schmidt numbers as this latter quantity is also close to be constant in common combustion scenarios. Thus, prescribing constant Sc_n and Pr *a priori* to the CFD computation allows to compute the searched diffusion coefficients D_n and thermal conductivity. The constant Sc_n and Pr can be adjusted from values taken experimentally and adapted to

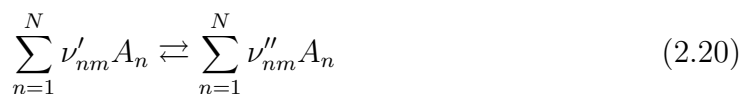
better fit macroscopic magnitudes such as laminar flame speed, adiabatic temperature, burnt products, ... It represents a convenient, and cost efficient way to model transport in a large spectrum of conditions with good confidence.

For the rest of this study, multi-component and mixture-averaged transports will be applied for the 0D-1D chemical solver Cantera [99], whereas the simplified transport will be preferred in the 3D CFD solver AVBP [37].

2.3 Chemical kinetics modelling

The reactive Navier-Stokes system of equations embarks source terms that account for chemical reactions in species conservation (Eq. 2.4) and energy conservation (Eq. 2.5). Chemical kinetics modelling allows to approximate species production rates $\dot{\omega}_n$ ($\text{kg.m}^{-3}.\text{s}^{-1}$) and heat release rate $\dot{\omega}_T$ ($\text{J.m}^{-3}.\text{s}^{-1}$). To compute these terms, the large number of species and their elementary reactions involved in the combustion processes must be encapsulated, including intermediate species that eventually influence the final stable equilibrium. this final state depends on temperature, pressure, and initial composition. A chemical kinetic scheme gathers a set of species and elementary reactions that reproduce the evolution of the chemical state of the mixture at hand. The precision of the reproduction directly depends on the precision of the scheme. It is either achieved by accounting for a sufficient number of reactions and species (e.g. detailed and semi-detailed/reduced schemes) which generalizes well to several chemical scenarios, or by considering a well fitted one or two-reactions scheme (global schemes), specialized for a limited range of scenarios. The way a scheme is built is further introduced in the next paragraphs.

The M reactions between N species can be written under a system [213, 145]:



where A_n is species n , ν'_{nm} and ν''_{nm} are the stoichiometric coefficient of species n in reaction m . The species production rate $\dot{\omega}_n$ writes as:

$$\dot{\omega}_n = W_n \sum_{m=1}^M \nu_{nm} Q_m \quad (2.21)$$

where $\nu_{nm} = \nu''_{nm} - \nu'_{nm}$, and Q_m ($\text{mol.m}^{-3}.\text{s}^{-1}$) is the reaction rate of progress of reaction m which is given by:

$$Q_m = K_m^f \prod_{n=1}^N [A_n]^{\nu'_{nm}} - K_m^b \prod_{n=1}^N [A_n]^{\nu''_{nm}} \quad (2.22)$$

with K_m^f and K_m^b are the forward and backward reaction rates of reaction m , and $[A_n]$ is the molar concentration of species n . The computation of K_m^f and K_m^b is directly dependant on the type of reaction involved. The fundamental brick is the Arrhenius equation [145]:

$$K_m^f = \alpha_m T^{\beta_m} \exp\left(-\frac{Ea_m}{RT}\right) \quad (2.23)$$

where α_m is the pre-exponential constant, β_m is the temperature dependence coefficient, Ea_m is the activation energy, R is the universal gaz constant. Forms of this equations are then adapted to fit the different types of reactions involved in combustion that are listed in the work of Cazères [33]. In reactions demanding a backward reaction rate, thermodynamic equilibrium is used [145]:

$$K_m^{eq} = \left(\frac{P_{atm}}{RT}\right)^{\sum_{n=1}^N \nu_{nm}} \exp\left(\sum_{n=1}^N \frac{\nu_{nm} G_n}{RT}\right) \quad \text{and} \quad K_m^b = \frac{K_m^f}{K_m^{eq}} \quad (2.24)$$

where $P_{atm} = 101\,325$ Pa, and $G_n = H_n - S_n T$ is the Gibbs free energy of species n , H_n and S_n are the standard enthalpy and standard entropy respectively of species n .

Lastly, the heat release rate $\dot{\omega}_T$ is linked to the species production rates $\dot{\omega}_n$ such that:

$$\dot{\omega}_T = - \sum_{n=1}^N \Delta h_{f,n}^0 \dot{\omega}_n \quad (2.25)$$

where $\Delta h_{f,n}^0$ is the mass enthalpy of formation of species n , which corresponds by definition to the heat released by one kilogram of species n at the reference temperature $T_0 = 298$ K. Alternatively, when the energy conservation equation is replaced by its temperature form, the heat release rate becomes [145]:

$$\dot{\omega}'_T = - \sum_{n=1}^N \left(\int_{T_0}^T C_{p_n} dT + \Delta h_{f,n}^0 \right) \dot{\omega}_n \quad (2.26)$$

where the added term is the sensible enthalpy.

The selection of an approach to produce a chemical kinetic scheme able to properly reproduce a large panel of combustion phenomena linked to Lithium-ion batteries is the subject of Part II.

2.4 Governing equations and canonical flow structures

Following the general definition of essential conservation equations necessary to apprehend reactive compressible flows, theoretical aspects of the flow structures expected around failing Li-ion batteries are given in the next chapter. Important features of turbulent flows (Chapter 3 Section 3.1), combustion (Chapter 3 Section 3.2), and supersonic compressible flows (Chapter 3 Section 3.3) are underlined. It is concluded by the presentation of simulation frameworks selected to reproduce the phenomena at hand (Chapter 4).

Chapter 3

Theoretical concepts for reactive compressible flows

Contents

3.1	Turbulent flows	26
3.2	Theoretical aspects of combustion	26
3.2.1	Mixing in combustion	27
3.2.2	Laminar flame structures	28
3.2.3	Turbulent combustion	31
3.3	Theoretical aspects of shocks and expansions	33
3.3.1	Shocks/expansions and failing batteries	33
3.3.2	Normal shocks jump relations	33
3.3.3	Oblique shocks relations	34
3.3.4	Prandtl-Meyer expansion	35
3.3.5	Moving shocks relations	35
3.4	Preparing a simulation setup	37

The general concepts needed to understand the phenomena observed around failing Lithium-ion batteries are presented in the following sections: turbulence, combustion (referring to fires and explosions), and shocks/expansions (cell opening, sustained venting). It helps to shed light on adequate general simulation frameworks (Chapter 4), and the steps necessary to tackle the specifics of failing Lithium-ion battery flows (Part II).

3.1 Turbulent flows

Theoretically, the equations of Chapter 2 fully describe any reactive flow. However, when targeting realistic non-laminar cases, an important limitation for simulation arises under the form of turbulence and its scales. A redefinition of the equations introducing modelling strategies for turbulence is necessary. To start with, an introduction to the main theoretical aspects of turbulence is given.

The Reynolds number, a key quantity to determine the turbulent state of the flow, is defined as the ratio between inertial forces and viscous forces: $Re = \frac{\rho U L}{\mu}$, where U is the magnitude of the velocity, and L corresponds to a characteristic length of the problem. As the Reynolds number increases, and depending on the flow geometry, a transition occurs from laminar to turbulent conditions. At high Reynolds numbers, the flow is driven by inertial forces which create coherent structures: vortexes or eddies, revealed by temporal and spatial velocity fluctuations. The velocity can be decomposed as the sum of the mean contribution and the fluctuation contribution: $u(t) = \bar{u} + u'(t)$, where here \bar{u} represents the time averaged velocity.

The eddies are inherently multi-scale, and three main zones can be defined to group them by size [216]. The largest structures lie in the integral zone, and are the most energetic ones. The wave number of these eddies is centered on the inverse of the turbulence integral length scale L_t , which is of the order of the size of the system. Turbulent energy is produced in this zone, and inertial effects dominate largely viscous effects. The turbulent integral Reynolds number characterizes this zone: $Re_t = \frac{\rho u' L_t}{\mu}$. The second zone groups eddies that interact, become unstable, and break, transferring energy from the largest scales to the smallest scales. This phenomenon is referred to as the Kolmogorov cascade. The last zone is delimited by the Kolmogorov scale, where structures smaller than this scale are destroyed by viscous forces, their turbulent energy transfer into heat. For homogeneous isotropic turbulence, this scale η_K is approximated by the relation [142, 216]:

$$\eta_K = L_t Re_t^{-\frac{3}{4}} \quad (3.1)$$

and its corresponding timescale writes: $\tau_K = \frac{L_t}{u'} Re_t^{-\frac{1}{2}}$. It can be easily compared to the integral turbulent timescale: $\tau_I = \frac{L_t}{u'}$

3.2 Theoretical aspects of combustion

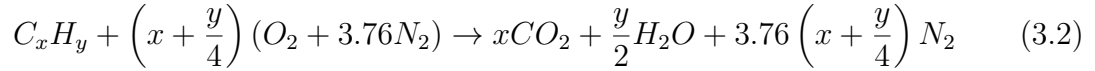
A brief summary of the theory of combustion is proposed in this section. It summarizes concepts exhaustively reported in combustion notebooks [286, 210, 145, 213].

Notions of mixing and stoichiometry are first given, followed by descriptions of canonical laminar flames structures. The interaction between combustion and turbulence is finally presented.

3.2.1 Mixing in combustion

Combustion is an exothermic oxidation reaction between fuel species and oxidizer species. When considering flames, two main regimes are to be introduced: premixed and non-premixed [213]. The first one describes processes where the oxidizer and the fuel are mixed prior to combustion. The second one refers to all other cases, the extreme one being diffusion flames where fuel and oxidizer come from two totally separated streams. In order to characterize the chemical process, measuring the relative amount of fuel *versus* oxidizer is key, for both regimes.

For hydrocarbons, the global stoichiometric combustion reaction in air (modelled by a mixture containing 79% of dinitrogen N_2 and 21 % dioxygen O_2) is [286, 145, 213]:



The stoichiometric ratio s can be defined as the mass ratio of air over fuel allowing a complete consumption of both fuel and oxidizer [213]:

$$s = \left(\frac{Y_{oxidizer}}{Y_{fuel}}\right)_{st} = \left(x + \frac{y}{4}\right) \frac{W_{oxidizer}}{W_{fuel}} \quad (3.3)$$

where W_a corresponds to the molar weight of a . By definition in this example, $W_{oxidizer} = X_{O_2}W_{O_2} + X_{N_2}W_{N_2}$ (taken into pure air, $X_{O_2} = 0.21$ and $X_{N_2} = 0.79$).

For premixed regimes ¹, the mixture is then represented by the equivalence ratio ϕ [213]:

$$\phi = \frac{Y_{fuel}}{Y_{oxidizer}} \times \left(\frac{Y_{oxidizer}}{Y_{fuel}}\right)_{st} = s \frac{Y_{fuel}}{Y_{oxidizer}} \quad (3.4)$$

so that excess fuel corresponds to $\phi > 1$ (rich regime) and excess oxidizer corresponds to $\phi < 1$ (lean regime).

¹Illustration: explosion of a closed vessel (module, storage room, ...) filled with gases vented out by a failing cell and air.

In non-premixed regimes², especially purely diffusion flames, a global equivalence ratio is defined as $\phi_g = s \frac{\dot{m}_{fuel}^1}{\dot{m}_{oxidizer}^2}$, where \dot{m}_{fuel}^1 is the mass flow of fuel in the inlet 1, and $\dot{m}_{oxidizer}^2$ is the mass flow of oxidizer in the inlet 2. However, to inspect locally the mixture, it is generally more convenient to introduce the mixture fraction Z defined as [213]:

$$Z = \frac{sY_{fuel} - Y_{oxidizer} + Y_{oxidizer}^0}{sY_{fuel}^0 + Y_{oxidizer}^0} \quad (3.5)$$

where $Y_{oxidizer}^0$ and Y_{fuel}^0 correspond to the mass fraction of oxidizer in the oxidizer stream and the mass fraction of the fuel in the fuel stream respectively. By construction $Z = 0$ (resp. $Z = 1$) corresponds to pure oxidizer (resp. pure fuel).

Being able to locally assert the equivalence ratio and/or the mixture fraction inside a computational domain is essential to build adequate flame modelling. Specific treatments concerning local equivalence ratio and mixture fractions measurements applied to Li-ion vent gases are introduced in Chapter 6.

3.2.2 Laminar flame structures

Flame structures are often put into categories such that adapted theory and models can be derived. The first distinction is made between premixed and diffusion flames. The second distinction is made between laminar and turbulent flames, where the laminar category refers to smooth flat flame fronts as opposed to flames wrinkled by the flow turbulence. The study of laminar flames, even if they are rare in common combustion applications, is essential as it is a fundamental brick in most turbulent combustion models. Laminar premixed and diffusion flames are the topic of the following paragraphs before introducing turbulent combustion in Section 3.2.3.

Laminar premixed flames

For premixed fuel and oxidizer, in absence of turbulence, a laminar flame can propagate. When the case is reduced to a one-dimensional problem, corresponding to a planar unstretched flame, the flame acts as a wave propagating from the burnt to the fresh gases at a constant speed namely the laminar flame speed s_L . Figure 3.2.1 a) shows the canonical structure of a laminar premixed flame. Three main zones can be highlighted in the reaction region. The preheat zone corresponds to the pre-flame heating of the fresh gases with thermal diffusion. The inner reaction zone is the thin flame front zone where the pre-heated fresh gases become hot

²Illustration: sustained flames at the cell outlet, made of pure vent gases jetting out in the atmosphere.

enough to trigger exothermic reactions. A large temperature gradient is observed corresponding to a peak of heat release. After the flame front, a thicker post flame region groups formation reactions of final products such as the CO/CO_2 conversion and the pollutant formation (soot particles, NO_x , ...). The mixture reaches the equilibrium state of burnt gases.

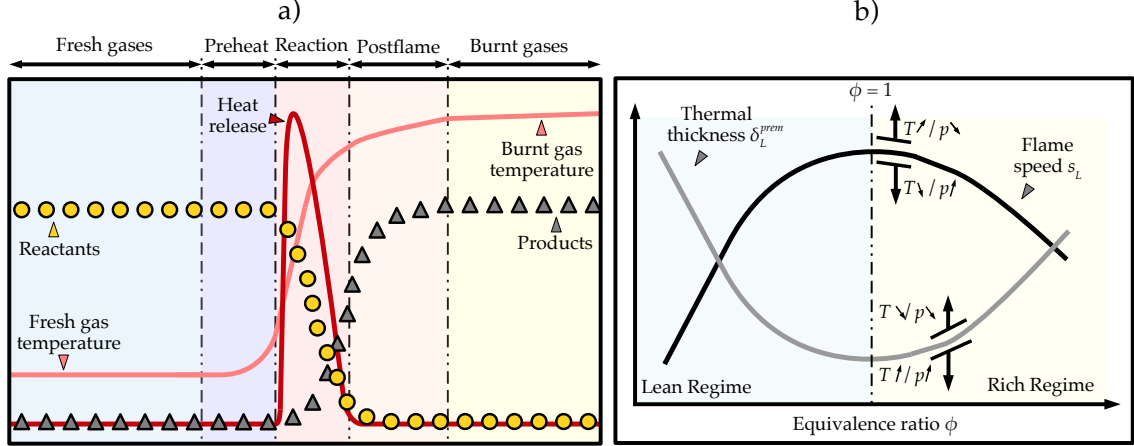


Figure 3.2.1: Structure of a 1D planar laminar premixed flame [145, 213]: a) Species, heat release rate and temperature profiles, b) typical response of flame thickness and speed to changes in fresh gases conditions.

Laminar premixed combustion of a given mixture is characterized by its laminar flame properties such as, using x as the propagation direction:

1. the laminar premixed flame speed s_L : it corresponds to the velocity of fresh gases needed to reach steady state, and is equal to the consumption speed for a laminar planar unstretched flame [213]:

$$s_L = u_{fresh} = s_c^{prem} = -\frac{1}{\rho_{fresh} Y_{fresh}^{fuel}} \int_{-\infty}^{+\infty} \dot{\omega}^{fuel} dx \quad (3.6)$$

2. the laminar flame thickness δ_L : in this study, the flame thickness is evaluated using the thermal thickness of the flame (see Fig. 3.2.1 a)) [213]:

$$\delta_L^{prem} = \frac{T_{burnt} - T_{fresh}}{\left(\frac{dT}{dx}\right)_{max}} \quad (3.7)$$

Laminar flame speed and thickness strongly depend on fresh gas conditions such as temperature, pressure, equivalence ratio, fuel (See Fig. 3.2.1 b)). The flame properties must be correctly retrieved by simulation, and are generally compared to experimental measurements using Bunsen burners or spherical bombs for example.

Laminar diffusion flames

When fuel and oxidizer are supplied by different streams, the diffusion of fuel and oxidizer creates the opportunity to have a laminar diffusion flame as an interface. Thanks to the separation between fuel and oxidizer, such flames are safer to produce. The canonical structure of a diffusion flame is given in Fig. 3.2.2 a). Reactions are centered at the stoichiometric line where fuel and oxidizer proportions meet stoichiometry. It corresponds to the location of maximal heat release and temperature. The flame displacement is exclusively controlled by the position of this line which is the resultant of flow motions.

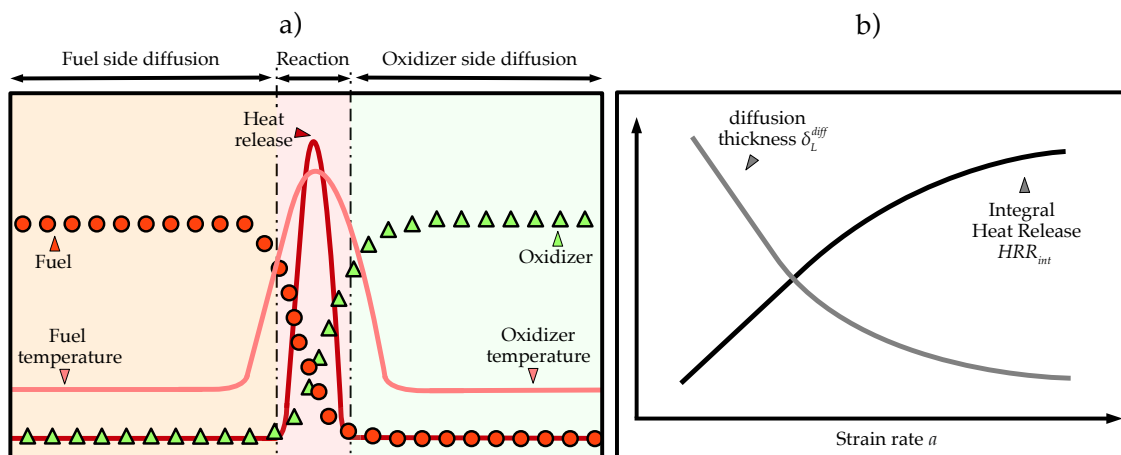


Figure 3.2.2: Structure of a 1D planar counter-flow diffusion flame [145, 213]: a) Species, heat release rate and temperature profiles, b) typical response of flame thickness and integral heat release to changes in strain rate.

Similarly to laminar premixed flames, a classical approach to study diffusion flames is the planar counter-flow diffusion flame which can be reduced to a one-dimensional problem [213]. The diffusion flame can be characterized by its intrinsic properties:

1. the peak temperature and peak of heat release rate T^{max} and $\dot{\omega}_T^{max}$.
2. the integral heat release rate HRR_{int} which corresponds to the integral along the diffusion direction, and measures the power of the flame:

$$HRR_{int} = \int_{-\infty}^{+\infty} \dot{\omega}_T dx \quad (3.8)$$

3. the diffusion flame gradient thickness: in a diffusion flame the mixture fraction goes from 1 in the fuel stream to zero in the oxidizer stream. Measuring the thickness of its gradient similarly to the thermal thickness in premixed flames allows to approximate the flame thickness, using the value of the gradient of mixture fraction at stoichiometry [59]:

$$\delta_L^{diff} = \frac{Z^{fuel} - Z^{oxidizer}}{\left(\frac{dZ}{dx}\right)_{st}} = \frac{1}{\left(\frac{dZ}{dx}\right)_{st}} \quad (3.9)$$

These parameters strongly depend on fuel and oxidizer composition, flow temperatures, ... The diffusion process is also controlled by the global strain rate a . For a planar counter-flow diffusion flame, its order of magnitude is often evaluated as [213]:

$$a = \frac{|u^{fuel}| + |u^{oxidizer}|}{L} \quad (3.10)$$

where u corresponds to flow velocity at the inlets, and L is the distance between the inlets. When considering experimental/simulation comparison of counter-flow configurations, a better evaluation of the global strain rate writes [240, 200]:

$$a = 2 \frac{|u^{oxidizer}|}{L} \left(1 + \frac{|u^{fuel}|}{|u^{oxidizer}|} \sqrt{\frac{\rho_{fuel}}{\rho_{oxidizer}}} \right) \quad (3.11)$$

where ρ is the density at the inlets. For equal fuel and oxidizer densities, a ratio of two exists between both evaluations. However, in this manuscript, and for the applications targeted, it has been verified that there is a limited relative difference between both formulations (30 % maximum), thanks to an overall lower density of the fuel stream compared to the oxidizer stream. Also, because no comparison with experimental counter-flow flames are performed, and owing to its simplicity and wide-spread use, Eq. 3.10 is preferred. General effects of strain on diffusion flames are depicted in Fig. 3.2.2 b).

In practice, premixing and diffusion often cohabit due to inhomogeneous mixing or because of particular flow conditions (e.g. triple flames [63], or partially premixed regimes). It is key to obtain the combustion regime on the fly in simulations. To do so, flame indexes can be introduced such as the Takeno index [294]. The question of an appropriate flame index for Li-ion vent gases is discussed in Chapter 7.

3.2.3 Turbulent combustion

Turbulent flow interacts with the flame, changing drastically its structure. The effect of turbulence can be observed using the characteristic time scales of the flow and the characteristic time scale of the combustion reactions. For premixed combustion (similar conclusions can be found for diffusion), the combustion time scale is [210, 213]:

$$\tau_C = \frac{\delta_L}{s_L} \quad (3.12)$$

which is the time taken by the flame to propagate by its own thickness.

Turbulence is usually described by two timescales (see Sec. 3.1): the integral timescale τ_I and the Kolmogorov timescale τ_K . The flame-turbulence interaction can be observed through three non-dimensional numbers, the Damköhler number $Da = \frac{\tau_I}{\tau_C}$ and the Karlovitz number $Ka = \frac{\tau_C}{\tau_K}$, and the ratio between turbulent velocity and laminar flame speed $\frac{u'}{s_L}$. The interaction regimes are then (see Fig. 3.2.3) [210, 213]:

1. For $Ka < 1$ and $Da > 1$, the flame depicts a thin flame front due to a fast chemistry compared to all turbulent scales. The flame is bent by the turbulence but the inner flame structure remains close to a premixed laminar flame structure: it is the flamelet regime. If $\frac{u'}{s_L} < 1$ turbulence only wrinkles the flame, it corresponds to the wrinkled flamelet regime. If $\frac{u'}{s_L} > 1$, the strong wrinkling creates flame-flame interactions and pockets of fresh or burnt gases. It is the corrugated flamelet regime.
2. For $Ka > 1$ and $Da > 1$, the largest structures in the flow still have larger timescales than combustion while the smallest structure can modify the inner structure of the flame. The flame appears to be thickened by turbulence, with a larger pre-heat zone but the reaction zone structure remains close to the one of the flamelet regime. It corresponds to the thickened-wrinkled regime.
3. Finally, for $Da < 1$, turbulence timescales are smaller than chemical timescales, meaning that all the turbulent structures enhance mixing: the flame is in the thickened flame regime. This regime asymptotically becomes a well-stirred reactor as Da decreases towards zero.

The direct effect of wrinkling, especially in the flamelet regime, is an increase of the flame surface. Thus, fuel consumption rises which promotes combustion. For free flames (e.g. explosions) this means that the flame is displacing faster and produces more heat. For anchored flames (e.g. furnaces) turbulence increases drastically the power of the flame. The turbulent brush flame speed s_t is related to the laminar flame speed s_L by [286, 213]:

$$\frac{s_t}{s_L} = \frac{A_t \bar{s}_c}{A_L s_L} \quad (3.13)$$

where A_t is the surface of the wrinkled flame, A_L is the surface of the corresponding non-wrinkled flame, and \bar{s}_c is the overall consumption speed (See Eq. 3.6). Figure 3.2.3 summarizes flame-turbulence interaction.

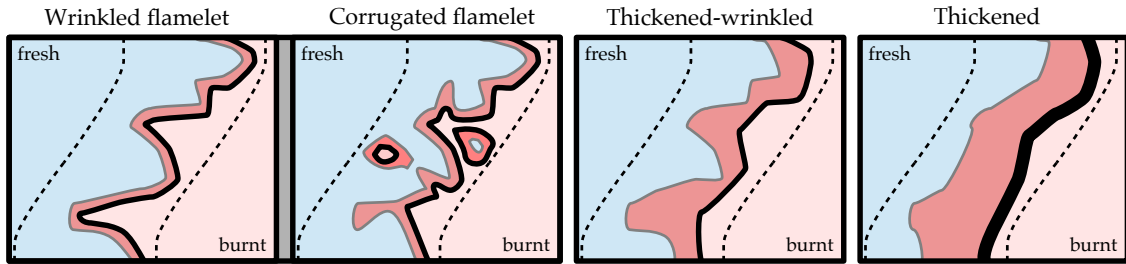


Figure 3.2.3: Flame-turbulence interaction regimes [210]: dashed line delimit the turbulent flame brush, the grey line depicts the limit between fresh gases and preheat zones, the reaction zone is depicted by the thick black line.

3.3 Theoretical aspects of shocks and expansions

3.3.1 Shocks/expansions and failing batteries

During the entire course of the thermal runaway, multiple flow particularities can be the source of a shock. It consists in a thin wave where flow quantities change rapidly. A shock-wave propagates at a velocity higher than the local sound speed. Different types of shocks can be observed around batteries, depending on the flow considered. At cell opening, moving shock-waves can propagate in the fluid at rest due to the strong discontinuity between the elevated pressure inside the cell and the atmospheric pressure. Then, series of shocks and expansion fans, forming diamonds can be stabilized around the cell lips due to the strong under-expanded jet flow. Finally, during explosion events, the rapid push of a mass of gas due to the flame can create shocks around obstacles, or the flame acceleration can reach a level where the flame itself tends towards the sound speed, making the transition from deflagration to detonation possible if conditions are met [154, 48].

The following paragraphs give equations governing shocks and expansions for simplified cases. References to these equations will be made throughout the manuscript, when shocks or expansions come into the picture. Figure 3.3.1 gives schematic representations of these flow features encountered in supersonic compressible conditions.

3.3.2 Normal shocks jump relations

Across a shock-wave perpendicular to the flow (obstacle in the flow, large turns), Rankine-Hugoniot jump relations [221, 115] can be derived from upstream to downstream using the conservation equations for a steady adiabatic inviscid flow, and a perfect gas. The relations link quantities upstream (marked \cdot_1) and downstream (marked \cdot_2) the shock, only depending on the heat capacity ratio γ and the Mach number upstream of the shock M_1 [195]:

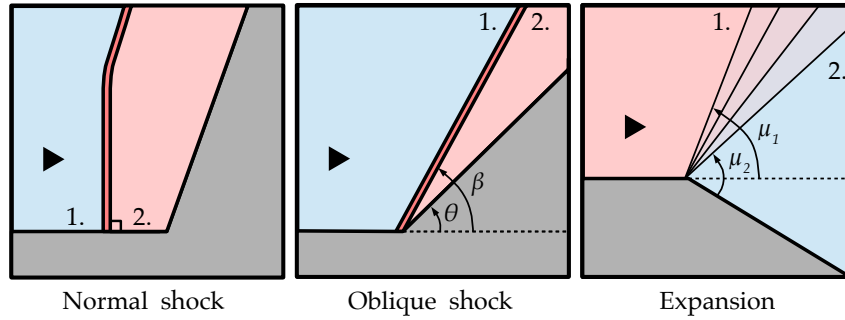


Figure 3.3.1: Canonical supersonic flow configurations where theoretical solutions can be derived [195].

$$M_2 = \sqrt{\frac{1 + \frac{\gamma-1}{2} M_1^2}{\gamma M_1^2 - \frac{\gamma-1}{2}}} \quad (3.14)$$

$$\rho_2 = \rho_1 \frac{(\gamma + 1) M_1^2}{2 + (\gamma - 1) M_1^2} \quad (3.15)$$

$$p_2 = p_1 \left(1 + \frac{2\gamma}{\gamma + 1} (M_1^2 - 1) \right) \quad (3.16)$$

and the perfect gas law gives $\frac{T_2}{T_1} = \frac{p_2 \rho_1}{p_1 \rho_2}$. These relations help to build equations for oblique shocks and give the profiles of propagating shocks, when looking closer at shock tube experiments.

3.3.3 Oblique shocks relations

When a supersonic flow encounters mild turns, the deviation creates an oblique shock. The angle β of the oblique shock is linked to the flow deviation angle θ , and the upstream conditions. β is derived, for a given upstream Mach number M_1 , and a given angle θ , by solving [195]:

$$\tan \theta = 2 \cotan \beta \left(\frac{M_1^2 \sin^2 \beta - 1}{M_1^2 (\gamma + \cos 2\beta) + 2} \right) \quad (3.17)$$

and the downstream conditions are retrieved using Eq. 3.14, Eq. 3.15 or Eq. 3.16 for $M_1 \leftarrow M_1 \sin \beta$ and $M_2 \leftarrow M_2 \sin(\beta - \theta)$.

3.3.4 Prandtl-Meyer expansion

Considering flow expansion, the reduced case of the Prandtl-Meyer expansion [219, 187] is generally taken for sharp corners [195]. The process is isentropic and the flow turns smoothly in the expansion fan spanning from $\mu_1 = \arcsin \frac{1}{M_1}$ to $\mu_2 = \arcsin \frac{1}{M_2}$ (See Fig. 3.3.1). The downstream Mach number M_2 is obtained by solving [195]:

$$\theta = \nu(M_2, \gamma) - \nu(M_1, \gamma) \quad (3.18)$$

where $\nu(M, \gamma)$ is the Prandtl-Meyer function:

$$\nu(M, \gamma) = \sqrt{\frac{\gamma+1}{\gamma-1}} \arctan \sqrt{\frac{\gamma-1}{\gamma+1}(M^2-1)} - \arctan \sqrt{M^2-1} \quad (3.19)$$

and because the process is isentropic, total quantities are conserved giving the ratio between upstream and downstream quantities as functions of M_1 , M_2 and γ .

3.3.5 Moving shocks relations

Through a propagating shock, flow quantities change following specific profiles where a normal shock and an expansion fan coexist. In particular, evaluating the pressure, velocity and temperature profiles is key. They can be obtained, for a one-dimensional moving shock, under the assumption of isentropic and inviscid flow, thanks to the resolution of a Riemann problem. The typical structure behind a shock is depicted in Fig. 3.3.2. It reproduces the theoretical course of a shock-tube experiment, where a driver gas is pressurized until the diaphragm breaks, and a shock propagates into the driven gas at the shock speed w . The interface between the driver gas and the driven gas is the contact surface moving slower at the contact surface speed u_p . The shock is accompanied by a rarefaction wave (expansion fan). The head of the expansion fan moves at a velocity $-c_{s4}$, where c_{s4} is the sound speed in the driver gas.

The domain is separated into four zones: 1. Driven gas, 2. Between the shock and the contact surface, 3. Between the contact surface and the expansion tail, 4. Driver gas. In the following, the subscript $.n$ denotes that the searched magnitude is taken from zone n . Given the driver (resp. driven) mixture compositions, initial pressures p_4 (resp. p_1), and initial temperature T_4 (resp. T_1), the solution to the problem of Riemann using the method of characteristics gives w , u_p , and the profiles of velocity, density, temperature, pressure behind a shock. Concerning the velocities w and u_p [262]:

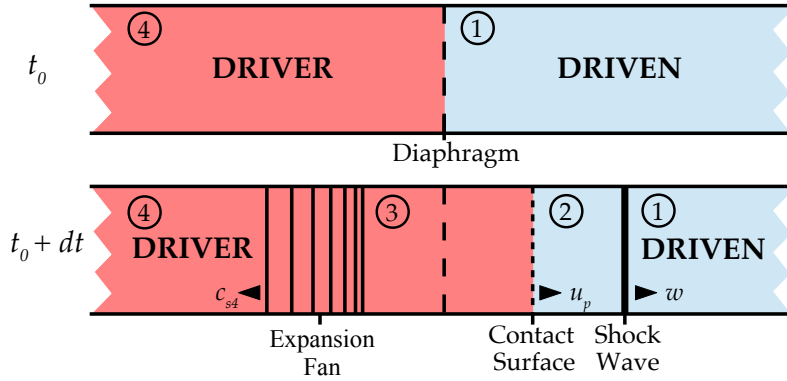


Figure 3.3.2: Schematic reproduction of a shock-tube experiment with a depiction of the typical shock profile [262].

$$w = c_{s1} \sqrt{\frac{\gamma_1 + 1}{2\gamma_1} \left(\frac{p_2}{p_1} - 1 \right) + 1} \quad (3.20)$$

$$u_p = \frac{c_{s1}}{\gamma_1} \left(\frac{p_2}{p_1} - 1 \right) \sqrt{\frac{2\gamma_1}{\gamma_1 - 1 + (\gamma_1 + 1) \frac{p_2}{p_1}}} \quad (3.21)$$

where c_s refers to the sound speed, γ is the heat capacity ratio. The method of characteristics applied to the expansion fan, and the fact that the expansion is isentropic leads to [262]:

$$\frac{p_4}{p_1} = \frac{p_2}{p_1} \left(1 - \frac{(\gamma_4 - 1) \frac{c_{s4}}{c_{s1}} \left(\frac{p_2}{p_1} - 1 \right)}{\sqrt{2\gamma_1 (2\gamma_1 + (\gamma_1 + 1) \left(\frac{p_2}{p_1} - 1 \right))}} \right)^{-\frac{2\gamma_4}{\gamma_4 - 1}} \quad (3.22)$$

where $\frac{p_4}{p_1}$ is known and $\frac{p_2}{p_1}$ can be found using an iterative solver, for example. The main profiles are then extracted similarly, and shown in Fig. 3.3.3.

Directly behind the shock, the temperature is elevated and mixing between driver and driven is possible close to walls. An ignition is then possible. It is used for ignition delay measurement [60, 38], or to analyze venting of pressurized flammable gases [95, 290, 293, 284, 298]. This latter studies motivates the observation of the chain of events occurring when a pressurized cell suddenly opens and flammable gases vent out and/or interact with obstacles (See Chapter 11).

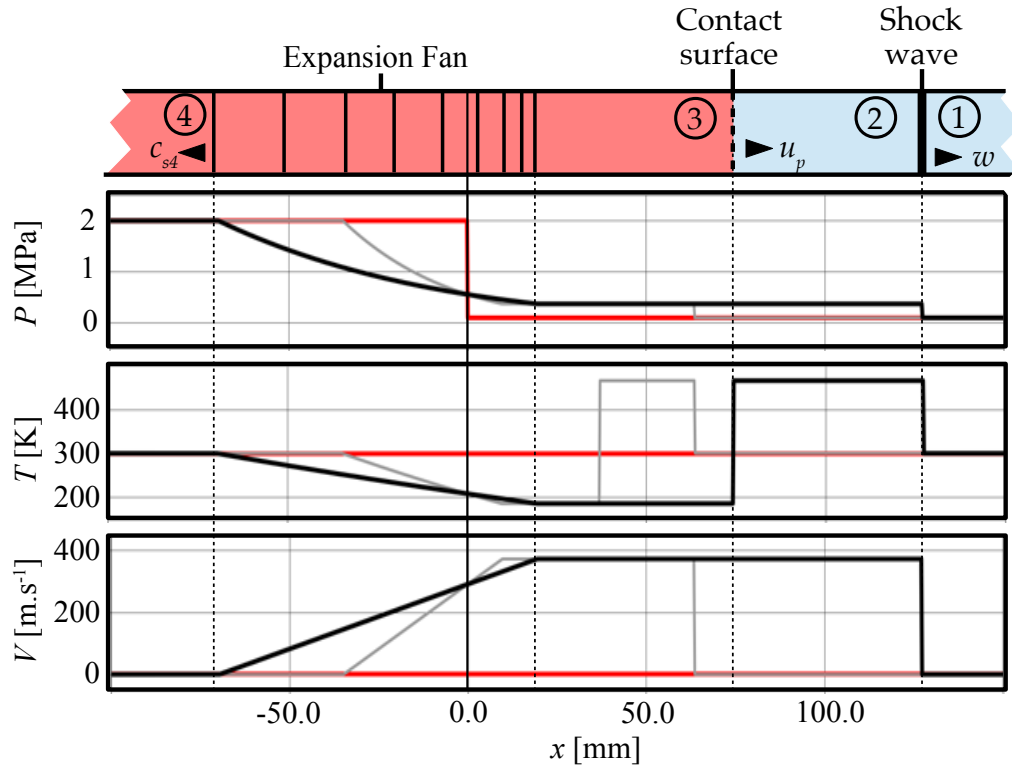


Figure 3.3.3: Profile of a shock propagating after the opening of a diaphragm. The driver gas (resp. driven gas) is air at $P = 2.0$ MPa and $T = 300$ K (resp. $P = 0.1$ MPa and $T = 300$ K). Pressure, temperature and velocity are depicted ((-) $t = 0.0$ ms, (-) $t = 0.1$ ms, (-) $t = 0.2$ ms)

3.4 Preparing a simulation setup

The problems targeted when considering turbulent combustion or supersonic flows in realistic 3D cases are generally too complex to be asserted theoretically and simulation is introduced to obtain estimation of flow properties. Simulation setups must guarantee fidelity and versatility to be generalized to varying flow conditions. Such setups and the inherent constraints are developed in the upcoming chapter.

Chapter 4

From theory to simulation

Contents

4.1 Numerical simulations and inherent constraints	40
4.1.1 Numerical schemes	40
4.1.2 The challenge of turbulent flow simulation	41
4.1.3 The challenge of turbulent combustion simulation	42
4.1.4 The challenge of shock simulation	43
4.2 A framework to unite LES and dedicated models	43
4.2.1 Governing equations for reactive Large Eddy Simulations	43
4.2.2 Dynamically Thickened Flame for LES	46
4.2.3 Shock handling methods	48
4.3 Solvers	50
4.3.1 Cantera	50
4.3.2 AVBP	50
4.3.3 Setting up the solvers for Li-ion specific cases	51

Because Navier-Stokes equations have analytical solutions only in simplistic configurations, the system is solved numerically under its discretized form, both in time and space. Therefore, the domain is divided into elementary volumes creating a mesh, and the timeline into time-steps. The simulation consists in integrating the discretized system at each time-step, starting from an initial time and an initialized mesh, including boundary conditions. The numerical scheme represents the method used to discretize the set of equation, which deeply influences the simulation's feasibility, stability, precision, and cost. In the next sections, main characteristics of common numerical schemes will be given, followed by the challenges encountered when simulating complex turbulent reactive flows. It leads to the presentation of

the Large Eddy Simulation as a strategy to compute efficiently the flows around a failing cell.

4.1 Numerical simulations and inherent constraints

4.1.1 Numerical schemes

Three main categories of methods are commonly used to discretize the Navier-Stokes equations: finite differences, finite volume, and finite elements, associated with implicit or explicit time integration. Depending on the method, and the way it is implemented, precision, stability, dispersive and diffusive properties vary. In this work, only explicit time-integration will be used.

The precision often refers to the order of the method. It consists in measuring the power at which the time-step Δt and the space-step Δx are elevated to inside the truncation error of the scheme. An order two scheme, in space and time, means that the difference between the true derivative and the discretized approximate derivative is of the form $O(\Delta t^2 + \Delta x^2)$. The higher the order is, the more improvements can be obtained by increasing time and space resolution.

The stability describes the property of the scheme to resist to error amplification both when integrating in time and space. For explicit integration, the Courant-Friedrichs-Levy number (CFL) and Fourier (FO) numbers are conveniently introduced [56, 254]:

$$\text{CFL} = (\|\mathbf{u}\| + c_s) \frac{\Delta t}{\Delta x} \quad \text{and} \quad \text{FO} = \alpha \frac{\Delta t}{\Delta x^2} \quad (4.1)$$

where c_s is the sound speed, and $\alpha = \nu$ for the viscosity-related Fourier, $\alpha = \frac{\lambda}{\rho C_p}$ for the thermal-related Fourier, $\alpha = D_n$ for the species-related Fourier. For explicit time-integration, imposing the stability of a scheme generally induces to constrain the CFL and FO numbers of a simulation to low finite values, which in turn links the space-step to the time-step. Demanding a high resolution (low Δx) drives a low time-step, which gives two major sources of extra costs.

Finally, the dispersive and dissipative properties refer to the behaviour of the numerical integration when confronted to gradients. As an example, let us assume that a wave packet is to be transported through the domain. A perfect scheme will propagate the waves without changing numerically their velocity or their amplitude through time and space. A dissipative scheme adds numerical diffusion to the physical diffusion, which will smooth numerically the solution. It is convenient in areas

of large gradients but reduces the precision of a solution. A dispersive scheme propagates the packet at non-physical velocities, which is, in the best case, reducing the final accuracy, and, in the worst case, triggering instability and simulation failures.

Depending on the application targeted, the numerical scheme can be chosen for its properties, easing the way to an accurate result at minimal costs. However, stability criteria are generally the most critical constraint. When a given flow pattern is to be reproduced with confidence, thus with a good resolution, the cost of the simulation can increase drastically. Introducing modelling approaches is generally the most efficient way to circumvent the issues. For turbulent flows, depicting complex structures (flames, shocks), resolving the flow leads to fine meshing, and through stability criteria, to low time-steps, thus high costs. More details about the challenges to overcome are given in the following sections.

4.1.2 The challenge of turbulent flow simulation

In a flow simulation, if the objective is to render perfectly the flow characteristics, at least all the turbulent structures larger than the Kolmogorov scale (Chap. 3 Sec. 3.1) must be computed, meaning that the discretization of the domain is constrained by this scale ($\Delta x^{min} < \eta_K$). This strategy is called Direct Numerical Simulation (DNS). Based on the link made between time and space-steps which enforces the stability of a numerical scheme, resolving entirely the turbulence demands high computational resources and thus only apply to small cases (low L_t) and/or low Reynolds cases. However, in practice, when targeting combustion cases such as furnaces, aeronautical combustion chambers, open fires and jets, the scales and duration of the phenomena become inaccessible with DNS.

As an example, let us consider the simulation of a fire in a battery module with an internal dead volume of $0.1 \text{ m} \times 1.0 \text{ m} \times 1.0 \text{ m}$ containing 18650 cylindrical Li-ion cells (18 mm in diameter, 65 mm in length). The associated integral length scale is estimated to be close to the Li-ion cell size: 20 mm. Typically, the turbulent integral Reynolds is of the order of 1000 (it depends on obstacles, flow conditions, presence of jets, ... and may be higher). The Kolmogorov scale becomes $\eta_K \simeq 1.1 \times 10^{-4} \text{ m}$. By meshing the volume with perfect regular tetrahedra of this size, it would require 6×10^{11} cells which is orders above the most expensive simulations currently affordable. Also, depending on the numerical scheme used, stability criteria will impose low time-stepping, making difficult to obtain converged flow statistics or compute lasting transient phenomena. While DNS is an ideal way to simulate turbulent flows, its cost makes it impractical for most industrial, and/or large turbulent laboratory scale configurations, where computational time cannot reach months in a development process.

To alleviate this problem, approaches to model the turbulence and its unreach-

able scales have been proposed. Two main families of solutions are the Reynolds Averaged Navier-Stokes (RANS) approach, and the Large Eddy Simulation (LES) approach.

RANS focuses on solving for mean temporal quantity based on a Favre averaged version of the Navier-Stokes system [286, 210, 213]. Closure for turbulent flows are insured by models that account for the effect of a given spectrum of the turbulence on the mean quantities. The strategy is however limited to steady flow simulations (which are not targeted in this work), and lacks representativeness regarding the largest vortexes driven by the flow geometry, as models are generally fitted for the smaller scales of the turbulence.

LES aims at separating large and small turbulent scales. Large eddy effects are resolved while small scales are modelled. LES solves the space-filtered Navier-Stokes set of equations so that the largest structures in the flow are accurately retrieved. Subgrid-scale models complete the equations for the smaller unresolved eddies. The approach is more specifically explained in Section 4.2.1.

4.1.3 The challenge of turbulent combustion simulation

Two main aspects are limiting when considering the simulation of turbulent combustion. On the one hand, the steep gradients inside the reaction zone must be sufficiently refined to give access to the right flame velocity, and power. It is true for both turbulent and laminar regimes. Generally, in premixed conditions, five to ten grid points are needed inside the laminar flame thermal thickness, which is of the order of 100-500 μm [287]. It is often even more constraining than solving for the Kolmogorov scale. For diffusion regimes, no hard limits can be defined [59], but a good practice is to apply the same criterion as in premixed cases to resolve the mixture fraction gradient (usually 1-2 mm thick). On the other hand, for turbulent flames, solving wrinkling is essential to retrieve the flame macroscopic characteristics.

Such mesh resolutions are only available for DNS-sized problems. When the choice is made to use RANS or LES approaches it becomes mandatory to introduce a flame-turbulence model which is able to alleviate the constraints imposed by both chemistry and turbulence. In premixed regimes, the main models are the Bray-Moss-Libby model [29], the G-equation model [189], the Filtered Tabulated Chemistry model [81] and the Thickened Flame Model [49]. For non-premixed flames, Probability Density Function applied to external flamelet library can be setup [55].

This work uses the Dynamically Thickened Flame Model adapted to LES (DT-FLES) for premixed regimes coupled with a Flame Index to deactivate thickening in non-premixed zones. There, no model is applied and sufficient refinement is to

be prescribed. More details are given in Section 4.2.2.

4.1.4 The challenge of shock simulation

Shockwaves are thin interfaces where quantities change in a nearly discontinuous manner. Typically, the thickness of a shock is of the order of a few molecular mean free paths (100-300 nm). This stiff problem makes it practically impossible to simulate moving shocks with classical space and time stepping methods, where the strong discontinuity must be imposed as a boundary condition. Shock capturing methods locally modifying the dissipative property of the fluid are often added to the CFD solvers [273], to avoid oscillations, and regularize the solutions. In this manuscript, in addition to localized artificial diffusion [125] enhancement, the Cook and Cabot hyper-viscosity sensor [54] and Localized Artificial Diffusion [251, 128] are used. The models are described in Section 4.2.3.

4.2 A framework to unite LES and dedicated models

The challenges posed by the simulation of a succession of stiff problems (turbulence, combustion and shocks) requires a framework able to gather models under the paradigm of LES where bricks can be tested separately, and appropriately fitted to tackle the specifics of Li-ion-related CFD problems. The following sections give details on the underlying filtered conservation equations of reactive LES and models selected to complete the approach.

4.2.1 Governing equations for reactive Large Eddy Simulations

Filtered Navier-Stokes equations

The Large Eddy Simulation paradigm uses the spatially filtered quantities such that for a given filter \mathcal{F}_Δ :

$$\overline{f(\mathbf{x})} = \int f(\mathbf{y})\mathcal{F}_\Delta(\mathbf{x} - \mathbf{y})d\mathbf{y} \quad (4.2)$$

and to avoid the addition of terms when applying filtering on the conservation equations, the Favre mass-weighted filtering is generally proposed [213]:

$$\bar{\rho}\tilde{f}(\mathbf{x}) = \overline{\rho f(\mathbf{x})} = \int \rho f(\mathbf{y})\mathcal{F}_\Delta(\mathbf{x} - \mathbf{y})d\mathbf{y} \quad (4.3)$$

In the following set of equations, the variables computed using the Favre mass-weighted spatial filtering are noted \tilde{A} and the Reynolds classical spatial filtering are respectively noted \bar{A} . For multi-species reacting flows adapted to solving combustion problems, the equations for LES are written as follows [213], with the simplified transport introduced in Section 2.2.3:

Mass conservation:

$$\frac{\partial \bar{\rho}}{\partial t} + \frac{\partial \bar{\rho}\tilde{u}_i}{\partial x_i} = 0 \quad (4.4)$$

Momentum conservation:

$$\frac{\partial \bar{\rho}\tilde{u}_j}{\partial t} + \frac{\partial \bar{\rho}\tilde{u}_i\tilde{u}_j}{\partial x_i} = -\frac{\partial}{\partial x_i} \left(\bar{p}\delta_{ij} + (\bar{\mu} + \mu^t) \left(\frac{2}{3} \frac{\partial \tilde{u}_k}{\partial x_k} \delta_{ij} - \left(\frac{\partial \tilde{u}_j}{\partial x_i} + \frac{\partial \tilde{u}_i}{\partial x_j} \right) \right) \right) \quad (4.5)$$

Species conservation:

$$\begin{aligned} \frac{\partial \bar{\rho}\tilde{Y}_n}{\partial t} + \frac{\partial \bar{\rho}\tilde{Y}_n\tilde{u}_i}{\partial x_i} &= \frac{\partial}{\partial x_i} \left(\left(\frac{\bar{\mu}}{Sc_n} + \frac{\mu^t}{Sc_n^t} \right) \frac{W_n}{W} \frac{\partial \tilde{X}_n}{\partial x_i} - \bar{\rho}\tilde{Y}_n (\tilde{V}_i^c + \tilde{V}_i^{c,t}) \right) \\ &+ \bar{\omega}_n (\tilde{Y}_n, \tilde{T}) \end{aligned} \quad (4.6)$$

Energy conservation:

$$\begin{aligned} \frac{\partial \bar{\rho}\tilde{E}}{\partial t} + \frac{\partial \bar{\rho}\tilde{u}_i\tilde{E}}{\partial x_i} &= -\frac{\partial}{\partial x_i} \left(\bar{p}\tilde{u}_j\delta_{ij} + \bar{\mu}\tilde{u}_j \left(\frac{2}{3} \frac{\partial \tilde{u}_k}{\partial x_k} \delta_{ij} - \left(\frac{\partial \tilde{u}_j}{\partial x_i} + \frac{\partial \tilde{u}_i}{\partial x_j} \right) \right) \right) \\ &+ \frac{\partial}{\partial x_i} \left(\bar{C}_p \left(\frac{\bar{\mu}}{Pr} + \frac{\mu^t}{Pr^t} \right) \frac{\partial \tilde{T}}{\partial x_i} \right) \\ &+ \frac{\partial}{\partial x_i} \left(\sum_{n=1}^N \left(\left(\frac{\bar{\mu}}{Sc_n} + \frac{\mu^t}{Sc_n^t} \right) \frac{W_n}{W} \frac{\partial \tilde{X}_n}{\partial x_i} - \bar{\rho}\tilde{Y}_n (\tilde{V}_i^c + \tilde{V}_i^{c,t}) \right) \tilde{h}_{s,n} \right) \\ &+ \bar{\omega}_T (\tilde{Y}_n, \tilde{T}) \end{aligned} \quad (4.7)$$

Variables denoted t represent the influence of the unresolved turbulent structures and are modeled using a subgrid scale model to compute the turbulent viscosity ν^t . For constant species Schmidt numbers Sc_n and Prandtl number Pr , the diffusion velocity correction is computed using:

$$\bar{\rho} (\tilde{V}_i^c + \tilde{V}_i^{c,t}) = \sum_{n=1}^N \left(\left(\frac{\bar{\mu}}{Sc_n} + \frac{\mu^t}{Sc_n^t} \right) \frac{W_n}{W} \frac{\partial \tilde{X}_n}{\partial x_i} \right) \quad (4.8)$$

The closure given by the subgrid scale models is introduced in the following section. Constant turbulent Prandtl and Schmidt numbers are chosen such that $Pr^t = 0.6$ and $Sc_n^t = Sc^t = 0.6$, for the simulations proposed in this work.

Subgrid scale closure

The unresolved subgrid scale (SGS) terms account for the small turbulent structures in the flow. Due to the dissipative effect of turbulence, the terms are modeled by promoting diffusion with a turbulent viscosity term ν^t . It completes the viscous stress tensor in the momentum conservation equation (Eq. 4.5), modifies the species flux vector in the species conservation equation (Eq. 4.6), and is added into the energy conservation (Eq. 4.7) through species and heat diffusion.

In this work two main models are used for the turbulent viscosity ν^t : the Smagorinsky model and the WALE model:

- The Smagorinsky model [245] introduces constants to link the filter characteristic length Δ to the resolved symmetric strain rate tensor norm $|S| = (2\bar{S}_{ij}\bar{S}_{ij})^{\frac{1}{2}}$:

$$\nu^t = (C_s\Delta)^2 (2\bar{S}_{ij}\bar{S}_{ij})^{\frac{1}{2}} \quad (4.9)$$

where $\bar{S}_{ij} = \frac{1}{2} \left(\frac{\partial \bar{u}_j}{\partial x_i} + \frac{\partial \bar{u}_i}{\partial x_j} \right)$, and C_s is a user defined constant ($C_s = 0.18$, is a common choice). This model has been used widely, as it can be easily implemented into a solver, it gives a first good approximation in most configurations. Nevertheless, it is generally asserted to be dissipative, particularly at the walls.

- Motivated by the necessity to better treat near wall turbulence, the Wall Adapting Local Eddy-viscosity (WALE) model has been proposed by Nicoud *et al.* [199]:

$$\nu^t = (C_w\Delta)^2 \frac{(S_{ij}^d S_{ij}^d)^{\frac{3}{2}}}{(\bar{S}_{ij}\bar{S}_{ij})^{\frac{5}{2}} + (S_{ij}^d S_{ij}^d)^{\frac{5}{4}}} \quad (4.10)$$

$$\text{with } S_{ij}^d = \frac{1}{2} \left(\left(\frac{\partial \bar{u}_i}{\partial x_j} \right)^2 + \left(\frac{\partial \bar{u}_j}{\partial x_i} \right)^2 \right) - \frac{1}{3} \left(\frac{\partial \bar{u}_k}{\partial x_k} \right)^2$$

with $C_w = 0.4929$. It recovers near wall flows more accurately where it has been checked that classical turbulent wall laws are retrieved.

Both closures link resolved and unresolved turbulent structures by proposing dissipative models which render properly the macroscopic behavior of the fluid. Thin structures such as shocks and flames must be treated using models which are described in the next sections.

4.2.2 Dynamically Thickened Flame for LES

For the simulation of premixed combustion using LES, the flame thickness is an order-one limitation as chemical processes need a minimal number of points inside this thickness to converge [287]. In this study, the Dynamically Thickened Flame (DTF) model is chosen to overcome this issue, enhanced by the modelling of flame-turbulence interaction (DTFLES).

The Dynamically Thickened Flame approach

Introduced by Colin *et al.* [49] the Thickened Flame (TF) model consists in thickening the flame front to ensure that typically five to ten mesh points are put in the thickness of the flame. To do so, a thickening factor F is applied on the pre-exponential term A (for a one-step chemistry). In practice, it is done by applying thickening to species production rates $\dot{\omega}_n$ [213]:

$$A \rightarrow \frac{A}{F} \quad \text{or} \quad \dot{\omega}_n \rightarrow \frac{\dot{\omega}_n}{F} \quad (4.11)$$

Similarly, thermal diffusivity D_{th} species diffusivities D_n are corrected:

$$D_{th} \rightarrow F D_{th} \quad \text{and} \quad D_n \rightarrow F D_n \quad (4.12)$$

for all species $n \in \llbracket 1, N \rrbracket$. A dimensional analysis of the laminar flame speed s_L and the thermal flame thickness δ_L gives $s_L \propto \sqrt{A D_{th}}$ and $\delta_L \propto \frac{D_{th}}{s_L} \propto \sqrt{\frac{D_{th}}{A}}$ [213]. The correction by a factor F effects these magnitudes as [213]:

$$s_L \rightarrow \sqrt{\frac{A}{F} F D_{th}} = s_L \quad \text{and} \quad \delta_L \rightarrow \sqrt{\frac{F D_{th}}{\frac{A}{F}}} = F \delta_L \quad (4.13)$$

The model thickens the flame front by a factor F without modifying the flame speed. Gradients across the flame front are smoothed while integrals of heat released and species production are conserved offering the possibility to work with coarser meshes. The limitation becomes the level of thickening to apply following that a number of points N_c must be prescribed in the front, knowing the flame thickness before thickening δ_L , and the mesh characteristic space-step Δx , $F = \frac{N_c \Delta x}{\delta_L}$.

To avoid applying thickening in the entire domain which would impact mixing behavior in places where combustion does not take place, Legier *et al.* [155] proposed a local thickening under the form:

$$F(x, y, z, t) = 1 + (F_{max} - 1)S(x, y, z, t) \quad (4.14)$$

where $F_{max} = \frac{N_c \Delta x}{\delta_L}$ and $S(x, y, z, t)$ is defined by a flame sensor able to detect reaction zones. The definition of a proper sensor is partly case dependant and will therefore be discussed in detail with more information on Li-ion vent gases specifics (see Chapter 7 Section 7.3.2).

Accounting for flame-turbulence interaction

In turbulent conditions, simulated with LES, the application of the DTF model underestimates largely the flame surface, hence the consumption speeds. In fact, the flame surface due to the resolved wrinkling (resolved flow structures) is dampened by the increased diffusivity, and the unresolved wrinkling (from the subgrid-scale model) is omitted. To correct this, an efficiency function Ξ is introduced, accounting for the ratio of total flame surface divided by the resolved flame surface. Ξ artificially increases the pre-exponential factor (in practice, the species production rates) and diffusivities [213]:

$$A \rightarrow \frac{\Xi A}{F} \quad \text{or} \quad \dot{\omega}_n \rightarrow \frac{\Xi \dot{\omega}_n}{F} \quad (4.15)$$

and:

$$D_{th} \rightarrow F \Xi D_{th} \quad \text{and} \quad D_n \rightarrow F \Xi D_n \quad (4.16)$$

Ξ is a function of local flame quantities and local turbulence quantities taken at the resolved scale, close to the thickened flame thickness scale $\Delta \sim F \delta_L$. In this study, the model proposed by Charlette *et al.* [39, 277] is selected:

$$\Xi \left(\frac{\Delta}{\delta_L}, \frac{u'_\Delta}{s_L}, Re_\Delta \right) = \left(1 + \min \left[\frac{\Delta}{\delta_L} - 1, \Gamma \left(\frac{\Delta}{\delta_L}, \frac{u'_\Delta}{s_L}, Re_\Delta \right) \frac{u'_\Delta}{s_L} \right] \right)^\beta \quad (4.17)$$

where u'_Δ is the subgrid scale Root Mean Square (RMS) velocity, $Re_\Delta = \frac{\rho u'_\Delta \Delta}{\mu}$, and Γ accounts for the straining effect of the turbulent scales lower than Δ . The model constant is the exponent β of the order of 0.5. For most applications, β is set constant. A dynamic evaluation of β is sometimes necessary, where large turbulence inhomogeneities are expected [40, 191]. Generally, simulations are sensitive to the value of this parameter, and it is still a step to take to define an entirely generic model

for flame-turbulence interactions. In the manuscript, static and dynamic Charlette models may be used, and parameter constants will be given explicitly.

The model is only valid for premixed combustion. When premixing and diffusion modes cohabit defining partially premixed combustion, where diffusion may locally be preponderant, or for diffusion flames, such models are to be used with care. Flame indexes are chosen to deactivate locally the model and in these zones, the mesh refinement must be sufficient to properly resolve the diffusion flame. Similarly to flame sensors, flame indexes are, to a certain extent, selected based on considerations specific to the gases to study (see Chapter 7 Section 7.4.3).

4.2.3 Shock handling methods

Due to the strong discontinuity from either side of a shock, and depending on the dispersion properties of the numerical scheme, non-physical oscillations are observed in the vicinity of the shock. These waves lead to non-physical results and, in the worst case, to the impossibility to perform the computation. Models to handle shocks are therefore introduced. Two main textbook strategies are available in this work: 1. The Cook and Cabot method [54], and 2. the Localized Artificial Diffusion [251].

1. **Cook and Cabot** : The method introduced in [54] consists in artificially modifying the bulk velocity inside the viscous stress tensor τ_{ij} such that:

$$\begin{aligned}\tau_{ij} &= -\frac{2}{3}\mu\frac{\partial u_k}{\partial x_k}\delta_{ij} + \mu\left(\frac{\partial u_j}{\partial x_i} + \frac{\partial u_i}{\partial x_j}\right) \\ \rightarrow \tau_{ij}^{mod.} &= \left(\beta - \frac{2}{3}\right)\mu\frac{\partial u_k}{\partial x_k}\delta_{ij} + \mu\left(\frac{\partial u_j}{\partial x_i} + \frac{\partial u_i}{\partial x_j}\right)\end{aligned}\quad (4.18)$$

with β as the bulk hyperviscosity given by a modification of the method to limit viscosity in presence of high vorticity and dilatation regions:

$$\beta = \widetilde{k_C \cdot k_V \cdot k_D} \quad (4.19)$$

where k_C is the original viscosity term from [53], k_V is the vorticity limiter [67], and k_D is the dilatation limiter [20].

$$k_C = \rho(\Delta x)^4 \left\| \widetilde{\nabla^2 \sqrt{S_{ij} S_{ij}}} \right\| \quad (4.20)$$

where Δx is the local space-step, and S_{ij} is the symmetric strain rate tensor.

$$k_V = \frac{(\nabla \cdot \mathbf{u})^2}{(\nabla \cdot \mathbf{u})^2 + \|\nabla \times \mathbf{u}\|^2 + C_V} \quad (4.21)$$

where $\nabla \cdot \mathbf{u} = \frac{\partial u_k}{\partial x_k}$ is the divergence of the velocity field, and $\nabla \times \mathbf{u} = \epsilon_{ijk} \frac{\partial u_k}{\partial x_j}$ is the vorticity field (using the Levi-Civita symbol ϵ_{ijk}). C_V is a user-defined constant that avoids spurious values in regions where the other terms of the denominator tend to zero.

$$k_D = \frac{1}{2} \left(1 - \tanh \left(2.5 + \frac{10\Delta x}{c_s} \nabla \cdot \mathbf{u} \right) \right) \quad (4.22)$$

where $\frac{10\Delta x}{c_s}$ acts as a non-dimensionalization by local space-step and sound-speed (c_s) of the divergence of the velocity field.

Both limiters avoid a triggering of the shock sensor in regions of strong turbulence, and where dilatation is sensed (shocks are compression waves), leading to a controlled impact of additional viscosity in the entire domain.

2. **Localized Artificial Diffusion** : The approach consists in the low-pass filtering of conservative variables following the prescription of a sensor, able to detect strong oscillations. In this study, the sensor is based on the pressure field p such that:

$$S = (\|\mathbf{u}\| + c_s) \frac{\Delta t}{\Delta x} \max \left[0, 100 \times \left| \frac{\mathcal{F}(p) - p}{p} \right| - C_{LAD} \right] \quad (4.23)$$

where a low-pass filtering $\mathcal{F}(\cdot)$ is applied to the pressure field, and C_{LAD} acts as a threshold to increase the robustness of the sensor (turbulence, flow inhomogeneities, ...). The sensor flags large discrepancies between the filtered and the non-filtered field.

Artificial diffusion is applied by filtering the conservative variables following the prescription of the sensor. It is made by introducing a low-pass filter built by the convolution of a Gaussian filter \mathcal{G} and an approximate of its inverse \mathcal{Q}^* obtained through a truncation of the series:

$$\mathcal{Q}_N = \sum_{n=0}^N (\mathcal{I} - \mathcal{G})^n \quad (4.24)$$

where \mathcal{I} is the identity operator, and $\mathcal{Q}^N \circ \mathcal{G} \xrightarrow{N \rightarrow +\infty} \mathcal{I}$ [251, 128]. The higher N is, the less damped the solution is. Also, the cost of the filtering step increases with N . A compromise is generally found with $N = 1$ or $N = 2$. In this manuscript $N = 1$ gives reasonable performances at costs comparable to the Cook and Cabot strategy for all numerical schemes tested.

The choice of a strategy depends on its collaboration with the numerical scheme and the targeted application. Tests are proposed in Chapter 7 Section 7.2.

4.3 Solvers

In this manuscript, using the conservation equations defined in Chapter 2 and in the previous section, it is possible to define simulation setups that solve either for simplified canonical combustion scenarios (Cantera [99]), or for more complex 3D scenarios (AVBP [37]). These solvers are shortly outlined in the next paragraphs.

4.3.1 Cantera

Cantera [99] is an open source code which groups methods to study chemical systems including transport and thermochemical properties, and is indicated for combustion. It solves 0D and 1D canonical configurations using all types of kinetic schemes, including detailed and semi-detailed/reduced schemes:

1. **Equilibrium:** It consists in solving for the minimum Gibbs free energy chemical equilibrium given an initial state and species thermo-chemical properties. It includes the computation of the adiabatic flame temperature of a mixture. The minimum is the result of an optimisation problem solved by the Lagrange multiplier method.
2. **0D isochoric reactors:** It solves the energy equation under the temperature form: $\rho C_p \frac{dT}{dt} = \dot{\omega}'_T$. It gives access to the auto-ignition delay of a mixture given an initial state that respects auto-ignition limits. The CVODES solver [89] is used for the integration of this stiff differential equation.
3. **1D laminar premixed flames:** The solution to the steady axisymmetric flow corresponding to a laminar premixed flame where the mixture of fuel and oxidizer is injected at one end of the domain is searched. An iterative Newton method aims at solving the simplified conservation equations, which gives access to flame profiles and thus macroscopic quantities such as the laminar flame speed of a given mixture.
4. **1D counter-flow diffusion flames:** Using a similar approach as the 1D laminar premixed flames, it depicts configurations where fuel and oxidizer are injected at opposite ends, and shows the response to the stream conditions including the strain rate.

4.3.2 AVBP

AVBP [37, 237] is a multi-purpose CFD solver for reactive and non-reactive 1D, 2D and 3D flow simulations. The fully compressible Multi-species Navier-Stokes system

can be solved using DNS or, under its filtered form using LES. Unstructured hybrid tetrahedra/prisms meshes are managed, making the simulation of complex geometries possible. Boundary conditions use the Navier-Stokes Characteristic Boundary Condition (NSCBC) formalism [214]. The numerical scheme used for diffusive fluxes is second order in space. Space and time discretization for convective fluxes are done following two main numerical schemes families:

1. The Law-Wendroff (LW) scheme: it is based on [152], adapted for cell-vertex formulation, and is a centered finite-volume scheme. It is second order both in time and space and uses a single step explicit time integration.
2. The Two-step Taylor Galerkin (TTG) schemes family [50]: they consist in finite-element schemes with explicit time integration. They reach third order precision in time and space.

The code is a platform for the combustion models and shock handling strategies, adapted to LES of large scale 3D cases.

4.3.3 Setting up the solvers for Li-ion specific cases

The first chapters highlighted the different fundamental bricks to produce when targeting reactive compressible problems. In the following part, the focus is to describe more specifically the gases vented-out by a failing Li-ion cell (Chapter 5) and propose a kinetic modelling applied to a range of combustion phenomena observed around batteries (Chapter 6). It is followed by a deeper analysis of canonical 1D cases (Chapter 7), helping to setup and/or adapt the models for combustion and the strategies for shock handling for the 3D simulation of the targeted events using AVBP.

Part II

Chemical kinetics for the combustion of Lithium-Ion cells vent gases

Chapter 5

Origin of the vented gaseous mixtures

Contents

5.1 Gas production during Thermal Runaway	55
5.1.1 Cell components and gas production	56
5.1.2 Gas production mechanisms	60
5.2 Electrolyte oxidation and combustion	64
5.2.1 Chemical kinetic schemes to assert electrolyte oxidation and combustion	64
5.2.2 Oxidation products in 0D isochoric reactors	65
5.2.3 Electrolyte species and 1D premixed laminar flames	67
5.2.4 Concluding remarks on electrolyte oxidation	70

5.1 Gas production during Thermal Runaway

Thermal Runaway (TR) is initiated by various abuse conditions (see the Introduction, Section 1.4.1) all leading to the decomposition of inner components. The decomposition, both thermal and electro-chemical, generates gases that are eventually vented out by the cell, causing fire. Identifying the sources of the species ejected is of first importance in the process of simulating relevant Li-ion cell fires, and helps to establish simplifying hypotheses as the ground of the study. In this section, more details on the constituents of a Li-ion cell will be given. The interconnection of these components, and how they react to produce gases will be shown. Species of interest that are eventually retrieved in gas analyzes and burning in cell fires will be reported. Finally, the hypotheses made to simulate cell fires will be given.

5.1.1 Cell components and gas production

Apart from the housing and safety devices, a functioning cell is composed of a cathode, an anode, a separator and electrolyte (see Fig. 5.1.1). A point by point description of these components follows, with a stronger focus on common material used. It helps to pre-select the sources of gases during TR, and identify the potential species observed after venting:

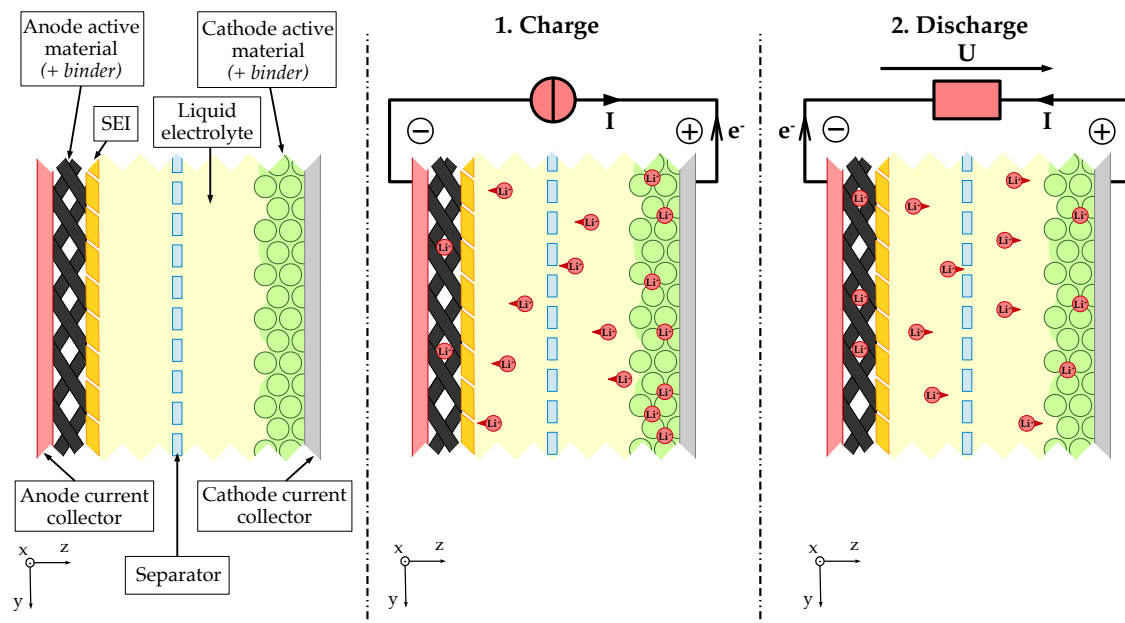


Figure 5.1.1: Detailed schematic representation of one layer of cathode-anode ensemble [233, 283]: Components, charging and discharging phases.

1. **Housing:** In general, metallic structures are targeted for the housing, with overall good fireproof performance, making the event of metallic combustion of the whole structure unlikely. However, small internal pieces of aluminum and copper may rapidly melt and burn generating sparks. Also, an additional quantity of gases due to polymeric bags may be observed during venting. In this study, it is assumed that the casing is fireproof and is not a source of gaseous species observed during venting. In particular, the 18650 cylindrical cell is the main subject in most studies due to its prevalence in all domains, and will be often targeted as an example in the manuscript.
2. **Cathode:** For Lithium-ion applications, the cathode is composed of a current collector covered by the cathode active material [283]. The current collector is a metallic sheet (usually made of aluminum), which can be the source of sparks when it is disintegrated. The cathode active material is the most crucial part of the cell. The choice of technology is influencing the behavior of the cell. The influence of the cathode chemical structure is first order when considering energy density, electrolyte composition, heat management, ... The

chemical compound is presented under the form of a metallic salt which includes Lithium. Table 5.1.1 summarizes the main specifications of the cathode compounds, along with comments on common applications. In addition to Lithium, the cathode material links metallic alloys (involving Manganese Mn , Iron Fe , Cobalt Co , Nickel Ni , Aluminum Al) to oxygen O . Phosphor P is an exception in LFP cells that are generally safer, more stable, and less energetic cells. The Lithium migrates from the cathode to the anode when the cell is charged and inversely, from the anode to the cathode during discharge. The *metal-oxide* or *metal-phosphate* structure is meant to remain unchanged at all time. However, when delithiated (when the cell is fully charged), the cathode active material may release oxygen [15, 279, 197, 249]. This phenomenon is accelerated at high temperature during TR, the cathode is therefore a non-negligible source of oxygen which may react with other gaseous species through oxidation, releasing heat.

Table 5.1.1: List of most common cathode active material with typical order of magnitudes of energy density at material level [69].

Abbrev.	Chemical composition	Energy density [Wh.L ⁻¹]	Specific energy [Wh.kg ⁻¹]
LFP	$LiFePO_4$	2200	320
NMC	$Li(Ni_xMn_yCo_z)O_2$	2800-3700	620-760
LCO	$LiCoO_2$	3300	650
NCA	$Li(Ni_xCo_yAl_z)O_2$	3700	760
LMO	$LiMn_2O_4$	2100	480
LNMO	$Li(Ni_xMn_y)O_4$	2600	570

3. **Anode:** Similarly to the cathode, the anode is made of a thin metallic current collector (usually a copper sheet) covered in active material [283]. A largely dominant technology for the active material is the graphite-based structure Li_xC_6 , for its cost and stability. Metallic structures have been tested [173] with less success under industrialization processes. During TR, if the battery is charged, the Lithium is imprisoned in the carbon structure. When the protecting coatings such as the Solid Electrolyte Interphase (SEI, presented as an **Additional** in this list) is destroyed, the Lithium is released allowing numerous reactions, all sources of gases including hydrocarbons (HC). In presence of oxygen the combustion of the carbon black at the anode is a source of carbon oxides.
4. **Separator:** The separator is the micro-perforated isolating layer(s) which simultaneously allows Li^+ ions to migrate from an electrode to another and prevents internal short-circuits by anode/cathode contact. Due to the use of corrosive electrolytes, because internal resistance has to be limited at the same time, the preferred materials for such an application are poly-ethylene

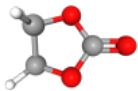
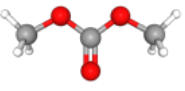
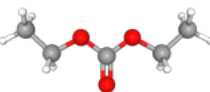
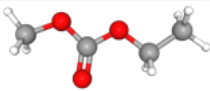
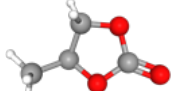
(PE) and poly-propylene (PP) multi-layer separators [299]. During TR, the shrinking of the separator is a key phenomenon occurring very early in the process and creating rapidly internal short-circuits. At temperatures above 110°C [174], the plastic of the separator melts, mixes with the HC-based electrolyte, and reacts further with Lithium or oxygen to form light flammable gases.

5. **Electrolyte:** In all batteries, electrolyte plays the role of ion carrier. Its prerogatives are to conduct efficiently the Li^+ during charge and discharge procedures. The selection of solutions of alkyl-carbonates come as good compromises that offer stability regarding reactions with electrodes, good conductivity for Li^+ and overall low toxicity when manipulated [10]. Mixtures of Ethylene Carbonate (EC), Dimethyl Carbonate (DMC), Diethyl Carbonate (DEC), Ethyl-Methyl Carbonate (EMC), and Propylene Carbonate (PC) are generally selected with variations in proportions to maximize the performance and stability of the cell, depending on the choice of cathode active material. In addition, Lithium Hexafluorophosphate ($LiPF_6$) is added as a Lithium enrichment salt, for its good solubility in alkyl-carbonates and relatively stable performance over charge and discharge cycles. During TR, the species composing the electrolyte are prompt to react with Lithium (at the unprotected anode) or with oxygen (released by the cathode) to promote the presence of hydrocarbons such as methane (CH_4), ethylene (C_2H_4), ethane (C_2H_6), propylene (C_3H_6), propane (C_3H_8), carbon oxides (CO and CO_2) and water. The boiling point of the liquid electrolyte mixture is a direct limitation to the use of Li-ion batteries under hot conditions. Irreversible chain reactions often start when electrolyte boils which rapidly increases the cell internal pressure. Table 5.1.2 summarizes the main chemical information and properties for the species composing the electrolyte solution.
6. **Additional:** In addition to the parts listed above, two other main elements play crucial roles in the production of gases during TR: 1. the binders mixed with electrode active material and 2. the Solid Electrolyte Interphase/Interphase (SEI). Their composition is further described:
 - (a) **Solid Electrolyte Interphase (Interface):** During the first discharge/charge cycles of the freshly produced battery, the liquid electrolyte is reduced by Li^+ ions at the anode forming a passivating layer. Once formed, the solid layer protects the anode and avoids further reaction of the electrolyte, while being permeable to the migrating ions. The layer is essential to the well-functioning of the cell but tends to limit its performance by modifying the overall impedance of the electrode [257]. Moreover, the loss of Lithium in the SEI is irreversible and the layer tends to thicken over the charge/discharge cycles further consuming available moving ions and influencing the resistance of the battery. The species involved in the composition of the SEI are products

of the reduction of the electrolyte species of the form $Li_aC_bH_cO_d$. At high temperature, the species decompose and produce in particular H_2O , CO , CO_2 , a phenomenon amplified in presence of Hydrogen Fluoride (HF) [65, 257]. The reactions incriminated here happen early in the TR process, and are identified as a trigger for the chain reactions when the anode stops to be protected and electrolyte is destroyed again violently at the anode [174].

- (b) **Binders:** The process of anode and cathode production demand an homogeneous layer of active material on the metallic sheets playing the role of current collector. The active material is mixed with a polymer-based liquid mixture called a binder. The binder has two main missions: it glues the active material to the current collector, and it must be as transparent as possible during charge and discharge, meaning that it must not react with migrating lithium. Often cited materials are the Polyvinylidene Fluoride (PVDF) and Carboxymethyl Cellulose (CMC) which can be important sources of HF and H_2 . Along with SEI decomposition, binders tend to react at the beginning of TR producing gaseous species useful to further reactions promoting other flammable species (CH_4 , C_2H_4 , ...) [96].

Table 5.1.2: List of common electrolyte solvents with relevant chemical properties [137].

Abbrev.	Full name	Chemical formula	Boiling point [°C]	Structure
EC	Ethylene Carbonate	$C_3H_4O_3$	248.0	
DMC	Dimethyl Carbonate	$C_3H_6O_3$	90.0	
DEC	Diethyl Carbonate	$C_5H_{10}O_3$	126.0	
EMC	Ethyl Methyl Carbonate	$C_4H_8O_3$	107.0	
PC	Propylene Carbonate	$C_4H_6O_3$	242.0	
$LiPF_6$	Lithium Hexafluorophosphate	$LiPF_6$	-	-

The mass distribution for the cited components has been analyzed by Golubkov *et al.* [97] for two different cathode materials technology (NCA and LFP). Figure 5.1.2 gives this distribution, without housing supposed to be non-reactive during decomposition. Even if some elements remain difficult to isolate such as the binder taking part in the anode and cathode active material, it can be seen that the mass distribution is comparable between two different technologies. Cathode and anode active materials are the most represented elements.

Now that the components playing a role in gas production have been identified, a precise zoom on the progressive destruction of the cell components is made in the following section. The production of the species vented out is highlighted, and linked to the source reactions.

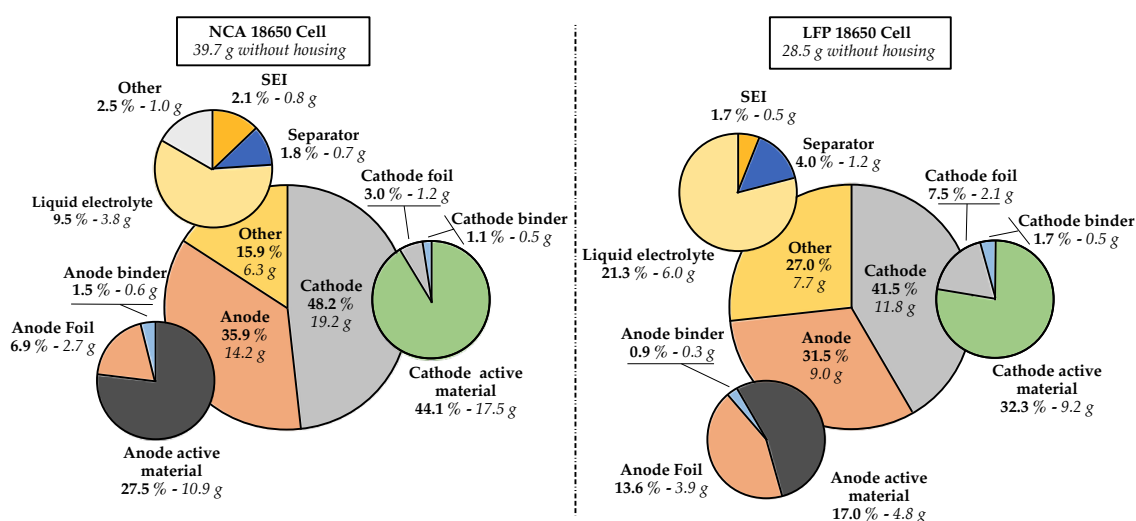


Figure 5.1.2: Mass distribution between the internal components of a lithium-ion cell subject to decomposition (housing is discarded), for two samples from two different cathode active material technologies (NCA and LFP). The data is extracted from [97].

5.1.2 Gas production mechanisms

Assuming that the cell behaves as a closed reactor, it is then possible to link the degradation of the components to simplified reactions producing gases. A depiction of the mechanism is obtained thanks to the schematic given in Fig. 5.1.3 p. 62. The sources of species are identified as the Anode, the Cathode, the Electrolyte, the Binders and the Solid Electrolyte Interphase (SEI). Components and species are linked by reactions that are categorized as E_{1-7} for electrolyte-centered reactions, C_1 for cathode-centered reactions, B_{1-2} for binders-centered reactions, S_{1-3} for SEI-centered reactions, and A_1 for anode-centered reactions. The reactions with corresponding citations are given in Table 5.1.3 p. 62. The inventory of the gas-producing reactions makes the link between the constituents of a sound cell and the gaseous species generally observed after venting [12, 96, 97, 171, 141]. Other

reactions may play roles such as the hydrolysis of the traces of water into hydrogen and oxygen, showing that such vision on the cell degradation may evolve with future expansion of the literature on this subject. Nonetheless, the species expected in Fig. 5.1.3 compare with the usual venting analyzes, which generally report H_2 , $C_1 - C_4$ species, CO , CO_2 [96, 97, 141, 171, 149, 110]. However most analyzes are made on average samples obtained after the TR event conclusion. A chronology of the reactions can be approached thanks to the work of Mao *et al.* [174] and Feng *et al.* [75]. Five stages were identified that can be grouped into three main phases. During the first phase, SEI decomposes, producing CO_2 and traces of C_2H_4 . As the TR advances, and because of the anode defoliation, Lithium is available to reduce the binders and the electrolyte mixture producing H_2 , $C_1 - C_4$ hydrocarbons, CO_2 and CO , which consists in the second phase. The third phase, the cathode releases O_2 , which oxidizes the electrolyte and further produce CO_2 , H_2O , and hydrocarbons when the oxidation is partial. Therefore, during venting, the composition of the vented gases evolves which makes it difficult to identify properly what is to be burnt in fire simulations. There is a need to make the link between the microscopic scale reactions inside the cell and macroscopic gaseous venting, where the average composition is well known experimentally [96, 97, 141, 171, 149, 110], where mixtures are mainly H_2 , CH_4 , C_2H_4 , ... mixed with CO and CO_2 . The main questions to answer, demanding hypotheses are:

1. Is it possible to use averaged mixtures obtained experimentally, is this average representative of the gases expected at a cell exit, or are other species expected and not captured by analyzes ?
2. Can oxygen be released by the cell, meaning a very different flame dynamics, or is there a way to assume that oxygen is absent in the vent gases ?
3. Do pure electrolyte species resist to internal decomposition (liquid or vapor), and vent out to influence the flame dynamics of common vent gas mixtures or is it possible to assume that, at first order, average gas analyzes remain applicable ?

Two ways to continue with this first introduction to the gaseous mixtures vented out by a failing Li-ion cell are proposed. In the next Section 5.2, the focus is put on one gas production mechanism: the oxidation of electrolyte species (**E₆**). Thanks to detailed chemical kinetic schemes [255, 132], 0D reactor simulations and 1D premixed flame simulations help to observe effects of electrolyte species on flame dynamics. The chapter is concluded by the prescription of simplifying hypotheses to pave the way for a small-sized chemical scheme ready for large scale 3D fire simulations. Then, in Chapter 6, the reduction process is setup and a kinetic scheme is produced and validated, under the hypotheses made.

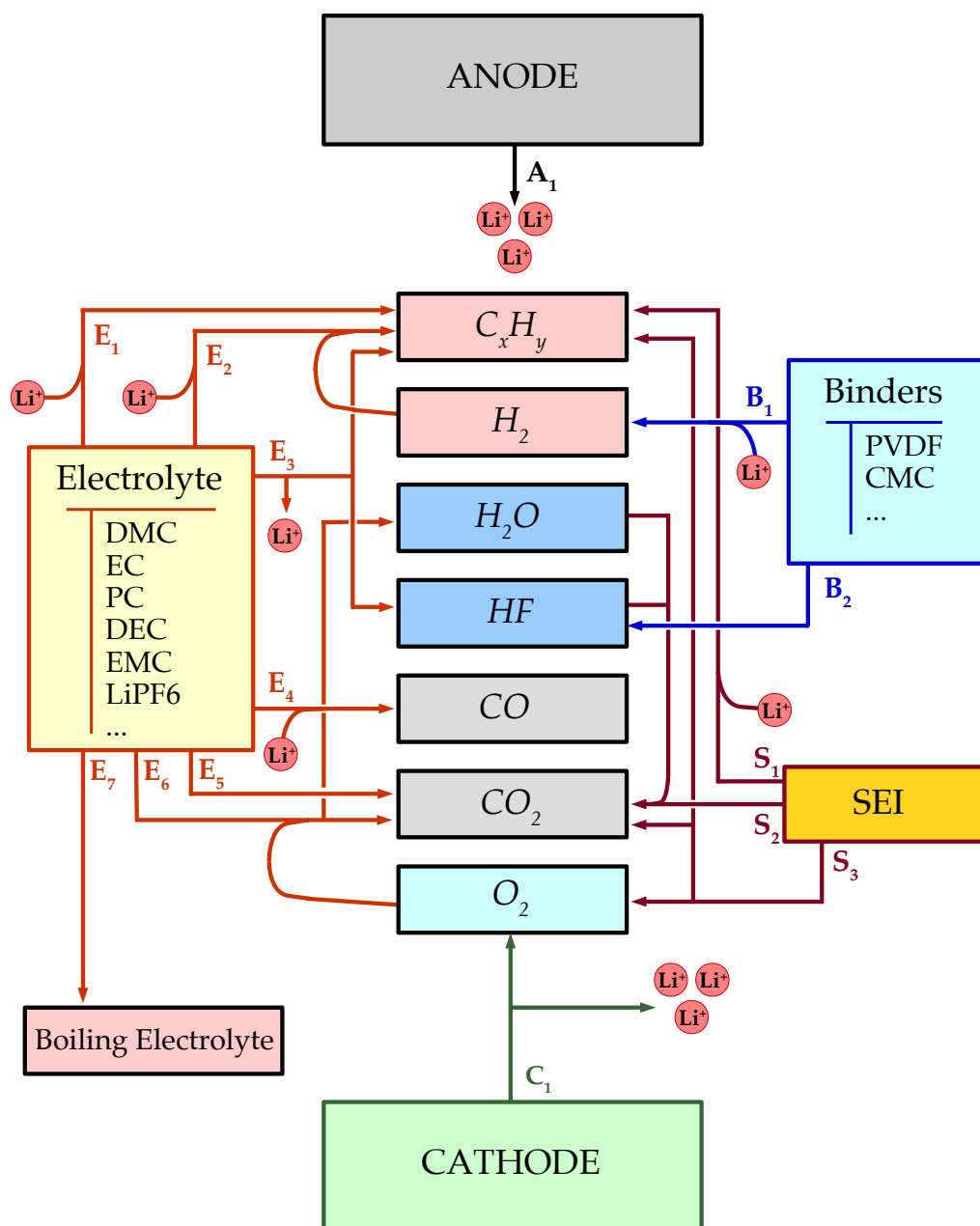


Figure 5.1.3: Schematic representation of the reactions of decomposition of the internal components of a Li-ion cell with a focus on the gases produced during the process.

Table 5.1.3: Summary of the reactions identified to play a role in the production of gases during the decomposition of a failing cell.

Reac.	Reaction summary	References
E_1	$DMC + \nu_{Li}Li \rightarrow \dots + \nu_{C_2H_6}C_2H_6$ $EC + \nu_{Li}Li \rightarrow \dots + \nu_{C_2H_4}C_2H_4$ $DEC + \nu_{Li}Li \rightarrow \dots + \nu_{C_3H_8}C_3H_8$ $PC + \nu_{Li}Li \rightarrow \dots + \nu_{C_3H_6}C_3H_6$	[296] [249] [243]

Continued on next page

Table 5.1.3 – Continued from previous page

Reac.	Reaction summary	References
E₂	$DMC + \nu_{Li}Li + \nu_{H_2}H_2 \rightarrow \dots + \nu_{CH_4}CH_4$	[296]
	$DEC + \nu_{Li}Li + \nu_{H_2}H_2 \rightarrow \dots + \nu_{C_2H_6}C_2H_6$	[243]
E₃	$LiPF_6 \rightarrow \dots + \nu_{Li}Li + \nu_{F^-}F^-$	[94]
	$DEC + \nu_{F^-}F^- \rightarrow \dots + \nu_{HF}HF + \nu_{C_2H_4}C_2H_4$	
E₄	$DMC + \nu_{Li}Li \rightarrow \dots + \nu_{CO}CO$	[296]
	$EC + \nu_{Li}Li \rightarrow \dots + \nu_{CO}CO$	[243]
	$DEC + \nu_{Li}Li \rightarrow \dots + \nu_{CO}CO$	
E₅	$DMC \rightarrow \dots + \nu_{CO_2}CO_2$	[279]
	$DEC \rightarrow \dots + \nu_{CO_2}CO_2$	
	$PC \rightarrow \dots + \nu_{CO_2}CO_2$	
E₆	$DMC + \nu_{O_2}O_2 \rightarrow \dots + \nu_{CO_2}CO_2 + \nu_{H_2O}H_2O$	[279]
	$EC + \nu_{O_2}O_2 \rightarrow \dots + \nu_{CO_2}CO_2 + \nu_{H_2O}H_2O$	[243]
	$DEC + \nu_{O_2}O_2 \rightarrow \dots + \nu_{CO_2}CO_2 + \nu_{H_2O}H_2O$	[249]
	$PC + \nu_{O_2}O_2 \rightarrow \dots + \nu_{CO_2}CO_2 + \nu_{H_2O}H_2O$	
E₇	Early venting of boiling electrolyte	[88]
C₁	$Li(Ni_xMn_yCo_z)O_2 \rightarrow \dots + \nu_{O_2}O_2 + \nu_{Li}Li$	[15]
	$Li(Ni_xCo_yAl_z)O_2 \rightarrow \dots + \nu_{O_2}O_2 + \nu_{Li}Li$	[279]
	$LiCoO_2 \rightarrow \dots + \nu_{O_2}O_2 + \nu_{Li}Li$	[197]
	$LiMn_2O_4 \rightarrow \dots + \nu_{O_2}O_2 + \nu_{Li}Li$	[249]
	$Li(Ni_xMn_y)O_2 \rightarrow \dots + \nu_{O_2}O_2 + \nu_{Li}Li$	
	$Li_2MnO_3 \rightarrow \dots + \nu_{O_2}O_2 + \nu_{Li}Li$	
$LiNiCoO_2 \rightarrow \dots + \nu_{O_2}O_2 + \nu_{Li}Li$		
B₁	$PVDF + \nu_{Li}Li \rightarrow \dots + \nu_{H_2}H_2$	[249]
	$CMC + \nu_{Li}Li \rightarrow \dots + \nu_{H_2}H_2$	[96]
B₂	$PVDF \rightarrow \dots + \nu_{HF}HF$	[65]
S₁	$SEI + \nu_{Li}Li \rightarrow \dots + \nu_{C_2H_4}C_2H_4$	[249]
S₂	$SEI + \nu_{HF}HF \rightarrow \dots + \nu_{CO_2}CO_2$	[243]
	$SEI + \nu_{H_2}H_2 \rightarrow \dots + \nu_{CO_2}CO_2$	[65]
		[257]
S₃	$SEI \rightarrow \dots + \nu_{C_2H_4}C_2H_4 + \nu_{CO_2}CO_2 + \nu_{O_2}O_2$	[96]
		[249]
A₁	Anode defoliation (after SEI destruction)	[96]

5.2 Electrolyte oxidation and combustion

Among the mechanisms of gas production, electrolyte destruction will play a crucial role. The mixture composing the liquid electrolyte can be easily vaporized under the usual temperatures reached inside a failing cell. Once under gaseous form, two main places are potential oxidation sites. First, electrolyte can react inside the cell with presence of oxygen released by the cathode and the SEI (see Fig. 5.1.3 p. 62). Then, electrolyte vapors and liquid may also be carried out during venting, mixed with the products of the other decomposition reactions. In the event of a fire, the electrolyte species burn together with the other products, influencing the flame dynamics. In this section, and in order to help simplify the problem when considering fires in further sections, two reduced problems are solved: oxidation of electrolyte species in 0D isochoric reactors, and 1D premixed flames of mixtures of electrolyte species and common vent gases. The first case helps to reproduce the reactions inside the cell before venting, of oxygen and electrolyte vapors at high temperature, allowing to see what are the resulting species of this kind of reactions. The second case targets the flame dynamics of electrolyte species burning in air, and assesses its influence on common vented gaseous mixtures' flame dynamics.

5.2.1 Chemical kinetic schemes to assert electrolyte oxidation and combustion

To simulate the 0D and 1D problems at hand, a relevant chemistry scheme must be chosen, capable of reproducing convincingly oxidation of a batch of common electrolyte species along with the species commonly observed in vent gas analyzes [96, 97, 141, 171, 149, 110]. The species involved in liquid electrolyte, and considered in this study are EC, DMC, DEC, EMC or PC (see Table 5.1.2 p. 59). In the past five years, and with the growing interest in biofuels and additives, the species cited above have been the center of more attention. In particular, kinetic schemes based on experimental flame characterization have been proposed, first for DEC by Nakamura *et al.* [196]. Later on, Sun *et al.* [253] gave access to a kinetic scheme able to reproduce DMC combustion and pyrolysis. The scheme and the approach were completed by Alexandrino *et al.* [7]. A final iteration has been recently made to propose a complete scheme merging DMC and DEC chemistry, and adding EMC by Takahashi *et al.* [255, 132]. The scheme is based on the C_1 - C_4 combustion scheme Aramco 2.0 [303, 186], and is composed of 371 species linked by 2076 reactions. It is adapted to the combustion and pyrolysis of DEC, DMC and EMC, and extends to the common small hydrocarbons observed in vent gas analyzes. This scheme is chosen to conduct the 0D and 1D evaluation of the effect of electrolyte species on vent gases, and their flame dynamics. Schemes including EC and PC are still to be proposed to assert the effect of all species in liquid electrolyte mixtures, the species have to be discarded in this work.

5.2.2 Oxidation products in 0D isochoric reactors

The example of DMC

To mimic the reactions between electrolyte and oxygen inside the failing cell, a simulation of a 0D isochoric reactor is setup using Cantera [99]. The reactor is filled at $T_0 = 1000$ K and $P_0 = 1$ atm with electrolyte mixed with pure oxygen. The level of oxygen is varied from lean conditions ($\phi = 0.2$) to conditions close to pyrolysis ($\phi = 20.0$). Once reactions occurred, the resulting mixtures along with the final temperature are sampled, allowing to see how the detailed kinetic scheme predicts the influence of the oxygen level on electrolyte species decomposition. Figure 5.2.1 shows the typical response of DMC to oxygen variation. Two main phases can be distinguished, the first for $\phi \in [\sim 4.0, 20.0]$, the second for $\phi \in [0.2, \sim 4.0]$. In the first phase, pyrolysis dominates, the heat produced is mild and hydrocarbon species remain un-burnt at the end of the simulation. Among them, methane and hydrogen are predominant in volume, to which acetylene (C_2H_2) and ethylene (C_2H_4) are added. As the level of oxygen increases, hydrocarbon level fades and is replaced by CO and H_2 , reaching a peak at $\phi = 4.5$ where hydrogen content is elevated ($> 30\%$). Under $\phi = 4.5$, end of combustion temperatures are reached, and the species produced are closer to end of combustion species: H_2O and CO_2 . A maximal temperature is obtained for $\phi = 1.0$, and corresponds to a nominal oxy-combustion of the electrolyte.

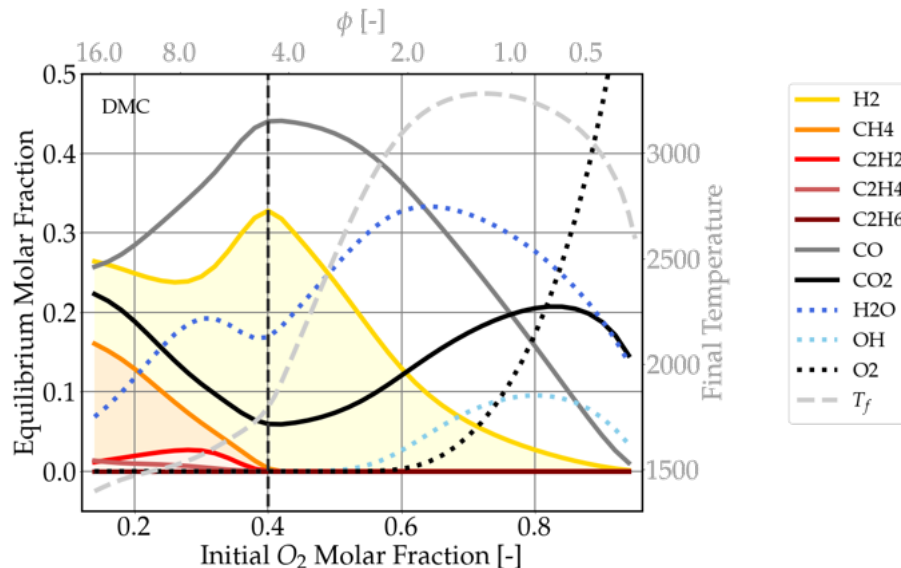


Figure 5.2.1: Analysis of the gas produced by oxidation of DMC in a 0D isochoric reactor, with increasing oxygen level. Flammable species are highlighted by coloring under the molar fraction curves. Maximum of hydrogen level is represented by a vertical hashed line.

This first example shows that, in presence of a limited amount of oxygen, and

at high temperature, electrolyte is predicted to react and produce a limited amount of heat with intermediate species consisting of smaller hydrocarbon chains.

Comparison between different electrolyte species

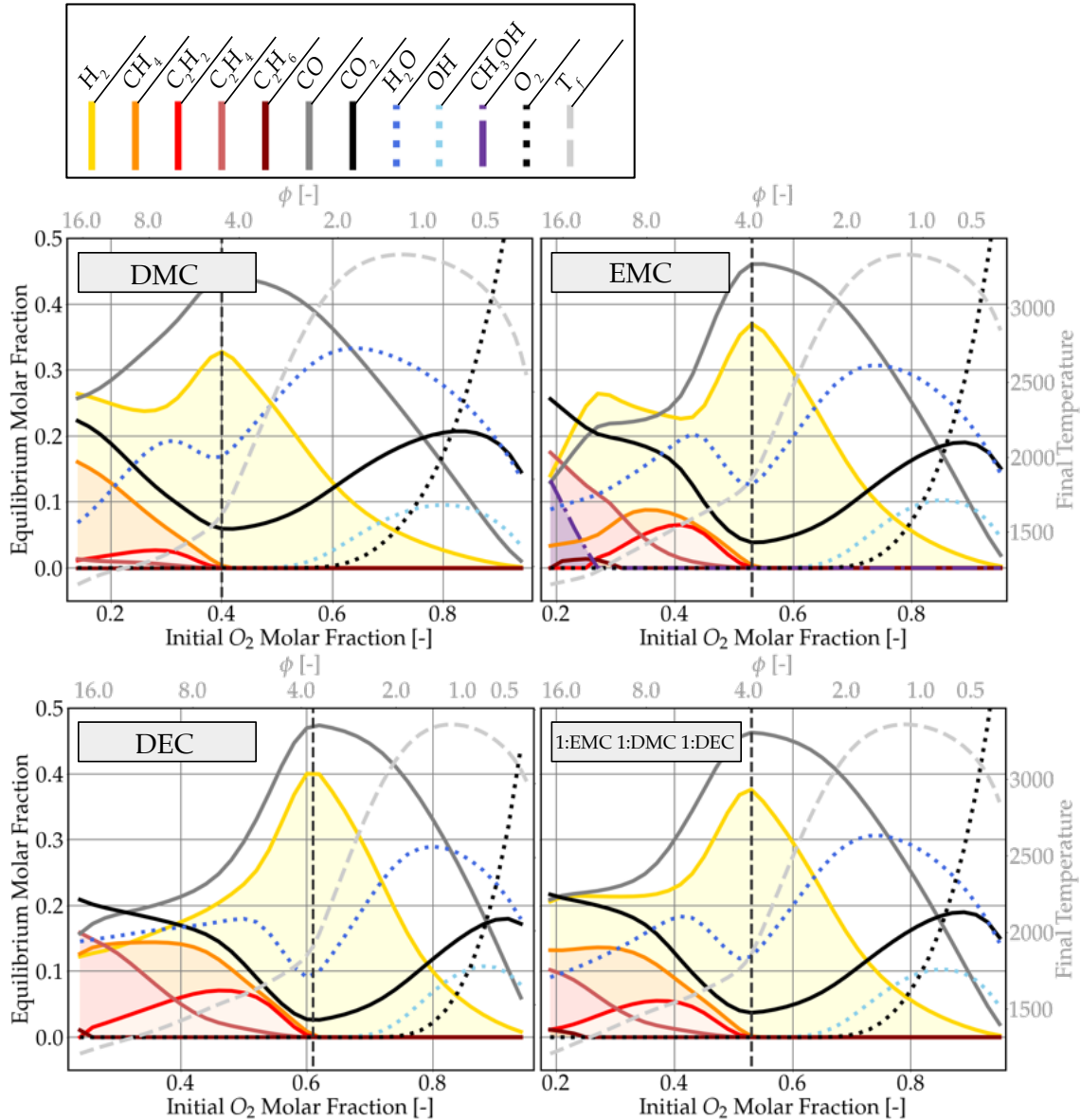


Figure 5.2.2: Analysis of the gas produced by oxidation of DMC, EMC, DEC and 1:EMC/1:DMC/1:DEC in a 0D isochoric reactor, with increasing oxygen level. Flammable species are highlighted by coloring under the molar fraction curves. Maximum of hydrogen level is represented by a vertical hashed line.

Figure 5.2.2 shows similar tendency for EMC and DEC. Again, at equivalence ratios higher than $\phi = 4.0$, hydrocarbons are produced and the level of hydrogen overall increases with the level of oxygen. The curves show strong similarities, but

differences can be observed concerning the species produced. For example, methanol CH_3OH is specific to EMC, methane production trends vary. The electrolyte mixture has therefore a strong influence on species produced and further vented out by the cell. A last case where EMC, DMC and DEC are mixed (EMC:1 DMC:1 DEC:1) shows that features of each species combine. Knowing the electrolyte mixture *a priori* would therefore allow to predict, to some extent, the type of species observed during venting.

Conclusion on electrolyte oxidation and pyrolysis in 0D

This first approach makes one link between the species generally observed in vent gases and partial oxidation of electrolyte species, with trends confirmed for DMC, EMC, and DEC. When the electrolyte is known [96, 97], a comparison between different technologies can be made. In addition, if produced in a limited amount, oxygen is predicted to be consumed which helps to justify its absence in the vent gases. The answer is similar concerning electrolyte species, which could be consumed through pyrolysis and oxidation prior to venting and therefore only small hydrocarbons, CO and CO_2 are obtained during the experimental sampling procedure.

5.2.3 Electrolyte species and 1D premixed laminar flames

Effect of electrolyte addition to common vent gases

In addition to the isochoric simulations, and because electrolyte can be ejected directly during certain phases of the venting under liquid or vapor form, it is important to assert the influence of electrolyte species on flame dynamics of common vent gases. As a reference of gaseous analysis, the work of Golubkov *et al.* is selected [96]. Here, the vent gases are sampled from a failing NMC 18650 cell with a State of Charge (SoC) of 100 % submitted to overheating. Gases are sampled out of the Argon atmosphere and is composed (volume fractions) as follows: H_2 : 30.8 %, CH_4 : 6.8 %, C_2H_4 : 8.2 %, CO : 13.0 %, CO_2 : 41.2 %. Laminar premixed flames are computed at $\phi = 1.0$ and $T = 300$ K. The combustible is then selected as a mixture between the reference vent gas and electrolyte species. The volume fraction X_{el} of electrolyte inside the combustible is varied in $[0.0, 1.0]$ until pure electrolyte is burnt, while the global equivalence ratio of the mixture with air always remains equal to 1.0. The addition of electrolyte to the vent gas can be observed in Figure 5.2.3 and 5.2.4. For all three electrolyte species DMC, EMC and DEC, as X_{el} increases, the laminar flame speed s_L decreases. The lowest value is reached for pure DMC at $s_L = 0.317 \text{ m.s}^{-1}$, versus $s_L = 0.432 \text{ m.s}^{-1}$ for the vent gas mixture alone, which represents a relative difference of 26.6 %. Concerning laminar flame thickness, the addition of electrolyte species tends to make the flames thinner. The thinnest flame

is obtained for pure EMC at $\delta_L = 0.389$ mm, *versus* $\delta_L = 0.416$ mm for the vent gas mixture, corresponding to a relative difference of 6.9 %.

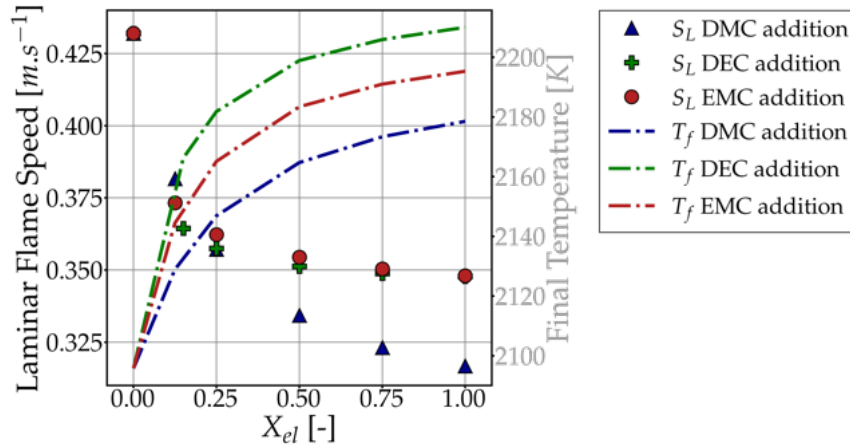


Figure 5.2.3: Effect of electrolyte enrichment on vent gases at $T = 300$ K and $\phi = 1.0$: Laminar flame speed s_L and burnt gases temperature.

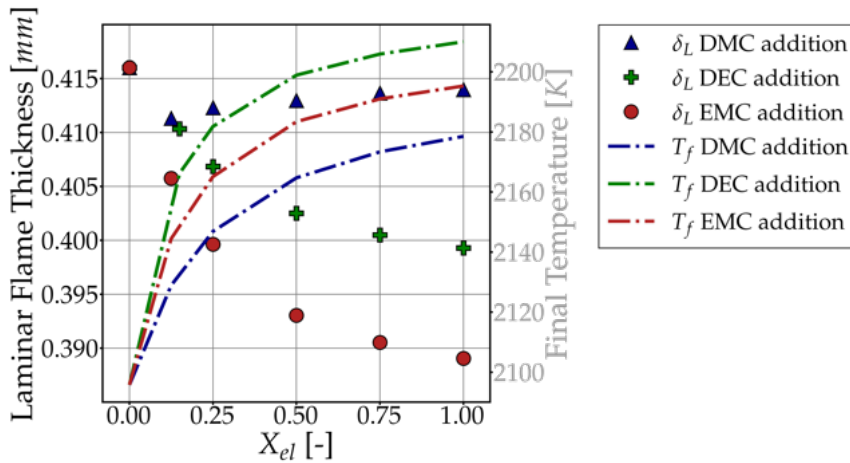


Figure 5.2.4: Effect of electrolyte enrichment on vent gases at $T = 300$ K and $\phi = 1.0$: Laminar flame thickness δ_L and burnt gases temperature.

Moreover, Fig. 5.2.5 shows how the transition from pure vent gases to pure electrolyte species changes the flame shape. The heat released is increased from $4.05 \times 10^9 \text{ J.m}^{-3}.\text{s}^{-1}$ for pure vent gases to $5.33 \times 10^9 \text{ J.m}^{-3}.\text{s}^{-1}$ for pure EMC (24 %).

Conclusion on the combustion of electrolyte in 1D

Overall, the addition of electrolyte to common vent gases tends to reduce flame speed and flame thickness while it increases the heat released and the burnt gases temperature. The influence is however limited to 30 % in the worst cases which means that the very high cost of taking into account electrolyte when simulating venting and fire is not a first order priority. Moreover, considering evaporation, which is feasible, would add costs in simulations, that are unnecessary for this initial study.

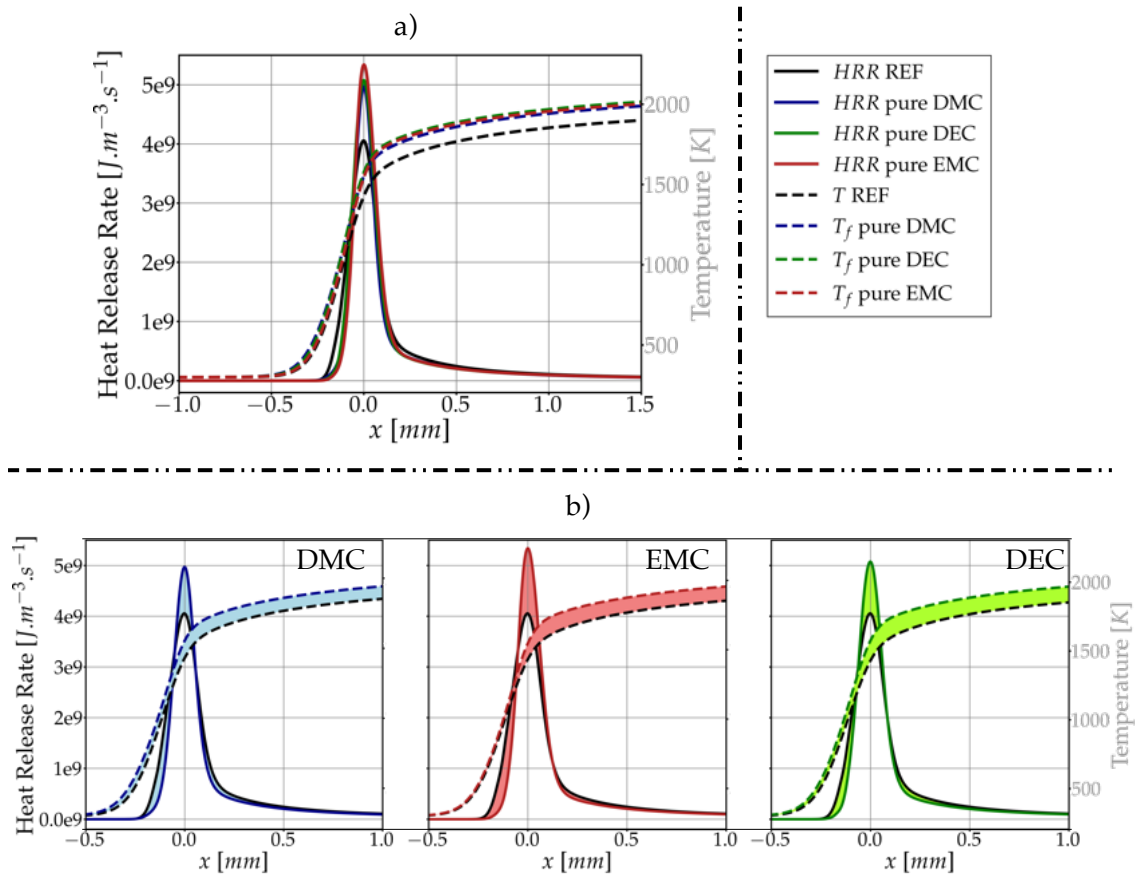


Figure 5.2.5: Profiles of electrolyte enriched vent gases at $T = 300$ K and $\phi = 1.0$. a) Comparison of the reference case (pure vent gases) to pure electrolytes. b) Detailed visualization of the range of changes from pure vent gas to pure electrolyte as electrolyte is progressively added.

5.2.4 Concluding remarks on electrolyte oxidation

The simulations performed in this section allow to familiarize with the behaviour of electrolyte species, that account for a large part of the gases further observed during venting and responsible for fires. In view of these results, three simplifying hypotheses are proposed, to continue with the study and allow the scaling up to more complex 3D simulations:

1. **H₁**: The oxygen produced at the delithiated cathode and by other decomposition reactions is supposed to react entirely before venting, explaining the absence of oxygen inside the ejected mixture.
2. **H₂**: The vented gas composition is constant and selected based on gas analysis of entire TR events, thus representative of the average mixture throughout a TR.
3. **H₃**: The gases produced by the cell are in equilibrium and are the result of the decomposition of carbon-based components (electrolyte, separator, binder, ...). The electrolyte vapors usually observed during the first phases of the TR are discarded, and supposed to be already transformed when vented out.

The gaseous mixtures considered in the study that follows are therefore of the form H_2 : X_{H_2} %, CH_4 : X_{CH_4} %, C_xH_y : $X_{C_xH_y}$ %, CO : X_{CO} %, CO_2 : X_{CO_2} %. Such mixtures pose crucial questions linked to combustion, such as preferential diffusion of hydrogen, effect of CO and CO_2 dilution, combustion models adapted to multi-component, which are the subject of the following chapters.

Also, although the hypotheses **H₁** to **H₃** are necessary to continue, there are perspectives to alleviate them by increasing the complexity of the chemical schemes considered during simulations, to account for burning electrolyte, by adding oxygen venting and observe flame structures. Eventually, spray flames and evaporation models are already applied to liquid fuel combustion (kerosene, diesel, gasoline, ...), and could be considered as a way to continue with liquid electrolyte.

In the next chapter, the reduction of detailed chemical schemes is asserted to produce 3D ready mechanisms for vent gas mixtures for various combustion scenarios (ignitions, jet flames, explosions, ...).

Chapter 6

A representative reduced kinetic scheme

Contents

6.1 Analytically reduced kinetic framework	72
6.1.1 Cost problem in multispecies environment	72
6.1.2 ARCANE	74
6.2 Vented gaseous mixtures	75
6.2.1 Selection of gaseous mixtures	75
6.2.2 Comparisons using detailed kinetic schemes	75
6.3 Derivation of the reduced scheme	78
6.4 Validation of the reduced kinetic scheme	81
6.4.1 0D isochoric auto-ignition validation	81
6.4.2 1D premixed laminar flame validation	81
6.4.3 1D counter-flow diffusion flame validation	82
6.4.4 Summary of the reduction process	82
6.5 Reduced scheme generalization test	84
6.5.1 Generalization to untested Li-ion vent gases	84
6.5.2 Generalization to pure fuels	86
6.6 Conclusion on kinetic scheme reduction	87

6.1 Analytically reduced kinetic framework

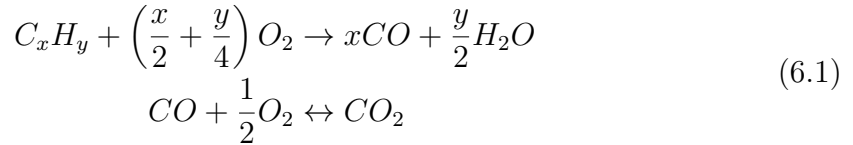
6.1.1 Cost problem in multispecies environment

When considering reacting flows, N equations for species conservation are added to the classical five Navier-Stokes equations to solve in non-reactive cases, N being the number of species taken into account (See Chapter 2). Battery fires involve generally hydrogen (H_2) and small hydrocarbons ($C_1H_x - C_4H_y$) at hot temperatures (See Chapter 5). Detailed schemes are available, suited for ignition problems, premixed and diffusion flames in simplified 0D and 1D configurations [223, 222, 41]. More specifically, the kinetic scheme CRECK_2003_TOT_HT [57] (named PM in this document) is composed of 368 species and 14462 reactions, for the combustion of $C_1 - C_{16}$ hydrocarbons, and the UC San Diego scheme (named SD in this document) [41] is composed of 57 species and 268 reactions, for the combustion of $C_1 - C_4$ hydrocarbons. The use of detailed combustion mechanisms for Li-ion vent gases has been tested experimentally by Henriksen *et al.* [110]. Measurements of premixed laminar flame speed in a spherical bomb are performed and compared to 1D simulations using Cantera [99] with detailed mechanisms including SD. Not all mechanisms are able to fit perfectly to the experimental observations but overall low errors are obtained. In particular, SD retrieves satisfactorily the differences in behavior of three gaseous mixtures.

However, the number of species to consider when using such detailed schemes in 3D CFD codes is a direct obstacle to the result in terms of computational time and storage space. Several approaches exist to produce a chemical modelling adapted to the cost constraint raised by large 3D CFD cases. A non-exhaustive selection of these approaches and their limitations is proposed here.

Global chemistry

The objective of Global chemistry is to reproduce macroscopic flame characteristics such as laminar flame speed and adiabatic flame temperature, with a minimal number of species and reactions. Generally one or two reactions involve less than ten species. For example, a two-step scheme for the oxy-combustion of hydro-carbons could write:



A Pre-Exponential Adjustment (PEA) function can be added to adapt the rate of the first reaction and better fit the macroscopic quantities targeted on a range of equivalence ratio [84]. The very low cost of such a scheme makes it perfect for large 3D CFD simulations. However, when considering the combustion of multi-species fuels with a large variety of combustion phenomena (ignition, premixed flames, diffusion flames, varying temperatures, pollutant emission), such a scheme will show strong limitations. More than one scheme will be needed making it difficult to quantitatively compare cases.

Tabulated chemistry

At the opposite of reaction mechanisms, the tabulated chemistry introduced by Peters [209] and its further developments [91, 81] consists in observing that species are linked by scalar measures in the flow such as the progress variable c or the mixture fraction Z . The knowledge of these quantities allows to search in a pre-computed table the local mixture composition and the associated heat-release and temperature. It is very-computationally efficient once the table is available. However, the quality of the prediction relies on the way the table is built. Extensive information must be obtained *a priori* on the flame to reproduce, and its interaction with boundaries. It is also necessary to ensure that the set of scalar measures properly defines the chemical processes. Having a table capable of generalizing to a large panel of combustion scenarios is still under discussion.

Analytically Reduced Chemistry

In this work, the approach selected is to produce a semi-detailed scheme. It accommodates the versatility and precision of detailed schemes to a better cost efficiency. One way to obtain such a scheme is to perform a reduction of a detailed scheme. Knowing that only specific sub-parts of the kinetic schemes are generally used for each operating point [33], non-significant species and reactions can be ignored through a systematic reduction process. A reduced chemical mechanism proposes under a unique scheme: 1. a relevant chemical modelling of a variety of combustion regimes for a batch of burning mixtures, 2. a decrease in computational time and disk space. The following sections emphasize the derivation of such a 3D-ready reduced kinetic, using the software ARCANE [35, 34], starting from a problem definition and a detailed scheme, until the validation of the scheme under relevant canonical cases.

6.1.2 ARCANE

The software Arcane [34] is used to generate a reduced kinetic scheme able to 1. be representative of the general behavior of mixture encountered during Li-ion battery fires and 2. reduce the cost of 3D CFD simulations. Arcane produces Analytically Reduced Chemistry (ARC) schemes based on three reduction paradigms [33]:

- a. the Direct Relation Graph with Error Propagation (DRGEP) method [207, 166]
- b. the Chemical Lumping [206]
- c. the Quasi-Steady State (QSS) assumption [167]

Each step is described in the work of Cazères et al. [35, 33] along with the automation process. They are recalled here.

a. DRGEP

The first step consists in linking each reaction and each species to a target quantity (laminar flame speed at a given operating point, ignition delay, final temperature, ...) with a non-dimensional coefficient. The species and reactions are then ranked by importance thanks to this coefficient. Species and reactions that fall under a user pre-defined tolerance are discarded and the relational graph is recomputed to follow the same procedure until no further reduction is possible without overshooting the tolerance. A scheme is obtained which is, on the one hand, of smaller size compared to the detailed original scheme, and on the other hand, still fitted for the computation of representative combustion cases with minimal errors.

b. Chemical Lumping

Detailed mechanisms often involve different isomers. Their atom composition is identical but due to differences in molecular agencements their thermodynamic properties vary. The Chemical Lumping step concatenates the isomers under a sole representative species without a drastic change of the reaction dynamics.

c. Quasi-Steady State

As a final step, species with the shortest residence timescales are identified and flagged as potential Quasi-Steady State (QSS) species. A set of analytical relations are defined to link QSS species to non-QSS species allowing to retrieve QSS species concentration knowing the concentrations of non-QSS species. Species switched to QSS species are kept if the error due to the switch respect the tolerance levels. These species do not require the resolution of a transport equation which in return saves

computational time and storage space. It also relieves the solver from stiff species with low chemical timescales which induces small time-steps.

Arcane automates the three steps in series. The tool efficiently reduces a detailed chemical scheme following specific reference cases where errors should be minimal. The reference cases are key to produce a relevant scheme. The next sections aim at presenting the choice made to produce a 3D-ready kinetic scheme, in particular concerning references.

6.2 Vented gaseous mixtures

6.2.1 Selection of gaseous mixtures

Chapter 5 emphasizes that, under abuse conditions, internal short circuits can trigger decomposition reactions that produce gases. The vented gaseous mixtures may vary in time during TR, as reactions priorities evolve and temperature increases, boiling electrolyte and oxygen may also be carried out. In this study, three main simplifying hypotheses are made in the previous chapter, justifying the focus on averaged vent gas mixtures of the form H_2 : $X_{H_2}\%$, CH_4 : $X_{CH_4}\%$, C_xH_y : $X_{C_xH_y}\%$, CO : $X_{CO}\%$, CO_2 : $X_{CO_2}\%$.

In order to produce a representative chemistry kinetic scheme, six mixtures have been selected from the literature. They form the reference points when asserting the precision of the Analytically Reduced Chemistry scheme obtained further. To broaden the scope of the study, four main types of cathode materials are part of the test : $Li(Ni_xMn_y,Co_z)O_2$ (NMC), $LiFePO_4$ (LFP) and $LiCoO_2$ (LCO) and combined $LiCoO_2 / Li(Ni_xMn_y,Co_z)O_2$ (LCO/NMC). The choice of one cathode material influences the choice of solvents which in return change the gases produced during thermal runaway [12]. The mixtures along with experimental information and sources are given in Table 6.3.1 at page 80.

6.2.2 Comparisons using detailed kinetic schemes

To account for the fact that Li-ion cell fires may occur under a range of temperature as large as [300 K, 1000 K], for hot gases ejected into cold atmosphere, densities, adiabatic flame temperatures and flame speeds are given for the two extreme temperatures 300 K and 1000 K. The latter case is relevant to guarantee that chemical paths for high temperature combustion are well retrieved, even if laminar flame speed at this temperature is not reachable experimentally. The pressure is kept at 101325.0 Pa for most simulations. In order to identify mix-

tures and see if trends emerge concerning each type of cell, comparisons using detailed schemes are conducted including, thermodynamic quantities, 0D auto-ignition and 1D laminar premixed flames. The kinetic schemes used in this section are CRECK_2003_TOT_HT [57] (PM) and the UC San Diego scheme (SD) [41].

First, the selected mixtures are evaluated regarding simple thermodynamic quantities. The density ρ , the Lower Heating Value (LHV) and the Lower Flammability Limit (LFL) are given in Table 6.2.1. LFL for burning species diluted into CO_2 are computed using the modified Le Chatelier's law presented in the work of Chen *et al.* [43]. This comparison shows that LCO and LCO/NMC sourced mixtures are potentially more dangerous with higher LHV, low LFL, together with a more volatile behavior.

Table 6.2.1: Thermodynamic quantities of the six mixtures.

$(P = 101\,325\text{ Pa})$	ρ [kg.m ⁻³]	ρ [kg.m ⁻³]	LFL [% vol. air]	LHV [MJ.kg ⁻¹]
	at $T = 300\text{ K}$	at $T = 1000\text{ K}$	at $T = 300\text{ K}$	at $T = 300\text{ K}$ and $\phi = 1.0$
NMC1	1.047	0.314	7.381	10.64
NMC2	1.116	0.335	8.514	9.69
LFP1	1.136	0.341	8.313	7.57
LFP2	1.115	0.335	8.085	8.61
LCO/NMC	0.942	0.283	6.698	14.60
LCO	1.017	0.305	7.647	11.93

This trend is confirmed in Fig. 6.2.1 which shows the differences in adiabatic flame temperature T_{ad} computed using the PM and SD detailed schemes introduced in Section 6.1.1, identified as two potential source-mechanisms for the reduction procedure. LCO and LCO/NMC rank in front of NMC cells in terms of adiabatic flame temperature, LFP ranking last.

The 0D isochoric auto-ignition delay is then computed using Cantera [99] for both detailed schemes PM and SD (Fig. 6.2.1). All mixtures behave similarly: the evolution of ignition delay with the reduced temperature is comparable for all schemes.

The 1D premixed laminar flame speed s_L is finally computed using once again Cantera [99], with multi-component transport, over a range of equivalence ratio $\phi \in [0.5, 1.5]$, from lean to rich mixtures. The inlet flow temperature is set to 300 K and 1000 K, and the domain width is set to 40.0 mm. At 1000 K the auto-ignition delay is always higher than w/s_L where w is the width of the grid and s_L is the laminar flame speed, ensuring that no auto-ignition occurs in the fresh gases flow, which allows stable simulations even at this high temperature. Figure 6.2.2 plots the laminar flame speed versus equivalence ratio for both detailed kinetic schemes at 300 K and 1000 K. Again, LCO and LCO/NMC sourced mixtures show greater laminar flame speeds. The difference is more pronounced for rich mixtures.

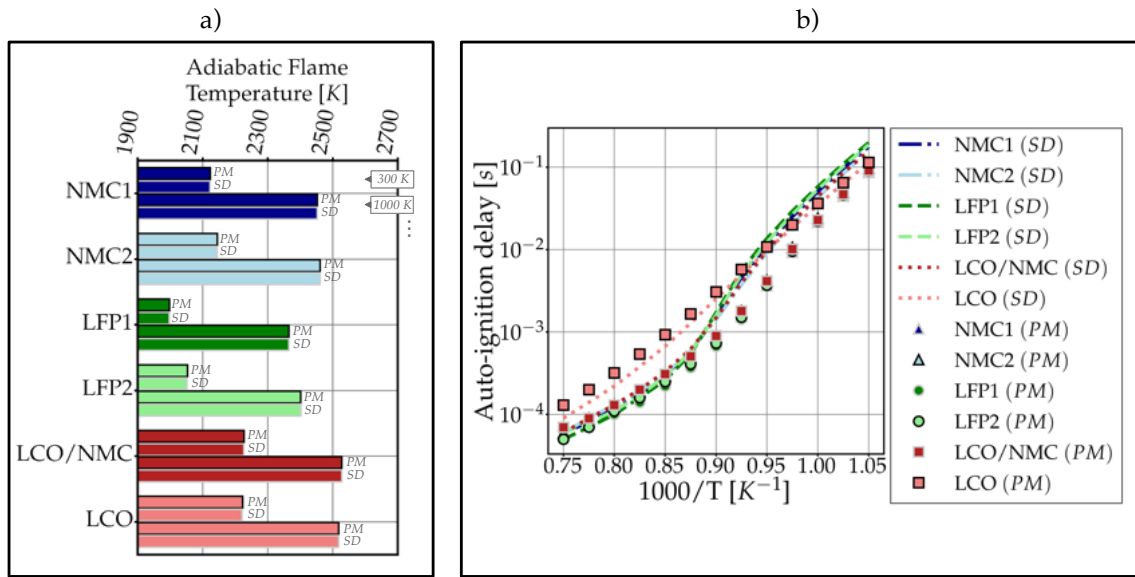


Figure 6.2.1: Vent gas comparison: a) adiabatic flame temperature for both detailed kinetic schemes at stoichiometry ($\phi = 1.0$) with the Polimi scheme (PM) and the San Diego scheme (SD), 0D isochoric auto-ignition delay for both detailed kinetic schemes.

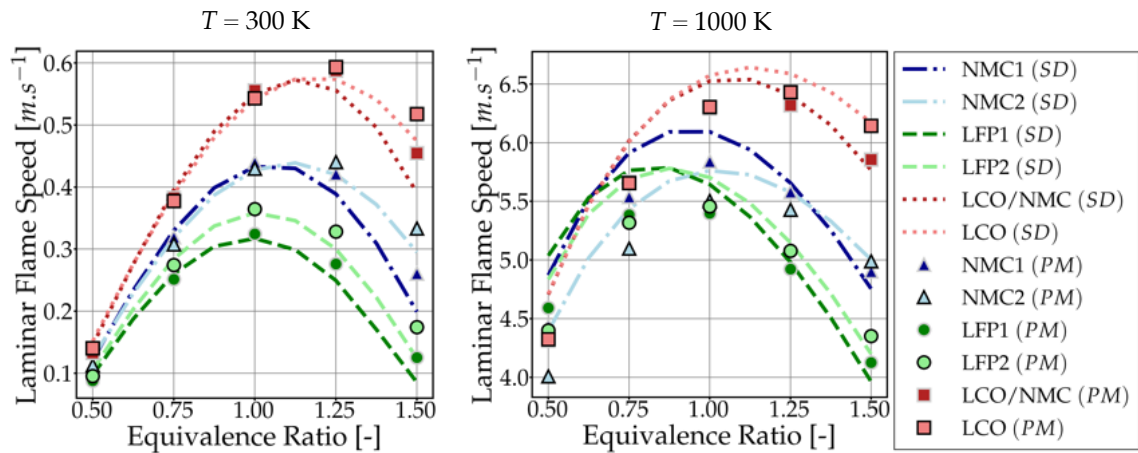


Figure 6.2.2: Comparison of the 1D premixed laminar flame speed for both detailed kinetic schemes at $T = 300$ K and $T = 1000$ K

With overall higher flame temperatures, flame speeds and lower LFL, LCO and LCO/NMC vent gases are estimated to be more dangerous than the vent gases from both NMC and LFP cells studied here¹. One key parameter responsible for this is the ratio of burning species volume fraction and diluting species (here CO_2). For LCO and LCO/NMC vent gases, it peaks at around 3.0:1 and 2.9:1 respectively. In comparison, NMC1 and NMC2 are at 1.4:1 and 1.7:1. Finally, LFP1 and LFP2 are at 0.9:1 and 1.1:1. However, the explanation of these differences in proportion should

¹Of course, this comparison holds for these gaseous analyzes, and precautions should be taken when generalizing to an entire Li-ion family. Numerous parameters may play roles (SoC variations, over-heating system, aging, ...), and attention to detail is primordial to erase as much as possible dissimilarity in the gas sampling procedure.

be linked to the choice of solvent and cathode, and it is still an open question [96, 97, 15, 253], evoked in Chapter 5.

6.3 Derivation of the reduced scheme

Two essential objects should be defined to start the reduction. First of all, the root mechanism to reduce is chosen. Then, a list of cases representative of the tracked combustion phenomena is prepared. Regarding the chemical scheme to use, it was shown in the previous section that both mechanisms SD and PM behave similarly for the six mixtures, and both remain good candidates for the reduction process. To compare the schemes, for one data point, relative error $RE = |y^A - y^B|/y^B$ is computed. Over a range, mean relative error (MRE) is considered:

$$\text{MRE} = \frac{1}{N} \sum_{i=1}^N \frac{|y_i^A - y_i^B|}{y_i^B} \quad (6.2)$$

where N is the number of points in the range tested (range of equivalence ratio, range of temperature, ...), y_i is the i -th value of the evaluated magnitude (laminar flame speed, auto-ignition delay, ...), the super script $.^A$ and $.^B$ refer to the two different fields compared. In the following comparisons, SD is the field A and PM is arbitrarily chosen as the reference and is therefore field B. For 1D premixed laminar flames, the mean relative error over the entire range of equivalence ratio [0.5, 1.5] is maximal among the six mixtures for LFP1: 11.5 % at $T = 300$ K and 5.3 % at $T = 1000$ K (see Fig. 6.2.2). In addition, adiabatic flame temperatures are nearly identical for all 6 mixtures (See Fig. 6.2.1 a)), auto-ignition delay predictions agree well at high temperature. Differences are contained at low temperature (See Fig. 6.2.1 b)). It motivates the choice of the SD scheme as its number of species and reactions is lower, which will limit the reduction time and insure a smaller final chemical scheme. In fact, computing a 1D premixed flame using the very detailed PM scheme is typically 200 times more expensive than computing it with SD (average computed for the six mixtures and a flame at stoichiometric conditions and 300 K on one Intel Skylake CPU core). Moreover, the use of SD for Li-ion vent gases has been validated experimentally by Henriksen *et al.* [110].

After the selection of the root mechanism, the reduction cases must be chosen. To account for the diversity of events to study in Li-ion related fires, for each mixture, five cases are considered:

1. 0D isochoric auto-ignition at $T = 1000$ K and $P = 101\,325$ Pa
2. 1D premixed laminar flame at $T = 300$ K, $P = 101\,325$ Pa and $\phi = 0.5$

3. 1D premixed laminar flame at $T = 300$ K, $P = 101\,325$ Pa and $\phi = 1.5$
4. 1D premixed laminar flame at $T = 1000$ K, $P = 101\,325$ Pa and $\phi = 0.5$
5. 1D premixed laminar flame at $T = 1000$ K, $P = 101\,325$ Pa and $\phi = 1.5$

Limiting errors are set to 20 % for both ignition delay and associated maximum heat release in 0D. In 1D, the same limiting error is applied to laminar flame speed, maximum heat release, burnt gases temperature and H_2O mass fraction in burnt gases. In practice the errors reached are lower and a complete set of verification is performed in the following sections.

The reduction including case running takes 72 min on one Intel Skylake CPU core. The result is an 18 species plus 6 quasi-steady state species with 93 reactions and is further denominated as ARC. The root mechanism (SD) contains 57 species and 268 reactions. The division by 3 of the number of transported species brings a speed up of 5.5 for laminar flames with SD. In fact, the final comparison between PM, SD and ARC shows that, on average for the six mixtures, a stoichiometric laminar flame at 300 K is computed in 10 163.0 s for PM, 52.9 s for SD and 9.6 s for ARC.

The gain in CPU time for this 1D test flame makes the ARC scheme a good candidate for 3D reactive CFD computations. However, validation tests have to be conducted to verify that the reduction is not deteriorating the precision. Therefore, ARC and SD are further compared for three major cases: 1. 0D isochoric auto-ignition (Section 6.4.1), 2. 1D premixed laminar flame (Section 6.4.2), and 3. 1D counter-flow diffusion flame (Section 6.4.3). The latter one is added as diffusion flames are expected when considering the venting of pure fuel into the atmosphere. With high velocity and turbulence, premixed flames must dominate but at lower velocity and turbulence level, diffusion flames can exist. It is necessary to verify that the transport properties of ARC are well translated under this latter constraint. Comparisons are given by computing relative errors and mean relative errors (See Eq. 6.2) using the SD scheme as the reference.

Table 6.3.1: Mixtures selected along with information on experimental conditions and sources.

Mix. Name	Cathode material	Vol. fractions ¹	Experimental information
NMC1	$Li(Ni_{0.45}Mn_{0.45}Co_{0.10})O_2$	H_2 : 30.8 % CH_4 : 6.8 % C_2H_4 : 8.2 % CO : 13.0 % CO_2 : 41.2 %	- 18650 cell ² - overheat-to-TR - SoC : 100 % - Argon atmosphere - [96]
NMC2	$Li(Ni_xMn_yCo_z)O_2$ <i>undisclosed ratios</i>	H_2 : 22.4 % CH_4 : 5.2 % C_2H_4 : 5.6 % C_2H_6 : 1.0 % CO : 28.9 % CO_2 : 36.8 %	- Pouch + Hard case cells - overheat-to-TR - SoC : 100 % - Air, reaction with O_2 considered negligible for the selected high volume venting - [141]
LFP1	$LiFePO_4$	H_2 : 31.0 % CH_4 : 4.1 % C_2H_4 : 6.8 % CO : 4.8 % CO_2 : 53.2 %	- 18650 cell - overheat-to-TR - SoC : 100 % - Argon atmosphere - [96]
LFP2	$LiFePO_4$	H_2 : 29.6 % CH_4 : 5.4 % C_2H_4 : 7.2 % CO : 9.2 % CO_2 : 48.6 %	- 18650 cell - overheat-to-TR - SoC : 100 % - Argon or N_2 atmosphere - [97]
LCO/NMC	$LiCoO_2$ → (66 %) $Li(Ni_{0.50}Mn_{0.25}Co_{0.25})O_2$ → (34 %)	H_2 : 30.0 % CH_4 : 8.6 % C_2H_4 : 7.7 % C_2H_6 : 1.2 % CO : 27.6 % CO_2 : 24.9 %	- 18650 cell - overheat-to-TR - SoC : 100 % - Argon atmosphere - [96]
LCO	$LiCoO_2$	H_2 : 26.0 % CH_4 : 4.9 % C_2H_4 : 4.8 % ³ C_3H_6 : 1.5 % CO : 36.9 % CO_2 : 26.0 %	- 18650 cell - overheat-to-TR - SoC : 100 % - N_2 atmosphere - [171]

¹ Volume fractions are normalized so that all the species volume fractions sum to 100 %. Species volume fractions strictly lower than 1.0 % after normalization are neglected and volume fractions are recomputed to sum again to 100 %.

² Cylindrical cells: 18 mm in diameter and 65 mm in length.

³ Content in Ethylene (C_2H_4) and Acetylene (C_2H_2) cannot be separated in the source study. In this thesis, based on the fact that both species have comparable LHV and molecular weights, it is modeled using Ethylene only.

6.4 Validation of the reduced kinetic scheme

6.4.1 0D isochoric auto-ignition validation

The 0D isochoric auto-ignition delay is computed using Cantera for both SD and ARC on the $[0.75, 1.05]$ range of reduced temperatures (corresponding to $[952\text{ K}, 1333\text{ K}]$) and is plotted in Fig. 6.4.1.

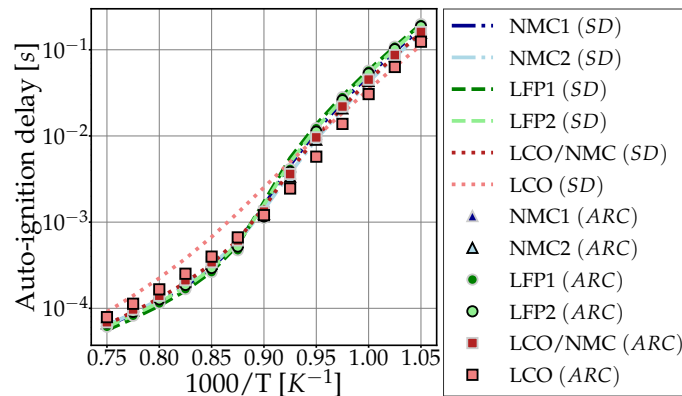


Figure 6.4.1: Comparison of the 0D isochoric auto-ignition delay for ARC and SD.

On the one hand, the general tendency is well retrieved by the ARC scheme. At the point $T = 1000\text{ K}$, which corresponds to a low temperature auto-ignition, the relative error is maximal for the LCO mixture at 11.6 % with the second largest error being 2.3 % for LCO/NMC. The mean relative error on the whole range of temperature is also maximum for the LCO mixture and is 28.6 %. This mean relative error is lower than 10 % for the five other mixtures, which guarantees a good agreement between reduced and detailed schemes for auto-ignition delays.

6.4.2 1D premixed laminar flame validation

1D premixed laminar flames are computed for the six mixtures at both $T = 300\text{ K}$ and $T = 1000\text{ K}$ for the range $\phi \in [0.5, 1.5]$ and a domain width of 40.0 mm. At low temperature, average errors are maintained under 5.5 % (corresponding to the LFP1 mixture) meaning that the reduction has kept the right chemical paths (Fig. 6.4.2, $T = 300\text{ K}$). The conclusion is the same for premixed flames at $T = 1000\text{ K}$ as the average relative error is under 3.4 % (NMC1 mixture). The highest relative error is 8.6 %, it corresponds to the point $\phi = 0.5$ for LFP1 (Fig. 6.4.2, $T = 1000\text{ K}$). Premixed flames are retrieved with the ARC scheme and reduction has not impinged the quality of the prediction of laminar flame speeds. The scheme is therefore applicable to cases where the flammable gases are mixed with air either during venting (turbulent jet flames, ...) or after venting (ignition in enclosed modules filled with gases, ...).

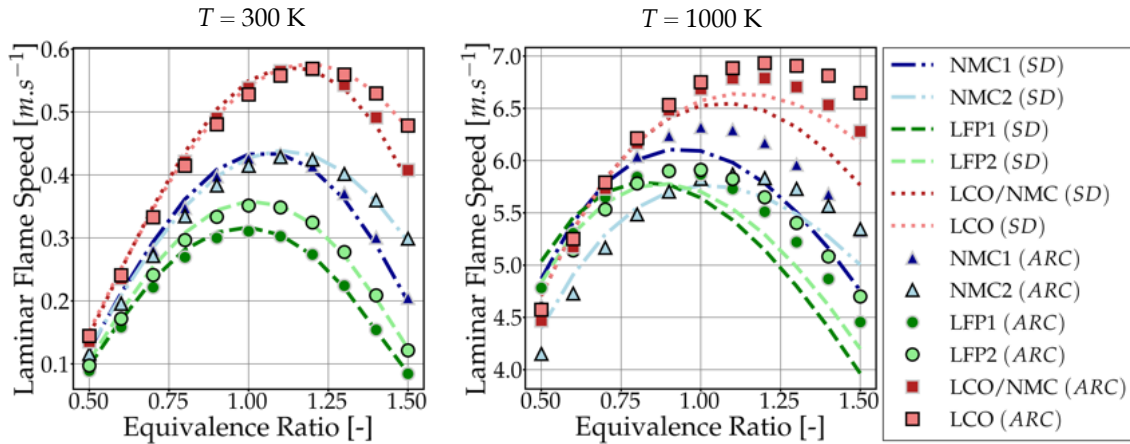


Figure 6.4.2: Comparison of the 1D premixed laminar flame speed for ARC and SD at $T = 300$ K and $T = 1000$ K.

6.4.3 1D counter-flow diffusion flame validation

During TR, gases produced by the failing cell are ejected through the vent device: these pure flammable gases meet air and a diffusion flame can be observed. In order to check the reduced scheme under these conditions, 1D counter-flow diffusion flames are computed for a range of strain rate a $[50, 500]$ (s^{-1}), computed using Eq. 3.10, which corresponds to a large set of diffusion flame conditions, from low to high strain rates (e. g. CH_4 extinction strain rate is experimentally measured close to $350 s^{-1}$ [264]). The domain width is set to 80.0 mm, and the fuel and air stream temperatures are 1000 K and 300 K respectively corresponding to approximate cell venting conditions. Two main quantities are compared for ARC and SD: 1. the integral heat release accounting for the heat produced by the flame and 2. the peak temperature of the flame. Figure 6.4.3 - *right* shows the very good agreement between ARC and SD in terms of integral heat release. The maximum average error is 2.5 %, and is reached for the LCO/NMC mixture. Figure 6.4.3 - *left* shows the maximum temperature comparing ARC and SD. Once again, the agreement is good with a maximum average error of 1.6 % (LCO/NMC). This exercise is also a way to compare again the six mixtures: LCO and LCO/NMC mixtures depict overall higher integral heat releases and maximum temperatures under the 1D diffusion combustion mode.

6.4.4 Summary of the reduction process

The reduction procedure applied to the San Diego scheme offers the possibility to generate an analytically reduced scheme. The scheme is able to reproduce the main cases for which it has been created and depicts overall low errors. Table 6.4.1 p. 84 summarizes the computed errors for the six mixtures under the different test cases and targeted magnitudes. In addition to the punctual relative error (RE) and the

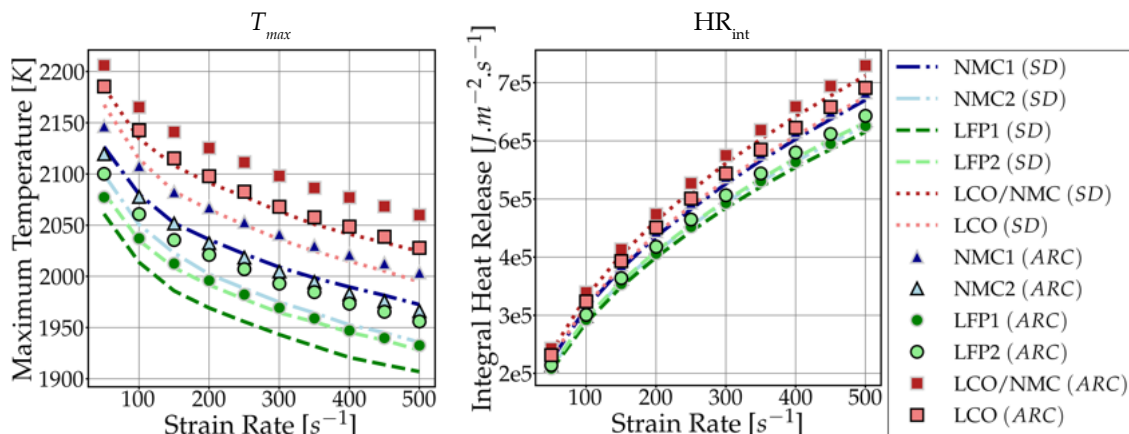


Figure 6.4.3: Comparison of the 1D counter-flow laminar diffusion flame maximum temperature and integral heat release for ARC and SD, for a fuel stream temperature $T_{fuel} = 1000$ K and an air stream temperature $T_{air} = 300$ K.

mean relative error (MRE, see Eq. 6.2) over a representative range, the normalized root mean square error is added to observe error dispersion as it tends to penalize large errors:

$$\text{NRMSE} = \frac{1}{\bar{y}^B} \sqrt{\frac{1}{N} \sum_{i=1}^N (y_i^A - y_i^B)^2} \quad (6.3)$$

where the root mean square error is normalized by the mean of the reference field \bar{y}^B . It allows to more easily compare NRMSE values from a set to another when there are strong value differences (e. g. at high temperature, flame speeds are inherently higher, and makes RMSE incomparable to lower temperature cases due to higher absolute errors). The reference field $.^B$ in this case is SD. The values of NRMSE tend to be higher for high temperature cases where dispersion can be observed in Fig. 6.4.2. But values remain low in general, meaning that high errors remain contained on the considered ranges.

In view of these results, the San Diego offered a good basis for the reduction. The scheme is detailed enough to produce results in various configurations and of sufficiently small size to allow a large number of cases during reduction. Nonetheless, there are ways to improve the procedure and reach other important phenomena that had to be discarded for this first step. Choosing source mechanisms able to take into account electrolyte species and pollutant emissions remains an on-going work. It would guarantee an applicability of the scheme on cases where boiling/liquid electrolyte is observed and influences flame dynamics.

Table 6.4.1: Summary of the performance of the reduced scheme (RED) in comparison to the source detailed scheme (SD). Ranges considered for error computations are $1000/T \in [0.75, 1.05] \text{ K}^{-1}$ for auto-ignition, $\phi \in [0.5, 1.5]$ for the premixed flames, and $a \in [50., 500.] \text{ s}^{-1}$ for the diffusion flames.

Type of error	0D auto-ignition		1D premixed flame			
	MRE	RE 1000 K	MRE		NRMSE	
			300 K	1000 K	300 K	1000 K
NMC1	8.4 %	1.0 %	3.4 %	5.3 %	0.030	0.059
NMC2	4.7 %	2.2 %	3.2 %	3.3 %	0.031	0.037
LFP1	8.9 %	1.0 %	3.1 %	5.5 %	0.034	0.059
LFP2	8.4 %	1.0 %	3.3 %	5.3 %	0.032	0.058
LCO/NMC	4.6 %	2.3 %	3.1 %	4.0 %	0.028	0.047
LCO	28.6 %	11.6 %	2.4 %	3.5 %	0.023	0.043

Type of error	1D diffusion flame			
	MRE		NRMSE	
	HR_{int}	T_{max}	HR_{int}	T_{max}
NMC1	2.1 %	1.5 %	0.022	0.015
NMC2	1.8 %	1.4 %	0.018	0.015
LFP1	1.7 %	1.3 %	0.018	0.013
LFP2	1.8 %	1.4 %	0.019	0.014
LCO/NMC	2.5 %	1.6 %	0.027	0.016
LCO	2.4 %	1.5 %	0.025	0.015

6.5 Reduced scheme generalization test

One key aspect to consider when generating a kinetic scheme for the combustion of complex mixtures is its capability to remain representative when the composition varies. In this study, six mixtures were selected to broaden the field of application of the scheme to gaseous surrogates with different reactivities. Avoiding an over optimization of the chemical pathways for one specific mixture allows to also look for mixtures that are not in the original batch and test how well the kinetic scheme generalizes. Laminar flame speed and auto-ignition delays will be used to compare ARC and SD for this new batch of gases.

6.5.1 Generalization to untested Li-ion vent gases

Five additional vent gas analysis are chosen for the generalization test. Pure methane (CH_4) completes the new batch of mixtures. Table 6.6.1 at page 88 gives the compositions, sources and information on the experimental framework.

Vent gas compositions originating from $Li(NiCoAl)O_2$ (NCA) are targeted from the study of Lammer *et al.* [149] for their content in hydrogen. NCA batteries tend to produce gases with overall higher flame speed [12]. It helps to check that the kinetic scheme is able to reproduce the combustion of these vent gases when considering worst case scenarios. Pure methane allows to compare the Li-ion-specific mixtures to a well studied reference, which must be reproduced properly by the reduced scheme. Additionally, it puts in perspective the dangerousness of the mixtures in comparison to a simpler well-studied reference.

Figure 6.5.1 highlights that auto-ignition delays are well retrieved especially for NCA-sourced vent gases. In Fig. 6.5.2, 1D flames are also correctly retrieved for the test batch showing that the kinetic schemes generalizes well to a variety of gases observed around Li-ion batteries after thermal runaway. Overall, these gases show higher laminar flame speed, and shorter auto-ignition delay than methane, which confirms that asserting safety designs with already existing methane schemes would undermine the quality of the analysis.

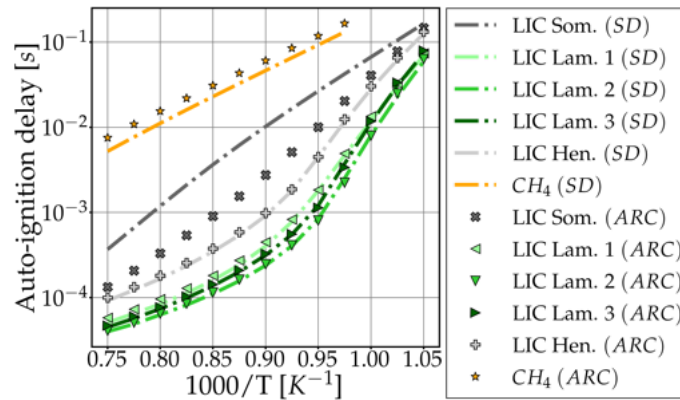


Figure 6.5.1: Comparison of the 0D isochoric auto-ignition delay for ARC and SD and the generalization test batch.

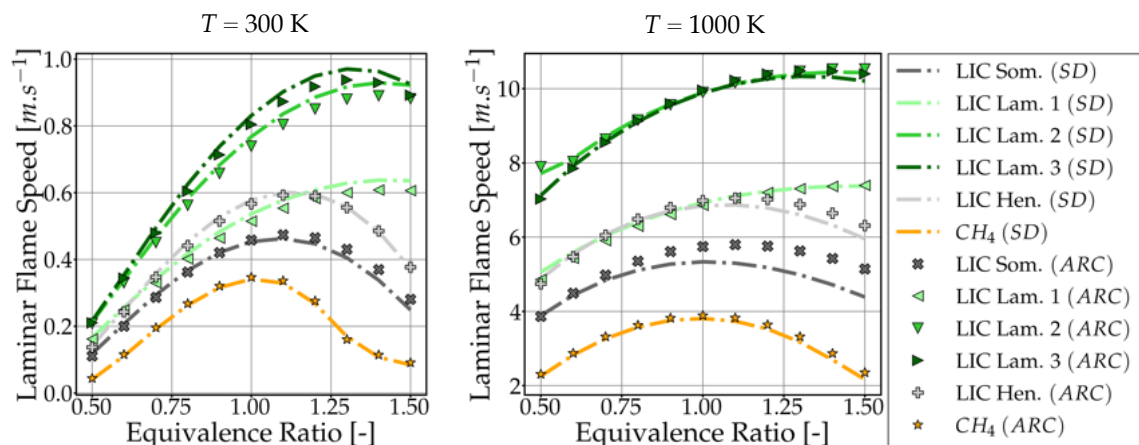


Figure 6.5.2: Comparison of the 1D premixed laminar flame speed for ARC and SD and the generalization batch at $T = 300$ K and $T = 1000$ K

Nonetheless, for both the 0D auto-ignition case and the 1D premixed flame case,

the maximum error is reached for the Somandepalli *et al.* mixture [247]. One possible reason is the presence in larger amount of propylene (C_3H_6) which is only rarely present in the original set of mixtures on which the reduction has been done. The evaluation of the scheme to pure fuels (hydrogen, methane, ethylene, ethane, and propylene) thus follows to conclude the evaluation of the reduced scheme.

6.5.2 Generalization to pure fuels

0D auto-ignition and 1D premixed flames are computed for pure methane (CH_4), pure ethylene (C_2H_4), pure ethane (C_2H_6) and pure propylene (C_3H_6).

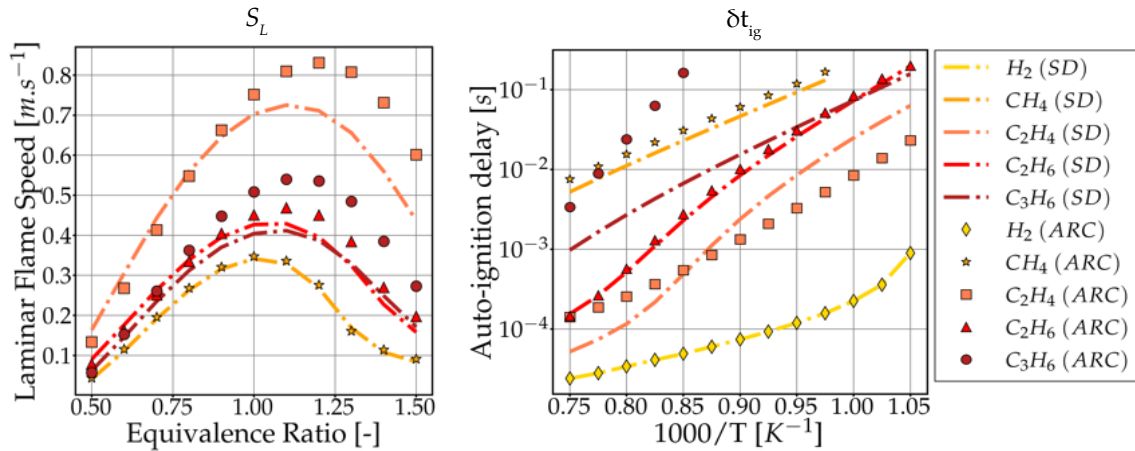


Figure 6.5.3: Comparison of the 0D isochoric auto-ignition delay and the 1D premixed laminar flame speed at $T = 300$ K, for ARC and SD, and pure methane (CH_4), pure ethylene (C_2H_4), pure ethane (C_2H_6), pure propylene (C_3H_6). The auto-ignition delay of hydrogen is added as a reference.

Fig. 6.5.3 shows that the species present in the initial reduction batch produce the smallest error (hydrogen, methane, ethylene). At $T = 300$ K, the average error on the laminar flame speed is 0.1 % for H_2 , 3.7 % for CH_4 , 15.3 % for C_2H_4 , and 28.8 % for C_3H_6 . Moreover, the auto-ignition delays are correctly retrieved for every species except C_3H_6 , where the reduced scheme diverges from the reference. It confirms that the species only rarely present in the reduction batch produce more discrepancy which could explain the observations made when the Somandepalli mixture is evaluated (see Fig. 6.5.1 and 6.5.2).

6.6 Conclusion on kinetic scheme reduction

The steps to derive an Analytically Reduced Chemistry kinetic scheme are given in this chapter. In order to make it representative of combustion phenomena commonly observed when studying lithium-ion cell fires, six mixtures experimentally obtained are tested. The six mixtures are the result of over-heat-to-Thermal-Runway experiments for four different cathode materials: NMC (Lithium - Nickel - Manganese - Cobalt oxide), LFP (Lithium - Iron - Phosphate), LCO (Lithium - Cobalt oxide) and LCO/NMC. The gaseous mixtures are first tested using detailed kinetic schemes to assert their specifications in terms of volatility, heating value, flammability limits, flame temperature, ignition delay and premixed laminar flame velocity. A root detailed kinetic scheme (57 Species, 268 Reactions) is then chosen and the reduction is performed following optimization cases set to guarantee the representativeness of the resulting scheme. The final reduced kinetic scheme includes 18 Species, 6 QSS Species and 93 Reactions.

The scheme is validated *versus* the root mechanism in terms of 0D isochoric auto-ignition at varying temperatures, 1D premixed laminar flame for low and high temperatures on a large range of equivalence ratio, and 1D counter-flow diffusion flame at varying strain rates. The capability of the scheme to generalize to mixtures not initially selected for the reduction of the scheme follows. It demonstrates a strong ability to adapt to mixtures that remain near the original batch. But, in particular, species that are only rarely represented in the original batch (*e.g.* C_3H_6) can be a source of error for mixtures with higher levels of these species. The error may be mitigated by adding the problematic mixture to a new reduction batch, which exposes to a larger number of species and reactions in the final reduced scheme.

The chemical kinetic scheme used is described in **Appendix A** p. 235, and can be made available on demand or is accessible in [36].

In the next chapter, using the scheme derived here, canonical cases are more thoroughly studied, in order to evaluate the need in models when targeting 3D configurations, and help setup the models for Li-ion vent gases.

Table 6.6.1: Mixtures selected along with information on experimental conditions and sources for the generalization test.

Mix. Name	Cathode material	Vol. fractions ¹	Experimental information
Som.	$LiCoO_2$	H_2 : 29.2 % CH_4 : 6.7 % C_2H_4 : 2.3 % C_2H_6 : 1.2 % C_3H_6 : 4.8 % CO : 24.1 % CO_2 : 31.6 %	- Pouch cell - overheat-to-TR - SoC : 100 % - Argon atmosphere - [247]
Hen.	$LiFePO_4$	H_2 : 34.9 % CH_4 : 15.0 % C_2H_4 : 5.0 % CO : 25.0 % CO_2 : 20.1 %	- Undisclosed format - overheat-to-TR - SoC : 100 % - inert atmosphere ³ - [110]
Lam. 1	$Li(Ni_{0.8}Co_{0.15}Al_{0.05})O_2$	H_2 : 15.9 % CH_4 : 2.5 % C_2H_4 : 2.4 % CO : 58.6 % CO_2 : 20.5 %	- 18650 cell ² - overheat-to-TR - SoC : 100 % - Argon atmosphere - [149]
Lam. 2	$Li(Ni_{0.8}Co_{0.15}Al_{0.05})O_2$	H_2 : 35.7 % CH_4 : 3.7 % C_2H_4 : 2.0 % CO : 44.0 % CO_2 : 14.5 %	- 18650 cell ² - overheat-to-TR - SoC : 100 % - Argon atmosphere - [149]
Lam. 3	$Li(Ni_{0.8}Co_{0.15}Al_{0.05})O_2$	H_2 : 43.2 % CH_4 : 7.0 % C_2H_4 : 2.7 % CO : 37.2 % CO_2 : 9.8 %	- 18650 cell ² - overheat-to-TR - SoC : 100 % - Argon atmosphere - [149]
CH_4		CH_4 : 100.0 %	

¹ Volume fractions are normalized based on all the species analyzed to sum to 100 %. Species depicting volume fractions strictly lower than 1.0 % after normalization are neglected and volume fractions are recomputed to sum again to 100 %.

² Cylindrical cells: 18 mm in diameter and 65 mm in length.

³ Unspecified inert atmosphere composition.

Chapter 7

Canonical cases and model setup for 3D simulations

Contents

7.1	Phases of TR and reduced canonical cases	90
7.2	Shock simulation	91
7.2.1	Theoretical 1D shock-tube profiles	92
7.2.2	Simulation of 1D shock propagation	93
7.3	Laminar premixed flame simulation	97
7.3.1	1D laminar premixed flames	97
7.3.2	Setting up the DTFLES approach	101
7.4	Diffusion flame simulation	104
7.4.1	Laminar diffusion flame profiles	105
7.4.2	Mixture fraction for Li-ion vent gases	106
7.4.3	Flame indexes	108
7.4.4	Summary of the strategies for 3D simulations	110
7.5	Selection of 3D scenarios to target	112

This chapter focuses on the definition of simple 1D canonical cases useful to setup strategies when targeting realistic 3D simulations of the three main phases of thermal runaway: 1. Opening, 2. Sustained venting and flames, 3. Explosion due to gas accumulation. The simulation of such canonical cases fills a tool box necessary for the 3D cases, with for example the familiarization to shock handling methods and the setup of the Dynamically Thickened Flame model adapted to large 3D cases with local mixture inhomogeneities and partially premixed/diffusion controlled combustion. It is concluded by the detailed list of 3D simulations conducted in the

following chapters, with intended aims regarding experimental/simulation validation and potential applications for battery design.

7.1 Phases of TR and reduced canonical cases

During thermal runaway, three main phases are highlighted as critical for the design of the structure of the battery, its safety devices, and the sizing of fire-prevention systems:

1. **Opening:** due to the high pressure inside the cell, the vent disk breaks creating a discontinuity between high pressure/high temperature vent gases and the atmosphere. A shock propagates first, interacting with walls. It then gives way to the formation of an under-expanded jet depicting high flow Mach numbers.
2. **Sustained venting:** Despite the fact that the opening followed by a sudden expansion cools down the cell, pacing down reactions, the reactivity is not stopped completely. Gas production increases again until a climax, where the sustained ejection of hot gases is prone to create jet diffusion flames. At high turbulence levels, partially premixed zones can be reached downstream, in the jet plume.
3. **Explosions:** In the event of a venting where combustion is limited or impossible in a first place, vent gases may accumulate inside the storage space or the casing of the module. A spark from a failing electrical device triggers an explosion, where obstacles-created turbulence plays a crucial role on flame acceleration and over-pressure measurements.

Three main canonical scenarios have been chosen in this thesis to setup models adapted to 3D simulations:

1. the 1D shock-tube scenario where the driver gas is the hot pressured vent gas mixture.
2. the 1D laminar premixed flame at atmospheric conditions, allowing to examine characteristic flame profiles and set adequately the thickened flame model for 3D cases.
3. the 1D laminar counter-flow diffusion flame with hot vent gases on the fuel side and air at atmospheric conditions on the oxidizer side, to define strategies for jet diffusion flames, and locally partially premixed combustion.

In the following sections, using the reduced kinetic scheme proposed in Chapter 6, it is possible to form a large dataset containing the 1D cases at a reduced cost. Figure 7.1.1 summarizes the different phases of TR targeted with canonical cases to prepare for more realistic 3D simulations.

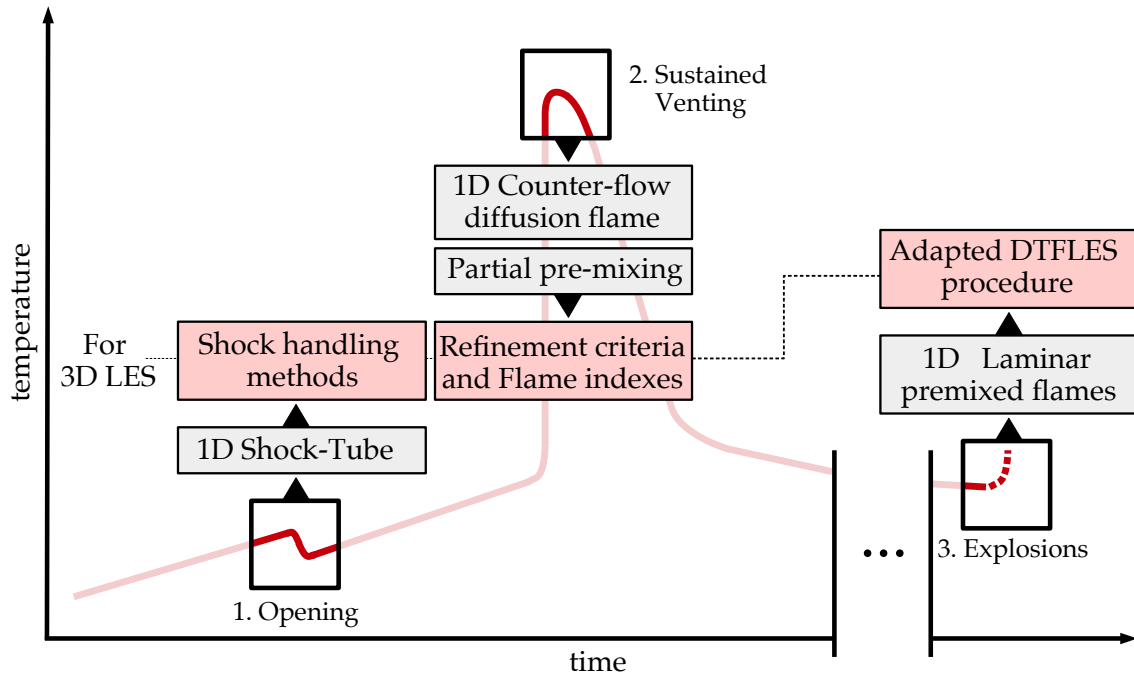


Figure 7.1.1: Summary of the phases of the Thermal Runaway targeted by the 1D canonical cases, along with the information obtained for the setup and calibration of models adapted to large 3D cases.

7.2 Shock simulation

Shortly after the onset of thermal runaway, the progressive decomposition of the cell is accompanied by the production of gases that accumulate in the housing. The pressure builds up until the structural resistance of the cell is reached: 1. either a safety disk breaks open and relieves the pressure, or 2. the weakest point of the cell cracks open (corners, welding, ...). This happens at pressures as high as 2.0 MPa [11] so that a shock is created. This shock propagates into the surrounding atmosphere immediately followed by a turbulent supersonic jet. Being able to confidently simulate flows with shocks in 3D is therefore essential to reproduce the scenarios of opening and venting.

The configuration described here can be compared, at first order, to a shock-tube experiment where the driver gas is modelled by hot vent gases and the driven gas is the atmosphere. In this section, the simulation of 1D shocks is proposed to draw modelling strategies from the existing and evaluate them using a numerical setup

close to the one available in 3D. Such a benchmark is essential to ensure the fidelity of the methods when scaling up to complex cases containing shock discontinuities, and is historically performed on similar shock-tube cases [246].

7.2.1 Theoretical 1D shock-tube profiles

Shock profiles are obtained using the theoretical solution for the 1D propagating shock proposed by Riemann and summarized in Chapter 3 Section 3.3.5. In [11], the opening pressure has been measured for multiple 18650 cells. On average this pressure reaches 2.0 MPa. Thus, the conditions chosen to be representative of the venting of pure hot decomposition gases into the air at atmospheric conditions are as follows:

1. **Driver gas** : the mixture is NMC1 [96]: H_2 : 30.8 %, CH_4 : 6.8 %, C_2H_4 : 8.2 %, CO : 13.0 %, CO_2 : 41.2 %, at $T_{driver} = 1000$ K, $P_{driver} = 2.0$ MPa.
2. **Driven gas** : the mixture is air: O_2 : 21.0 %, N_2 : 79.0 %, at $T_{driven} = 300$ K, $P_{driven} = 101\,325$ Pa.

The theoretical solution for such a configuration gives access to the characteristic velocities at which the shock, the contact surface and the rarefaction waves propagate. Values are given in Table 7.2.1 and 7.2.2 and summarized under a Riemann $x-t$ diagram in Fig. 7.2.1

Table 7.2.1: Characteristic velocity for the propagating shock (in $m \cdot s^{-1}$).

Shock (w)	820.1
Contact surface (u_p)	560.7
Expansion head ($-a_4$)	-624.0
Expansion tail ($u_p - a_3$)	-5.0

Table 7.2.2: Conditions from either side of the shock.

	In front	Behind
P (Pa)	101 325.0	640 232.7
T (K)	300.0	599.5
ρ ($kg \cdot m^{-3}$)	1.17	3.71

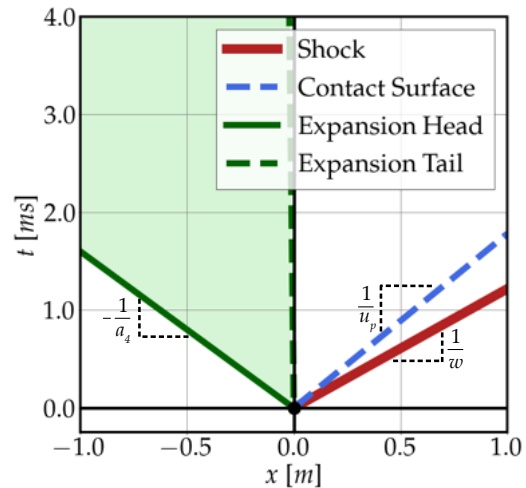


Figure 7.2.1: Riemann $x-t$ diagram corresponding to the shock at opening.

Such a theoretical solution, including shock profiles, is key to initialize a simulation, as the discontinuity is often too strong to be properly handled numerically if

a crude initialization is used. Furthermore, it serves as a reference to evaluate the performance of a numerical setup regarding the capture of shock discontinuity. In the next section, the simulation of a 1D shock-tube configuration is presented, along with typical shock handling methods for CFD simulation.

7.2.2 Simulation of 1D shock propagation

All simulations are performed using AVBP where two shock handling methods are available (see Chapter 4 Section 4.2.3), and should be compared in relation with the numerical scheme.

Methods comparison

The shock-tube canonical case allows to test the methods introduced when they collaborate with different mesh refinement and numerical schemes. The parameters of the study are thus:

1. Mesh refinement : $\Delta x = 0.5$ mm, $\Delta x = 0.2$ mm, $\Delta x = 0.07$ mm homogeneous grids are tested.
2. Numerical schemes : Lax and Wendroff [152] (LW), and Two-steps-Taylor-Galerkin-4A [50] (TTG4A) are selected for their diffusive properties helping in the vicinity of shocks.
3. Shock handling : Cook and Cabot (CC), Localized Artificial Diffusion (LAD), and no modelling (NM).

AVBP is used to simulate the propagation of the shock, starting from the initial profile at $t_{init} = 50$ μ s, and compared to the theoretical profile at $t_{final} = 200$ μ s. A first comparison of the general profile is done for the intermediate mesh $\Delta x = 0.2$ mm, without shock handling method for both LW and TTG4A. Figure 7.2.2 shows an overall good agreement between theoretical profiles and simulation. But as expected, the discontinuity of the shock creates oscillations for both numerical schemes. In particular, TTG4A depicts strong negative velocity and pressure peaks, that must be damped.

Using the same mesh, a more detailed comparison of the shock-wave profile is given in Fig. 7.2.3 p. 95. Shock handling methods succeed in suppressing or damping spurious waves. The improvements of the profiles are very well visible for the order-three finite element scheme TTG4A, where no negative impulses are observed at the foot of the shock. With the current settings, Cook and Cabot and LAD have very

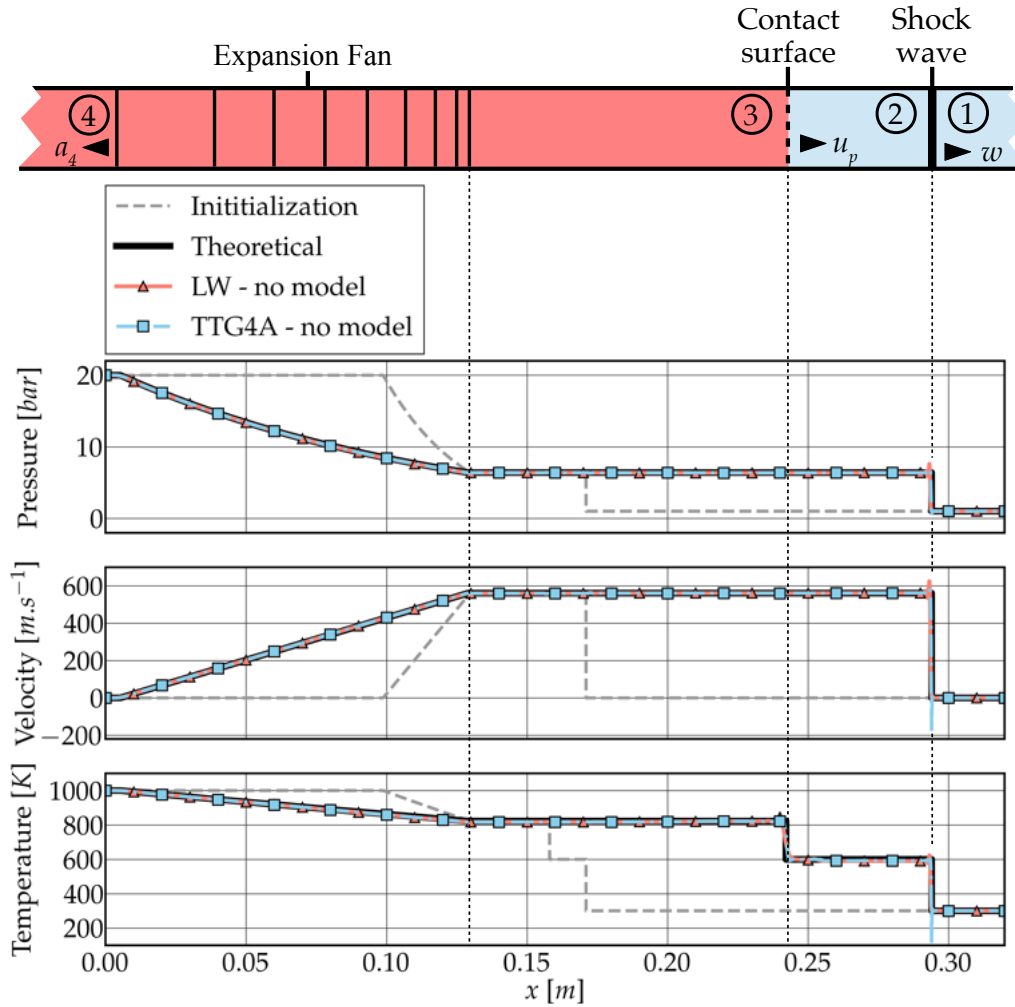


Figure 7.2.2: Simulation of the propagation of a 1D shock for the mesh $\Delta x = 0.2$ mm, with $t_{init} = 50 \mu\text{s}$, and $t_{final} = 200 \mu\text{s}$. Both LW and TTG4A are compared without shock handling strategy.

similar performances. However, oscillations are not completely erased when using LW. The unwanted waves amplitude regarding pressure is reduced by a factor 2.4 for LW - CC (resp. 2.0 for LW - LAD).

Moreover, in Fig. 7.2.4 p. 96, it can be seen that the amplitude of the spurious waves are identical for all three meshes. The attenuation level is close to identical when refinement increases, showing the good consistency of the methods selected for shock handling.

Table 7.2.3 summarizes the cost of the simulations. Such a comparison holds in 1D and can only be extrapolated to 3D with much precautions. However, it helps to determine that the gain of one order of precision between LW and TTG4A is done at a 2.73 times higher cost (on average). Also, the cost of LAD is 10.6 % larger than Cook and Cabot in combination with LW, and only 2.2 % larger with TTG4A.

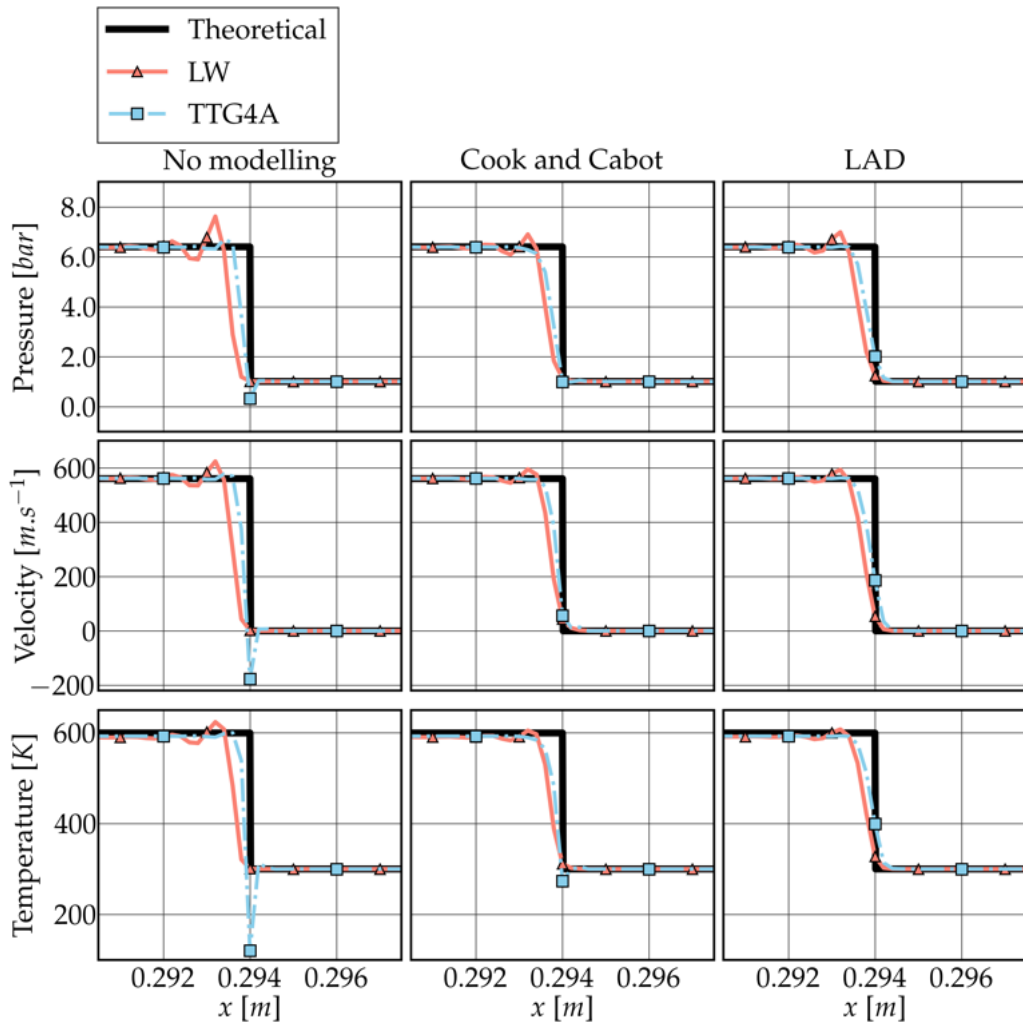


Figure 7.2.3: Zoom on the shock-wave profiles, and comparison between numerical schemes and their collaboration with shock handling methods.

With very similar performances, both methods are recommended.

Table 7.2.3: Comparison of costs for 1D shock propagation. For completion, values are given in sCPU/it./cell as averages for the three meshes, reproducing the simulation three times, using one core of an Intel Skylake CPU.

	No Mod.	Cook and Cabot	LAD
LW	5.00×10^{-6}	5.49×10^{-6}	6.07×10^{-6}
TTG4A	1.44×10^{-5}	1.53×10^{-5}	1.56×10^{-5}

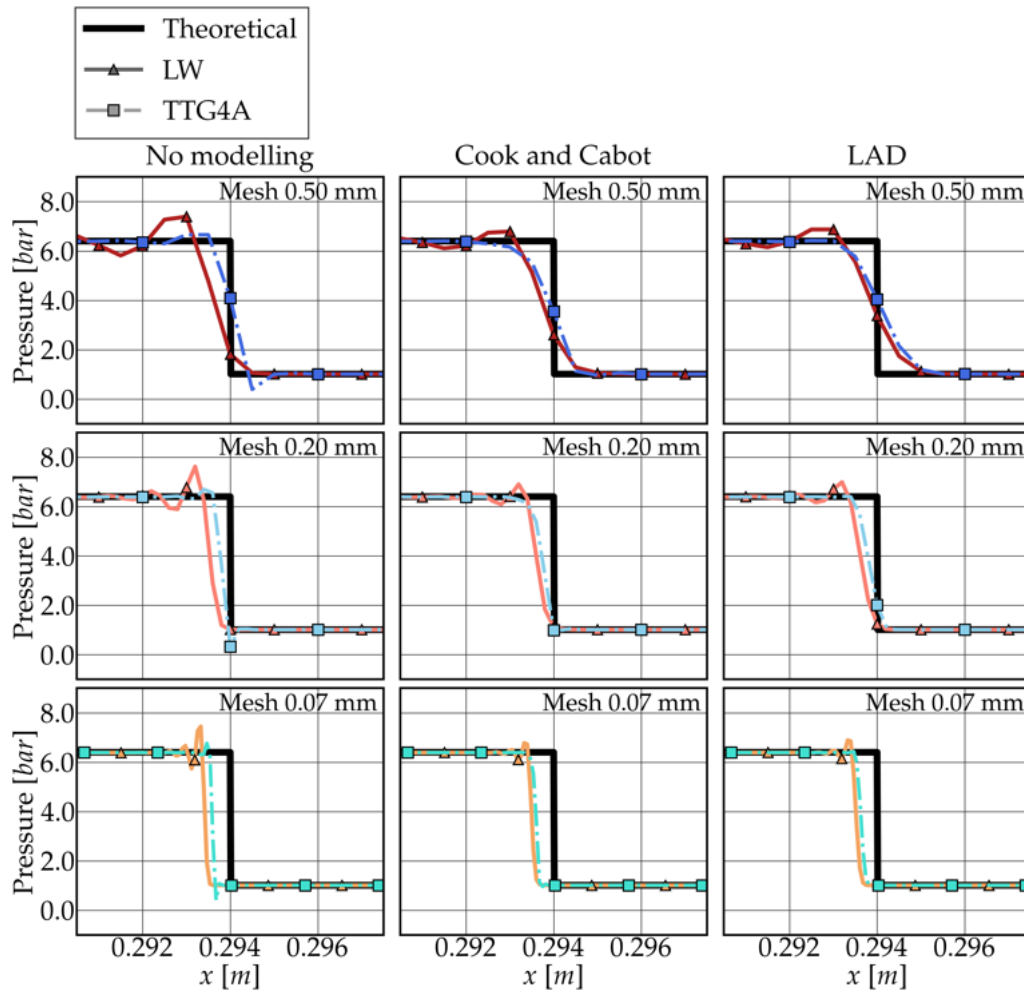


Figure 7.2.4: Zoom on the shock-wave pressure profiles, and comparison between numerical schemes, shock handling methods and mesh refinement.

This first familiarization with the canonical propagating shock configuration helps to define guidelines for the 3D simulations that follow. On the one hand, the mesh refinement is not a limiting factor and should be defined as small as computationally available to guarantee sharp shock profiles. Shock handling methods are to be used in all scenarios involving shocks. Cook and Cabot and LAD depict similar performances for this 1D canonical problem. Costs are also comparable despite a slight step ahead for Cook and Cabot. An application to a 3D case is then necessary to settle properly, which one objective of Part III.

Concerning numerical schemes, TTG4A is recommended for most applications involving shocks. Its better precision is obtained at seemingly higher computational prices. But to be fair, it is recalled that the interest of the higher order is to obtain very good precision on coarser meshes than low order schemes, meaning that cost comparisons on same meshes are generally unfair. However, two main reasons make LW a good substitute in particular cases:

1. TTG4A is less robust than LW to mesh irregularities, and strong shock/turbulence interactions. Given these constraints, LW depicts overall reasonable performances (often sufficient) with a stronger robustness at low cost, becoming a good compromise.
2. Also, when the mesh refinement criteria are imposed by other phenomena such as combustion, the advantage of the order partly disappears.

Thus, it makes LW sometimes essential in 3D configurations where mesh quality is less easily controlled, and where turbulence and combustion introduce stiffness in the cases, imposing small space-steps.

7.3 Laminar premixed flame simulation

The second canonical case is the laminar premixed flame. A closer look on such flames for Li-Ion vent gases burning with air at atmospheric conditions helps to better understand the specificity of the mixtures. It allows to determine the best approach to simulate and model the flames in larger 3D cases. Two main topics are the focus of the next paragraphs: 1. the description of typical Li-ion vent gas premixed flame profiles, and 2. the assertion of the effect of the hydrogen level on flame behaviour. The database containing flame information is computed using the reduced scheme and Cantera.

7.3.1 1D laminar premixed flames

Specificity of Li-ion vent gases

Similarly to Chapter 5, the gaseous mixture used as a reference in this section is the one extracted by Golubkov *et al.* and named NMC1 in Chapter 6 Table 6.3.1: H_2 : 30.8 %, CH_4 : 6.8 %, C_2H_4 : 8.2 %, CO : 13.0 %, CO_2 : 41.2 %.

The Heat Release Rate (HRR) and temperature profiles are plotted versus the position in Fig. 7.3.1 for three equivalence ratios, $T = 300$ K and $P = 101\,325$ Pa. Profiles are centered on the position of the HRR peak. As expected, the maximum heat released HRR_{max} , the flame speed s_L , and the final temperature T_f are reduced when the mixture moves away from $\phi = 1.0$. In practice, due to the presence of hydrogen, the mixture for which the maximum of s_L is reached is slightly richer than stoichiometry at $\phi = 1.05$ (for pure hydrogen, the maximum of s_L is obtained at $\phi \simeq 1.8$, under similar conditions).

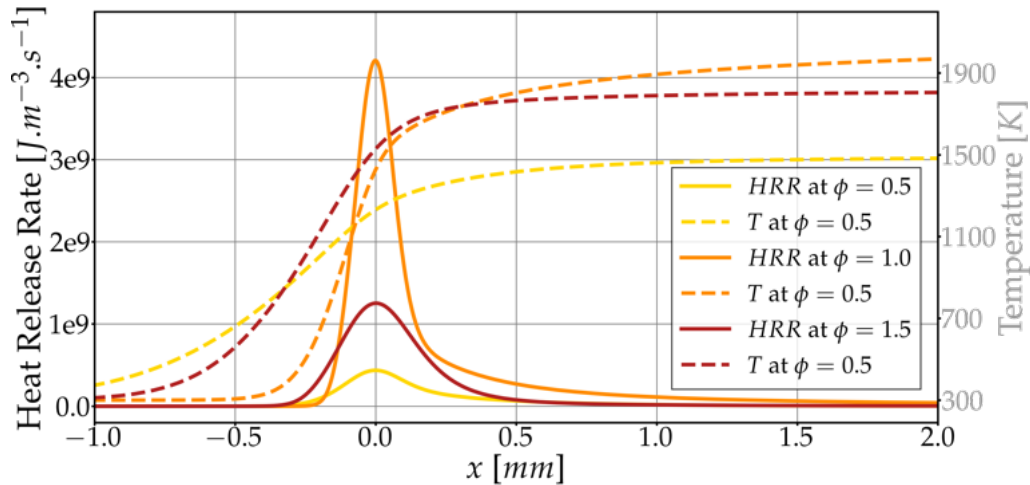


Figure 7.3.1: Heat Release Rate and temperature profiles for mixture NMC1 (Chapter 6 Table 6.3.1) at $\phi \in \{0.5, 1.0, 1.5\}$, $T = 300$ K and $P = 101\,325$ Pa.

At stoichiometry, the thermal flame thickness $\delta_L = 0.406$ mm and laminar flame speed $s_L = 0.426$ m.s⁻¹ are comparable to the ones of ethane ($\delta_L = 0.380$ mm and $s_L = 0.426$ m.s⁻¹). When looking into the details of species profiles in Fig. 7.3.2, it is possible to locate the zones where the fuel species are consumed. Due to differential diffusion phenomena, because the molar weights and diffusivity of each species are heterogeneous, the consumption of hydrogen occurs further towards the burnt gases than methane and ethylene. This is a key information when the objective is to locate heat release ridge lines using species consumption. In this case, ethylene or methane consumption peaks are better centered on the peak of heat release, ensuring a better flame detection for flame models (see Section 7.3.2). Also, the presence of carbon monoxide in the fresh gases, extends the post-flame zone where slow reactions of CO transforming to CO_2 , producing the last percents of heat necessary to reach the adiabatic flame temperature, requiring flame models where the window of action can be properly setup to take into account all the reaction zones.

Effect of the hydrogen level

One specificity of Li-ion vent gases is the variability in species composition, inherent to variations in the compounds of the cell, in TR triggering, in the State of Charge of the battery, ... In particular, the ratio of burning species over CO_2 is found to be key on the macroscopic flame quantities (s_L , δ_L , T_{ad} , ...) as it was already mentioned in Chapter 6 Section 6.2.2. To observe the effect of this diluting ratio, and especially when the most reactive and diffusive species H_2 is changed, a set of laminar premixed flames are computed with varying H_2 levels at fixed equivalence ratios. The use of the reduced scheme developed in Chapter 6 helps to obtain a large database with minimized costs and allows to draw trends rapidly. At atmospheric conditions, starting from the NMC1 mixture without hydrogen: H_2 : 0.0 %, CH_4 : 9.8 %, C_2H_4 :

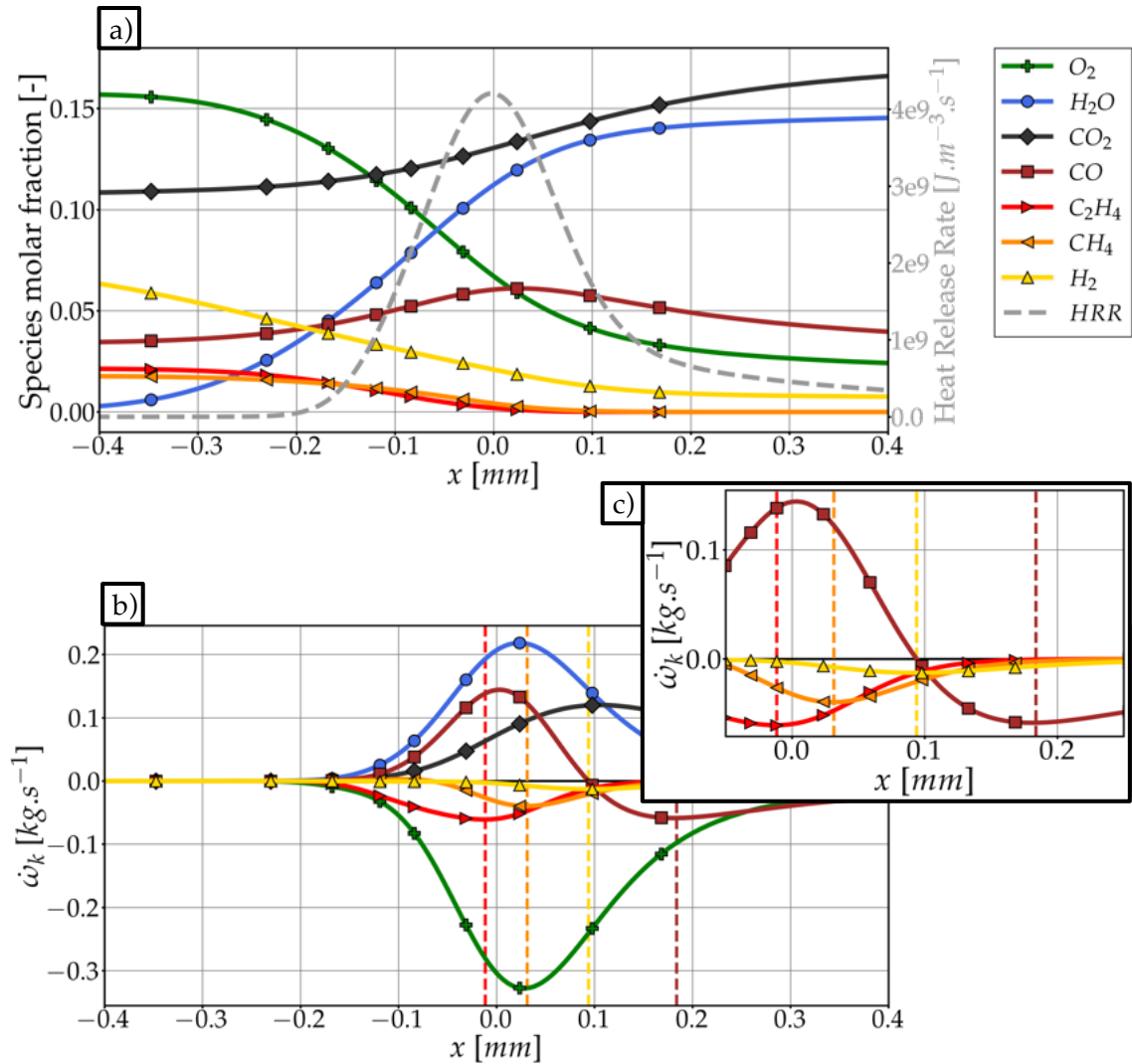


Figure 7.3.2: Main species profiles for NMC1 at $\phi = 1.0$, $T = 300 \text{ K}$ and $P = 101\,325 \text{ Pa}$: a) species molar fractions, b) species production rates, c) zoom on species production rates of reactive fuel species. vertical dashed lines locate the maximum of consumption of the four reactive species of the fuel blend.

11.8 %, CO : 18.8 %, CO_2 : 59.6 %, the level of hydrogen is progressively increased until the mixture becomes pure hydrogen, reaching the worst case scenario. The laminar flame speed and thermal flame thickness *versus* the level of hydrogen X_{H_2} are given in Fig. 7.3.4. The "Original mixture" represents a level $X_{H_2} = 30.8\%$.

Unsurprisingly, the laminar flame speed increases with X_{H_2} , and the flame thickness is reduced. Besides, an inversion occurs at $X_{H_2} = 0.74$ where the curves at $\phi = 1.0$ cross the ones at $\phi = 1.5$. It is due to the fact that pure hydrogen laminar flame speed peaks under rich conditions. Thus, for an explosion scenario involving Li-ion gases, the worst case scenario in terms of flame acceleration, is not necessarily the stoichiometry, and is found in the rich zone depending on the H_2 level. It should also be noted that for very high levels of hydrogen, under lean conditions,

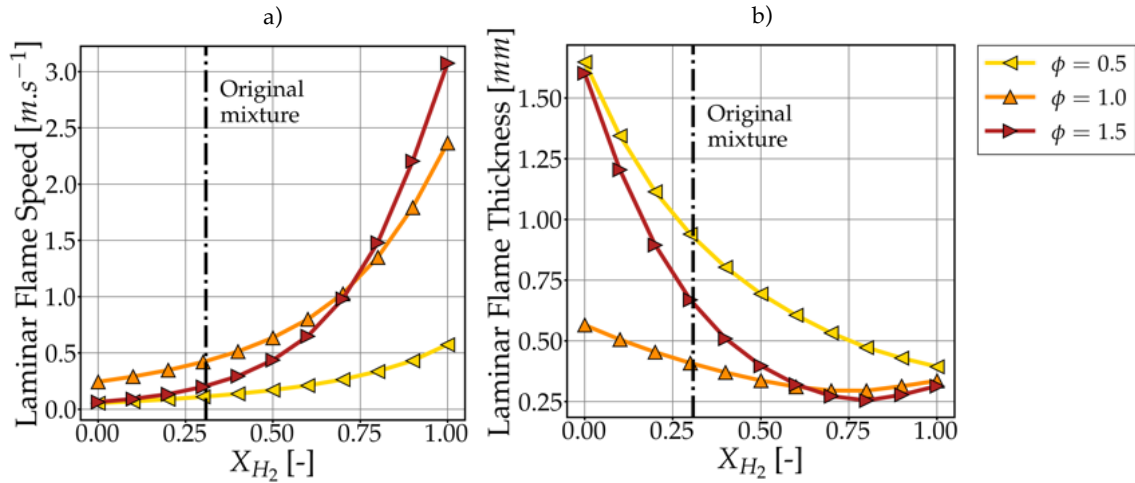


Figure 7.3.3: Effect of hydrogen level on a) laminar flame speed and b) flame thermal thickness for $\phi \in \{0.5, 1.0, 1.5\}$, $T = 300$ K and $P = 101\,325$ Pa.

thermo-diffusive instability due to Lewis numbers far from unity may accelerate the flame [17, 18]. In this work, only cases where the level of hydrogen remains reasonable and/or the mixture is under mildly lean conditions are targeted, guaranteeing that the Lewis numbers remain close to unity. An effort is still needed for the side of the spectrum where hydrogen content is high and conditions are lean as it could become the worse case scenario for explosions.

The heat released by the flame increases up to ten folds when going from NMC1 to pure hydrogen, with higher end-of-combustion temperatures (see Fig. 7.3.4). For battery designers, it is therefore interesting to consider several vent gas mixtures with varying hydrogen levels when producing accident scenarios. Defining the worst case is highly dependent on this initial mixture, and including pure H_2 cases during the simulation step partly guarantees that this worst case is considered.

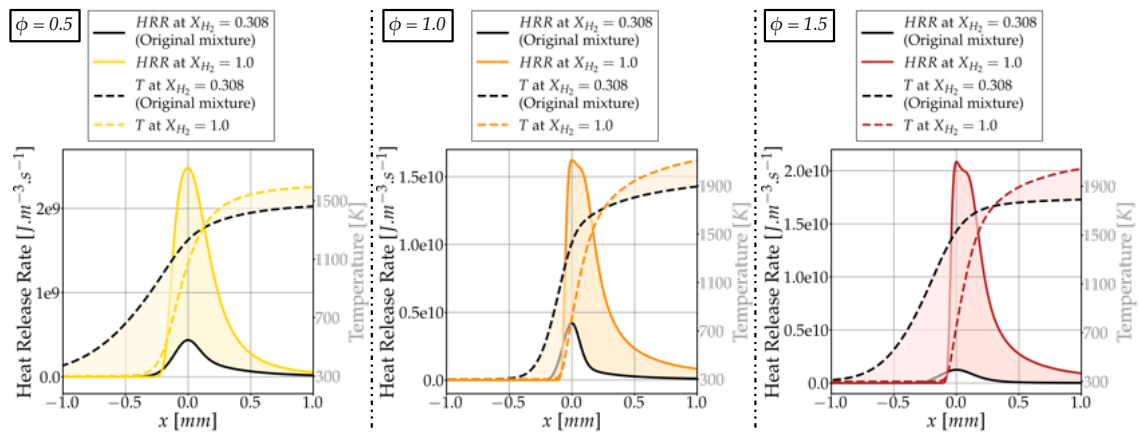


Figure 7.3.4: Effect of hydrogen level on HRR and temperature profiles for $\phi \in \{0.5, 1.0, 1.5\}$, $T = 300$ K and $P = 101\,325$ Pa.

With this closer look on flame profiles and with a better understanding of the

specificity of Li-ion vent gas mixtures, it is then time to define strategies to scale-up to larger 3D cases, where the discretization makes impossible to ensure a minimal number of points inside the flame front to reproduce the chemical reactions and thus the macroscopic flame quantities such as s_L , δ_L , HRR_{max} , ... and where turbulence interacts with the front. Strategies to model turbulent flames in 3D LES frameworks, for Li-ion vent gases must be adapted from the existing.

7.3.2 Setting up the DTFLES approach

The Dynamically Thickened Flame strategy has been selected to model turbulent premixed flames. First of all, a sensor adapted to the mixture at hand is to be chosen.

Flame sensors have been developed searching for the most generic approach for large cases (involving mesh partitioning for multi-cores CFD simulation), and complex flames (multi-species detailed/semi-detailed chemistry, liquid phases). An example of sensor is given by Rochette *et al.* [225] and consists in detecting heat release rate fronts and artificially propagating particles from the ridge to extend the thickening in the domain, and move from partition to partition. In this manuscript, a second approach is preferred. Formulated by Jaravel [126], it proposes a so-called "relaxation sensor" that reads:

$$S = \mathcal{G} \left[\max \left(\min \left(2 \frac{F_{max} |\dot{\omega}_F|}{|\dot{\omega}_F|_{max}^{1D}} - 1, 1 \right), 0 \right) \right] \quad (7.1)$$

where $\dot{\omega}_F$ corresponds to the production rate of the fuel, and $|\dot{\omega}_F|_{max}^{1D}$ is the maximum absolute value of the production rate of the fuel when considering a 1D premixed laminar flame. The sensor therefore detects the flame front by comparing local values of production rates to the production rate of a canonical case known *a priori*. The sensor is then filtered with a filter \mathcal{G} to broaden the zone of action of the thickening to pre-heat and post-flame zones. The filter is set to smoothly relax towards zero away from the reaction zone. Such an approach therefore demands a tabulation of $|\dot{\omega}_F|_{max}^{1D}$ and δ_L at the conditions estimated to be encountered in the domain (temperature, pressure, and equivalence ratio). For Li-ion vent gases, or more precisely, for multi-species fuels, it is also necessary to define what is to be considered as $\dot{\omega}_F$. From Fig. 7.3.2, it has been observed that methane and ethylene consumption peaks coincide well with the peak of heat release on the range of equivalence ratio considered. As methane consumption is more central in the flame, and because methane is always present in Li-ion vent gases, it is chosen as the reference species for the sensor such that $|\dot{\omega}_F|_{max}^{1D} = |\dot{\omega}_{CH_4}|_{max}^{1D}$.

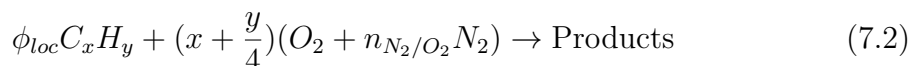
Once the tabulation is performed, the local conditions are then to be evaluated, such that the model can search, in the table, values to compute local F_{max} , and S ,

giving the local thickening F to apply.

In addition to the values tabulated for the flame sensor S ($|\dot{\omega}_F|_{max}^{1D}$ and δ_L), the values of s_L for conditions expected inside the domain must be retained in order to feed the efficiency function of the flame-turbulence interaction model (see Chap. 4 Sec. 4.2.2). During the simulation, with a proper evaluation of the local equivalence ratio, pressure and temperature, the model can adapt to local variations in mixing conditions that may occur in inhomogeneous turbulent flames. In particular, a robust definition of the local equivalence ratio must be chosen. Furthermore, for partially premixed combustion, where diffusion processes may locally drive the combustion, or for diffusion flames, such models developed for premixed combustion are unsuitable without taking precautions. An introduction to flame indexes is given in Section 7.4.3 to amend the DTFLES procedure.

Local equivalence ratio for Li-ion vent gases

To simulate premixed combustion of complex blends of species, or when inhomogeneity is predicted to occur inside the volume, it is crucial to define a consistent local equivalence ratio ϕ_{loc} that can be measured at each time-step in the entire domain. To be consistent, the value of the equivalence ratio must be constant through a perfectly premixed flame front (fresh gases, reaction zones and burnt gases). Following the work of Cazères, a definition using an atomic budget can be introduced for the combustion of C_xH_y in air [33, 22]:

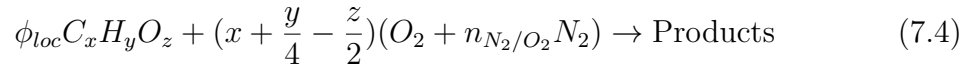


The conservation of atoms ensures that everywhere in the domain the number of atoms of oxygen, hydrogen and carbon (resp. n_O , n_H , and n_C) remains constant. Thus, $n_C = \phi_{loc}x$, $n_H = \phi_{loc}y$, $n_O = 2x + \frac{1}{2}y$, which allows to write ϕ as a local oxygen-hydrogen-carbon budget B [33, 22]:

$$\phi_{loc} = B = \frac{2n_C + \frac{1}{2}n_H}{n_O} \quad (7.3)$$

which can be conveniently retrieved by replacing the number of atoms by atoms molar fractions X_O , X_H , X_C , or atom mass fractions divided by atomic molar mass $\frac{Y_O}{W_O}$, $\frac{Y_H}{W_H}$, $\frac{Y_C}{W_C}$, available at each point/each iteration in a computation.

However, in this study, the Li-ion vent gases are mixtures involving hydrogen, light alkanes, and carbon monoxide, diluted into carbon dioxide. The generic formula for the mixture is of the form $C_xH_yO_z$:



By rewriting the atom conservation, $n_C = \phi_{loc} x$, $n_H = \phi_{loc} y$, $n_O = 2x + \frac{1}{2}y - z + \phi_{loc} z$, it appears that the presence of oxygen in the fuel makes the relation $\phi_{loc} = B$ impractical. Nonetheless, an interesting relation arises:

$$B = \frac{2n_C + \frac{1}{2}n_H}{n_O} = \frac{\phi_{loc}\alpha}{\phi_{loc} - 1 + \alpha} \implies \phi_{loc} = \frac{(\alpha - 1)B}{\alpha - B} \quad (7.5)$$

where $\alpha = \frac{2x + \frac{1}{2}y}{z}$ is the oxygen-hydrogen-carbon budget of the pure fuel. The equivalence ratio is therefore derived from the oxygen-hydrogen-carbon budget of the entire mixture, with the information of the pure fuel oxygen-hydrogen-carbon known *a priori*. The identity devolves appropriately to Eq. 7.3 when the fuel does not contain oxygen ($z \rightarrow 0 \implies \alpha \rightarrow +\infty \implies \phi_{loc} \rightarrow B$).

Such a definition therefore loses the property of Eq. 7.3 where no knowledge about the fuel composition is necessary prior to computation, but is opportune as it ensures a continuity between the chemical solver and the CFD solver, and it is transparent for $C_x H_y$ cases. Also, this formulation is equivalent to the method of Bilger *et al.* [21, 22], with the advantage of summarizing the input parameters into α only.

Preferential diffusion effects

A problem remains to be highlighted as it could become a limitation for local equivalence ratio measurement: preferential diffusion. Mixture fractions, as well as definitions such as Eq. 7.5, are correctly defined only in mixtures with equal diffusivities for all species [213]. The presence of highly diffusive species in both the fresh gases and as intermediate species in the flame generates local variations in hydrogen levels, which impacts the measured local equivalence ratio ϕ_{loc} defined in the previous section. Figure 7.3.5 a) shows ϕ_{loc} undershoots substantially in the preheat zone, and the phenomenon is amplified at rich conditions due to higher levels of H_2 in the fresh gases. When aiming for local quantities such as s_L or δ_L , the error on ϕ_{loc} becomes an error on these local quantities. Ideally, ϕ_{loc} should be equal to ϕ_{fresh} in the whole domain to guarantee a perfect discussion between the flame models and the pre-computed tabulation.

In order to see the impact of preferential diffusion on the estimation of local laminar flame quantities, the relative errors computed as $(x_{loc} - x_{fresh})/x_{fresh}$ are given in Fig. 7.3.5 b). x_{loc} refers to the value of local ϕ , s_L and δ_L measured at the location of maximum heat release (accounting for the preferential diffusion effect), respectively x_{fresh} refers to the value of ϕ , s_L and δ_L measured in the fresh gases

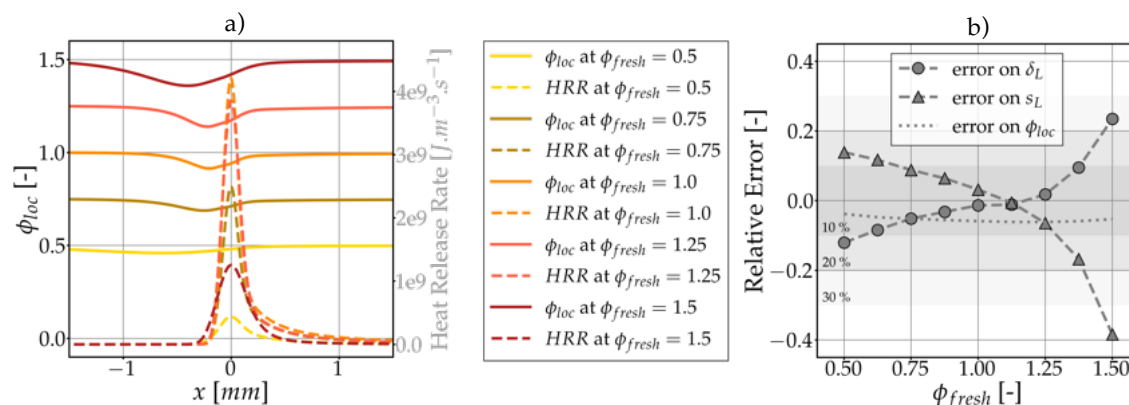


Figure 7.3.5: Effect of preferential diffusion on local equivalence ratio measurements: a) local equivalence ratio ϕ_{loc} measurement for varying global equivalence ratio ϕ_{fresh} , b) relative error on the laminar flame speed, thermal flame thickness and local equivalence ratio measurement due to preferential diffusion.

(where there is no effect of preferential diffusion). For $\phi_{fresh} \in [0.70, 1.26]$, the effect of preferential diffusion is contained. However, outside these limits, it is necessary to take it into account when tabulating the quantities used by the models, otherwise errors may influence model performance. In this work, conditions are kept so that $\phi_{fresh} \in [0.70, 1.26]$. Further developments to extend to cases where preferential diffusion plays a more constraining role are part of future works, including the tabulation of local equivalence ratio mismatches.

7.4 Diffusion flame simulation

The last canonical case is the laminar counter-flow diffusion flame. Diffusion flames are expected to be predominant when considering the ejection of pure vent gases into the atmosphere. After ignition, a Bunsen-like jet flame formed of a tubular diffusion flame is observed [88] for each venting hole. Due to the turbulence level, mixing can also occur in the plume, showing both diffusion and premixed combustion modes. The strategy adopted in this manuscript for the simulation of partially premixed turbulent flames is to 1. model premixed flames with DTFLES, 2. deactivate locally the model for diffusion processes and rely on mesh refinement to perform DNS-like simulations, and 3. define a flame index able to discriminate between both modes. Diffusion flame profiles must be closely studied for vent gases at typical vent conditions so that proper mesh refinement rules can be set up. Flame profiles are first given, followed by the evaluation of local mixture fraction to obtain mesh refinement criteria. It is concluded by the definition of flame indexes able to discriminate between combustion modes. Similarly to premixed cases, Cantera and the reduced scheme are used to compute flame profiles.

7.4.1 Laminar diffusion flame profiles

The gaseous mixture used as a reference in this section is NMC1: H_2 : 30.8 %, CH_4 : 6.8 %, C_2H_4 : 8.2 %, CO : 13.0 %, CO_2 : 41.2 %. To approach the condition of the sustained venting of a cell, the laminar counter-flow diffusion flame is set so that the pure fuel side is at $T_{fuel} = 1000$ K, and the air side is at $T_{air} = 300$ K. The pressure is kept constant at $P = 101\,325$ Pa. The strain rate a (see Eq. 3.10) is varied from $a = 50\text{ s}^{-1}$ to $a = 500\text{ s}^{-1}$.

Figure 7.4.1 depicts the typical profile of the diffusion flame of the NMC1 mixture versus air. The heat release rate front can be decomposed in two separate peaks, the first one on the fuel side, the second one on the oxidizer side.

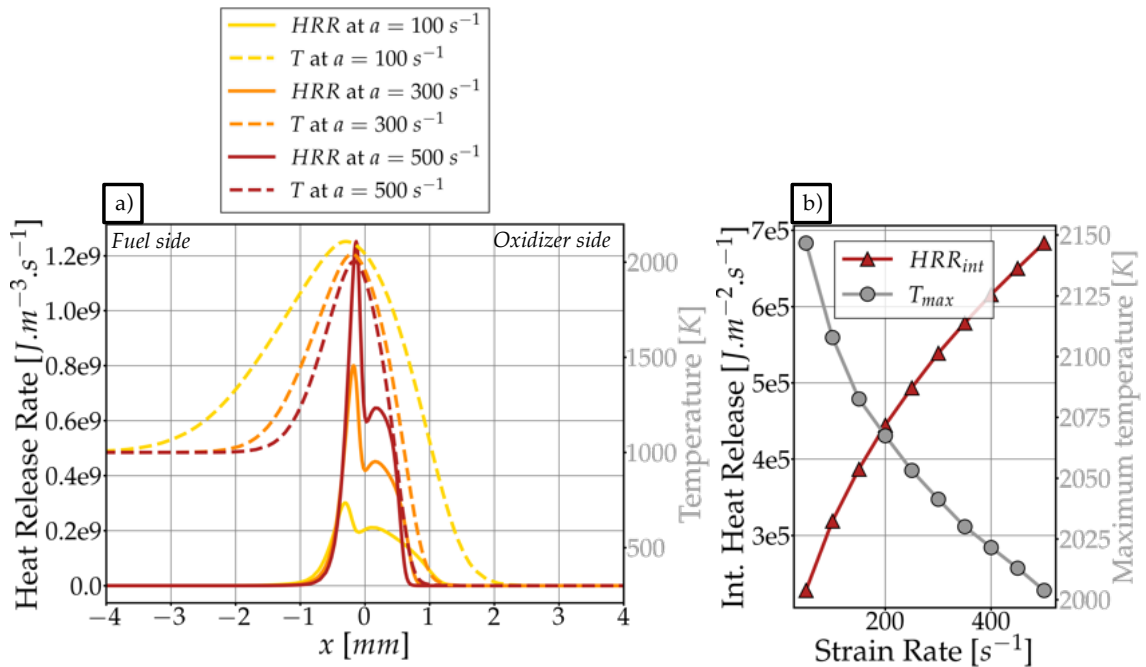


Figure 7.4.1: Flame profile for the counter-flow diffusion flame of the NMC1 mixture burning into air with $T_{fuel} = 1000$ K, $T_{air} = 300$ K: a) Heat release rate and temperature profiles for three strain rates, b) Integral heat release and maximum temperature depending on the strain rate.

Hydrogen in the fuel, accompanied by the hydrogen radicals resulting from the decomposition of methane and ethylene (correlated to the HRR peak on the fuel side), diffuses towards the oxidizer side where reactions with oxygen (such as $H + O_2 \rightarrow HO_2$) create a secondary heat release peak. Figure 7.4.2 shows that hydrogen disappears further on the oxidizer side than methane and ethylene. Moreover, it is accompanied by the production of O , H , and OH radicals that are consumed endothermically, explaining the gap in the HRR profile, and the artificial separation between the two reaction zones.

In order to define properly the advancement of the diffusion from the fuel side

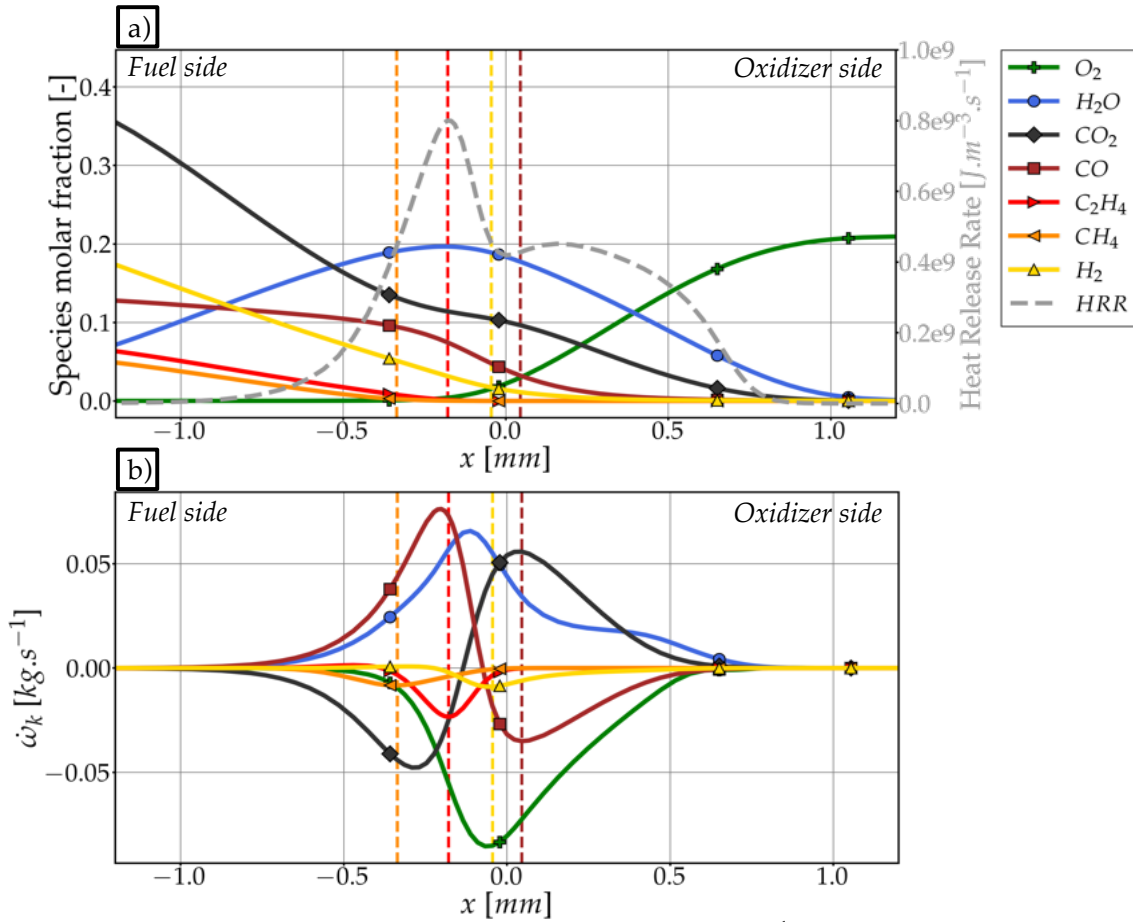


Figure 7.4.2: Main species profiles for NMC1 at $a = 300 \text{ s}^{-1}$: a) species molar fractions, b) species production rates.

to the oxidizer side, a mixture fraction adapted to the fuel blend considered here is to be set up. For the sake of coherence, the definition of the equivalence ratio underlined in Section 7.3 is the starting point of this definition. The mixture fraction and its gradient help to evaluate a diffusion flame thickness, useful to prescribe a mesh refinement adapted to resolve such flames in 3D.

7.4.2 Mixture fraction for Li-ion vent gases

Following the definition given for the local equivalence ratio, and in order to propose a coherent way to assert local mixture properties in diffusion mode, a local mixture fraction is used. Based on the relation between the equivalence ratio and the mixture fraction [213]:

$$\phi_{loc} = \frac{Z_{loc}}{1 - Z_{loc}} \frac{1 - Z_{st}}{Z_{st}} = \frac{Z_{loc}}{1 - Z_{loc}} \frac{sY_{fuel}^0}{Y_{oxidizer}^0} \quad \text{since} \quad Z_{st} = \frac{1}{s \frac{Y_{fuel}^0}{Y_{oxidizer}^0} + 1} \quad (7.6)$$

where $Y_{oxidizer}^0$ and Y_{fuel}^0 correspond to the mass fraction of oxidizer in the oxidizer stream and the mass fraction of the fuel in the fuel stream respectively. The stoichiometric ratio s can be rewritten using the fact that the vent gases are of the form $C_xH_yO_z$:

$$s = \frac{\left(x + \frac{y}{4} - \frac{z}{2}\right) \times 2W_O}{xW_C + yW_H + zW_O} = (\alpha - 1) \frac{zW_O}{xW_C + yW_H + zW_O} \quad (7.7)$$

where $\alpha = \frac{2x + \frac{y}{2}}{z}$ is the oxygen-hydrogen-carbon budget of the pure fuel introduced earlier. By using $\beta = \frac{zW_O}{xW_C + yW_H + zW_O}$, and injecting Eq. 7.5, the local mixture fraction becomes:

$$Z_{loc} = \frac{B}{(\alpha - B)\beta \frac{Y_{fuel}^0}{Y_{oxidizer}^0} + B} \quad \text{and} \quad Z_{st} = \frac{1}{(\alpha - 1)\beta \frac{Y_{fuel}^0}{Y_{oxidizer}^0} + 1} \quad (7.8)$$

Similarly to ϕ_{loc} , the local mixture is therefore a function of the local oxygen-hydrogen-carbon budget B , the pure fuel oxygen-hydrogen-carbon budget α , to which the term β and fuel/oxidizer stream conditions $\frac{Y_{fuel}^0}{Y_{oxidizer}^0}$ must be added. It is a rephrasing of the method of Bilger [22]. For the flames considered, $\alpha = 2.26$, $\beta = 0.59$, $Y_{fuel}^0 = 1.0$, and $Y_{oxidizer}^0 = 0.23$. Figure 7.4.3 shows the profile of mixture fraction and its gradient for the counter-flow diffusion canonical case.

One application of this representation is to set the minimal space-step required to properly refine the gradient of mixture fraction inside a diffusion flame. Knowing that the strategy chosen to simulate 3D diffusion flames and partially premixed flames is to deactivate the DTFLES model (only adapted to fully premixed combustion) in diffusion controlled zones, it is necessary to resolve the gradient ∇Z_{loc} in the flame. Using the definition of the diffusion flame thickness introduced in Eq. 3.9, in Chapter 3, Fig. 7.4.3 b) shows that in order to enforce approximately ten points in the flame thickness $\delta_L^{Z_{loc}}$, a refinement of $\Delta_x = 0.2$ mm should be applied for the range of strain rate estimated to be observed. In addition, a second flame thickness is computed, related to the heat release peak (δ_L^{HRR}). It delimits the zone where the HRR is higher than its maximum value divided by 500¹. A refinement of $\Delta_x = 0.2$ mm thus ensures a reasonable number of points in both thicknesses.

¹The value is chosen to encapsulate the reaction zone corresponding to the main heat release.

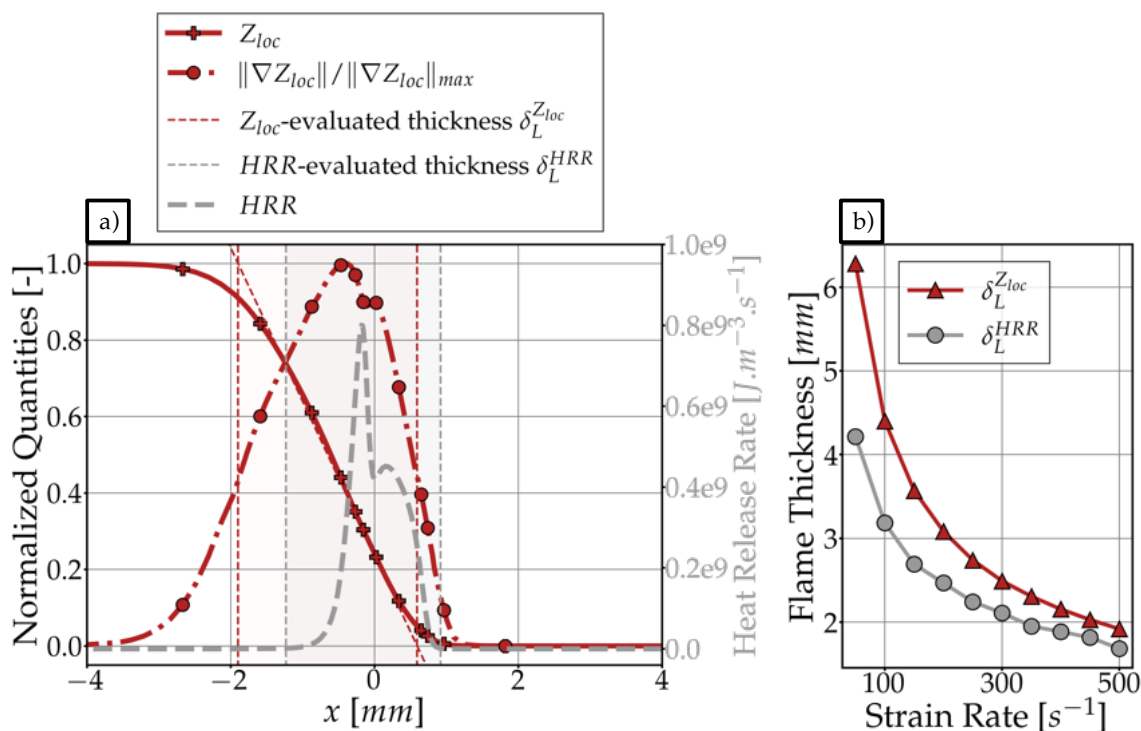


Figure 7.4.3: Mixture fraction and flame thickness: a) Mixture fraction and normalized gradient of the mixture fraction for $a = 300 \text{ s}^{-1}$, b) Approximation of the diffusion flame thickness using the relation of Eq. 3.9.

This refinement criteria will thus be applied by default in all the cases where diffusion flames are expected, which poses a limit on the dimensions of the problems to treat, and the duration of the scenarios to target. For strain rates higher than 500 s^{-1} (not evaluated here), it is also worth noticing that recent studies have shown that diffusion flames tend to adapt naturally to the mesh resolution [59], where if the resolution is too low, peak values are dampened but integral values and consumption speeds are conserved. It helps to still aim for integral results even if the resolution cannot theoretically satisfy a sufficient number of points in the gradient of the mixture fraction.

The following section then focuses on flame indexes able to identify combustion modes locally and deactivate the DTFLES model when it is not adapted.

7.4.3 Flame indexes

To conclude on the treatment of combustion modes, the use of a flame index allows to link the choice made for premixed flames to the one made for diffusion flames. A flame index that robustly discriminates between local premixing and local diffusion is generally chosen, and multiple solutions are already available. Most flame indexes originate from the work of Yamashita *et al.* [294], more often referred to as the

Takeno index θ_{Takeno} . It consists in evaluating the alignment of fuel and oxidizer gradients such that under a non-dimensional form [305]:

$$\theta_{Takeno} = \frac{\nabla Y_F \cdot \nabla Y_O}{|\nabla Y_F \cdot \nabla Y_O|} \quad (7.9)$$

where ∇Y_F (resp. ∇Y_O) corresponds to the gradient of the fuel species (resp. the oxidizer species). Thanks to the normalization, the sensor gives two values: $\theta_{Takeno} = -1$ for diffusion controlled flames, and $\theta_{Takeno} = +1$ for premixed combustion. An illustration is given in Fig. 7.4.4.

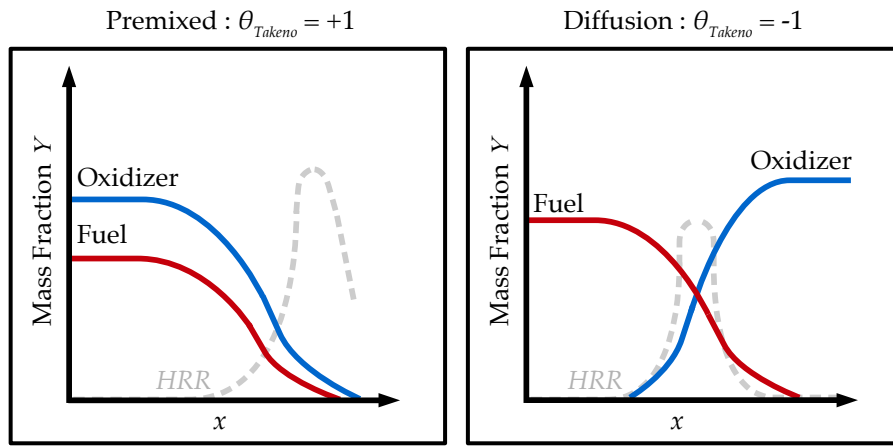


Figure 7.4.4: Principle of the Takeno flame index.

The method is generally completed by applying thresholds on gradient norms ($\|\nabla Y\| > \epsilon$, ϵ being pre-set by the user) to avoid spurious results in zones where combustion is non-existent, or mass fractions are noisy. For these zones, the value taken by the sensor is zero.

Various definitions have been adapted from the original Takeno flame index [305]. A common difficulty lies in the choice of what should be taken for Y_F . With multi-species blends such as the one at hand for Li-ion vent gases, the question is open. In [276], a summation of the mixture fractions of species of interest is proposed, which is generalized in [287]. Inspired by these studies, and in order to guarantee that the flame index adapts well to the non-typical mixture considered, two different approaches are tested in this manuscript.

1. First, the fuel mass fraction is modelled by the sum of the mass fractions of species of interest. For the sake of clarity, this approach will be named "*global*", and a set of species is selected. The species considered to write Y_F are the species of the blend that are reactive, which is translated by $Y_F = Y_{H_2} + Y_{CH_4} + Y_{C_2H_4}$ for the NMC1 mixture. CO is discarded as its mass fraction is not monotonous through all flame fronts. It is produced and then consumed in both premixed and diffusion flames, making difficult to assert

properly the direction of the mass fraction gradient with respect to the oxidizer mass fraction gradient [228]. This behaviour may reduce the applicability of the flame index, once added into the computation of Y_F , knowing that its representation in mass in all mixtures may amplify its importance in the computation of Y_F .

This flame index will be referred to as θ_{glob} .

2. For vent gases, the presence of H_2 at high level may hinder the performance of the index. Its diffusivity is high and its mass fraction is inherently low in comparison to the other species of the mixture. Its low participation in the final value of Y_F may lead to the mislabelling of parts of a diffusion flame such as the second peak showed in Fig. 7.4.2 on the oxidizer side. A precaution is taken by introducing a "preferential" flame index, such that for each species selected, a classical Takeno index is computed. If at least one species depicts a negative Takeno, the flame index returns -1. It leaves the cases where all the species Takeno are positive or zero. If the sum of all Takeno is strictly positive the index is set to +1. The only remaining case is when all species depict a Takeno equal to zero: the index is put to zero. With such a precaution, species with the highest diffusivity control the sensor in diffusion zones. Similarly to the "global" strategy, the species of interest for NMC1 are H_2 , CH_4 , and C_2H_4

This flame index will be referred to as θ_{pref} .

For smooth 1D canonical cases, the discrimination between the two approaches is difficult as gradients are always well computed and flame fronts mimic planar flames. However, in 3D turbulent cases, where the computation of gradients may be difficult, or when turbulence interacts with the flame, the two flame indexes θ_{glob} and θ_{pref} behave differently. The comparison of these formulations is made further in Chapter 10 where 3D jet flames are to be reproduced. The strength and weaknesses of each index are underlined, leading to the recommendation of one strategy.

Once the flame index θ is set, the thickening model defined in Eq. 4.14 is amended such that:

$$F(x, y, z, t) = [1 + (F_{max} - 1)S(x, y, z, t)] \times \min(1, \max(0, \theta(x, y, z, t))) \quad (7.10)$$

7.4.4 Summary of the strategies for 3D simulations

Based on the results obtained through 1D canonical cases, models have been selected and prepared to adapt to the combustion of Li-ion vent gases. The strategies raised in the previous sections can be summarized as:

1. **Shock simulation:** Mesh refinement should be as tight as possible to offer proper definition of the shocks, while minimizing the cost of the simulation. Shock handling methods (Cook and Cabot or LAD) are essential to avoid spurious oscillations, in collaboration with both Lax Wendroff and Two-steps Taylor-Galerkin 4A numerical schemes. The choice of the scheme is closely linked to the targeted application where the stiffness of the problem, the cost of the simulation, and/or the requirement in terms of precision will drive the decision.
2. **Premixed turbulent combustion:** In presence of turbulent premixed flames, and insufficient mesh refinement, the Dynamically Thickened Flame Model (DTFLES) is used with the relaxation sensor based on the detection of consumption peaks of methane. Efficiency is modelled by either static or dynamic formulations of the Charlette efficiency function. 1D premixed flames are tabulated in pressure, temperature and equivalence ratio so that models can adapt locally to the mixture based on laminar flame speed, methane consumption peak values, and flame thickness. In regions of partial premixing, and diffusion, the model must be deactivated using an adapted flame index.
3. **Partial premixing / Diffusion flames:** the DTFLES is deactivated by Flame indexes able to evaluate the local combustion mode. Diffusion flames must be resolved and based on the evaluation of diffusion flame thicknesses, a minimal space-step of $\Delta x = 0.2$ mm is necessary under the range of strain rate considered.

7.5 Selection of 3D scenarios to target

Once the simulation framework is set up, and in order to assert a variety of scenarios encountered during Thermal Runaway, three main objective cases have been selected to show the potential of 3D simulations for the design of batteries. The applications are backed by experimental *versus* simulation comparisons, specifically designed for Li-ion vent gases and TR relevant conditions. Figure 7.5.1 and Table 7.5.1 summarize the applications in relation to the TR phases, its main objective, along with the corresponding experimental tests, when available.

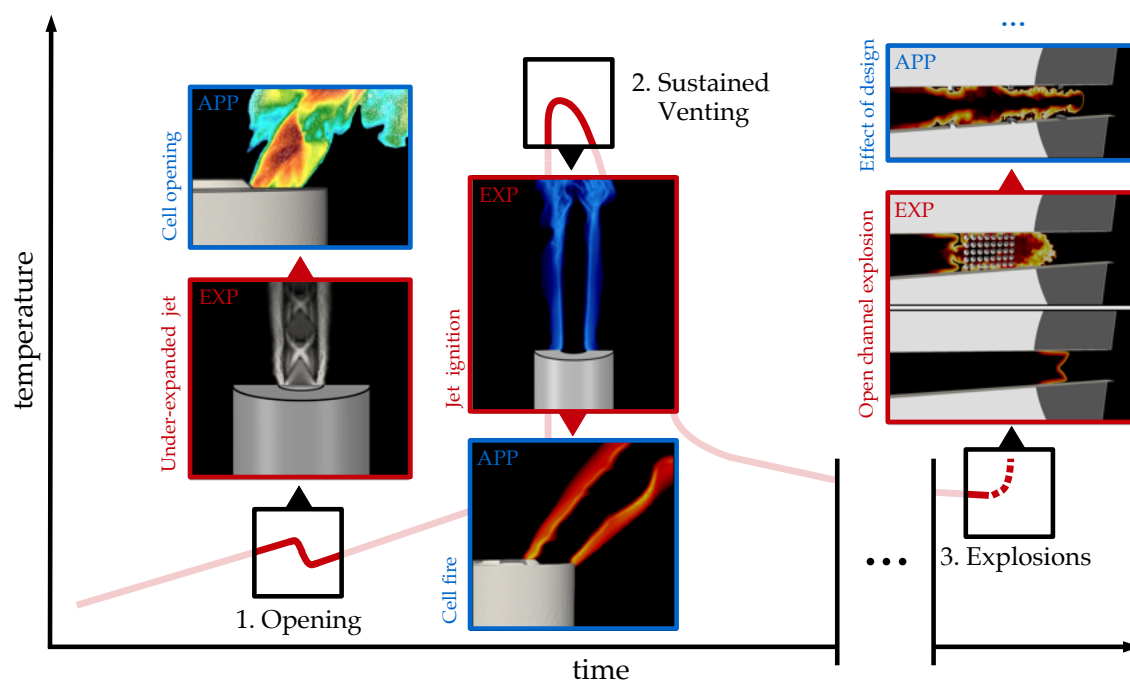


Figure 7.5.1: Summary of the phases of the Thermal Runaway targeted by 3D simulations. It includes the experimental/simulation validation step (EXP), and the intended application for the design of batteries (APP). More information is available in Table 7.5.1.

Table 7.5.1: Description of the 3D simulations proposed to target main Thermal Run-away events, including experimental/simulation validation (**EXP**), applications (**APP**).

	EXP		APP
	Experimental	LES validation	Application
1. Opening	<p style="text-align: center;">Part III Chapter 9</p> <ul style="list-style-type: none"> - Pre-heated under-expanded inert jet into the atmosphere. - Reproduction of venting conditions at cell opening (high p - high T). 		<p style="text-align: center;">Part IV Chapter 11</p> <ul style="list-style-type: none"> - Validation of the simulation setup for N_2 and an He/CO_2 surrogate to mimic vent gases behavior. - Comparison of numerical frameworks. <p style="text-align: center;">Part IV Chapter 11</p> <ul style="list-style-type: none"> - Simulation of the sudden opening of a realistic 18650 cell. - Effect of storage conditions on the venting procedure.
2. Sustained venting	<p style="text-align: center;">Part III Chapter 10</p> <ul style="list-style-type: none"> - Pre-heated reactive jet of pure vent gases into the atmosphere. - Forced ignition through successive sparking until anchoring. 		<p style="text-align: center;">Part IV Chapter 12</p> <ul style="list-style-type: none"> - Flame structure and ignition sequence comparisons to validate the simulation framework. <p style="text-align: center;">Part IV Chapter 12</p> <ul style="list-style-type: none"> - Sustained venting of a 18650 cell followed by forced ignition. - Impact of cell design choices.
3. Explosions	<p style="text-align: center;">Part V Chapter 13 & 14</p> <ul style="list-style-type: none"> - Deflagration inside a rectangular channel at atmospheric conditions. - Mixture extracted from a vent gas analysis. - Influence of cylindrical obstacles mimicking cells inside a module. 		<p style="text-align: center;">Part V Chapter 13 & 14</p> <ul style="list-style-type: none"> - Reproduction of tulip flame formation and propagation. - Effect of boundary conditions. - Simulation with cylindrical obstacles. <p style="text-align: center;">Part V Chapter 13 & 14</p> <ul style="list-style-type: none"> - Perspectives to evaluate different simple obstacles on flame acceleration.

The study is thus segmented in three parts:

1. **Part III**: A laboratory scale configuration set to reproduce Li-ion TR-relevant jet conditions at the scale of a single cell is first presented (**Chapter 8**)². Using the simulation setup presented and prepared in the first two parts. The configuration helps to characterize vent gases turbulent jets at high mach numbers modelling cell opening (**Chapter 9**), and an ignition to anchoring procedure creating a turbulent diffusion jet flame of hot vent gases (**Chapter 10**).
2. **Part IV**: Following first experimental versus simulation comparisons, applications to the design of lithium ion cells are proposed. The influence of structure and flow conditions for cases representative of 18650 Li-ion cell experiencing TR are targeted. A procedure to mimic cell opening is given in **Chapter 11**, and sustained venting leading to fire is emphasized in **Chapter 12**.
3. **Part V**: For larger scale applications, in case of delayed ignition, an explosive atmosphere is created. The overpressure due to the propagating flame, accelerated by interacting with obstacles is studied based on experiments³ of open tube explosions of vent gases premixed with air. A first case of tulip flame in a smooth rectangular tube is presented in **Chapter 13**. It is completed by an obstructed case (**Chapter 14**).

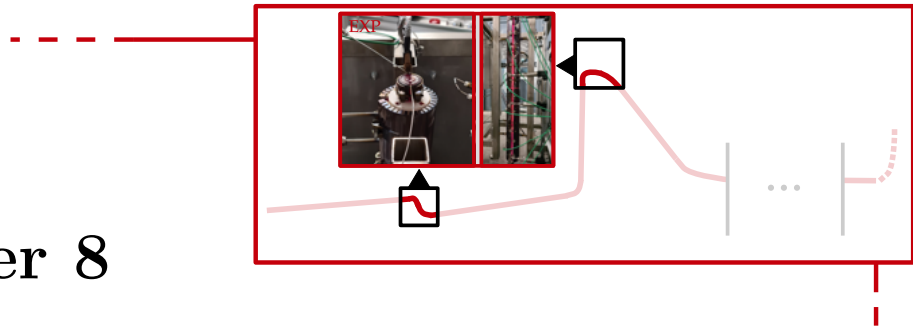
²Experimental results have been obtained using a novel setup installed at the Pprime institute, in collaboration with SAFT batteries, TotalEnergies, and CERFACS. The study ran in parallel with the present thesis work. Setup description and operation are made available in Chapter 8.

³Recent experimental results have been shared by Henriksen *et al.*, helping reproduction using CFD solvers [108, 109, 111, 112].

Part III

Experimental characterization of Li-ion vent gases jets and fires

Chapter 8



Experimental and simulation setups and objectives

Contents

8.1	The BTR test bed	118
8.1.1	Targeted TR events	118
8.1.2	Description of the setup	118
8.1.3	Diagnostics	120
8.2	Test bed operation	121
8.3	Experimental/simulation validation process	122
8.4	Simulation setup	123

In order to guarantee a better confidence in 3D simulation tools, when used in the specific context of Lithium-ion cells venting and fires, an experimental setup is proposed as a platform to compare simulation under relevant flow conditions. The system has been built and operated at the Pprime institute¹, in parallel with the numerical study proposed in this manuscript. It was funded by SAFT batteries and TotalEnergies. In this chapter, a description of the Battery-Thermal-Runaway (BTR) test bed is proposed, along with the objectives in terms of experimental/simulation validation. Finally, elements of the simulation setup are outlined.

¹Located in Poitiers (France) on the joint campus of the École Nationale Supérieure de Mécanique et d'Aérotechnique (ISAE-ENSMA) and the Université de Poitiers.

8.1 The BTR test bed

8.1.1 Targeted TR events

This study is placed at the scale of the cell and targets the two first flow scenarios selected in the TR course: 1. Opening with supersonic jet formation, 2. Sustained venting, ignition and flames². The reproduction of these critical phases under controlled environment is difficult using real cells, due to the highly statistical behavior of such systems under abuse conditions [96, 97]. Reproducibility is not guaranteed, flow parameters can only be approximated (mass-flow, mixture, temperature, ...), and comprehensive diagnostics are generally out of reach. The BTR test bed is developed to avoid these issues, while offering a degree of similarity to TR typical venting and fires. More details about the experimental setup follow.

8.1.2 Description of the setup

Figure 8.1.1 gives an overall description of the BTR setup. It consists in a pre-heated jet of a mixture stored in a pressured tank.

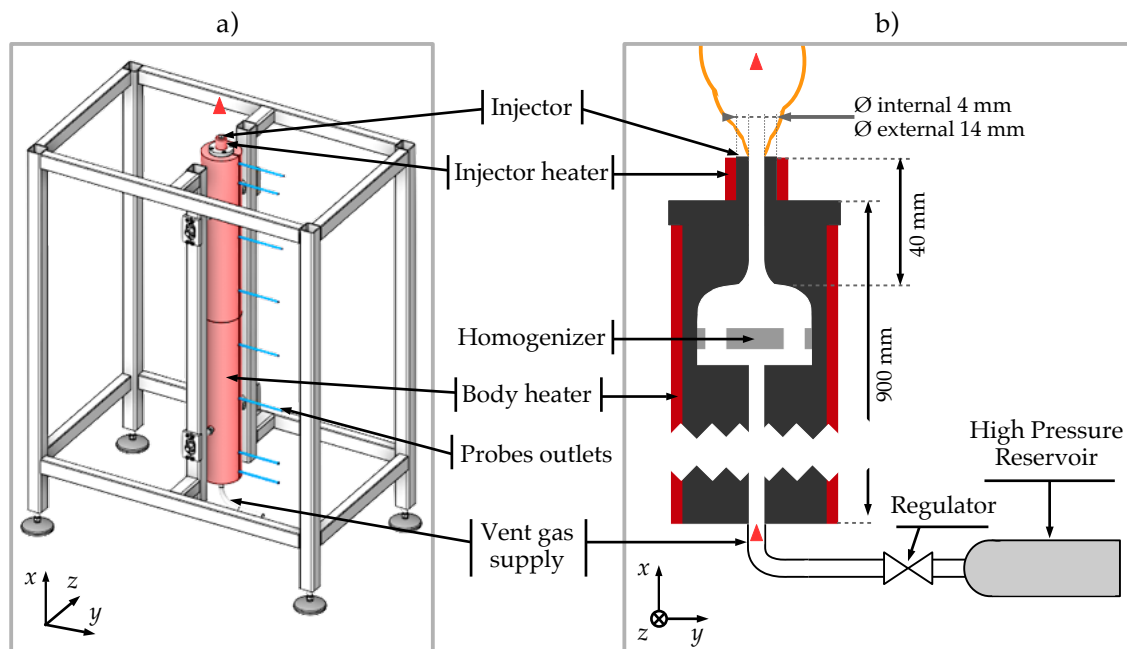


Figure 8.1.1: Description of the BTR experimental setup: a) Overall view of the CAD of the system, b) Schematic of the system.

To reproduce the critical venting conditions, three main parameters must be controlled:

²See Chap. 7 Sec. 7.5 for the complete list of scenarios in the timeline of TR.

1. **Pressure:** Cell opening happens under high pressure [11] and is followed by the formation of an under-expanded jet meaning that venting driven by high pressures must be ensured by the test bed.
2. **Temperature:** The internal exothermic decomposition reactions induce high temperatures during venting so that gases and flame anchoring surfaces must be heated.
3. **Mixture composition:** A strong variability in mixture composition has already been identified in Chap. 6. Being able to test different mixtures is of first importance. Also, having inert, non-toxic surrogates is mandatory to assert aerodynamics without risking delayed ignition or unnecessary pollution.

The experimental setup gathers these specifications. The pressure inside the reservoir can be modified to fit different venting conditions and a valve is added to regulate the flow. A driving pressure up to 12.5 bar can be set inside the reservoir allowing at least 5.0 bar inside the homogenization chamber. Once released from the reservoir, gases pass a 900-mm-long surrounded by annular body heaters optimized to guarantee a vented flow temperature above 1000 K (highlighted in red in Fig. 8.1.1). It is supplemented by an injector heater to counteract thermal losses due to the flow and the surrounding cold atmosphere (see Fig. 8.1.2). It can be added if necessary, namely when flame-wall interaction is to be observed. To add turbulence, the homogenization chamber features a 12 mm thick homogenizer plate pierced with six holes, 5 mm in diameter (colored in grey in Fig. 8.1.1 b)). The injector internal diameter reduces to 4 mm, to approximate 18650-type cells venting holes typical diameters [11, 79]. The external diameter is 14 mm, offering a hot surface to test flame anchoring and auto-ignition for highly reactive mixtures (e.g. pure hydrogen). Concerning the mixtures tested in the study, synthetic vent gases are made available (e.g. NMC1 in Chap. 6 Tab. 6.3.1) along with inert surrogates. More details follow in the dedicated chapters Chap. 9 and Chap. 10.

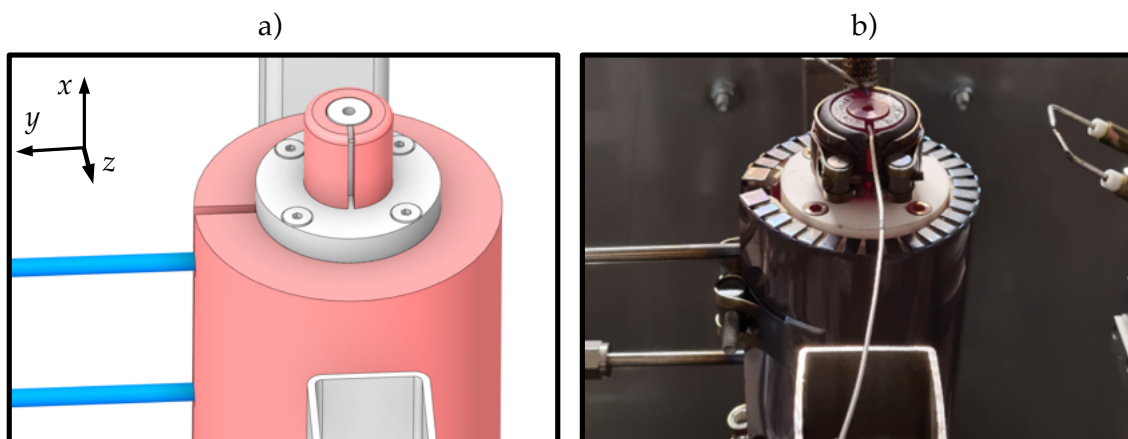


Figure 8.1.2: View of the injector: a) CAD, b) Photograph taken when the system is heated up.

To assert jet specifications and compare to simulation, the test bed is equipped with diagnostics. They are listed in the next section.

8.1.3 Diagnostics

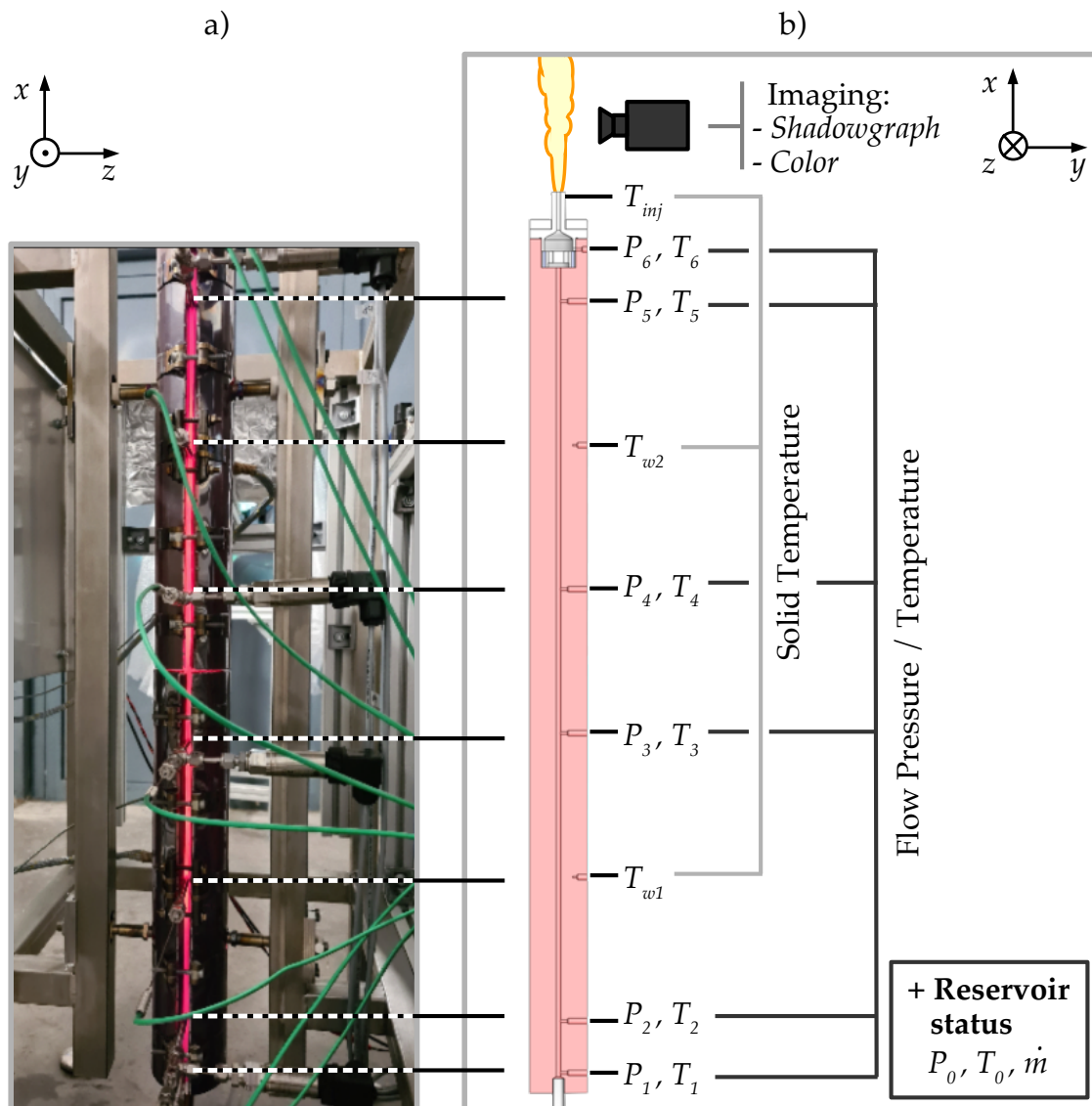


Figure 8.1.3: Illustration of the diagnostics location: a) Photograph of the body with probe locations, b) Description of all the diagnostics, located on the schematic of the system.

The state of the system under test is evaluated thanks to multiple pressure and temperature sensors: seven Druck UNIK 5000 pressure sensors are associated with type K thermocouple temperature probes. The probes location is given in Fig. 8.1.3. In addition to the sensors at the reservoir outlet (P_0, T_0), (P_1, T_1) to (P_5, T_5) document the heating process and pressure loss. Conditions inside the

homogenization chamber, after the homogenizer, are retrieved by (P_6, T_6) . Three temperature sensors T_{inj}, T_{w1}, T_{w2} help to check the solid temperatures inside the body and the injector, following a heating command. A Coriolis flow meter finalizes the sensor setup, located at the pressure reservoir. Jet and flame imaging is obtained through two main pieces of equipment, depending on the flow specificity to assert. For shocks, shadowgraphs come from a Photron SA-Z³. For flames, a Phantom V310 is selected⁴ and delivers color videos of ignition procedures.

8.2 Test bed operation

A summary of a typical operation of the BTR is proposed in this section. It shows the multiple possibilities in terms of experimental/simulation validation. In Fig. 8.2.1 a), the glowing system when commanded to heat up to 1000 K is shown, before a test is run. In Fig. 8.2.1 b), the pressured reservoir is opened at $t = 0$ s. In less than one second, a climax is reached where P_1 to P_6 peak and shocks form at the injector. After the climax, driving pressure and thus flow velocity reduces slowly during 8 s until complete emptying. Thanks to injector and body heaters, nearly constant temperatures can be commanded, allowing to reproduce high temperature venting. The peak pressure at P_6 is also sufficient to establish diamond shocks. A constant injector temperature is also retrieved, which is key to properly reproduce flame dynamics at hot surfaces. To complete the venting procedure, and to test forced ignition, a Beru ZSE030 spark plug is used and placed 10 mm above the injector. It is triggered at $t = 0$ s following the power demand given in Fig. 8.2.2 a). An impulse lasts 5 ms and is repeated every 20 ms.

Figure 8.2.2 b) summarizes the key phases of a test. After the supersonic venting climax, a time lapse is needed so that mass-flow reduces and meets values where successful ignition followed by flame anchoring and stabilization are possible. The two operating points identified as the "sustained venting climax" (representative of cell opening and supersonic jet formation) and the "flame anchoring" (representative of cell-level flame ignition and sustained fire) are of first importance to obtain experimental information on a given vent gas mixture at relevant venting conditions. They serve as reference points for the validation of a 3D simulation platform.

³**Frame rate:** 1000 frames per second, **Resolution:** 1024×584 , **Shutter speed:** 500 μ s.

⁴**Frame rate:** 1000 frames per second, **Resolution:** 1280×304 , **Shutter speed:** 990 μ s.
Lens: \varnothing 55 mm, F 100 mm, O f/2.8

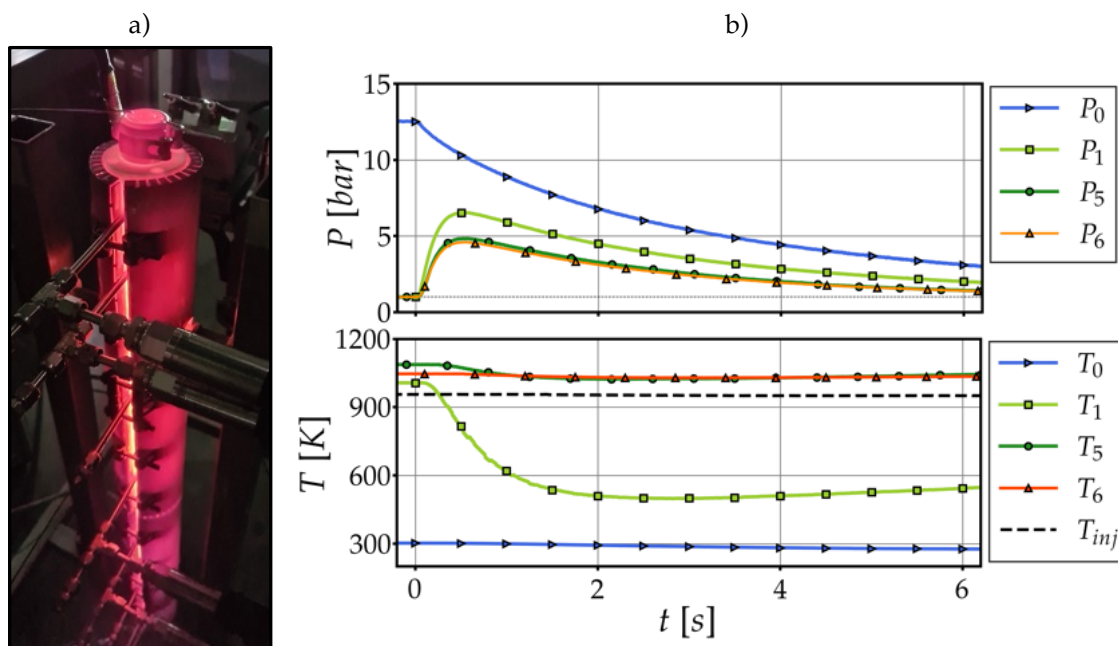


Figure 8.2.1: Typical operation of the BTR test bed: a) Photograph of the test bed glowing before a test is triggered, b) Pressure and temperature characteristics during a test at a reservoir pressure of 12.5 bar.

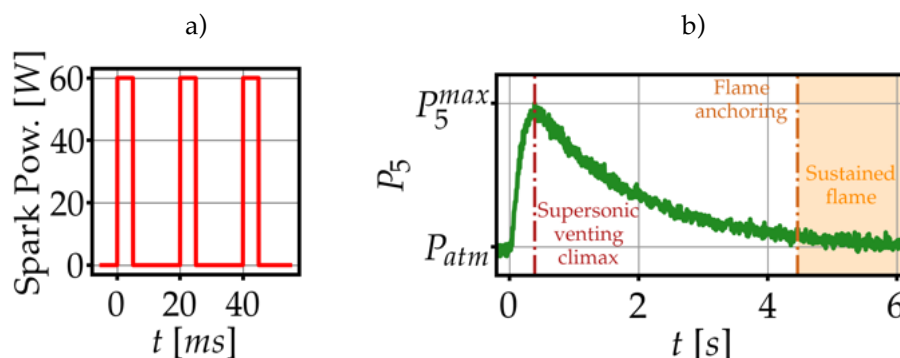


Figure 8.2.2: Ignition procedure: a) Spark plug power command, b) Typical succession of events during a test, from the supersonic venting climax to the flame ignition and anchoring and sustained fire.

8.3 Experimental/simulation validation process

Thanks to the experimental setup, reference operating points can be documented and used to initialize simulations, apply appropriate boundary conditions and observe characteristic flow structures that must be precisely rendered. The validation of the simulation setup is therefore divided into two cases:

1. **Chapter 9:** Inert supersonic jets are asserted with the aim to reproduce properly the succession of diamond shock structures. A comparison between

shock handling methods and numerical schemes set in Chap. 7 Sec. 7.2 is proposed.

2. **Chapter 10:** The spark ignition of the vent gas plume is targeted, with the aim to reproduce the succession of events leading to flame anchoring.

Direct application to realistic cell-related problems is proposed in Part IV (Chap. 11 and Chap. 12).

8.4 Simulation setup

In order to demonstrate the versatility of the simulation framework selected for this study, common choices for both under-expanded jets and flame ignition are preferred. In particular, the structure, and most boundary condition treatments are shared. The section outlines these common features. Case-specific models, initialization procedures, or detailed boundary conditions are found in the dedicated chapters (Chap. 9 or Chap. 10).

The first step towards the simulation of the setup is to encapsulate the parts of the system that have the most impact on the phenomena to reproduce. For the simulation, the structure is cut at the plane (P_5, T_5) where information is sufficient to prescribe correct inlets. Figure 8.4.1 shows the part of the system considered for CFD. Starting at (P_5, T_5) , it contains the homogenization structure, the nozzle and the injector. (P_6, T_6) helps to verify that conditions given at (P_5, T_5) fit experimental values. Due to their proximity with the injector, electrodes are added to the computational domain when used (forced ignition cases), which helps to assert their influence on the flow.

The entire domain considered for simulation is given in Fig. 8.4.2 a) and consists in a cylinder of 900 mm in length and 1000 mm in diameter so that the jet streams in an open atmosphere. The back plane is modeled as an adiabatic wall and side walls are treated with slip conditions. The outlet of the domain is the upper surface of the cylinder, and the inlet is the (P_5, T_5) plane at the interface between the body heater and the homogenization chamber where conditions are imposed based on static pressure, static temperature and mixture fractions. In the framework of AVBP (see Chap. 4 Sec. 4.3.2), inlets and outlets are enforced using Navier-Stokes Characteristic Boundary Conditions (NSCBC) [260, 214, 198].

Two meshes are introduced depending on the use case: *Mesh 1* has no injector heater and no igniter (for shock simulation, in Chap. 9) and *Mesh 2* takes into account electrodes and injector heater (flame ignition and anchoring simulations, in Chap. 10) The unstructured tetrahedral meshes use common strategies for both shocks and flames simulations (see Fig. 8.4.2 a)). Mesh refinement inside the system

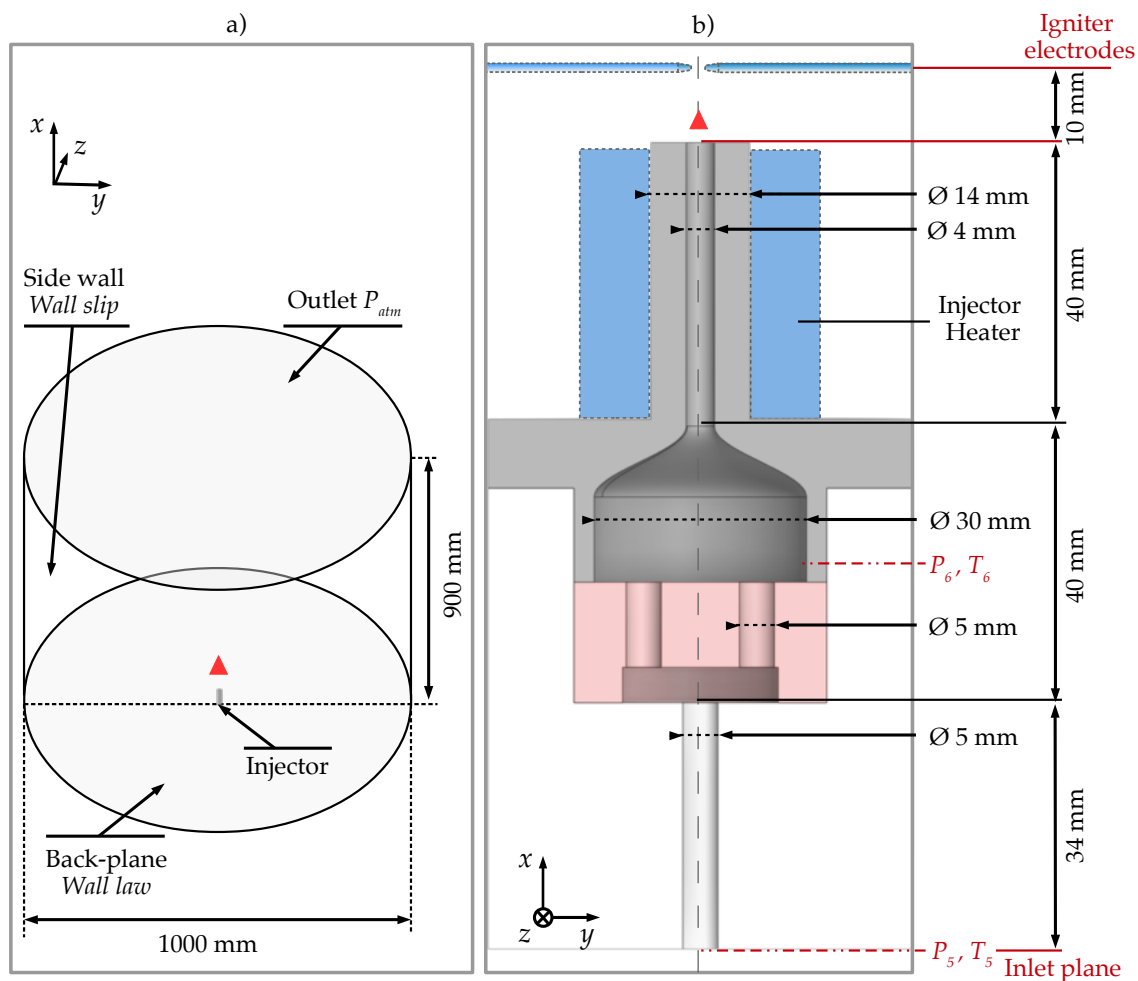


Figure 8.4.1: Simplification of the system to reproduce main operating points using simulation: a) View of the domain considered for simulation, b) Internal structure of the simplified system, where devices used for ignition cases only are highlighted in blue (electrodes and injector heater).

is summarized in Fig. 8.4.2 b). It guarantees 20 points in the diameter of the final injector tube ($\Delta x = 0.2 \text{ mm}$) and more than 15 points in the channels, lower. Adiabatic wall laws are selected for all internal boundary conditions, based on the fact that the body heater and injector heater limit the heat losses and maintain total temperatures close to constants. The top surface of the injector is assumed to play a crucial role in jet properties and flame anchoring. Its treatment is discussed in the next chapters. Figures 8.4.2 c) and d) show that mesh refinement at the jet foot is imposed to be $\Delta x = 0.2 \text{ mm}$. The choice is motivated by the observation made in the conclusion of Chap. 7 in Sec. 7.4.4, namely that it enables a proper diffusion flame definition. Concerning shock simulation, it has been observed in Chap. 7 that there is no practical limit to refine or de-refine a mesh. This level of refinement thus ensures a compromise between proper shock definition and reasonable costs. In addition, a previous study from Lacaze *et al.* [146, 148] demonstrated the ability of a similar mesh refinement to reproduce experimental jets [5, 261], considering pure air

flows and methane/air jet flame ignition. The refinement relaxes to $\Delta x = 0.7$ mm after a distance $x/D = 15$, for the jet plume⁵. *Mesh 1* totals 29.7 M cells, and *Mesh 2* totals 32.4 M cells.

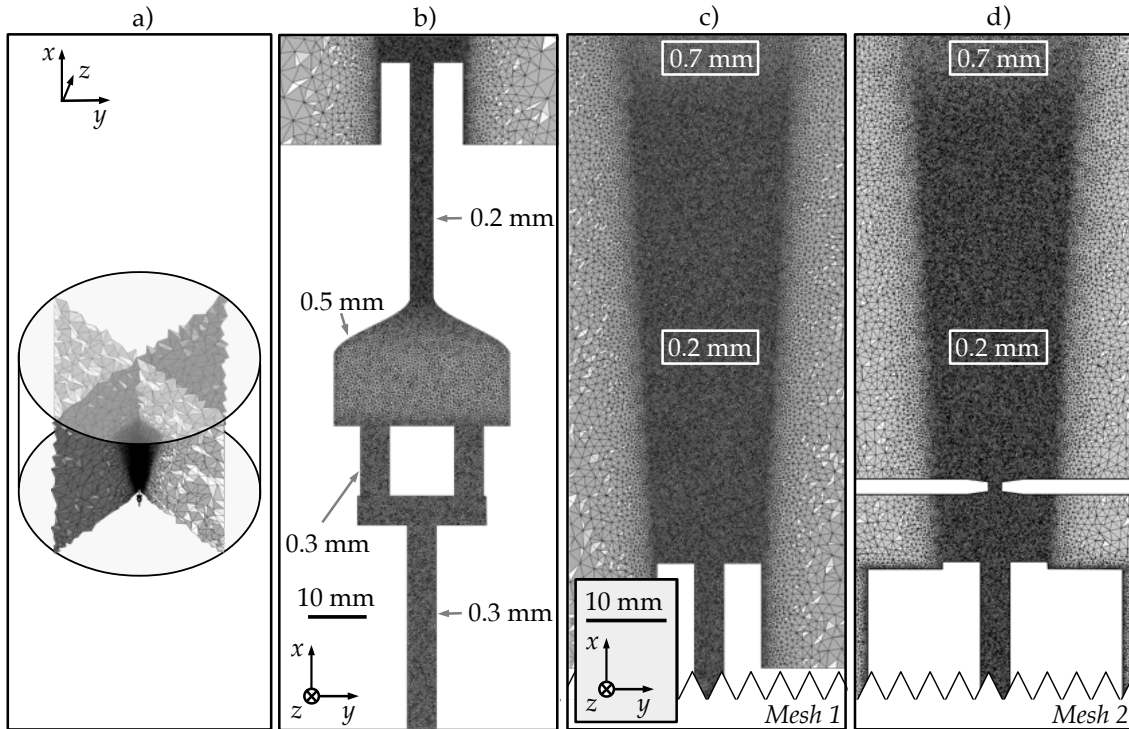
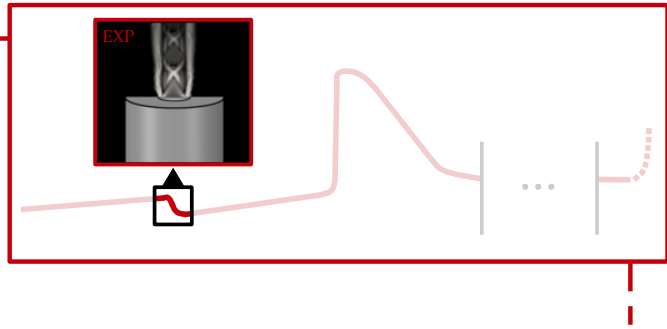


Figure 8.4.2: Mesh of the simplified BTR test bed: a) overall view of the mesh through cuts with selected refinement criteria, b) Zoom on a cut of the mesh inside the system, c) Refinement criteria inside the jet for *Mesh 1* (shock simulation), d) Refinement criteria inside the jet for *Mesh 2* (ignition simulation).

More details about initialization procedures and models choices are given in the next chapters, starting with the simulation of the under-expanded jet specific to the experimental ejection climax.

⁵For reactive flows, thickening levels are kept close to ten in the plume for the worst cases.

Chapter 9



Li-ion vent gas under-expanded jets

Contents

9.1	Under-expanded jet simulation	128
9.2	Case-specific numerical setup	128
9.3	Selection of validation operating points	128
9.3.1	Inert surrogates	129
9.3.2	Conditions expected theoretically	130
9.3.3	Initialization of the flow	131
9.3.4	Diagnostics to compare	132
9.4	Comparison of simulation frameworks	132
9.4.1	Shock handling methods	132
9.4.2	Numerical schemes	135
9.5	Validation versus experimental	137
9.6	Conclusion on under-expanded jet simulation	142

Under-expanded jets are expected during the venting process of a cell given the high pressures reached before cell opening [188]. Using experimental results of pre-heated under-expanded jets, conditions representative of a failing cell are reproduced and set the basis for experimental versus simulation comparisons. A proper validation increases the confidence in simulation tools for the diagnostic of flow structures around realistic cell designs, proposed in Chap. 5. Specifics of the numerical setup are highlighted, followed by expected flow structures. Assertion of the effect of shock handling methods and numerical schemes follows. It is concluded by comparisons between experimental and simulation for varying driving conditions.

9.1 Under-expanded jet simulation

Under-expanded jet configurations are challenging for CFD simulation frameworks, and often serve as benchmark for shock-handling methods and to test numerical precision. Considering unsteady scenarios (tank emptying, leak creation), while DNS offers proper ways to simulate the multiple shocks/expansion structures [184, 267], its cost and the fact that it still demands shock handling tends to set LES as a preferred solution for most applications [83]. Three-dimensional under-expanded jet LES have been validated against experimental [168, 165], and used to observe the influence of venting conditions on jet structures [42, 104, 103], accounting for questions of combustion [147, 292, 27, 291]. In this chapter, the specific case of the hot Li-ion vent gases under-expanded jet is used as a validation step to further perform the simulation of the opening sequence of a Li-ion cell. The evaluation of various numerical setups versus experimental helps to define a strategy for this application proposed in Chap. 11.

9.2 Case-specific numerical setup

In addition to Chap. 8 Sec. 8.4, specifics of the numerical setup must be highlighted. For the cases presented here, the under-expanded jet structure is obtained using Lax Wendroff [152] as the reference numerical scheme and the shock handling method is source of discussions in the following sections (see Sec. 9.4.1). TTG4A [50] is also tested to describe the effect of higher order schemes on solutions (see Sec. 9.4.2). WALE is selected to be the subgrid scale model [199]¹. CFL and Fourier numbers are 0.7 and 0.1 respectively. The choice of a shock handling method is part of the objectives of the study (see Sec. 9.4.1). Second and fourth order artificial viscosity terms complete the setup [125]. The gaseous mixture targeted is NMC1 (see Chap. 6 Tab. 6.3.1).

9.3 Selection of validation operating points

The objective being to reproduce climax flow, inflow conditions (P_5 , T_5) are selected at the time of peak P_5 pressure (see Fig. 9.3.1 a)), where a frame of shadowgraph imaging is available. To evaluate the effect of pre-heating temperature on flow structures and broaden the validation spectrum, three temperatures are commanded: $T_{heater} \in \{35, 400, 800\}^\circ\text{C}$. Due to high velocity in the jet, thermal losses at the injector lip are assumed to play only a minor role on the jet formation, no injector-heater is added experimentally, and simulations consider adiabatic no-slip conditions

¹Turbulent Prandtl and Schmidt numbers are both equal to 0.6

(see Fig. 9.3.1 b)). Also, because no ignition is expected, and to avoid pollution of the experimental room with toxic and flammable gases, inert surrogates are preferred for this phase. This question is developed in the following section.

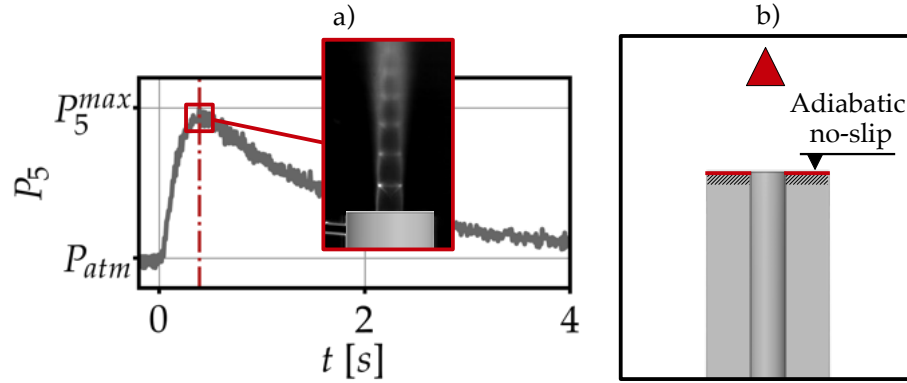


Figure 9.3.1: Under-expanded jet simulation: a) Selection of climax as a steady operating point for simulation, b) Zoom on the injector shape and lip boundary condition.

9.3.1 Inert surrogates

In view of the potential risk of working with flammable gases without igniting them, two inert mixtures are introduced. The first one aims at reproducing the parameter of NMC1 that is essential when considering flow expansion: the ratio of specific heat γ . The surrogate contains 84.2 % CO_2 and 15.8 % He to fit the γ of NMC1 at $T = 1073$ K. A second mixture is added to help assert the capability of the solver to generalize to other venting conditions: pure N_2 . In Fig. 9.3.2, γ and the density ρ are plotted versus the temperature for the reference NMC1 mixture ("NMC1 *reactive*"), the first mixture ("NMC1 *inert*") and N_2 . The good agreement in γ between the surrogate "NMC1 *inert*" and "NMC1 *reactive*" over the range of pre-heating temperature offers the possibility to observe safely multiple venting while reproducing the most important flow structures expected with the original mixture.

In the rest of the chapter, "NMC1 *inert*" is shortened to "NMC1" and is the center of attention. Experimental versus simulation validation of pure N_2 flows are found in Appendix C. The two mixtures tested with three pre-heating temperatures define six validation operating points and are summarized in Table 9.3.1. The atmosphere is identical for all cases and is considered to be air ($X_{O_2} = 21$ % and $X_{N_2} = 79$ %) at $T_{atm} = 300$ K and $P_{atm} = 101\,325$ Pa.

Based on the pressure and temperature ratios, it is possible to anticipate the type of flow theoretically.

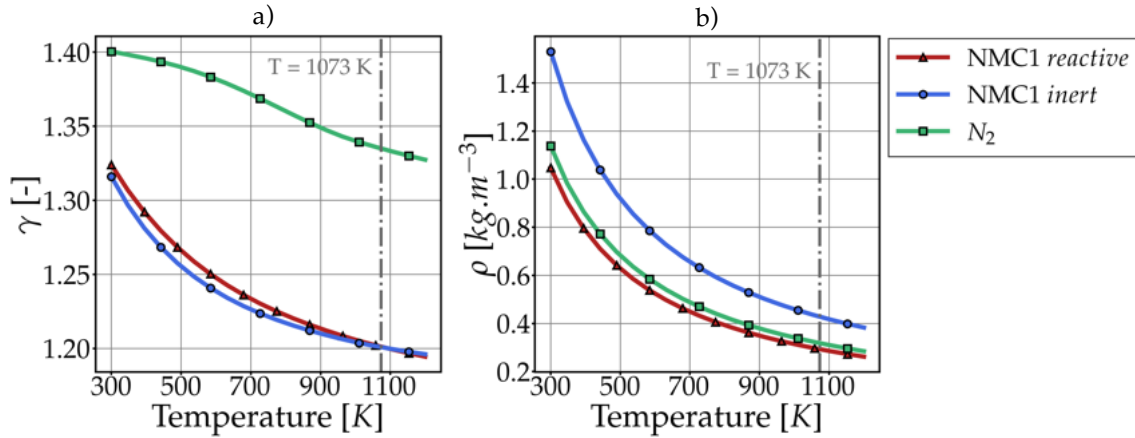


Figure 9.3.2: Comparison of two inert surrogates to the reference NMC1 mixture: a) ratio of specific heat γ versus temperature, density ρ versus temperature.

Table 9.3.1: Experimental conditions at venting climax.

Case Name	T5 [K]	P5 [bar]	T6 [K]	P6 [bar]
NMC1-800	1065.6	5.04	1038.0	4.79
NMC1-400	666.9	4.69	681.4	4.48
NMC1-035	305.2	3.53	305.7	3.49
N_2 -800	1075.4	4.77	1037.9	4.52
N_2 -400	685.6	4.49	685.4	4.28
N_2 -035	308.2	3.59	307.8	3.52

9.3.2 Conditions expected theoretically

Figure 9.3.3 a) outlines three locations of interest to assert the flow conditions. Starting from the conditions in the homogenization chamber, and assuming that the Mach number is sufficiently low to be considered at rest, total pressure and temperature will be taken as P_6 , and T_6 . In the following, the case NMC1-800 (see Tab. 9.3.1) is selected as an example. The strong constriction coupled with a large pressure ratio leads to the choking of the venting tube:

$$\frac{P^*}{P_6} = \left(\frac{2}{\gamma + 1} \right)^{\frac{\gamma}{\gamma - 1}} \simeq 0.56 > \frac{P_{atm}}{P_6} \quad (9.1)$$

Sonic conditions are reached inside the tube with a static pressure $P_{tube} = P^* = 2.70$ bar. Franquet *et al.* [83] have summarized main information on jet expansion configurations and recalled the conditions to produce an under-expanded jet with air. Based on the ratio $\frac{P_{tube}}{P_{atm}}$, a *moderately* under-expanded jet is to be observed at the exit plane. The outline of such a jet is given in Fig. 9.3.3 b) and consists in a succession of "diamond"-shaped structures.

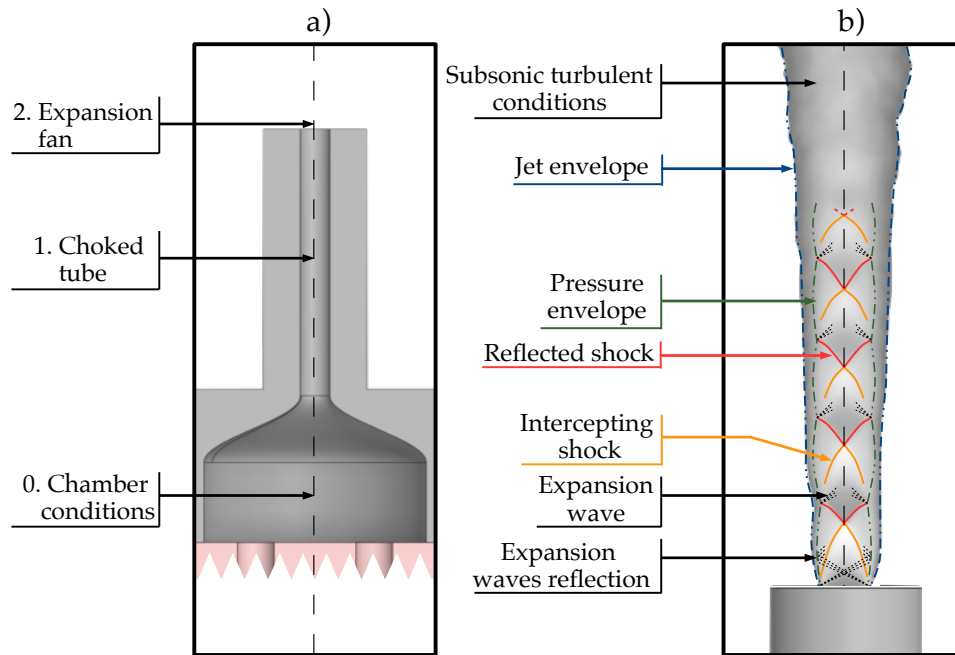


Figure 9.3.3: Expected conditions and flow structure: a) schematic referring to the theoretical flow conditions, b) structure of the moderately under-expanded jet.

As recalled in [83], this structure is formed by the expansion fan at the injector's lip which propagates waves towards the pressure envelope where they reflect. The resulting compression waves converge to the jet center-line forming *intercepting* oblique shocks. At the center-line, the shocks reflect to create secondary oblique shocks (*reflected* shocks) facing outer jet boundaries, which restarts the structure by forming expansion waves at the pressure envelope. It is essential to note the fact that the vented mixture is not cold air, and only experimental results for the six cases are able to confirm these expectations. From a CFD perspective, the succession of thin characteristic structures with steady positions give opportunities to validate quantitatively and qualitatively simulation frameworks at TR-relevant venting conditions. After the presentation of the initialization procedure, a comparison of these frameworks is given.

9.3.3 Initialization of the flow

For all simulations, the under-expanded jet is initiated to meet the target steady (P_5 , T_5) conditions at the inlet, using Lax-Wendroff and Cook and Cabot shock capturing method². The gas ejected in simulation is *reactive* NMC1 (H_2 : 30.8 %, CH_4 : 6.8 %, C_2H_4 : 8.2 %, CO : 13.0 %, CO_2 : 41.2 %). The structures to observe are converged, and stable homogenization chamber conditions (P_6 , T_6) are reached

²The combination being the cheapest, it helps to minimize simulation costs

and compared to experimental. An additional 5 ms window³ is used to average flow properties or test framework configurations such as numerical schemes and shock handling methods.

9.3.4 Diagnostics to compare

In addition to the (P_6, T_6) conditions, shadowgraphs coming from the Photron SA-Z⁴ must be compared to a numerical equivalent. The numerical Schlieren S^{num} is approximated by the often-used scaled density gradient [64]:

$$S^{num} = \frac{1}{\rho} \|\nabla \rho\| \quad (9.2)$$

Due to the thinness of the structures, contrast is enhanced similarly to experimental imaging to enforce a better readability of the figures. The resulting scalar S^{num} allows a location of shocks, along with jet inner and outer boundaries.

9.4 Comparison of simulation frameworks

Before proceeding to the comparison for each NMC1- T case, information on the effect of the simulation framework on result quality is given. To begin with, shock handling methods are compared, followed by numerical schemes. The reference case is selected to be NMC1-800, such that the highest temperature is reached, which constrains simulation by imposing lower time-steps and steep gradients between the jet core and the surrounding atmosphere.

9.4.1 Shock handling methods

In this section, following initialization, two simulations are continued with the Lax Wendroff numerical scheme. The first one uses a default Cook and Cabot setup, the second one the LAD sensor (see Chap. 7 Sec. 7.2, and Chap. 4 Sec. 4.2.3). Figure 9.4.1 details visualization of the jet structure, and compares experimental shadowgraph to numerical Schlieren.

³Given the high velocity reached in the system, it is 50 to 100 injector-tube flow-through times depending on the case.

⁴**Frame rate:** 1000 frames per second, **Resolution:** 1024×584 , **Shutter speed:** 500 μ s.

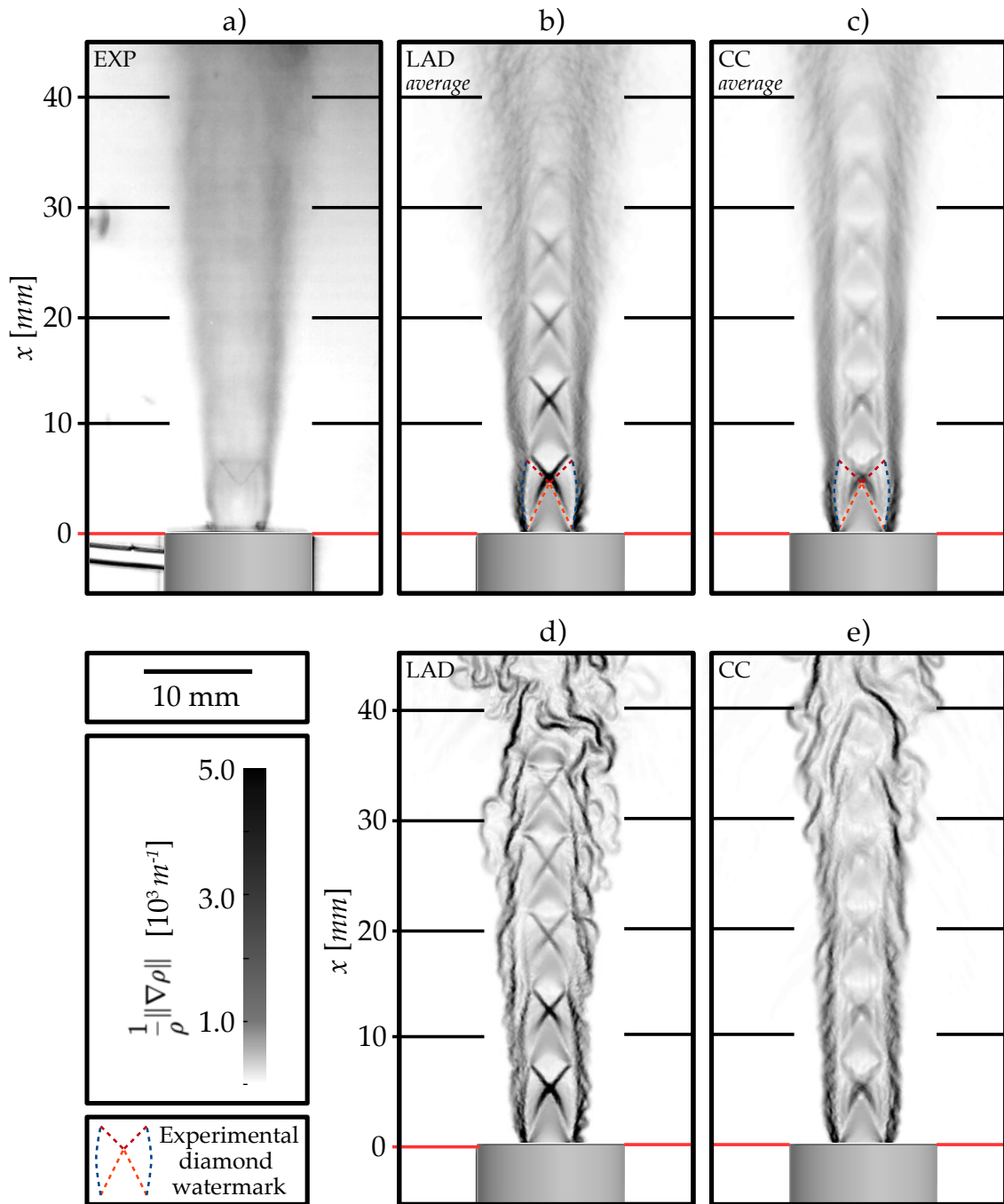


Figure 9.4.1: Jet visualization for NMC1 pre-heated at 800°C , comparing experimental to simulations with LW and different shock handling methods: a) Experimental shadowgraph imaging, b) 5.0 ms averaging of numerical Schlieren z -normal cut with LAD, c) 5.0 ms averaging of numerical Schlieren z -normal cut with Cook and Cabot, d) Instantaneous numerical Schlieren z -normal cut with LAD, e) Instantaneous numerical Schlieren z -normal cut with Cook and Cabot.

Both shock handling methods retrieve the diamond-shaped shock-expansion system and compare well to the first structure easily identified experimentally. To help comparison this experimental structure is watermarked on simulation visualization and a plot of the intensity along the symmetry axis of the injector is given in Fig. 9.4.2 a). Although the positions are well retrieved and the overall jet structure compares for both shock handling methods, the hyperviscosity technique used in Cook and Cabot tends to trigger an over-diffusion of shocks in comparison to LAD. For this type of scenario where no strict normal shock appears, LAD better benefits from the natural dissipation introduced by the numerical scheme along with low levels of artificial viscosity necessary for other sections of the computation such as mesh refinement decay zones and sharp edges. The crossing of intercepting and reflecting shocks and the edge of the injector where a strong expansion occurs are the most critical points, while the resulting oblique shocks represent weaker gradients, comparatively. The exercise is demanding for Cook and Cabot, well adapted for strong normal shocks, which successfully detects all shocks and smooth them in consequence, but too violently. LAD completes better classical second and fourth order artificial viscosity and limits its influence to the strongest gradients that could not be treated. Overall, lower classical second and fourth order artificial viscosity can be applied leading to better turbulence definition in the plume.

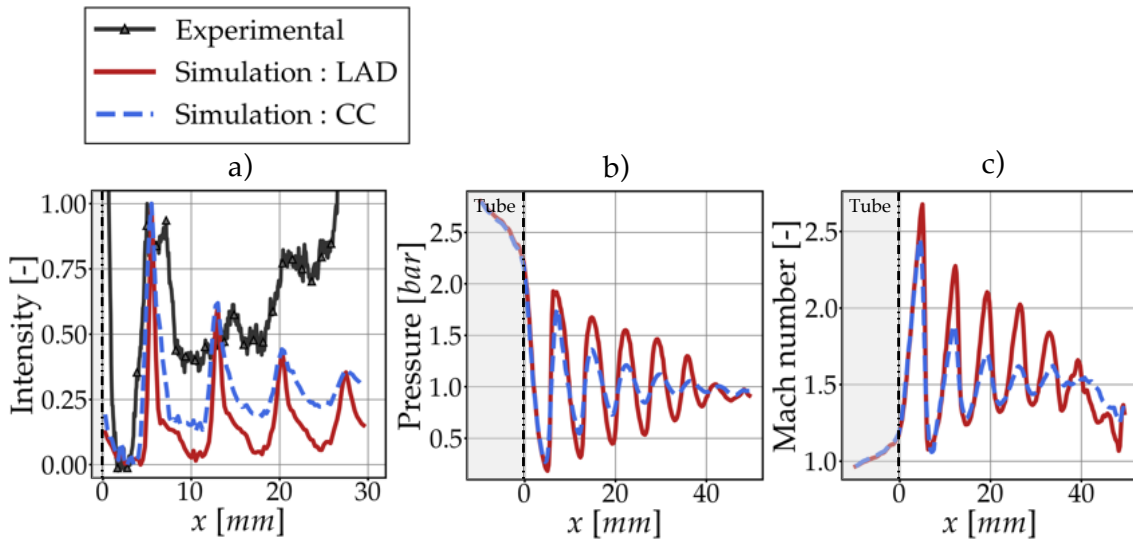


Figure 9.4.2: Longitudinal profiles for NMC1 pre-heated at 800°C, comparing experimental to simulations with LW and different shock handling methods following the jet center-line: a) Comparison of intensity from shadowgraph (exp.) and numerical schlieren (sim.), b) Pressure profile, c) Mach profile.

Therefore, despite its higher cost (additional cost of 9.9 %.), LAD will be preferred for the rest of the study. It is worth noticing, that a non-default version of the Cook and Cabot sensor may be case-dependently set to avoid this spurious behavior. It would cost the ability to generalize to different cases, which is a mandatory feature when working with multiple scenarios such as cell opening (Chap. 11) or explosions (Chap. 14).

9.4.2 Numerical schemes

To complete the study, the choice of the numerical scheme is to be discussed. The order-two scheme Lax and Wendroff [152] is compared to order-three TTG4A [50]. Both numerical schemes are supplemented with LAD. Figure 9.4.4 shows only slight discrepancies between the two setups, showing mainly on the upper part of the jet, in the turbulent brush. This is more visible using Fig. 9.4.3 where small differences appear for $x > 30$ mm, downstream the diamond structures. The higher order of TTG4A is observed to have an influence on the turbulent structures, which is depicted in Fig. 9.4.5 as a comparison of the Power Spectrum Density (PSD) of the fluctuation kinetic energy on a 5 ms time window. It is defined as the PSD of $E^t = \frac{1}{2}(u'^2 + v'^2 + w'^2)$, where e.g. $u' = u - \bar{u}$ is the temporal fluctuation of the x -direction velocity component at the given probe location. In this figure, it appears that the smallest structures inside the jet decay more rapidly due to the dissipation introduced by Lax Wendroff.

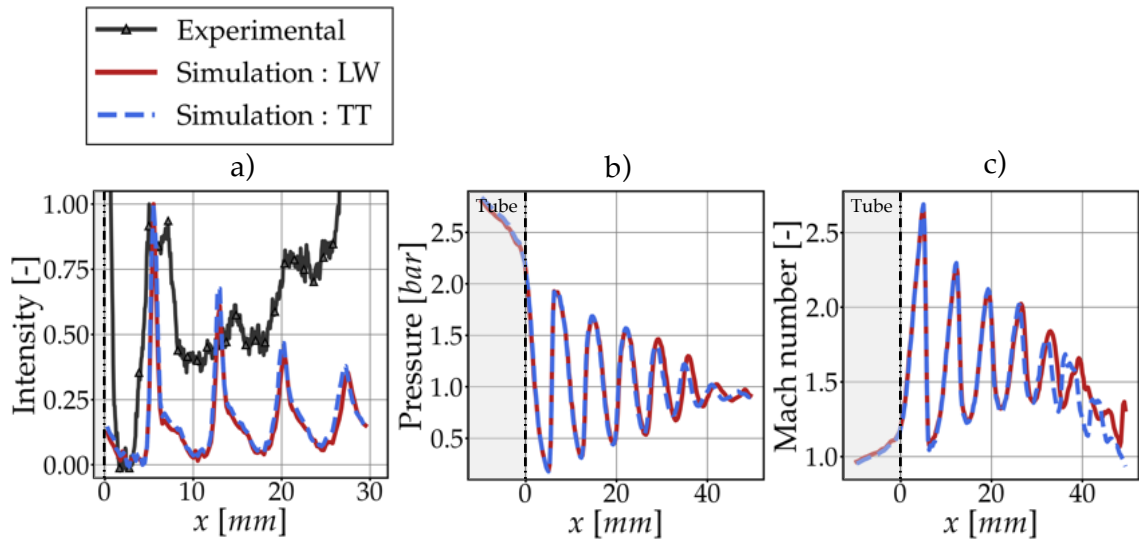


Figure 9.4.3: Longitudinal profiles for NMC1 pre-heated at 800°C, comparing experimental to simulations with different numerical schemes and LAD following the jet centerline: a) Comparison of intensity from shadowgraph (exp.) and numerical schlieren (sim.), b) Pressure profile, c) Mach profile.

The focus being to reproduce well the shock structures, and considering the already well refined mesh suggested in this study, the benefit of using higher order schemes than Lax Wendroff remains marginal. At this fixed mesh size, with the same shock handling method, solving with TTG4A instead of Lax Wendroff multiplies by 1.7 the computational cost. For the next section the framework is therefore set to Lax Wendroff and LAD. A comparison at three different pre-heating temperatures follows.

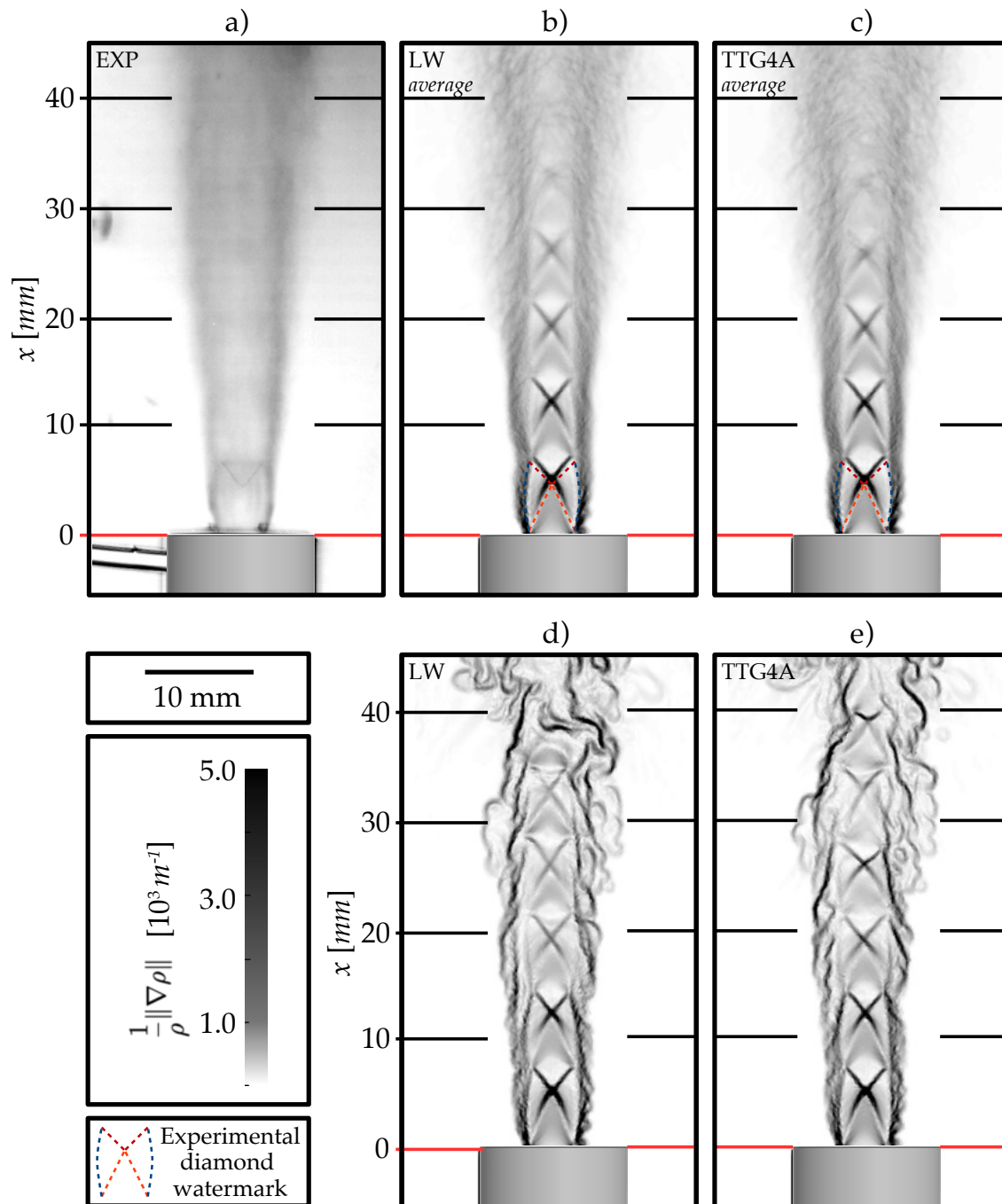


Figure 9.4.4: Jet visualization for NMC1 pre-heated at 800°C, comparing experimental to simulations with different numerical schemes and LAD: a) Experimental shadowgraph imaging, b) 5.0 ms averaging of numerical Schlieren z -normal cut with LW, c) 5.0 ms averaging of numerical Schlieren z -normal cut with TTG4A, d) Instantaneous numerical Schlieren z -normal cut with LW, e) Instantaneous numerical Schlieren z -normal cut with TTG4A.

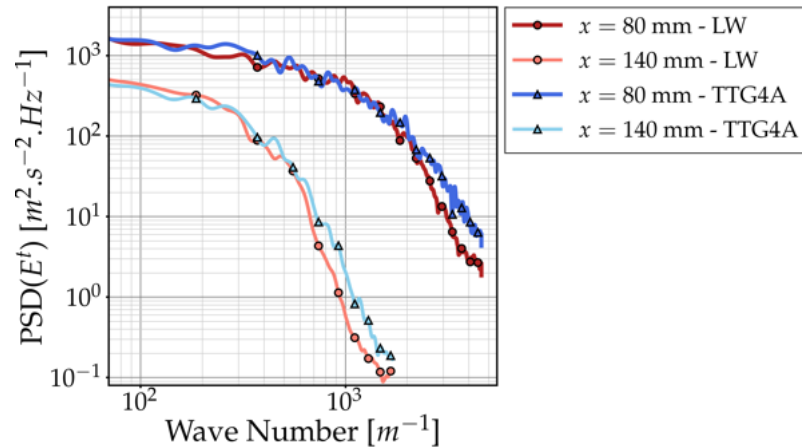


Figure 9.4.5: Turbulence spectrum inside the jet at $x = 80$ mm and $x = 140$ mm, comparing LW and TTG4A.

9.5 Validation versus experimental

To conclude the validation of simulation framework choices versus experimental results, the three operating points defined in Tab. 9.5.1 are computed. In experiments, the reservoir pressure is kept constant leading to three different climax P_5 pressure levels due to choking. Mach profiles are thus identical for the three cases inside the tube (see Fig. 9.5.1). Shorter diamond structures are expected for lower pre-heating temperatures, offering a larger panel of validation points.

Table 9.5.1: Experimental and simulation conditions at venting climax for *inert* NMC1.

Case Name		T5 [K]	P5 [bar]	T6 [K]	P6 [bar]
NMC1-800	Exp.	1065.6	5.04	1038.0	4.79
	Sim.	"	"	1074.6	4.82
NMC1-400	Exp.	666.9	4.69	681.4	4.48
	Sim.	"	"	673.5	4.49
NMC1-035	Exp.	305.2	3.53	305.7	3.49
	Sim.	"	"	309.0	3.36

Figures 9.5.2 refers to the already-seen $T = 800^\circ\text{C}$ case. It is followed by $T = 400^\circ\text{C}$ (Fig. 9.5.3) and $T = 35^\circ\text{C}$ (Fig. C.0.3). First shocks positions are retrieved consistently for all three pre-heating temperatures.

Two difficulties are to be pointed out downstream the first structure. At $T = 400^\circ\text{C}$ and $T = 800^\circ\text{C}$, due to weak contrasting when shock intensity is lowered (starting from the second diamond structures), it is generally difficult to obtain a proper experimental visualization of more than the first diamond. However, when plotting intensity at jet center-line, the periodicity appears, and confirms a good

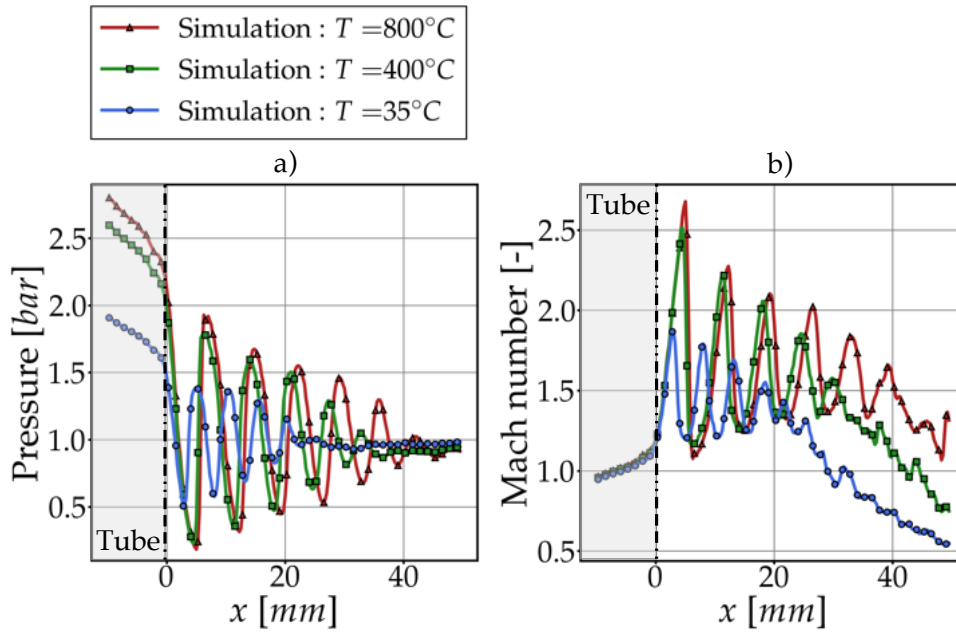


Figure 9.5.1: Comparison of profiles at jet center-line for NMC1 for the three pre-heating temperatures: a) Pressure profile, b) Mach profile.

agreement with simulation. Inversely, at the lowest pre-heating temperature, experimental better describes shocks after the third diamond. Tests with higher order numerical schemes could not correct this, meaning that the source of this over-diffusion may come from artificial viscosity, already set to a minimal value to counter stiffness problems at injector lips and for the numerous edges encountered before the homogenization chamber. A potential source of improvement could be to increase refinement from the inlet to the end of the diamond structure, at the cost of a drastic increase in computational costs. It should be noted that this condition of temperature is the furthest from realistic Li-ion cell venting, improving its prediction is thus kept as a target to reach in future works. A second source of error is the use of the inert surrogate in comparison to the real surrogate. This point can be nuanced as results from the second inert gas (N_2) in Appendix C show similar behavior of the low temperature case.

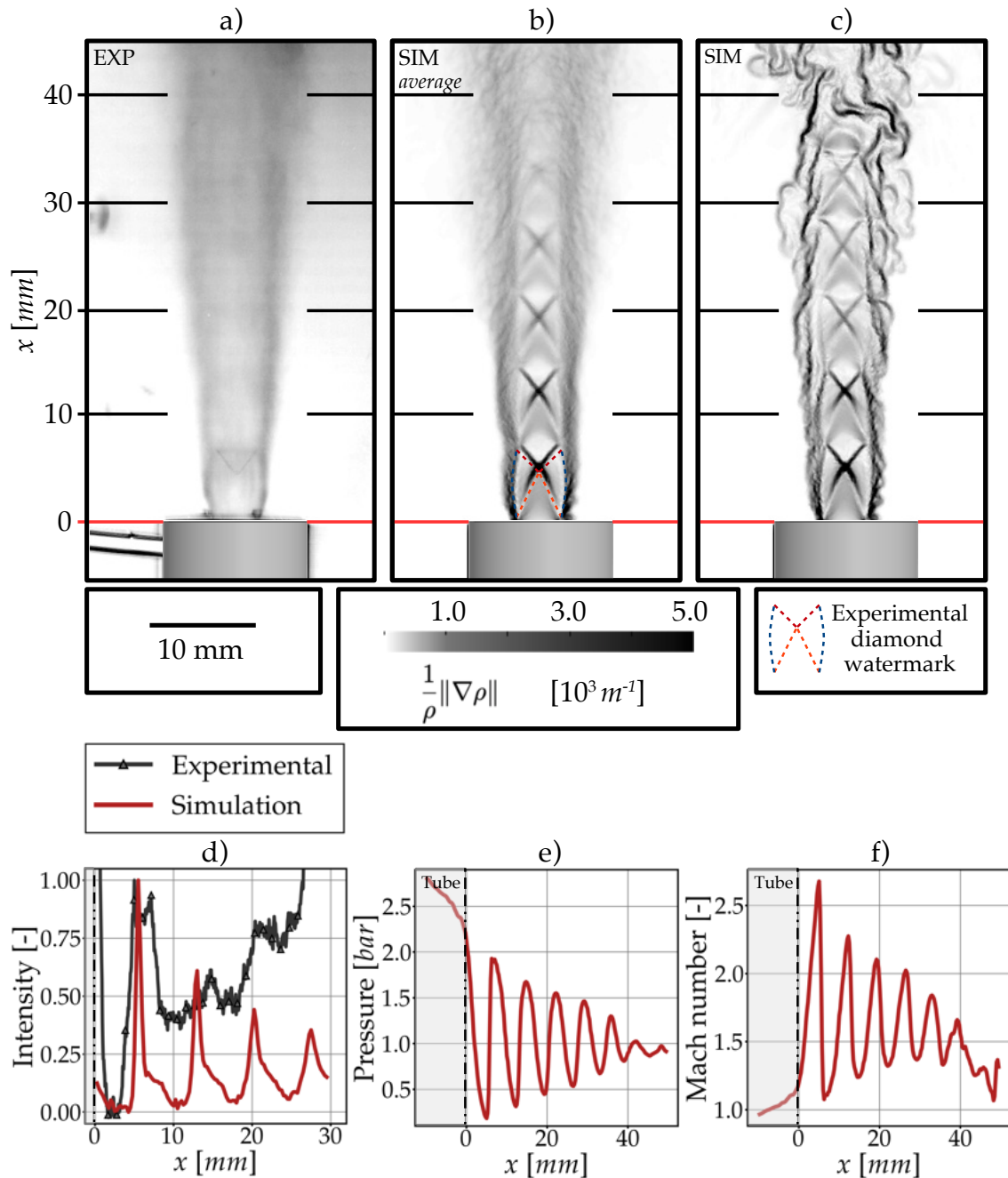


Figure 9.5.2: NMC1 pre-heated at 800°C, comparing experimental to simulations: a) Experimental shadowgraph imaging, b) 5.0 ms averaging of numerical Schlieren z -normal cut, c) Instantaneous numerical Schlieren z -normal cut, d) Comparison of intensity from shadowgraph (exp.) and numerical schlieren (sim.), e) Pressure profile, f) Mach profile.

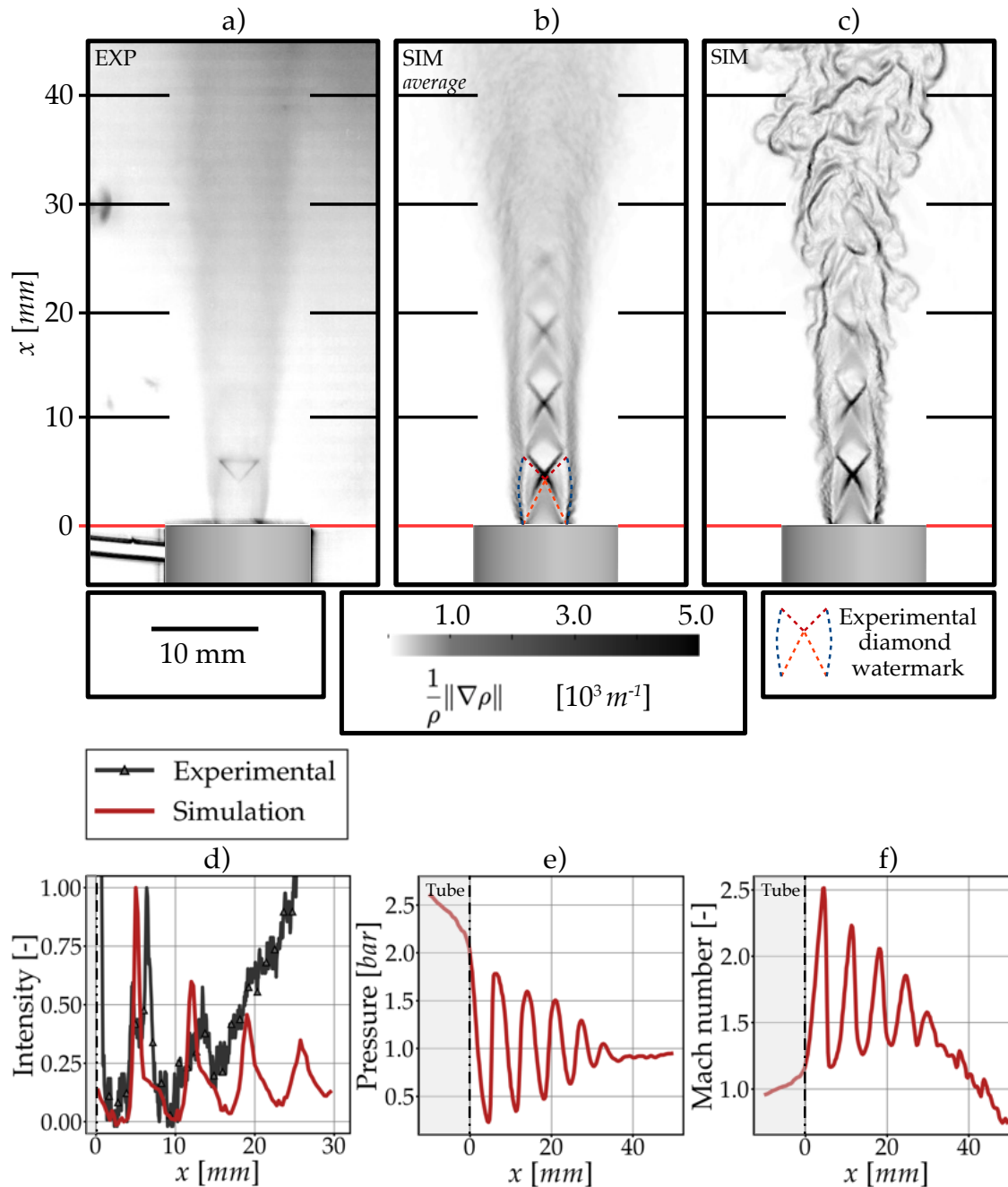


Figure 9.5.3: NMC1 pre-heated at 400°C, comparing experimental to simulations: a) Experimental shadowgraph imaging, b) 5.0 ms averaging of numerical Schlieren z -normal cut, c) Instantaneous numerical Schlieren z -normal cut, d) Comparison of intensity from shadowgraph (exp.) and numerical schlieren (sim.), e) Pressure profile, f) Mach profile.

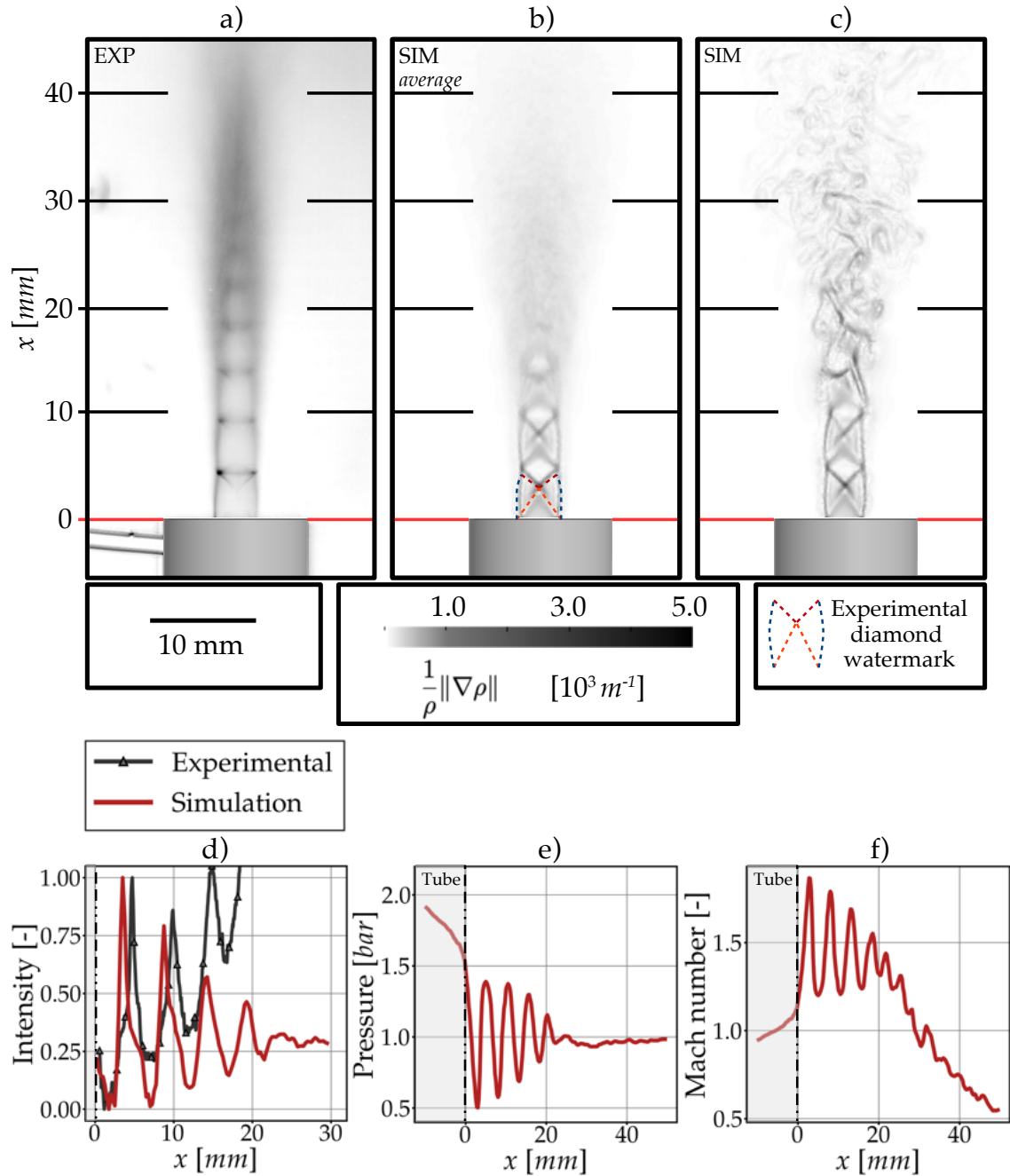
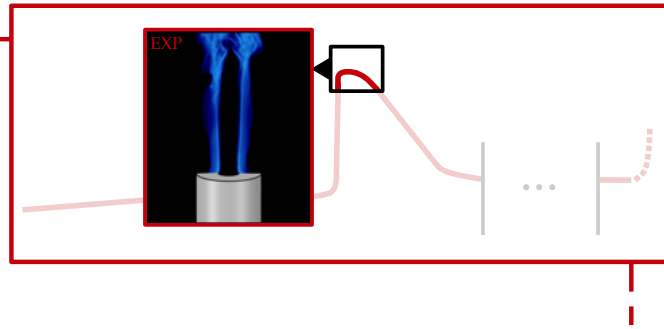


Figure 9.5.4: NMC1 pre-heated at 400°C, comparing experimental to simulations: a) Experimental shadowgraph imaging, b) 5.0 ms averaging of numerical Schlieren z -normal cut, c) Instantaneous numerical Schlieren z -normal cut, d) Comparison of intensity from shadowgraph (exp.) and numerical schlieren (sim.), e) Pressure profile, f) Mach profile.

9.6 Conclusion on under-expanded jet simulation

The simulation of the moderately under-expanded jet proposed in this chapter helps to familiarize with numerical configurations necessary to solve questions of pressured cell opening and venting. Conclusions lead to the selection of LAD as a preferred shock handling method for the rest of the manuscript. An overall agreement has been reached for multiple operating points, which ensures applicability to a range of conditions, from cold to hot, and the robustness of simulation tools to changes in surrogates. A direct application to under-expanded jet simulation is proposed in Chapter 11, focusing on the scenario of cell opening of a realistic 18650 cell. It helps to observe effect of design at opening, in representative high velocity flows.

Chapter 10



Li-ion vent gas jet ignition

Contents

10.1 Jet flame simulation	144
10.2 Selection of a validation operating point	144
10.3 Simulation objectives	146
10.4 Case-specific numerical setup	147
10.5 Cold flow simulation	148
10.5.1 Flow initialization process	148
10.5.2 Numerical scheme comparison	148
10.6 Ignition procedure	151
10.6.1 Modelling spark ignition	151
10.6.2 Selection of a flame index	152
10.6.3 Overview of the numerical procedure versus experimental	156
10.7 Ignition to electrode anchoring	158
10.8 Timing of the electrodes crossing	159
10.9 Electrode to lip anchoring	161
10.9.1 Experimental versus simulation	161
10.9.2 Reduced Modelling	163
10.10 Conclusion on jet flame ignition simulations	165

During TR, once the cell is opened, reactions may continue, reaching a point where the temperature reaches a climax creating sustained jets of hot flammable gases. The presence of electric sparks, hot metallic surfaces, or even incandescent metallic pieces of the cell leads to ignition and fire. To reproduce ignition, anchoring and sustained cell burning in a controlled environment, a pre-heated jet ignition is obtained using the BTR setup. The results set experimental references to compare

versus simulation. Such a validation translates to the test of simple design choices on flame topology around 18650 cells (see Chap. 12). Following the presentation of the operating point selected for validation, the numerical setup is highlighted, and used to perform a cold flow. The ignition sequence is then reproduced, completed by discussions about choices regarding models and numerical schemes.

10.1 Jet flame simulation

In numerous configurations where a reservoir filled of a flammable mixture leaks, a jet diffusion flame may appear. The study of jet flames is essential to predict and characterize a fire, helping to setup models and test simulation frameworks on well-documented cases. The flame dynamics starting from ignition, to stabilization or blow-off has been an experimental challenge in the past decades [180, 169, 130, 129, 131]. After a successful ignition, the role of the triple flame on anchoring or stable lifting processes has been identified as key [138, 30, 169] and motivated numerical [229, 77, 127] and experimental [138, 194, 140, 153, 46] studies on this special object in laminar and turbulent flows. It leads to a better understanding of the conditions necessary to obtain anchoring, lifted or blown-off flames in diffusion or partially premixed jets. It also underlines the flow objects to retrieve when considering the use of CFD. Full scale experiments of free jets, jet in co-flow, or piloted jet flames with complete diagnostics are proposed in the literature to observe the mechanisms and validate simulation choices. Considering the characteristic size and timing of the events, LES is largely used in such scenarios. For example, reproductions of the Sandia piloted flames [13, 185, 236] compose common benchmarks for CFD approaches [212, 274, 268, 297], completed by the Ahmed and Mastorakos [5] jet in co-flow flame simulated in [148], or the Delft Jet in Hot Co-flow experiment [202, 203] computed in [297]. In this study, a step towards the LES of a Li-ion specific jet flame is proposed, involving a pre-heated jet of vent gases into the atmosphere. The ignition to anchoring sequence is here the central question, with the observation of a triple flame.

10.2 Selection of a validation operating point

The target for this study is the course of event leading to the presence of a flame anchored at the lips of the injector. To evaluate the level of repeatability of a venting followed by ignition and anchoring, three different initial reservoir pressure P_0 are selected: {2.0,2.5,3.0} bar. The homogenization chamber driving overpressure $\Delta P_6^{ign} = P_6^{ign} - P_{amb}$ is measured at the instant of flame anchoring for the three venting. The maximum error relative to the average value of ΔP_6^{ign} is 16.7%. Repeated venting thus deliver similar conditions at the instant of successful ignition, helping

to select one venting as a reference to compare with simulation. The event can be summarized as follows. Starting from a reservoir pressure $P_0 = 3.0$ bar, a body pre-heating temperature of 800°C , and an injector pre-heating temperature of 690°C , a venting procedure is launched. During the venting, the ignition system is triggered with sparks every 20 ms, waiting for mass-flow conditions suitable for a successful ignition (under the blow-off regime). First, the mass-flow rapidly increases reaching its maximum at climax with a value of $2.4\text{ g}\cdot\text{s}^{-1}$. While the reservoir pressure decreases, the mass-flow progressively decreases. Following multiple unsuccessful ignition, at $t = t_{ign} = 4.425$ s, conditions are finally met and a spark ignites a flame that first anchors to the electrodes and eventually propagates towards the injector to anchor at the lips at $t = t_{ign} = 4.459$ s. Considering the short duration of the whole sparking-to-anchoring sequence (under 50 ms) with respect to the complete venting procedure (10 s), driving conditions are assumed constant. It is confirmed by the measurement of the mass-flow, varying by less than 3 % on this short period of time. Figure 10.2.1 depicts the succession of events leading to anchoring¹.

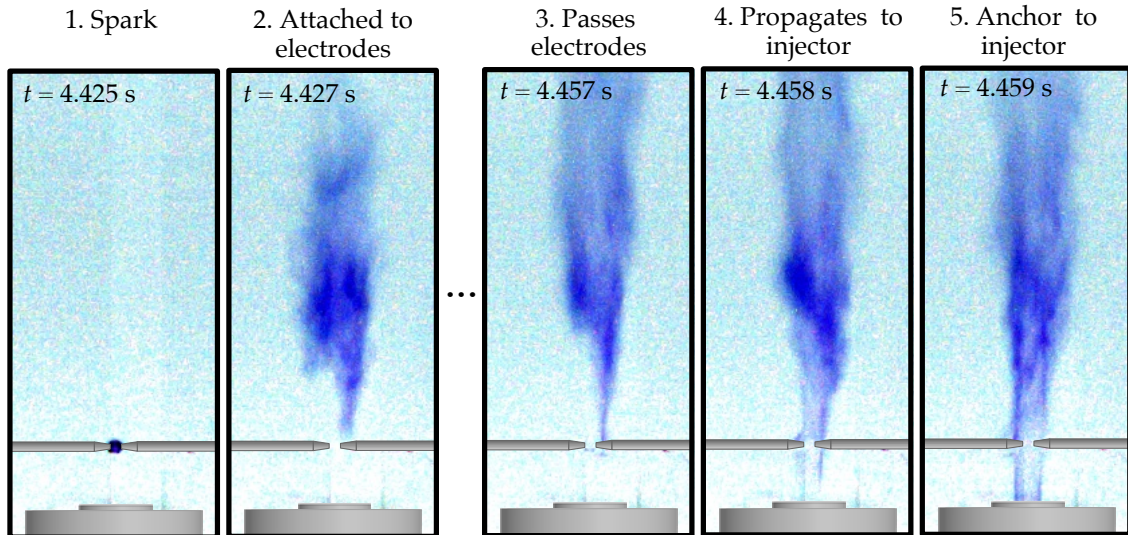


Figure 10.2.1: Rapid camera imaging of the flame anchoring phases for the selected operating point.

The sensor data monitoring the sequence offers input parameters for the simulation of this ignition-to-anchoring phase. The corresponding operating point is given in Table 10.2.1, and associated boundary conditions are illustrated in Fig. 10.2.2. (P_5, T_5) defines the inlet, and (P_6, T_6) helps to validate simulation, along with reservoir mass-flow². Thanks to the presence of the body heater, weak heat losses are expected inside the system and boundaries are treated using adiabatic laws

¹Phantom V310 set to: **Frame rate:** 1000 frames per second, **Resolution:** 1280×304 , **Shutter speed:** $990\ \mu\text{s}$. **Lens:** $\varnothing 55$ mm, F 100 mm, O f/2.8. The flame is contrasted, inverted to reduce the impact of black background on printing, and reset to a more realistic blue color.

²The reservoir mass-flow is not used as inlet condition due to its far-upstream position, too far from the inlet plane, inducing delay. Nonetheless, its value offers a good approximation of the flow condition and retrieving values close to sensor data using simulation is expected.

of the wall. Closer to the injector, the injector heater is added to allow a better characterization of the anchoring surface. The injector heater in itself is modelled using adiabatic wall laws, and the injector lip uses no slip conditions with heat losses. A thermocouple measures the solid temperature 2.5 mm under the surface at $T_{lip} = 944$ K. Using an approximate of the thermal conductivity of the stainless steel (17-4PH) at this temperature [230], the thermal resistance is evaluated: $R_{th} \simeq 1.14 \times 10^{-4} \text{ K.m}^2.\text{W}^{-1}$. Adiabatic wall laws are used for the electrodes, assuming that no heat is lost through the electrodes, given their small diameter. To conclude, the vented mixture is NMC1 (see Chap. 6 Tab. 6.3.1): H_2 : 30.8 %, CH_4 : 6.8 %, C_2H_4 : 8.2 %, CO : 13.0 %, CO_2 : 41.2 %. Ignition characteristics will be further discussed in Sec. 10.6. The operating point being set, it is necessary to highlight expectations from simulations.

Table 10.2.1: Operating conditions during flame ignition and anchoring. Pressures are measured with respect to ambient.

Sensor position	.5	.6
ΔP (Pa)	2590.0	2210.0
T (K)	1093.0	1063.0
Mixture	NMC1	
T_{lip} (K)	944.0	
Reservoir mass-flow (g.s^{-1})	0.33	

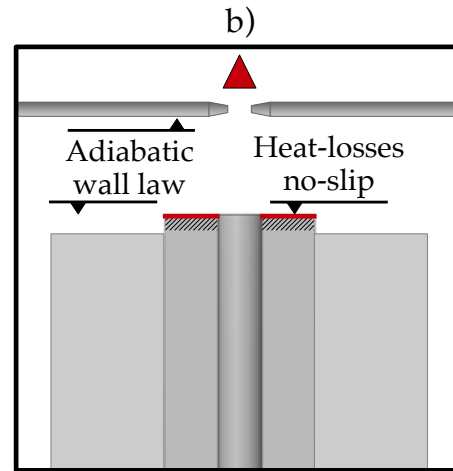


Figure 10.2.2: Configuration at the jet lips regarding structure and boundary conditions.

10.3 Simulation objectives

Multiple elements of the anchoring phase are of interest regarding the physics involved. From an experimental versus simulation validation point of view, three flames must be observed:

1. The first one is the partially premixed flame stabilized on one electrode. waiting for conditions sufficient to pass the electrodes. The sequence from spark ignition to this flame lasts two to three frames experimentally, giving an approximate of the related timescale to retrieve with LES (2-3 ms). Moreover, the peculiarity to have only one branch attached, is assumed to be due to the state of the flow at the instant of ignition. The system being symmetric in

the plane of the electrodes, this assymetry in the anchoring phase should be linked to the correlation between the jet turbulent slight oscillation and the opportunistic nature of the flame to reach for locally lower velocity, better mixed regions. LES must help to observe such a phenomenon.

2. The second one is the flame anchoring phase following the crossing of the electrode. In this section, the low turbulence and the absence of mixing are suitable for the observation of a triple flame [138, 229, 194] propagating towards the lips. This event is also approximately timed using camera imaging (3-4 ms) and helps to assert the timescales to reproduce using simulation. Theoretical aspects of the triple flame also allows to predict its behavior, and perform simple sanity checks on simulations.
3. Eventually, the anchored jet diffusion flame topology formed by a first tubular quasi-laminar flame attached to the lip up to the electrodes, topped with a turbulent partially premixed plume flame is also of interest when comparing simulation to experimental.

Both flame topologies and transition timing are therefore aimed at, which will help to reveal forces and weaknesses of the framework in each phases. One highlight is the triple flame propagation, essential to assert flame anchoring in further applications, and a special care will be given to this section. Following last details on the numerical setup, a cold flow simulation is performed to assert effects of numerical schemes on turbulence and converge the jet before ignition.

10.4 Case-specific numerical setup

Following Chap. 8 Sec. 8.4, more specific information are given about the numerical setup. Two numerical schemes are tested: Lax Wendroff [152] and TTGC [50] to see the effect of higher order scheme on the solution both in terms of aerodynamics (cold flow) and flame topology (ignition sequence). The subgrid scale model is WALE [199]³, CFL and Fourier numbers are 0.7 and 0.1 respectively in all cases. Numerical stability is enhanced by second and fourth order artificial viscosity terms [125]. The chemical kinetic scheme is the one set in Chap. 6, and in the DT-FLES framework, the static Charlette efficiency formulation with a constant equal to 0.5 is chosen (See Chap. 4 Sec. 4.17).

³Turbulent Prandtl and Schmidt numbers are both equal to 0.6

10.5 Cold flow simulation

10.5.1 Flow initialization process

Before ignition, a cold flow simulation is performed. Starting from a domain filled with air at atmospheric conditions ($P_{atm} = 101\,325\text{ Pa}$, $T_{atm} = 300\text{ K}$ at rest, the venting system from the inlet up to the injector tube is filled with hot NMC1 at (P_{atm} , T_5). The simulation is then run applying the inlet conditions (see Table 10.2.1) for 150 ms of physical time using Lax Wendroff. From this new initial state, two simulations are computed in parallel for an additional 40 ms each⁴. One continues with Lax Wendroff, the other uses TTGC. The inlet (P_5 , T_5) conditions invariably lead to the constant mass-flow $\dot{m}^{sim} = 0.31\text{ g.s}^{-1}$ which compares well with the value found experimentally at the reservoir $\dot{m}^{exp} = 0.33\text{ g.s}^{-1}$.

10.5.2 Numerical scheme comparison

A key information to take before trying ignition is the ability of a numerical scheme to render turbulence, and measure its performance with respect to its cost. In Fig. 10.5.1 a) averaged velocity fields for the order-two Lax Wendroff scheme is depicted versus the order-three TTGC scheme. Both schemes agree in terms of magnitudes and qualitatively compare in terms of spatial distribution. Moreover, mixing, given by the stoichiometric lines, are comparable for both frameworks. This agreement for mean fields is expected, and differences must come when looking into the details of how turbulence markers evolve. Figure 10.5.1 b) displays Turbulent Kinetic Energy (TKE) for the entire jet. TKE writes as:

$$\text{TKE} = \frac{1}{2} \left(u_{RMS}^2 + v_{RMS}^2 + w_{RMS}^2 \right) \quad \text{with} \quad u_{RMS} = \overline{u'^2} \quad (10.1)$$

Once again, very few differences can be observed and iso-contours positions match. The conclusion remains the same when zooming on the critical near-electrode zone (see Fig. 10.5.2).

Differences appear when comparing fluctuation energy $E^t = \frac{1}{2}(u'^2 + v'^2 + w'^2)$ spectra. Its Power Spectrum Density (PSD) is computed at three different locations in the jet: At the injector lips ($x = 0.0\text{ mm}$), 10 mm above the electrodes ($x = 20.0\text{ mm}$), and further downstream in the plume ($x = 80.0\text{ mm}$). While spectra fit at the injector lips, smaller structures are more difficultly reproduced by Lax Wendroff after the electrodes. This dissipative property is amplified further downstream where a smaller cut-off frequency coupled with a steeper slope is observed, and mainly due

⁴Corresponding to 90 to 100 injector tube flow-through times.

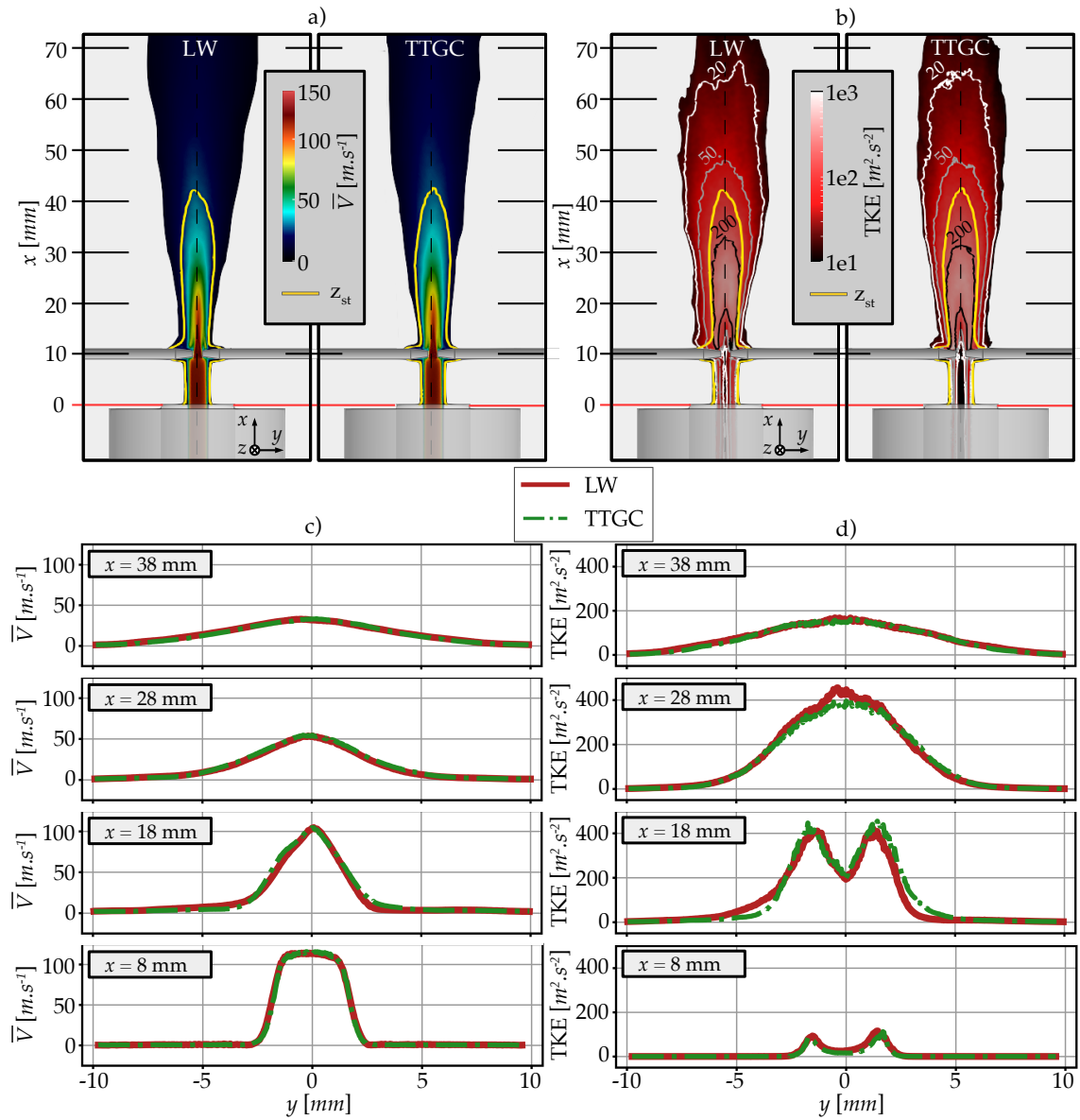


Figure 10.5.1: Cold flow simulation of the jet, comparison of numerical schemes: a) longitudinal z -normal cut of the average velocity magnitude (\bar{V}) field, b) longitudinal z -normal cut of the Turbulent Kinetic Energy (TKE) field, c) plot over line of \bar{V} at varying x , d) plot over line of the TKE at varying x

to the progressive coarsening of the mesh starting in this region of the domain (see Chap. 8 Sec. 8.4).

Given the reasonably well detailed mesh chosen due to combustion constraints, increasing the order of the numerical scheme only offers marginal improvements in this setup. The objective being to simulate the ignition-to-anchoring phases, the most critical regions of the domain are located from the injector lip to approximately $x = 60$ mm ($x/D = 15$) where refinement is $\Delta x = 0.2$ mm. TTGC remains indicated for a better definition of the entire plume, at steady state conditions, but at higher

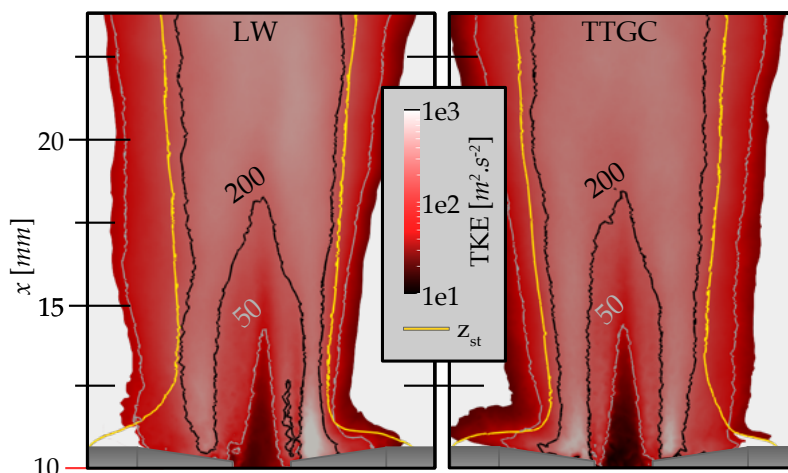


Figure 10.5.2: Cold flow simulation of the jet, comparison of numerical schemes regarding longitudinal z -normal cut of the Turbulent Kinetic Energy (TKE) field at the electrodes.

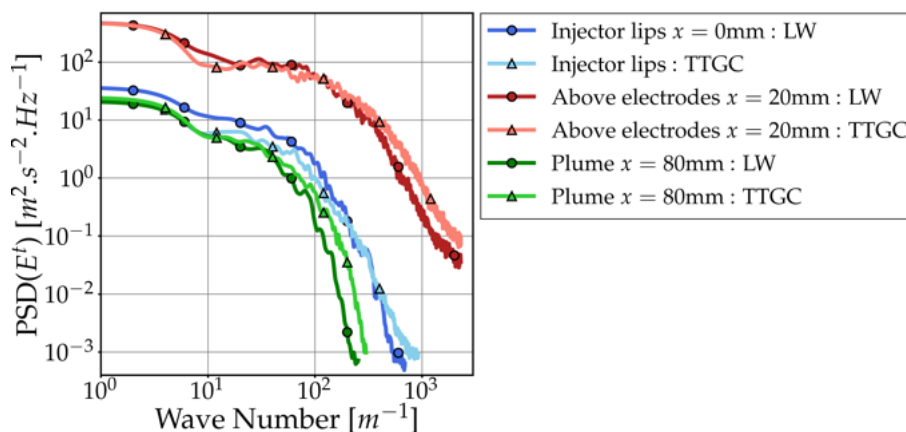


Figure 10.5.3: Spectrum of the fluctuation kinetic energy E^t at three different locations: injector lips, 10 mm above the electrodes, downstream in the jet $x = 80$ mm.

cost. In this example, costs must be multiplied by 1.82 for TTGC. The comparison is continued using Lax Wendroff, helping to compare multiple configurations at a minimal cost, and helping to validate an efficient setup for further applications in Part IV. However, one ignition procedure is reproduced using TTGC and proposed in Appendix E to observe differences to expect.

10.6 Ignition procedure

10.6.1 Modelling spark ignition

The first step to simulate ignition is to model the ignition device. The Energy Deposition model (ED) is selected [148]. Its detailed presentation can be found in Appendix B Section B.1. The model allows to apply a spherical source term of energy, mimicking a spark plug, while controlling the total deposit in terms of energy, spatial distribution and timing. The model avoids temperatures that would exceed ionization limits, letting space for a smooth runaway of the reactions until a kernel is formed. Three main parameters are to be selected with care: the deposition time, the deposition duration, and the total deposited energy (which controls the deposition diameter, see App. B Sec. B.1). In this study, the Beru ZSE030 spark plug is commanded to deliver impulses every 20 ms and a similar ignition device has been studied by Benito [16], helping to discuss ways to setup the model.

1. **Deposition time:** The highly statistical dimension of ignition depends on local conditions that may evolve rapidly due to the transient behavior of a jet. Turbulence, equivalence ratio and velocity may rapidly shift from conditions sufficient to ignite to blow-off conditions. Non-optimal time for ignition can be avoided based on velocity and flammability criteria [148] helped by probabilistic maps of success [5]. In this experiments, the uncertainty to ignite is reduced by triggering multiple sparks until conditions are suitable, which is generally impossible with simulation given the cost. Because in this chapter, multiple simulation frameworks are to be compared, a unique ignition time is selected, corresponding to $t_{phys} = 190.3$ ms, which follows the cold flow establishment. The deposition duration and energy then must ensure a robust ignition for all the cases compared.
2. **Deposition duration:** Schematically, the device used in this work depicts three distinct phases during sparking: a sudden breakdown ($\simeq 1$ μ s) followed by an arc phase (100 to 500 μ s) concluded by a glow phase (1 to 2 ms) [16]. In practice, reproducing the phases, their timescales and the corresponding energy distribution is out of the scope of ED. The ED model summarizes the phases into a Gaussian profile in time chosen to be closer to the arc phase duration as it avoids the creation of shockwaves (shorter durations) or a source term too low to trigger chemical runaway at reasonable total energy (longer durations) [208]. This duration will be set to 100 μ s for all simulations.
3. **Deposition energy:** Concerning energy, during the entire venting procedure, the Beru ZSE030 spark plug is commanded to deliver impulses every 20 ms. The total electrical energy spent for an impulse represents 300 mJ. From this total energy, only a small fraction is actually transmitted to the gaz [148, 172,

259]. In [16], for air at atmospheric conditions, the measured electrical and thermal energy at the electrode reach up to 50 mJ and 20 mJ respectively. In the present case where the spark is triggered in hot flowing gases with an effect of history due to multiple sparking, no direct access to the energy deposited is available. Therefore, it has been chosen to set the minimal energy necessary for a successful ignition-to-anchoring procedure in simulation. By incrementally reducing energy until ignition leads to blow-off, the optimal energy is found at 50 mJ, corresponding to a deposit Gaussian diameter of 8.0 mm.

Simulation spark properties can be summarized as a single 50 mJ total energy spherical source following a Gaussian profile in time ($\Delta t = 100 \mu\text{s}$) and space ($\Delta x = 8.0 \text{ mm}$). One true benefit of this choice is its robustness such that ignition to anchoring is ensured for all simulation frameworks (Lax Wendroff, TTGC, Comparison of Takeno indices). However there would be multiple ways to improve the physical representativeness of the deposition model in this application. In particular, the position of the igniter in a region where mixing is only starting poses numerical problems as most of the energy is lost inside a non-reactive mixture. In experiments, this non reactive mixture (pure vent gas) can ionize and trigger reactions that are not represented in the numerical chemical scheme. Moreover, in simulation, the heat is mostly dissipated by turbulence before reaching a better mixed region. It partly explains the high value of the deposited energy that was expected to be lower primarily. Refining the ED model to better adapt the large variety of ignition devices is a topic of interest for future iterations of this work.

10.6.2 Selection of a flame index

The configuration at hand presents a turbulent jet with an interaction between the flow and electrodes. The level of turbulence allows partial premixing in the plume, downstream the electrodes, and the presence of a propagating triple flame during the ignition-anchoring phase [138, 229, 194]. For this application, the Dynamically Thickened Flame (DTFLES) model is used. It is presented in Chap. 7 Sec. 7.3.2. Two formulations for a flame index were introduced to distinguish diffusion from premixing (see Chap. 7 Sec. 7.4.3). The first formulation involves the computation of the scalar product of gradients of $Y_F = Y_{H_2} + Y_{CH_4} + Y_{C_2H_4}$ and Y_{O_2} and will be referred to as "*global*". The second one computes three scalar products, one for each species in the batch $\{H_2, CH_4, C_2H_4\}$. For each point in the domain, if at least one of the three scalar product is negative, the index indicates diffusion. The approach is named "*preferential*". Once ignition is triggered, two instants are targeted as critical cases to compare both indices. First of all, similarly to experimental, after a period of anchoring to the electrodes, the flame propagates upstream under the form of a triple flame. Capturing the physics of the flame is essential to predict anchoring and its duration. After anchoring, a steady tubular diffusion flame topped with

a turbulent partially premixed plume is captured. The correct detection of the diffusion flame is also mandatory. To illustrate the behavior of the two indices, they are compared in Fig. 10.6.1 at identical flame states.

Cuts of the flame indices are given and illustrated by the corresponding Heat Release Rate (HRR). Here, and throughout the thesis, due to the use of the Thickened Flame model, the profiles are unbiased by scaling them with the thickening field (F). This choice does not modify the physics of the case and only helps visualization, it is nonetheless motivated in Appendix D, and will be applied consistently for all applications.

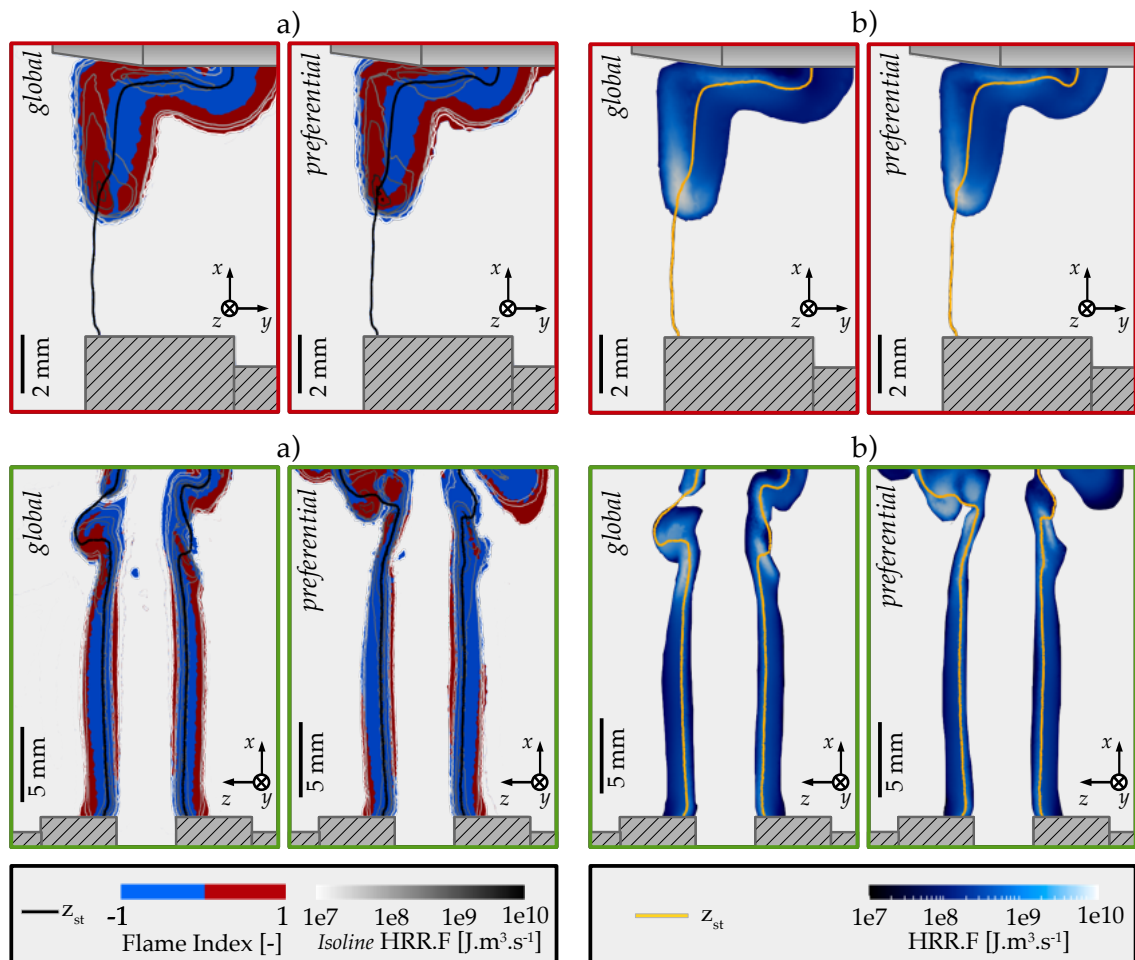


Figure 10.6.1: Comparison of flame indices for the triple flame propagation and the steady diffusion jet: *top a)* z -normal cut of the Flame Index in the triple flame structure ($y > 0$), *top b)* z -normal cut of the corresponding HRR.F field ($y > 0$), and *bottom a)* y -normal cut of the Flame Index in the jet diffusion flame, *top b)* y -normal cut of the corresponding HRR.F field.

Observations are summarized as follows:

1. **Triple flame** (Fig. 10.6.1 *top*): The triple flame is canonically made of a rich premixed branch (inner jet side), a lean premixed branch (outer jet side) and a diffusion flame in-between. The detection of this peculiar structure is achieved by both indices. By construction, the "global" formulation gives overall larger premixed zones in comparison to the "preferential" index. This is assumed to be due to the under-representation of H_2 in the sum Y_F , leading to a different location of the frontier between the rich premixed branch and the diffusion branch (the excess hydrogen diffusing rapidly to form the diffusion front). A side-effect of this difference in detection is the application of thickening, in particular in the region between the rich premixed branch and the diffusion flame. In this crucial area, gases are hot, and if detected as premixed, the thickening tabulation will automatically search for conditions that correspond to a hot rich premixed flame where the laminar flame thickness is the lowest. The corresponding thickening level is detrimental to the structure of the triple flame, artificially broaden and slowed down. Figure 10.6.3 plots the mean thickening level in the domain (masked to focus on regions of combustion) versus the triple flame tip position with respect to the injector lips (see Fig. 10.6.2), confirming this observation. The "preferential" index circumvents the issue by selecting the dot product of H_2 versus O_2 in this region, pushing the limit of the detected diffusion zone closer to the rich-premixed branch reaction zone.
2. **Jet diffusion flame** (Fig. 10.6.1 *bottom*): Once the flame is anchored, the tubular quasi-laminar section is expected to be in diffusion mode. Once again, very low values of Y_{H_2} in the sum Y_F lead to a misinterpretation of the flame as premixed in the outer section, while it corresponds to part of the H_2/O_2 equilibrium occurring further on the oxidizer side (see Chap. 7 Sec. 7.4). It can lead to a triggering of thickening of this section which is unwanted, and avoided with the "preferential" index.

Both definitions suit to detect the main structures of the flames targeted in this application. However, differences in the management of thin frontiers between diffusion and premixing, are biased by the hydrogen content diffusing differently. When used in collaboration with a thickening model, these frontiers are of importance and may impinge on the thinness of the result. Therefore, for the remaining of this work, the "preferential" formulation of the flame index is selected.

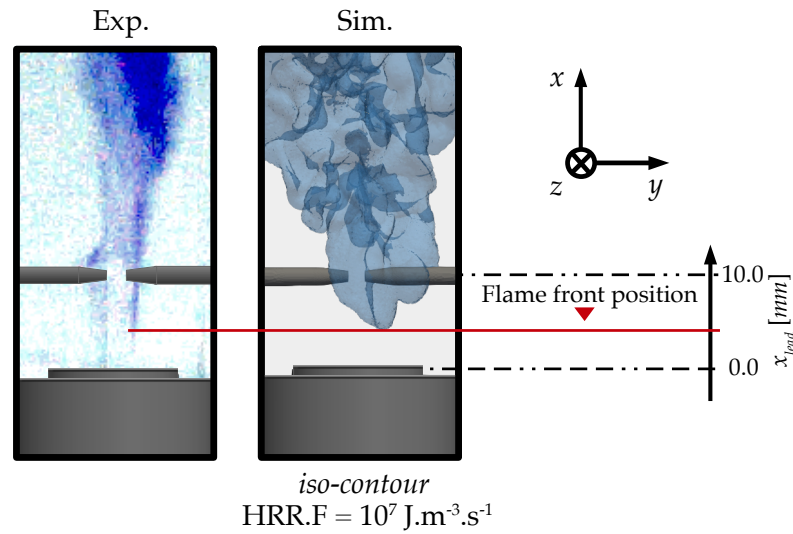


Figure 10.6.2: Flame front tracking to time anchoring.

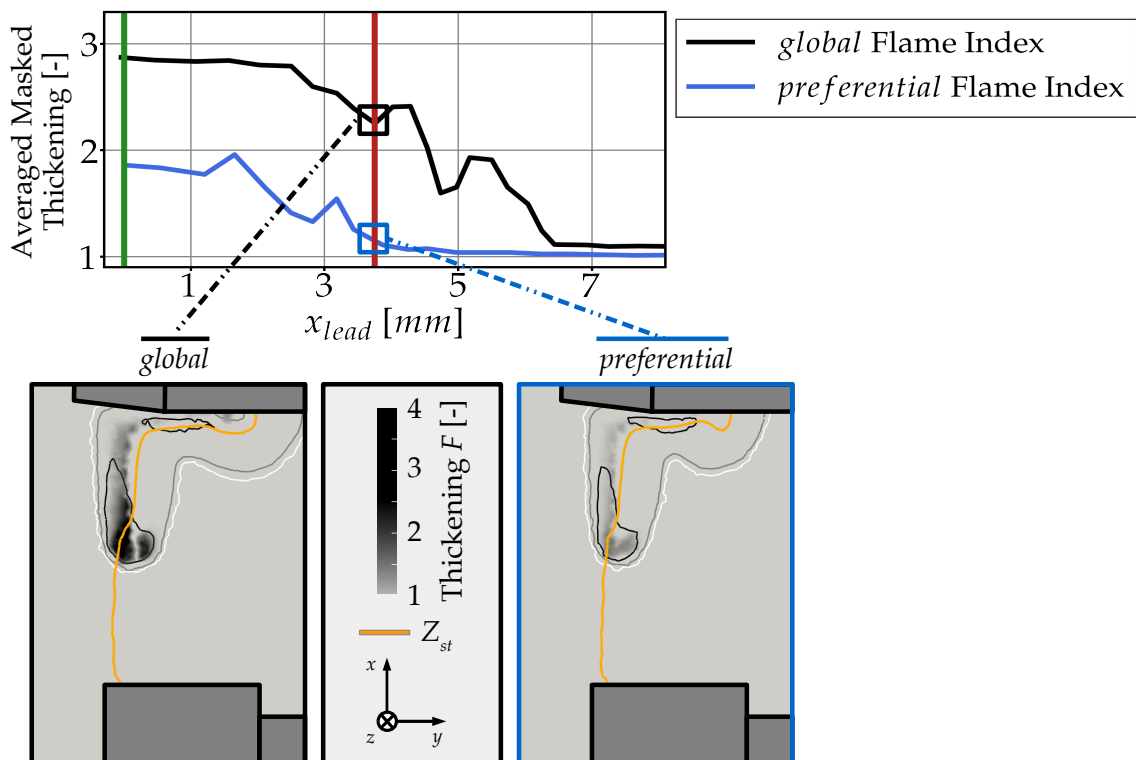


Figure 10.6.3: Evolution of the averaged masked thickening factor in regions of combustion as a function of the position of the triple flame x_{lead} . Addition of z -normal instantaneous cuts of thickening.

10.6.3 Overview of the numerical procedure versus experimental

Now that details of the numerical setup are established, the full ignition-to-anchoring procedure obtained numerically is compared to experimental. Figure 10.6.4 shows the comparison between experimental contrasted photography and longitudinal cuts of the temperature field obtained by LES. The main phases of ignition are highlighted. While the main aspects of the flame shape and structure are qualitatively recovered, more details need to be put to interpret every section and its timing, which is the focus of the next sections. In particular, the timing of the whole procedure is very dependent on the phase of electrode anchoring, explaining the discrepancy between experimental and simulation. It is discussed in Section 10.8. A critical evaluation of the framework follows, and threads to go after are highlighted, for future improvements.

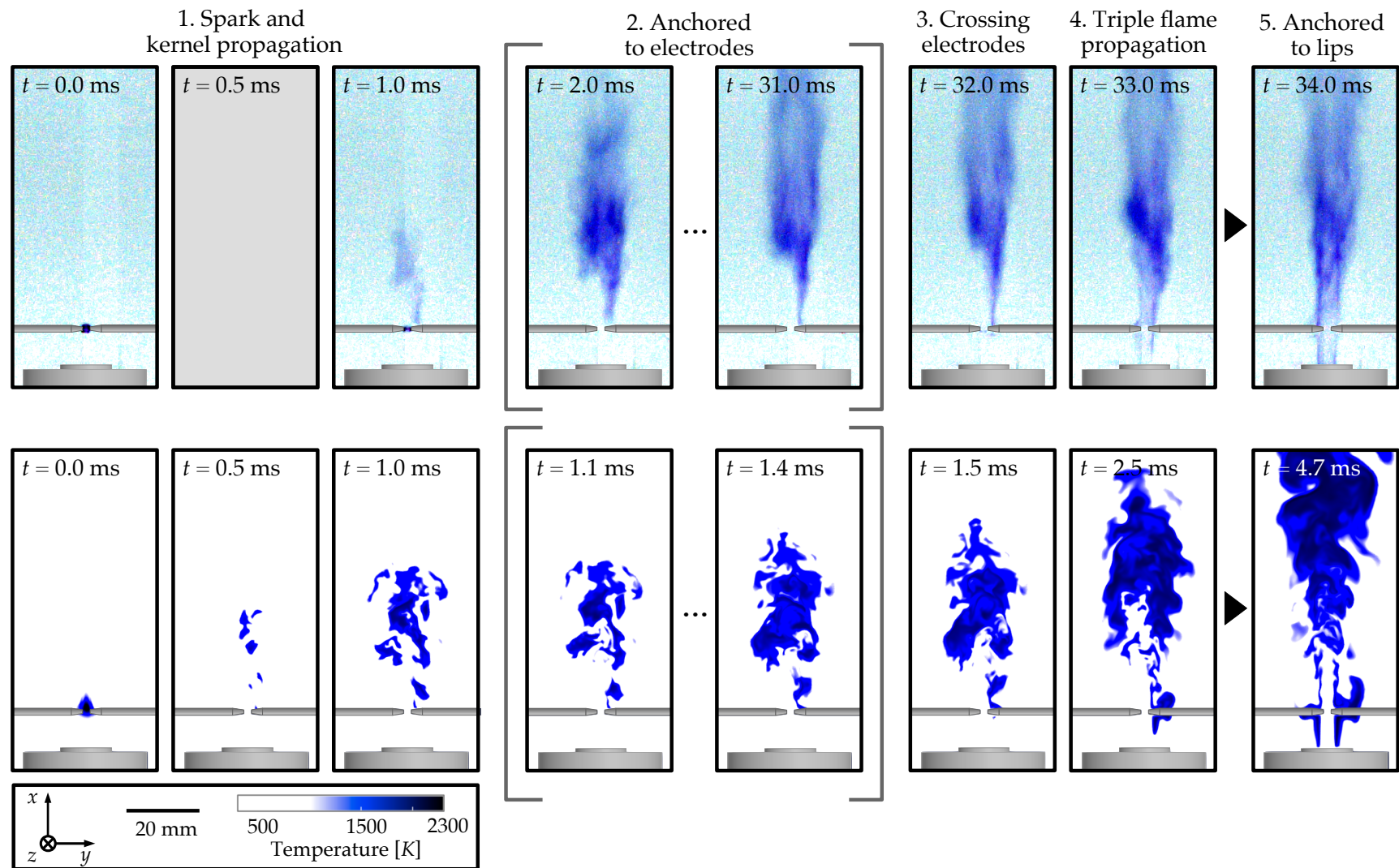


Figure 10.6.4: Experimental versus simulation comparison of the three phases of the ignition-to-anchoring procedure. Experimental visualization corresponds to contrasted photography of the flame, simulation shows z -normal cuts of the temperature field.

10.7 Ignition to electrode anchoring

After ignition, the hot reactive material is rapidly convected downstream due to the high velocity.

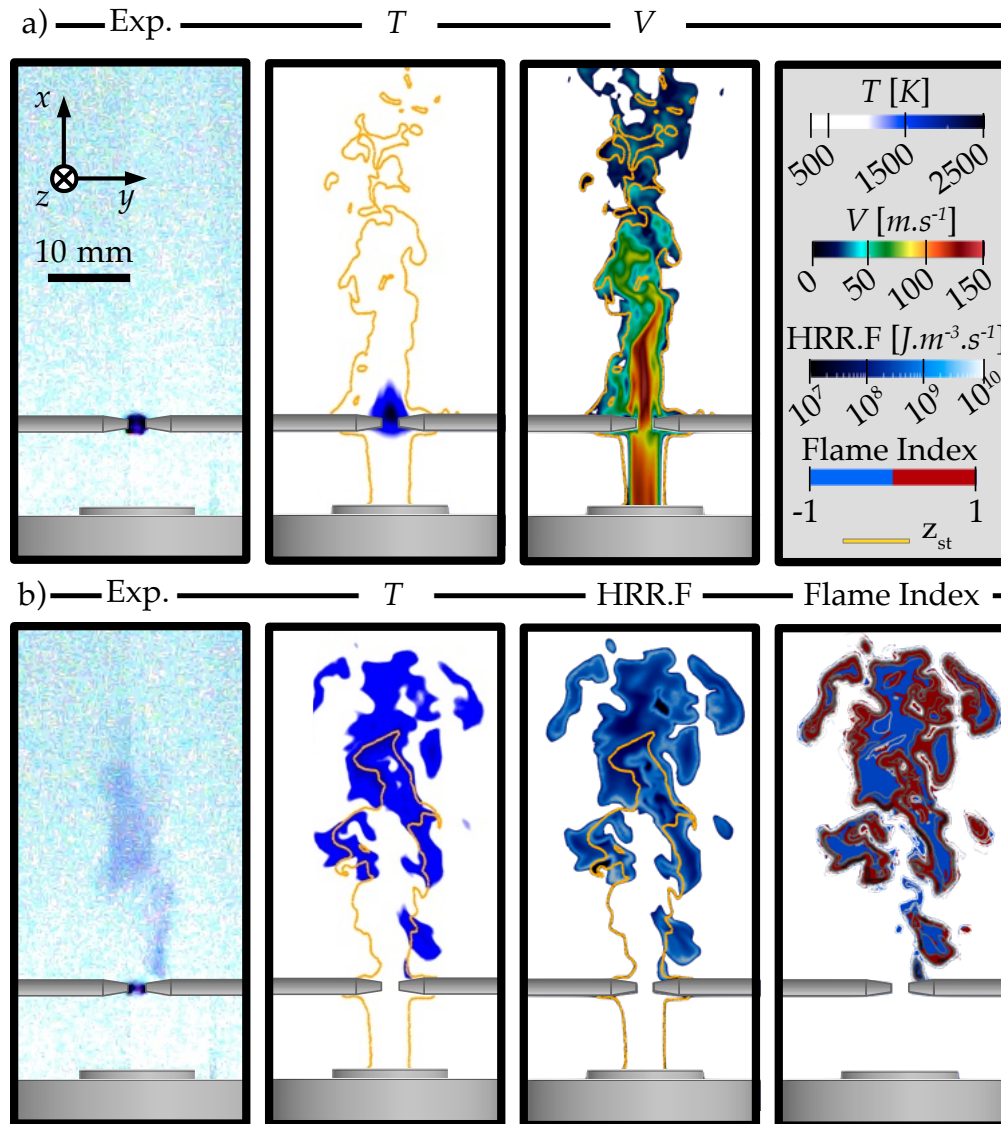


Figure 10.7.1: Comparison of profiles during the flame ignition phase: a) $t = 0.0$ ms: z -normal cuts of temperature (T), and velocity (V), b) $t = 1.0$ ms: z -normal cuts of temperature (T), Heat Release Rate (HRR.F), and Flame Index.

Figure 10.7.1 a) shows that in the inter-electrode space, the blockage is responsible for a localized high velocity region. Knowing that mixing is bad in this zone, a successful ignition becomes a stiff problem. In simulations, the absence of plasma phases makes difficult to properly set a model for ignition. With ED, an ignition energy lower than 50 mJ corresponding to smaller diameters than 8.0 mm invariably leads to blow-off. A sufficient energy must be given to obtain a wide-enough

high temperature kernel that can resist to the velocity and turbulence until reaching $x > 20$ mm. Runaway starts in the plume $x > 30$ mm above the electrode which corresponds to a lower velocity/higher turbulence region (see Sec. 10.5.2), beneficial to the creation of wrinkled premixed flame fronts. At the time of ignition, the slight jet swinging leads to a low velocity pocket above the right electrode, giving the opportunity to a random anchoring on the right electrode, captured with simulation. Although it is also observed experimentally, the side is assumed to be non-predictable knowing that the system is symmetric in this plane. Once the flame is anchored to the electrode, it is only a matter of time to see electrode crossing and triple flame propagation towards the lips. The timing of this section is discussed in the next section.

10.8 Timing of the electrodes crossing

The flame stabilized over the electrodes waits for conditions sufficient to pass the electrodes. Experimentally, this phase lasts 30 ms and giving time for a second sparking with no direct effect on the flame anchoring, while it is largely underestimated by LES at only 0.4 ms for the framework proposed here. Interestingly, the timing of the kernel to early attached flame phase does not drift from the 1-2 ms observed experimentally, and similarly, the electrode-to-injector flame propagation phase is well timed (see Sec. 10.9). It means that flame velocity, and flow velocity cannot be solely responsible for this two orders of magnitude difference. Two main hypotheses are thus formulated to understand why this behavior is observed:

1. In simulations, electrodes are modelled using adiabatic walls based on the fact that their diameter is low (2.0 mm), and their successive sparking during 4.425 s before ignition preheats the tips. However, losses may exist and play the role of a retardant to the flame crossing the electrodes. Without a proper evaluation of losses experimentally, asserting the temperature and corresponding thermal resistance is thorny. The use of coupling to solve the heat equation inside electrode tips may become the solution in such a configuration, and thus help to test this hypothesis. It is a promising way to increase the physical resemblance with experimental. In addition, radiative losses may play a role during the kernel formation, and while the flame propagates from electrodes to injector lips. It adds a second perspective: completing the coupling procedure with a radiative transfer equation solver [226].

2. A more acceptable hypothesis is linked to the operating point in itself. The operating point selected is inherently close to blow-off limits as it is the first spark that successfully leads to ignition during a progressive decrease of mass-flow. Measure uncertainties in unsteady pressure and temperature sensing may be responsible of slight variations of the mass-flow throughout the procedure, decreasing by a small percentage between the spark and the lip anchoring. This hypothesis can be tested easily by evaluating the sensitivity of LES to a small increase in mass-flow. The case at hand corresponds to an inlet mass-flow $\dot{m}^{sim} = 0.31 \text{ g.s}^{-1}$. A second case is set with a 5% increase at $\dot{m}^{sim} = 0.326 \text{ g.s}^{-1}$. Figure 10.8.1 compares the two ignition sequences. A complete blow-off is observed at a 5% higher mass-flow, giving two information. On the one hand, the experimental operating point, during the electrode-anchored flame sequence, may be located in-between the two cases, delaying the electrode to lip anchoring. On the other hand, assuming that this operating point is close to blow-off, LES is capable to contour the frontier of blow-off of such a configuration. It ensures a better applicability to real use-cases such as the one proposed in Chap 11

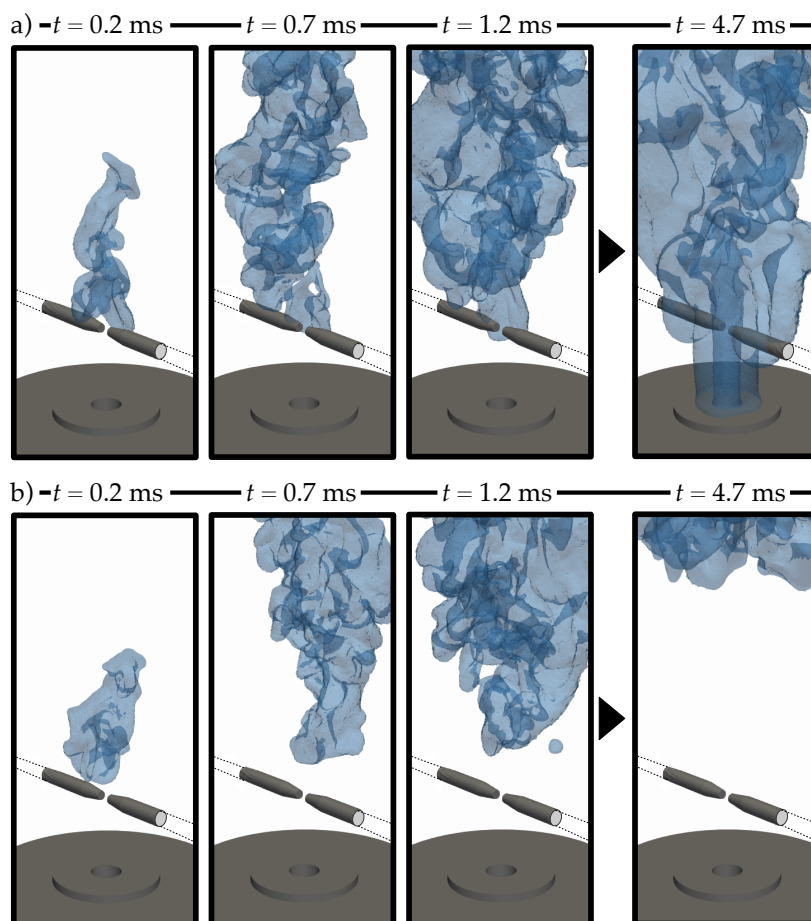


Figure 10.8.1: Effect of mass-flow on the ignition procedure outlined as 3D contour of HRR (iso-level $\text{HRR.F} = 1 \times 10^7 \text{ J.m}^{-3}.\text{s}^{-1}$): a) $\dot{m}^{sim} = 0.31 \text{ g.s}^{-1}$, b) $\dot{m}^{sim} = 0.326 \text{ g.s}^{-1}$.

This section emphasizes one limitation of the selected framework in the timing of the complex electrode-anchored flame. While the operating point definition may be in cause, it opens the path to a future evaluation of a coupled simulation taking into account losses in the electrodes, to fully close the hypothesis. It is important to note that a similar behavior is observed using the higher order scheme TTGC (see Appendix E). Once conditions are suited for the electrode crossing, a triple flame forms and propagates towards the lips, which is a key phenomenon to cover in order to predict flame anchoring or blow-off in other applications.

10.9 Electrode to lip anchoring

For this key sequence, two sections are proposed. The first one presents LES versus experimental and compares timing and flame positions, validating the framework for this triple flame configuration. The second is focused on the use of a model to predict anchoring probability and timing using cold flow simulation only, showing its potential to obtain preliminary information on a case without going to full combustion simulation.

10.9.1 Experimental versus simulation

The structure of the triple flame has been observed experimentally in presence of gradients of mixture fraction [63, 138], where diffusion jet flames are special cases. A triple flame controls the jet flame lifted stabilization [5] and define anchoring processes if conditions are met [176]. Their reproduction using DTFLES becomes a crucial test-case for simulation setups [148].

Starting from the electrode, and from a 2D-cut perspective, the three branches form. Once formed, the structure propagates downstream following the stoichiometric line, depending on local axial velocity conditions. A cut of the flame showing the leading point is given in Fig. 10.9.1 b). At the time where the leading point of the flame touches the lips, the second half of the flame rapidly catches up, which is concluded by the formation of the tubular diffusion flame (see Fig. 10.9.2).

To better follow the timing of this phase, the flame leading point is tracked (see Fig 10.6.2). The time of anchoring is set to the time at which the flame touches the lip of the injector. In Fig. 10.9.3, the position of the flame front with respect to the lip is reported. Available experimental points are added. Knowing that a certain uncertainty exists to determine precisely the exact time of electrode crossing⁵, the agreement with simulation is acceptable. Simulation returns correctly

⁵The 1 kHz frame rate limits the observation of such a rapid event, making exact timing difficult, in comparison to simulation.

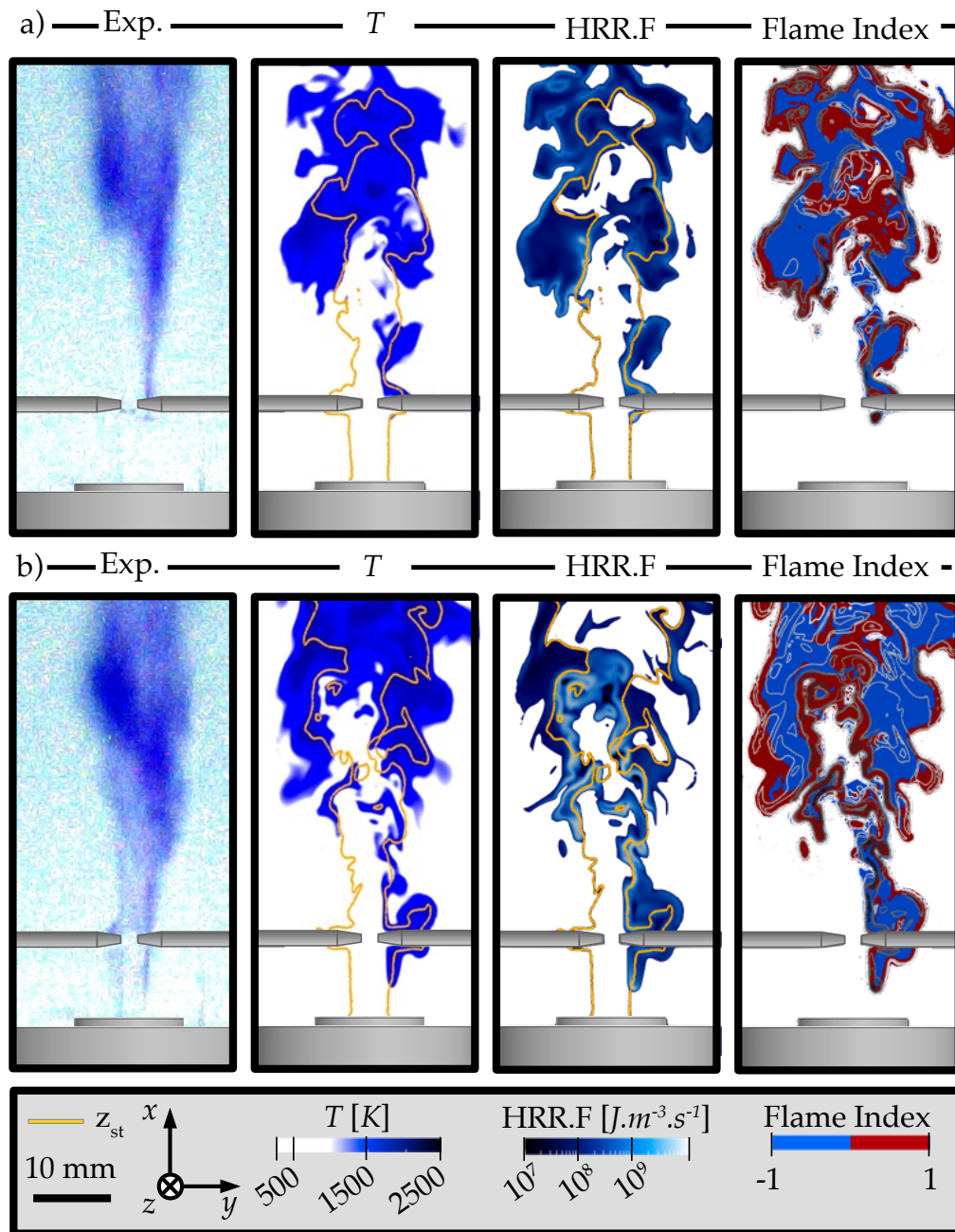


Figure 10.9.1: Triple flame propagation as z -normal cuts of temperature (T), HRR (HRR.F) and flame index: a) Instant of flame crossing t_{cross} , b) Propagating flame $t_{cross} + 1$ ms.

ignition timing and flame displacement, reassuring on its capability to reproduce the phenomenon in this special configuration, dedicated to hot Li-ion vent gases, and preparing an application to setups closer to Li-ion manufacturer concerns.

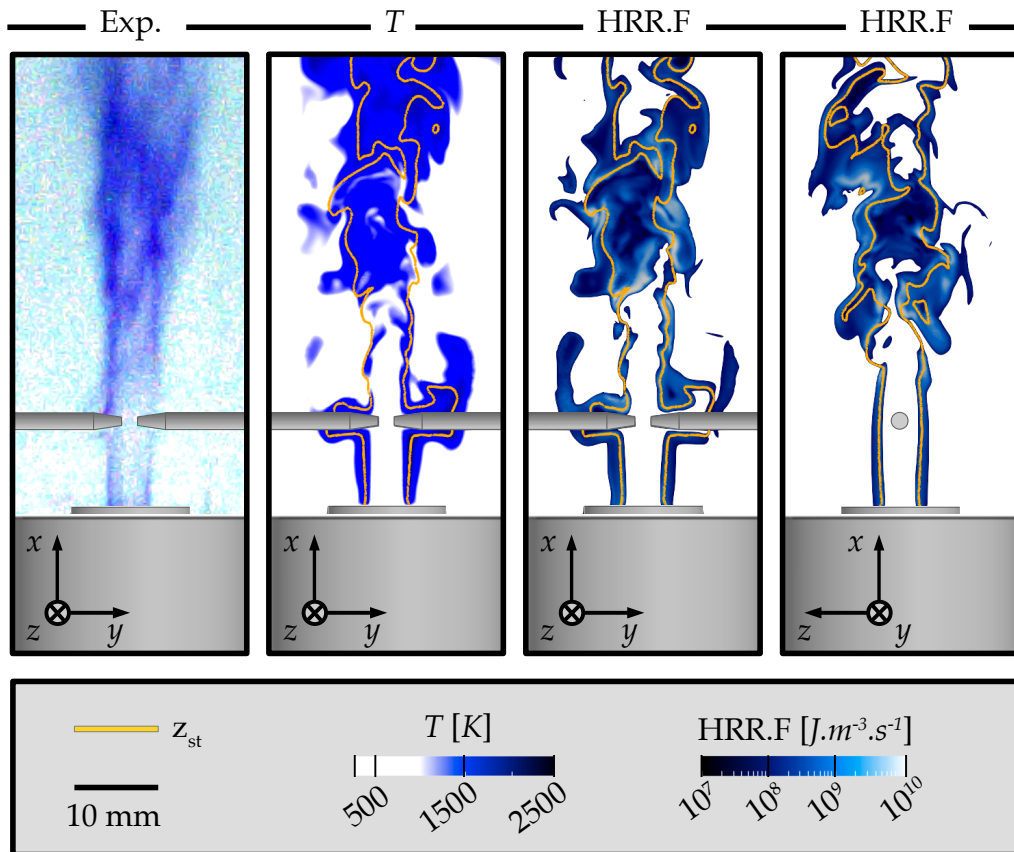


Figure 10.9.2: Anchored flame as z -normal cuts of temperature (T), HRR (HRR.F) and flame index, completed by the y -normal cut of HRR.

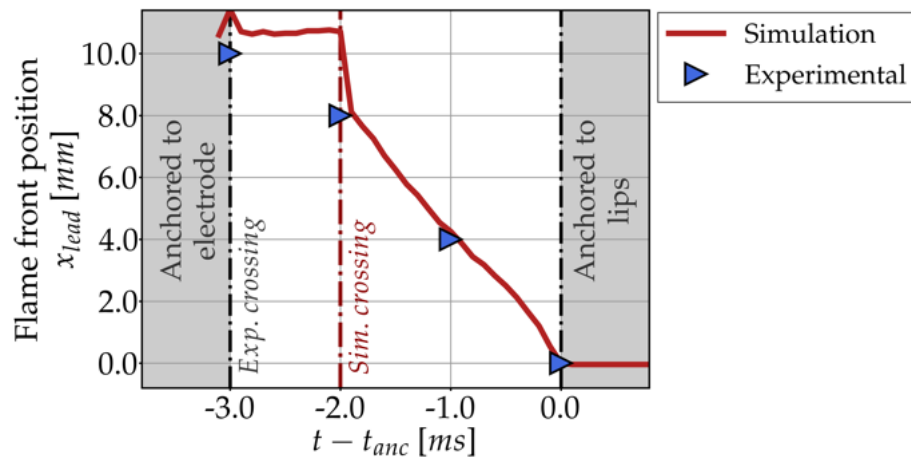


Figure 10.9.3: Flame front position with respect to the lips during the anchoring phase.

10.9.2 Reduced Modelling

Based on the work of Marragou *et al.* [176], the application of the Triple Flame Upstream Propagation (TFUP) criterion is proposed to evaluate anchoring probability and delay on cold flow simulations. The method uses scaling laws from Ruetsch *et*

al. [229] that estimate the triple flame propagation speed s_{tf} as:

$$s_{tf} = \sqrt{\frac{\rho_u}{\rho_b}} s_L^0 \quad (10.2)$$

where s_L^0 is the planar laminar flame speed at stoichiometry, ρ_u (resp. ρ_b) is the corresponding unburnt gas density (resp. burnt). The cold flow simulations performed to initialize the ignition sequence (see Sec. 10.5.2) is taken and for one frame of the z -normal cut of the domain, a focus is done on the $y > 0$ semi-plane, between the right electrode and the lips ($x \in [0.0, 8.0]$ mm). The temperature and velocity fields are taken and interpolated along the stoichiometric isoline (see Fig. 10.9.4). For every interpolation point of the line, s_{tf} is computed with Cantera [99], the ARC kinetic scheme (see Chap. 6), and using the local temperature. The difference in velocity $\Delta V_{TFUP} = s_{tf} - u$ where u is the axial velocity at the interpolation point is eventually kept. The TFUP model, guarantees propagation when $\Delta V > 0$ so that for one frame, a proportion of points agreeing with TFUP can be extracted $p_{TFUP} (\in [0, 1])$, along with the average value of ΔV_{TFUP} and the length L_{st} of the stoichiometric line. The procedure is repeated for 20 cold flow simulation frames to better converge the statistics and obtain an average timing $\overline{\Delta t_{TFUP}} = \overline{L_{st}} / \overline{\Delta V_{TFUP}}$ and average anchoring probability $\overline{p_{TFUP}}$.

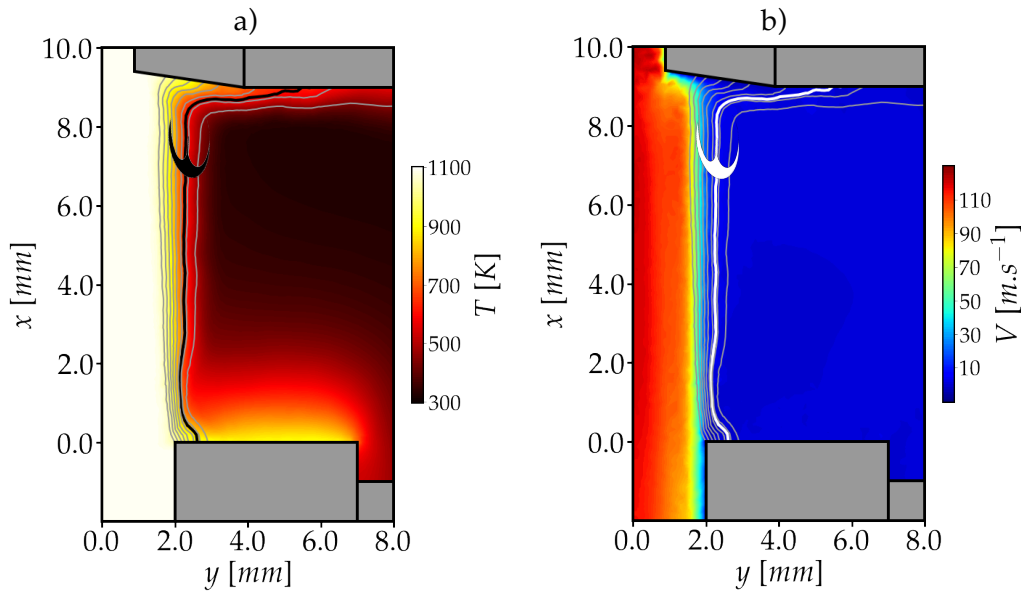


Figure 10.9.4: Temperature and velocity fields for one frame of cold flow used in the TFUP model.

For the operating point considered in this study $\overline{p_{TFUP}} = 0.81$ with a standard deviation of 0.10, predicting confidently anchoring. The anchoring time reads $\overline{\Delta t_{TFUP}} = 3.28$ ms ($\sigma_{\overline{\Delta t_{TFUP}}} = 0.9$ ms) which also agrees with timescales found experimentally and with simulation (see Fig. 10.9.3). For the higher mass-flow case presented in Fig. 10.8.1, a lower anchoring probability $\overline{p_{TFUP}} = 0.62$ coupled with a

higher anchoring time $\overline{\Delta t_{\text{TFUP}}} = 4.58$ ms is coherent with the fact that blow-off is observed with simulation, and that no ignition is observed experimentally for ignition attempts before the one selected here, inherently at higher mass-flow. Table 10.9.1 summarizes the results.

Table 10.9.1: Application of the TFUP model on the operating point considered for ignition simulation.

mass-flow \dot{m}^{sim} [g.s ⁻¹]	$\overline{p_{\text{TFUP}}}$	$\sigma_{\overline{p_{\text{TFUP}}}}$	$\overline{\Delta t_{\text{TFUP}}}$ [ms]	$\sigma_{\overline{\Delta t_{\text{TFUP}}}}$ [ms]
0.310	0.81	0.12	3.28	0.48
0.326	0.62	0.10	4.58	0.91

Such a reduced model, when fueled with multiple cases can help to predict the anchoring of an operating point at minimal cost. It may be adapted to other cases, by taking care to project the velocity along the stoichiometric line when the jet is not entirely vertical such as the one presented in this study.

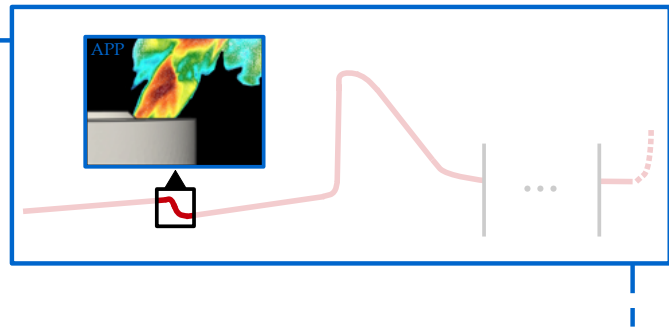
10.10 Conclusion on jet flame ignition simulations

The simulation framework setup proposed here gives the opportunity to perform ignition procedures of the BTR setup at Li-ion TR-relevant conditions. A cold flow simulation is first used to compare the performance of two numerical schemes in terms of turbulence rendering. The phases of ignition are then presented and reproduced using LES. In particular, the triple flame propagation and its timing is confidently retrieved, opening the path for an application to a realistic case in Chap. 11. A reduced model helps to predict flame anchoring using cold flow simulations only, which may be of use for pre-dimensionning studies. In the following part, the link between experimental and applications is made by approaching the behavior of failing 18650 cells in realistic conditions.

Part IV

Simulations of failing 18650 cells

Chapter 11



Cell opening and initial venting

Contents

11.1 Cell opening experiments and CFD simulations	170
11.2 Case definition	170
11.2.1 Structure presentation	170
11.2.2 Opening conditions	172
11.2.3 Numerical setup	174
11.3 Simulation of the opening	175
11.4 Effect of confinement on the flow topology	179
11.4.1 Outline of the case	179
11.4.2 Comparison of the venting behavior	180
11.5 Conclusion on cell opening simulation	182

Following the validation versus experimental of models and strategies to simulate opening (Chap. 9) and venting (Chap. 10) during thermal runaway, applications to realistic cases are proposed. To start with, the opening phase of a pressured cell is targeted¹. In the following sections, a generic case representative of a 18650 cell is presented and vent opening conditions are reproduced. Effects of cell confinement modification on the course of events complete the study.

¹See Chap. 7 Sec. 7.5 for the complete list of scenarios in the timeline of TR.

11.1 Cell opening experiments and CFD simulations

The cell opening procedure initializes the venting and guarantees a controlled over-pressure evacuation, avoiding the shredding of the casing. Direct visualization of the phenomenon are rare due to its timescale. However several experimental studies help to better encompass the operating conditions at opening [151, 79, 96, 97]. Especially, the works of Mier *et al.* [11] and Li *et al.* [160, 159] measured vent disk opening pressures for several 18650 cells. The study of Li *et al.* [161] also proposed a first CFD simulation of the steady venting of a cell at opening conditions, showing the feasibility and interest in producing such results at designing steps. With this in mind, the next sections propose the simulation of the emptying procedure of a cell starting from cell opening conditions (high pressure - high temperature), allowing to see effects of design on this event.

11.2 Case definition

11.2.1 Structure presentation

Once gas production has reached an exponential phase, the pressure inside the airtight cell housing increases rapidly. Venting is triggered by the breaking of the weakest point in the cell. For prismatic cells, corners are inherently weak and crack. For cylindrical cells, and especially small sized ones such as 18650, a weak point must be added to control the cell opening at lower pressures than the one given by the structure. Pre-constrained venting disks are generally chosen [79]. The opening suddenly puts in contact hot pressured vent gases with the atmosphere creating propagating shocks, followed by an under-expanded jet. The topology of this peculiar flow is asserted in the next sections by reproducing this sudden opening given a generic design of 18650 cell. This design is built to reproduce and simplify the main flow restrictions observed experimentally when dismantling cells or by tomography [80, 79, 144, 160, 188, 161, 159]. Figure 11.2.1 a) gives the external view of the five holes cell. To save computational time, the natural axi-periodicity of the case is used, dividing by five the number of cells composing the mesh (see Fig. 11.2.1 b-c)). This assumes that internal obstacles are also axi-periodic, which is not necessarily true for all designs. To avoid dealing with complex interfaces between periodic planes, a cylindrical cut of radius 0.4mm is added (see Fig. 11.2.1 d)) making the case a sector of an annulus with an angle of 72°. More details on the obstacles modeled is given in Fig. 11.2.2, where the most important devices of a cell are represented: the vent disk, the current collector, the mandrel (to vent gases from the bottom) surrounded by the jelly roll. In Fig. 11.2.2 a) the cell is in its closed

configuration, while in Fig. 11.2.2 b) the cell is opened which is the case considered for simulation.

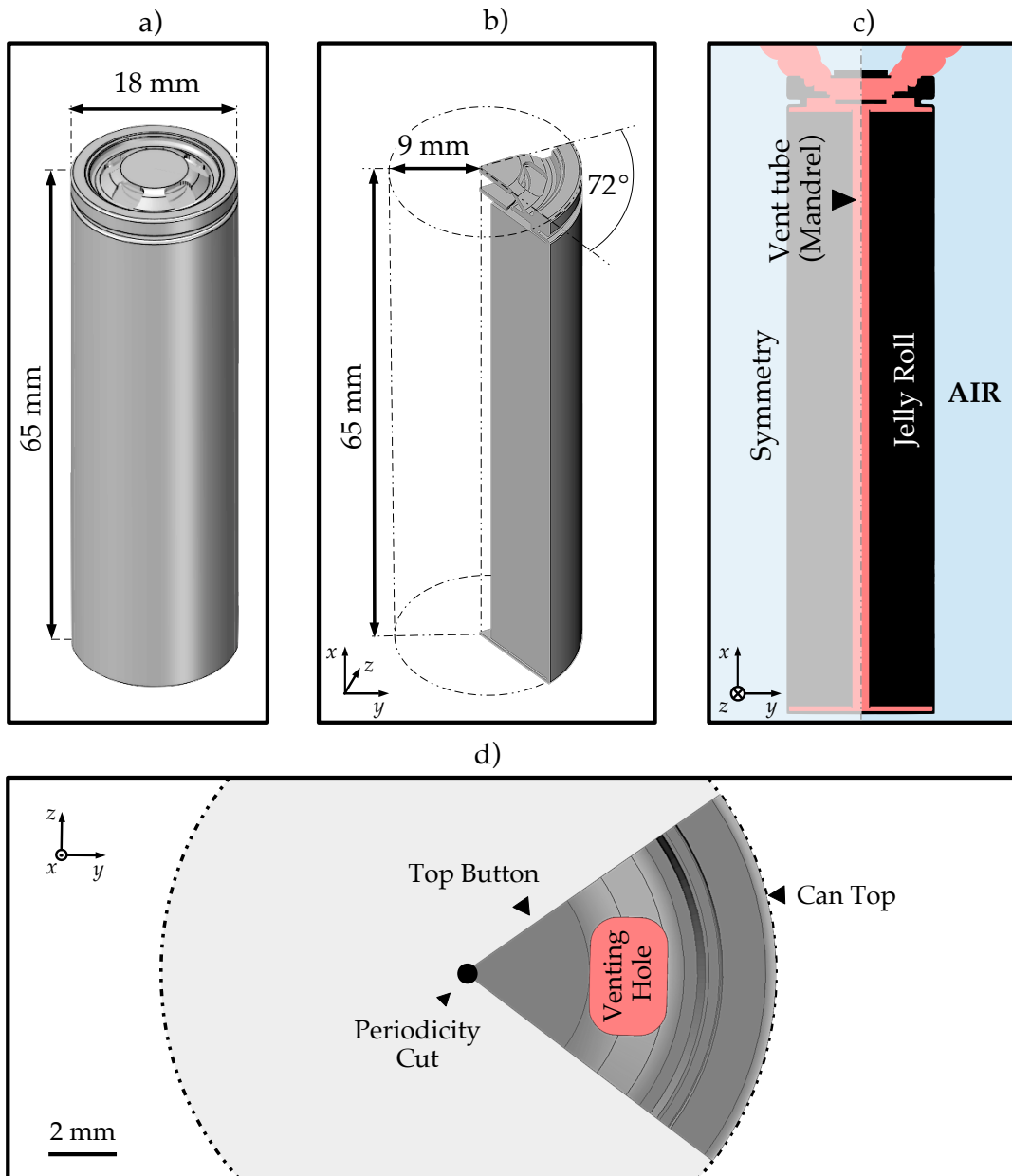


Figure 11.2.1: View of the structure of the 18650 cell targeted for high pressure venting: a) General view of the cell, b) Axi-symmetric section of the cell used to save computational time, c) z-normal cut of the cell, d) View of the section of the top cap.

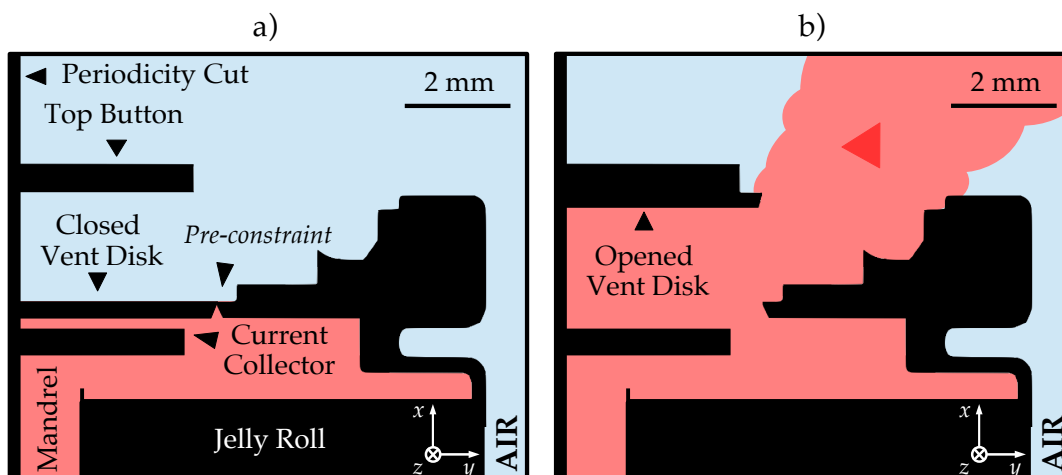


Figure 11.2.2: Cut view of the obstacles inside the 18650 cell: a) closed configuration, b) opened configuration.

11.2.2 Opening conditions

The key parameters to define at opening are the pressure and temperature conditions inside the cell when opening, along with the gaseous mixture composition. Thus, six elements are essential to obtain:

1. X_{vent} : Vent gas composition
2. X_{atm} : Atmosphere composition
3. P_{vent} : Pressure inside the cell at opening
4. P_{atm} : Pressure of the atmosphere
5. T_{vent} : Temperature of the gases inside the cell at opening
6. T_{atm} : Temperature of the atmosphere

In the following sections, the reference experiment is the one of Golubkov *et al.* [96]. In particular, they conducted an overheat-to-TR experiment on a commercial NMC cell by increasing the atmosphere temperature until complete TR. The gaseous mixture is already cited in Chap. 6 Tab. 6.3.1 as NMC1 [96], which gives X_{vent} : H_2 : 30.8 %, CH_4 : 6.8 %, C_2H_4 : 8.2 %, CO : 13.0 %, CO_2 : 41.2 %. The tested NMC cells opened at casing temperatures of approximately 400 K. At this step, the casing temperature is at the equilibrium with the atmosphere temperature giving $T_{atm} = 400$ K. The composition of the atmosphere is chosen to be air at $P_{atm} = 1$ atm to see if auto-ignition reactions could occur with the vent gases.

Asserting the internal P_{vent}, T_{vent} conditions is more complex as no invasive measurement are generally available inside the cell. For P_{vent} , Mier *et al.* obtained experimentally the breaking pressure for commercial 18650 cells. The average along all references is $P_{vent} = 20.03$ bar. The internal temperature is finally selected by choosing the temperature reached during the climax in [96], thus assuming that the products of decomposition are obtained at a constant high temperature of $T_{vent} = 1000$ K. This temperature creates a most critical case for both the physical phenomenon at hand (faster shocks, higher temperature, potential auto-ignition, ...) and the numerical problem to solve (higher sound-speed meaning lower time-stepping, thinner turbulence, ...).

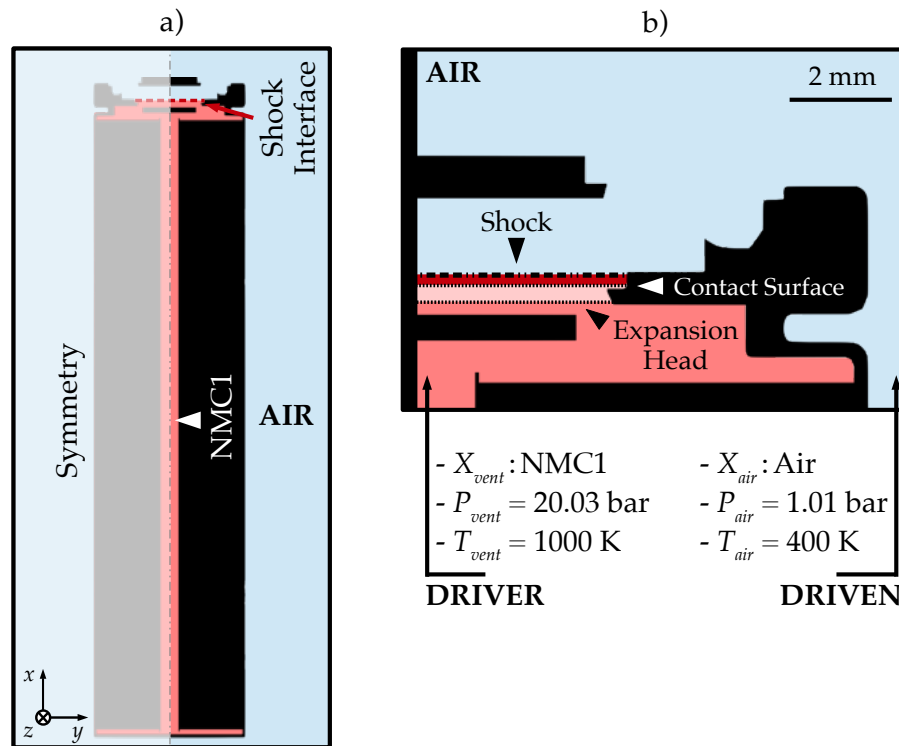


Figure 11.2.3: Initialization step: a) state of the cell, b) zoom on the interface between the vent gases and the atmosphere.

Figure 11.2.3 a) summarizes the state of the cell at the initial frame. Dealing with the interface between the hot pressured gases and the atmosphere is the next issue. In the most realistic scenario, the vent disk cracks open and is pushed against the top cap. Numerically, it could be treated as a moving part in the domain, driven by a velocity law in time to determine. As this may be costly, and in view of the stiffness of the flow structures that will be created around the slowly opening disk, a simplifying hypothesis is preferred. The strong similarity between this problem and a classically studied shock-tube helps to consider that the mass and inertia of the vent disk is negligible regarding the pressure forces applied, and thus that the displacement of the disk is identical to the one of a moving shock. The problem is reduced to a static structure where the disk is already pushed against the top cap, and the interface between the vent gases and the atmosphere is then modelled by

the theoretical solution of a shock between a driver gas (vent gases) and a driven gas (air). The cell is thus treated as a shock-tube, comparably to the case presented in Chap. 7 Sec. 7.2 (see Fig. 11.2.3 b)).

11.2.3 Numerical setup

Figure 11.2.4 outlines the structure of the case and the corresponding mesh. Due to the number of details necessary to capture adequately the behavior of a realistic cell when suddenly opened, the mesh selected is constrained to be refined close to the obstacles, reaching $50\ \mu\text{m}$ close to walls in the upper part of the cell. Inside the jet, $70\ \mu\text{m}$ are prescribed to ensure a fine resolution of the moving shock. Lower in the cell (mandrel to the bottom) coarser meshing is allowed. In the section where the moving shock profile is initialized, $50\ \mu\text{m}$ are set. The mesh sums up to 17.8 M tetrahedra. For the boundary conditions, the outlet relaxes towards the atmospheric pressure using NSCBC [260, 214, 198]. The periodic surface pair and cut allows to treat this case as a sector. Considering the shortness of the event to observe (of the order of 0.1-1 ms), and because combustion (auto-ignition) is improbable, the heat transfers inside the cell are assumed to be negligible and adiabatic no-slip boundary conditions are selected in the upper part of the cell, and adiabatic law of the wall for the lower part of the cell where the mesh is coarser. The outer surfaces of the cell follow the same rule. Adiabatic no-slip conditions are selected for the refined top cap region, and adiabatic wall law for the lower part of the casing. For this study, where the objective is the cell emptying specifications, no inlet is added to sustain the venting.

The numerical scheme is from Lax Wendroff [152] along with WALE as the subgrid scale model [199]. Turbulent Prandtl and Schmidt numbers are both equal to 0.6 with a global CFL number of 0.7 and a Fourier number of 0.1. The shock handling method preferred in this case is LAD² to treat the propagating shock expected. It is completed by second and fourth order artificial viscosity terms added to stabilize the computation [125]. To scan for eventual auto-ignition events due to shock impinging at walls, creating a local sharp increase in temperature, the simulation is made reactive using the scheme developed in Chap. 6 also tested for auto-ignition delays.

²See Chap. 4 Sec. 4.2.3, Chap. 7 Sec. 7.2 for its application in 1D, and Chap. 9 for the application in 3D.

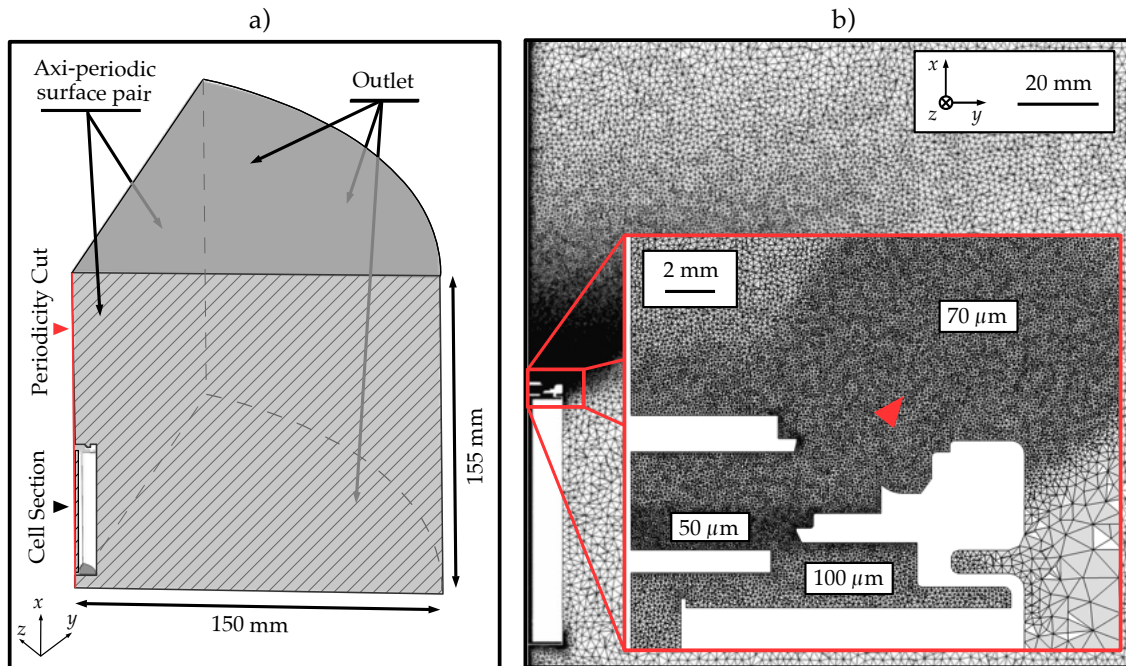


Figure 11.2.4: View of the computational domain: a) description of main boundary conditions, b) z -normal cut of the mesh.

11.3 Simulation of the opening

Figure 11.3.1 describes the process of shock propagation and under-expanded jet formation. Initially the shock creates a piston effect by impinging gases on the vent disk at the top cap. Once the shock has hit the top cap, part of it is reflected, the rest is ejected through the vent hole. At $t = 5 \mu\text{s}$, a shock wave of spherical form spreads. The peak Mach number equal to 3.04 is reached at $t = 15 \mu\text{s}$ and a larger pocket of supersonic flow starts to drive the formation of an under-expanded jet. The pressure inside the cell begins to decrease and modifies the jet shape. Asymmetric diamond shocks are formed at $t = 50 \mu\text{s}$. The shape is a consequence of the asymmetry of the venting hole. In fact, the hole is close to a rectangular shape, but its symmetry is broken by a partial clogging from the vent disk pushed against the top cap. The diamond shocks profiles are rapidly devolved towards subsonic, due to the rapid change in driving pressure. Here, after $200 \mu\text{s}$ (characteristic time inherent to the cell design and initial pressure/temperature conditions), the under-expanded jet leaves room for a turbulent subsonic jet. The natural direction of venting is retrieved with an angle to the vertical x -axis of 47° . In comparison, the supersonic jet forming at $t = 50 \mu\text{s}$, driven by an expansion that deviates the flow, depicts an approximate angle of 32° to the vertical x -axis. In their work, Li *et al.* [161] obtained the Detached Eddy Simulation of a cell steadily venting cold air with a pressure ratio of 23.7 between the cell internal pressure and the atmosphere. The flow features a similar under-expanded jet corresponding to the frame at $t = 50 \mu\text{s}$ which is reassuring.

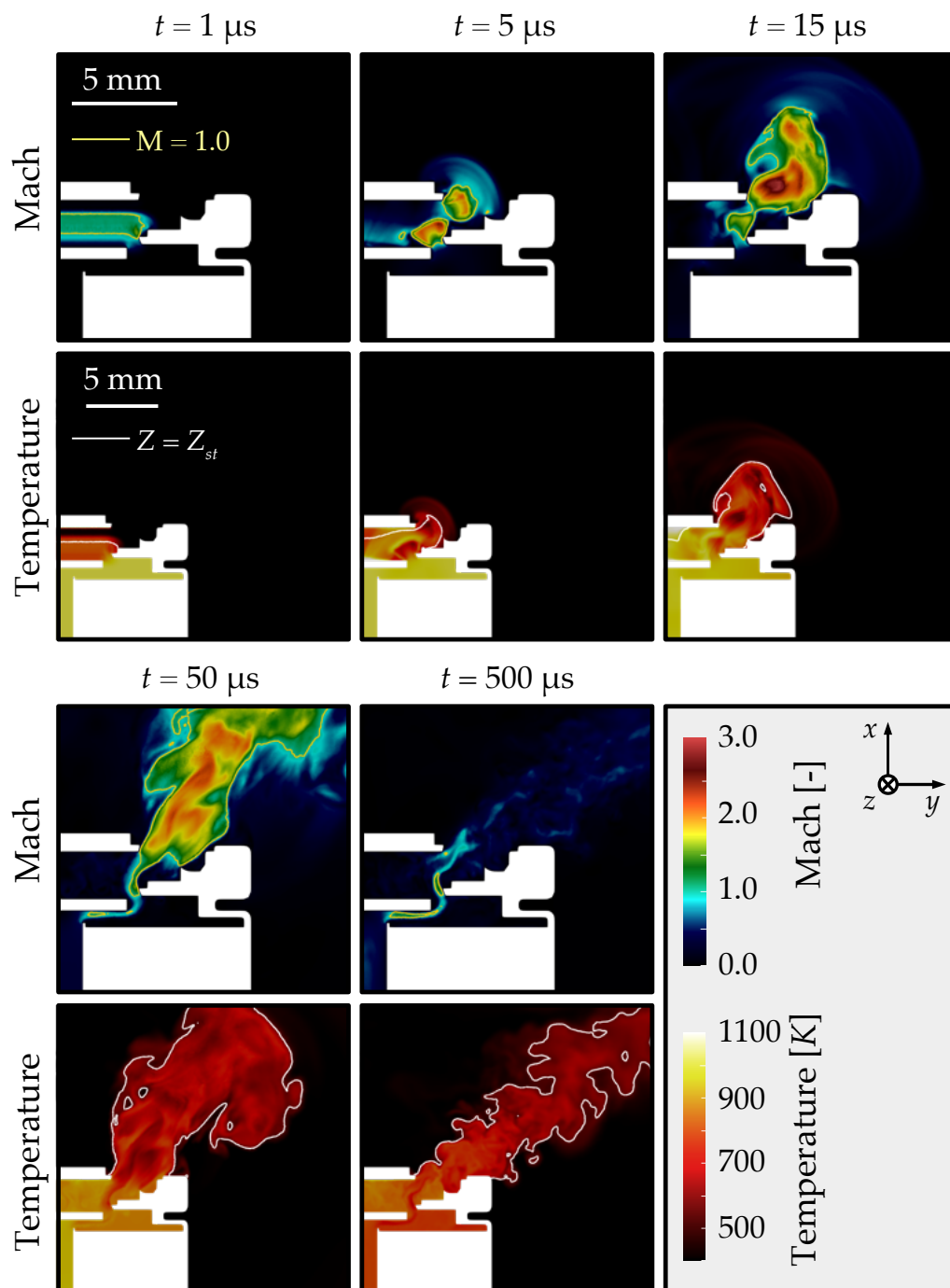


Figure 11.3.1: Course of events following the opening: Mach and temperature profiles at $t = 1 \mu\text{s}$, $5 \mu\text{s}$, $15 \mu\text{s}$, $50 \mu\text{s}$, $500 \mu\text{s}$ after opening.

Figure 11.3.2 gives more details on the early propagation of the shock inside the cell, under the top cap using numerical Schlieren³. At $t = 1 \mu\text{s}$, the initially flat

³Schlieren visualization is numerically approximated by computing $\frac{1}{\rho} \|\nabla \rho\|$. The field is normalized by its maximum throughout the entire volume and timeline. Similarly to experimental, contrast is enhanced to locate properly key density gradients. See Chap. 9 for more details.

moving shock bends to fit the shape of the step it passes. It impinges on the wall at $t = 2 \mu\text{s}$ where, thanks to the presence of a vent, part of the shock continues outside the cell. The rest is reflected and propagates downstream. This reflected wave meets a second compression wave creating a shrinking squared shape structure (annular in 3D). During this phase of shock reflections, the pressure under the vent cap oscillates with a large positive impulse detrimental to the structure, potentially explaining the fact that cells may shatter [79] when opening at high temperature with a weakened metal.

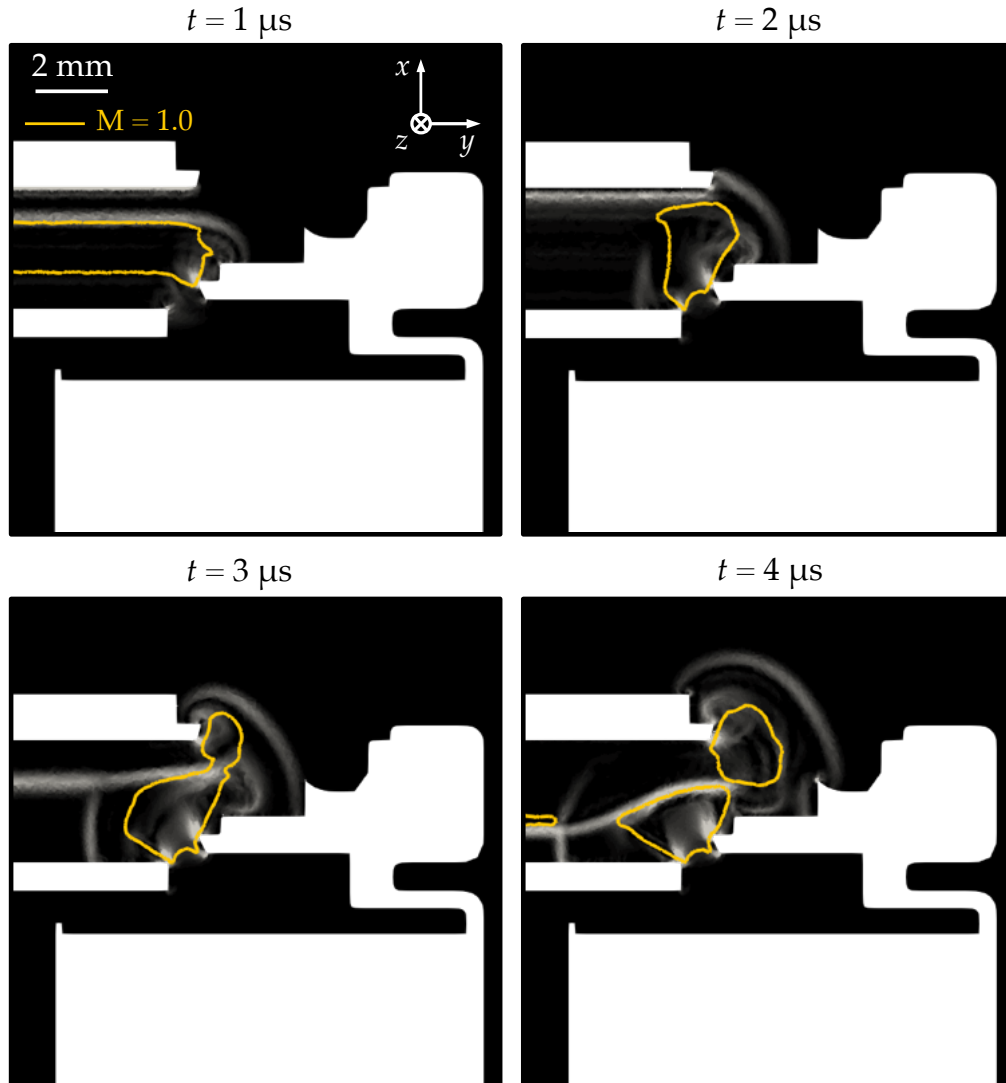


Figure 11.3.2: Propagation of the shocks under the top cap: Numerical Schlieren at $t = 1 \mu\text{s}$, $2 \mu\text{s}$, $3 \mu\text{s}$, $4 \mu\text{s}$ after opening.

The general behaviour of the cell when emptied can be further described by the characteristic temperature and pressure profiles at different probe locations (see Fig. 11.3.3). The pressure and temperature at key points inside the cell allow to assert the duration of the event, the effect of the sudden expansion on internal temperature, and evaluate choking pressures inside the cell. For the cell design and

operating conditions considered in this section, three main phases are identified. The first $50\ \mu\text{s}$ see the propagation of shocks inside the vent device, followed by the formation of the under expanded jet. This phase is critical and, as mentioned earlier, the probe located under the top cap sees a sudden peak of pressure that could lead to the destruction of this thin metal piece. After this phase, choked conditions are maintained between $t = 50\ \mu\text{s}$ and $t = 200\ \mu\text{s}$. Inside the vent device, a constant pressure of 2.9 bar fuels the jet. The progressive decrease in pressure after $t = 200\ \mu\text{s}$ defuses the choked flow, and the jet establishes at subsonic conditions. Still, $\text{Mach} > 1.0$ can be reached inside the cell at the strongest flow restrictions. The entire event lasts less than 1 ms from the opening to a pressure inferior to 2 bar at the bottom of the cell. The sudden decrease in temperature thanks to expansion helps to reduce cell reactivity and is observed experimentally when measuring casing temperature [96].

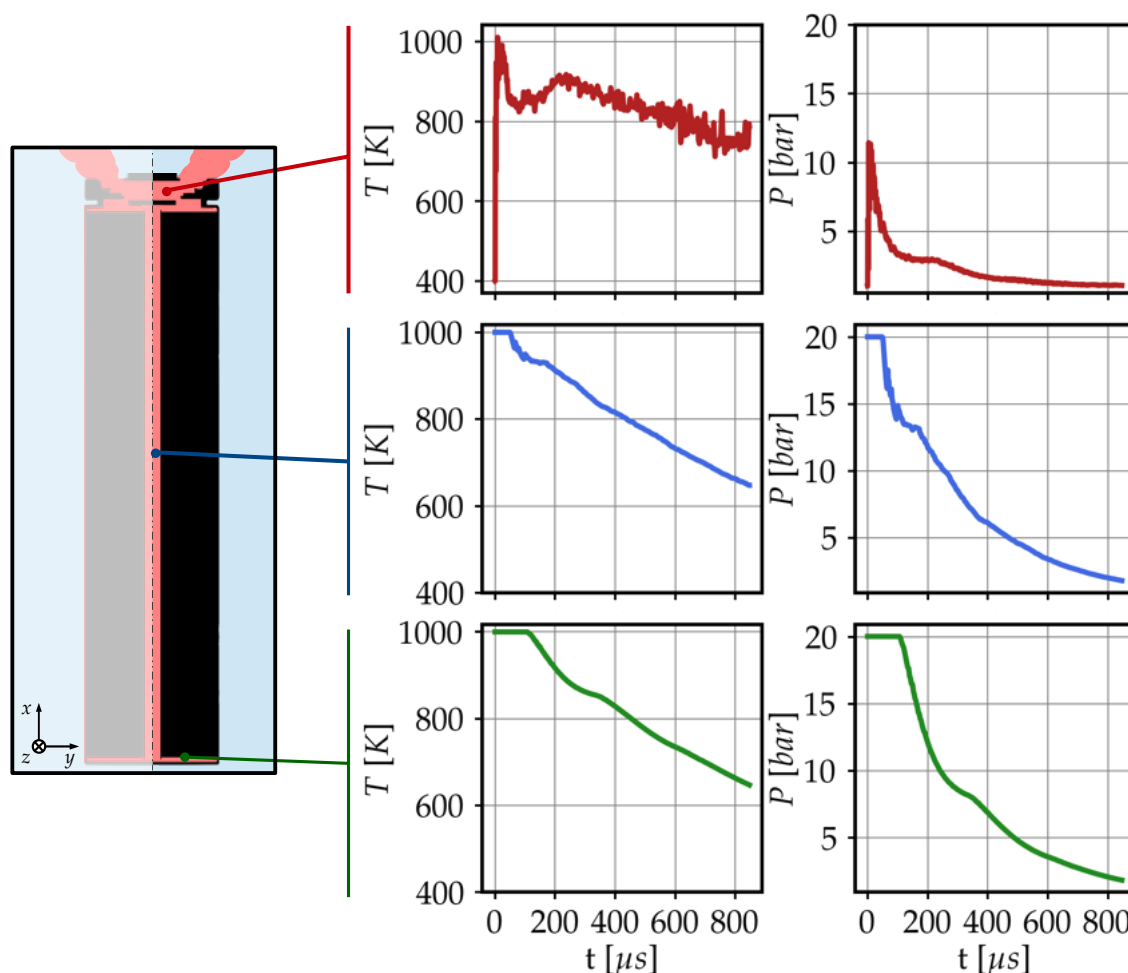


Figure 11.3.3: Temperature (T) and pressure (P) measurements at probe locations inside the cell. From top to bottom, locations are the vent device, the mandrel and the lower dead volume (see left schematic).

Eventually, throughout the entire event, no auto-ignition was detected. For this configuration and conditions, temperature and mixing never coincide so that. When the shock impinges on the top cap, a small pocket of mixture is submitted to hot temperatures and a stationary flow. However, the temperature reached never exceeds 1100 K and due to the strong flow rapidly created by the expansion through the vent hole, the reacting material is rapidly blown-away. Later, the strong expansion always reduce the temperature to reach values under the auto-ignition temperature inside the jet. Overall, the high mass-flow encountered in all phases of the opening event reduces the residence time to values that do not let enough delay for reactions to trigger an ignition runaway. Under different conditions (higher atmosphere temperature, higher pressure ratios, different vent gas mixtures) the conclusion may be changed explaining that in some events, ignition follow opening. But actually, in most scenarios, the ignition is delayed to the second venting, where reactivity peaks, casing and jelly roll temperature rise, and gases vented out may depict a higher hydrogen content [88].

Perspectives for such a simulation are multiple. First of all, it is possible to shed light on the internal device producing the most restriction. Here, the small space between the current collector and the vent disk holder along with the space between the current collector and the mandrel are critical flow choking areas. A place for optimization of internal flow conditions could be to minimize the impact of the collector by shrinking its size or by piercing it differently. The priority being mechanical and electrical design constraints, such improvements may not be possible for all prototypes, but considering flow simulation as a secondary constraint may help to produce safer systems when margins exist. A second application is the assertion of the influence of the opening cell on its environment. Because cells are generally confined into small volumes where venting is limited (modules, hermetic devices, ...), describing the interaction between the jet and impinging surfaces is essential. In the next section, a setup is proposed to help illustrate this application.

11.4 Effect of confinement on the flow topology

11.4.1 Outline of the case

Using the case of the previous section as a reference, a second structure is introduced to assert the influence of confinement on flow parameters at opening. To model confinement, a wall is added above the cell, leading to jet impingement. The distance between the top cap and the wall is 0.5 mm. The choice of this distance is arbitrary and accounts for the thickness of a potential welding point between the wall (that can be a cell current collector) and the cell. Figure 11.4.1 compares cuts of the two meshes used in this section. The mesh that accounts for confinement (Fig. 11.4.1 b)) is composed of 22.3 M tetrahedra and uses similar refinement criteria as the mesh

of the previous section which is made of 17.8 M tetrahedra (Fig. 11.4.1 a)). The added wall uses an adiabatic no-slip boundary condition.

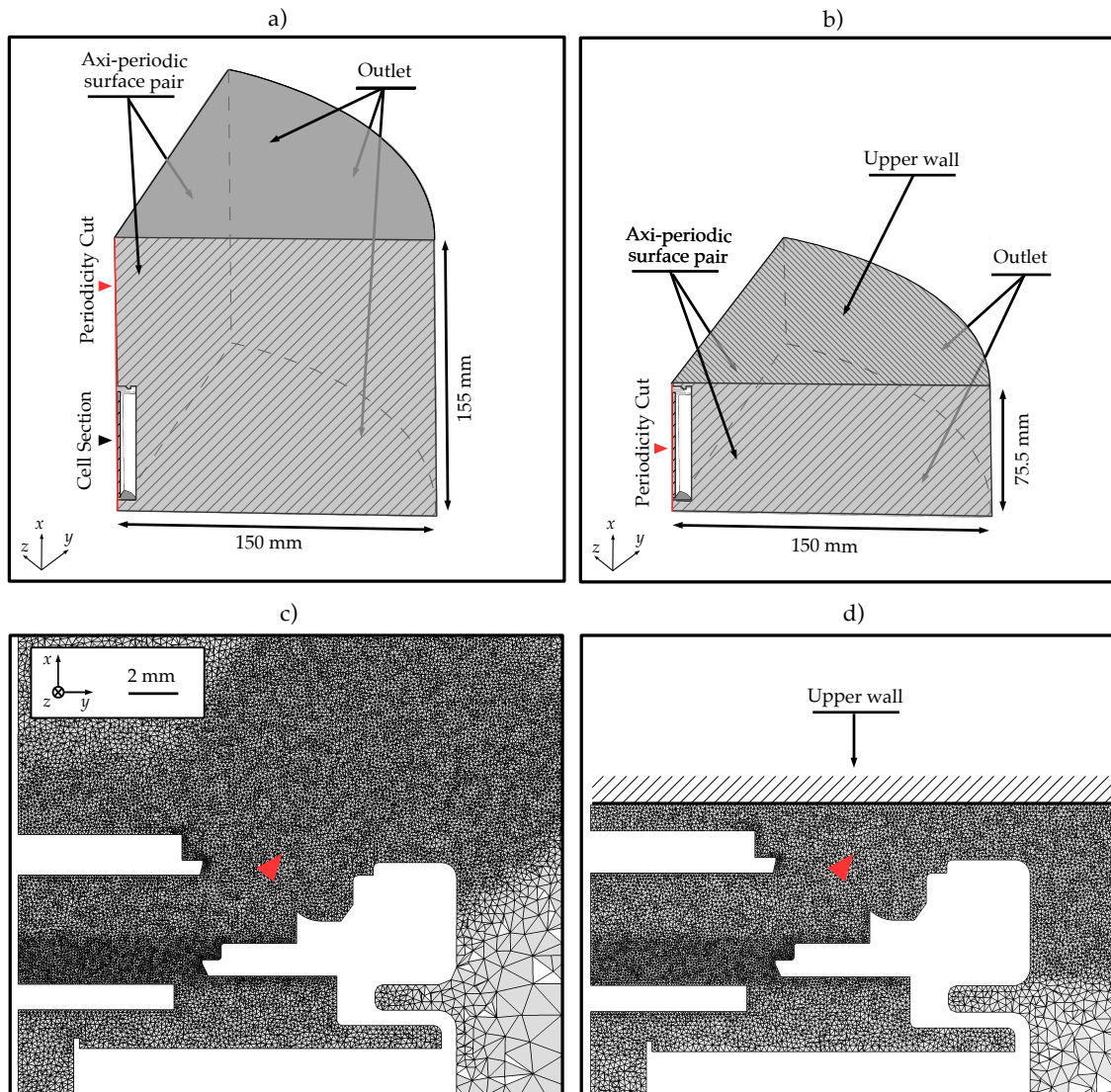


Figure 11.4.1: Comparison of mesh cuts: a) Reference case venting into the atmosphere, b) Modified case where venting is impinged on a wall, c) z -normal cut of the mesh of the reference case, d) z -normal cut of the mesh of the impinging wall case.

11.4.2 Comparison of the venting behavior

Following the first phase of shock reflection and flow preparation that is identical for both cases as the internal layout is the same, the shock impinges on the confinement wall (see Fig. 11.4.2 at $t = 6 \mu\text{s}$). A pressure of 7.5 bar is reached at the confinement wall, in the jet, showing the level of constraint to which it must resist. After $500 \mu\text{s}$, the profile of temperature shows how the impinging jet creates a heating

film (see Fig. 11.4.2). A 3D view of this film is given in Fig. 11.4.3. In addition to mechanical constraints, the prediction of the radius of influence of one cell venting, in terms of balance between conduction and convection, can be used to propose thermal insulation material and cooling systems able to avoid a complete melting of a module casing. The influence of such a management system is a perspective for this approach.

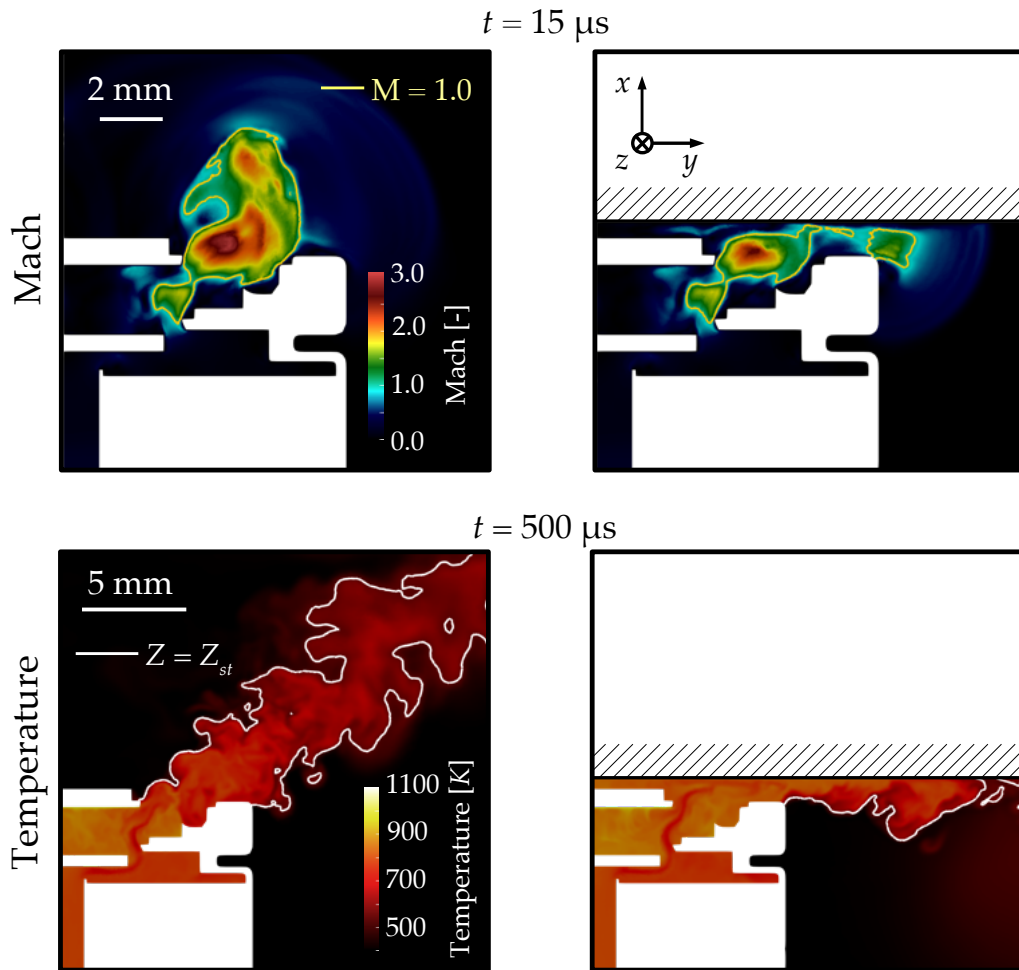


Figure 11.4.2: Comparison of flow structures between free and confined configurations: Mach profiles at $t = 15 \mu\text{s}$, Temperature profiles at $t = 500 \mu\text{s}$.

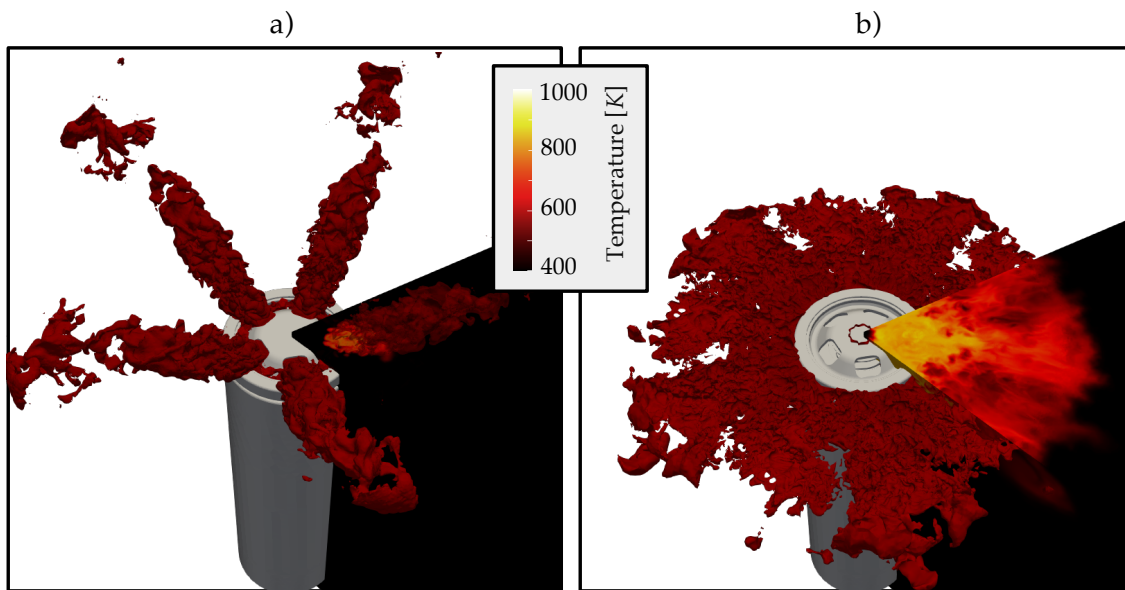
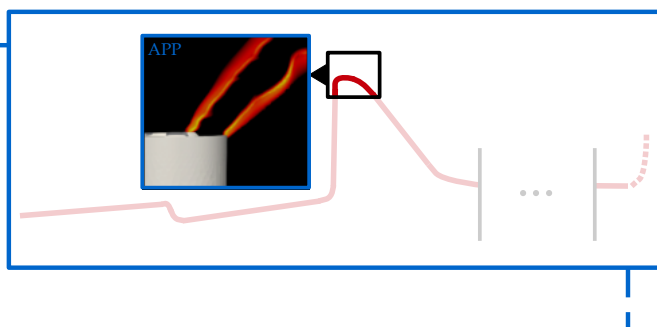


Figure 11.4.3: Comparison of flow structures between free and confined configurations with restored axi-periodicity. Iso-surface $Z = Z_{st}$ colored by temperature depicts the jets, and a slice of the domain depicts the temperature profile on the wall surface: a) reference case, b) impinging wall case.

11.5 Conclusion on cell opening simulation

The simulation of the opening of the cell helps to identify key phenomena on which cell designers may want to act to slow-down/accelerate the venting process, dampen the pressure rises and shock waves, ... The strongly unsteady phenomena depicted here can only be captured by adapted frameworks (LES/DNS). Another force of LES is the ability to zoom on particular locations and events. With modifications of the flow restrictions, and opening conditions (different pre-constrained vent disk), new results can be obtained and their qualitative comparison can define directions of optimization to target safer opening procedures, including avoiding cell braking, or reducing cell mass-flow to extend the venting procedure. The starting point of such a study is the production of a CAD fitted for CFD which demands detailed tomography or proper dismantling of one cell identified as promising and on which design increments may help to improve safety and understanding. Once this step is performed, repeated simulations with small geometrical and initialization changes may be done easily until converging on satisfying improvements of the original design.

Chapter 12



Sustained venting and flame dynamics

Contents

12.1 Cell fire experiments and CFD simulations	184
12.2 Case definition	184
12.2.1 Targeted fire	184
12.2.2 Presentation of the structure	185
12.2.3 Numerical setup	186
12.3 Non-reactive flow characterization	188
12.4 Forced ignition	188
12.5 Effect of design choices	190
12.5.1 Vent design	190
12.5.2 Cell internal chemistry	191
12.5.3 Summary of the effect of design choices	192
12.6 Comparison to experimental observations	193
12.7 Conclusion on sustained venting simulation	193

In this chapter, a 3D test case is set up to show the potential use of simulation for the prediction of the behavior of a generic 18650 cell when forcefully ignited in the sustained venting phase¹. A reference setup venting the NMC1 mixture (see Chap. 6 Tab. 6.3.1), through five holes is compared to a setup where only three holes are pierced in the vent cap, and a setup where the mixture is representative of a more energetic internal chemistry (LCO/NMC). Changes in flame dynamics are observed and reported, showing that simulation is an opportunity to select venting scenarios based on user specifications.

¹See Chap. 7 Sec. 7.5 for the complete list of scenarios in the timeline of TR.

12.1 Cell fire experiments and CFD simulations

Cell fire experiments and corresponding CFD simulations are recent topics where the corpus is limited but growing rapidly. Experimental data, essential to perform physics-informed simulations, help to set cases and check their sanity. The first step towards a cell fire simulation is the definition of suitable operating conditions. In particular, the mass-flow is an essential parameter which can be obtained from the work of Golubkov *et al.* [96]. The works of Garcia *et al.* [88] and Fu *et al.* [85] give visualization data and heat production levels to confirm qualitatively simulation results. Applying CFD simulation, including combustion processes, to Li-ion fires is a new topic where promising results have been obtained by Kong *et al.* [143], and where an effort is still to be put, motivating the study that follows.

12.2 Case definition

12.2.1 Targeted fire

In order to simulate representative operating conditions of a cell fire, experimental results from Golubkov *et al.* [96] are used as a reference. In this scenario, the NMC1 mixture is considered (see Chap. 6 Tab. 6.3.1): H_2 : 30.8 %, CH_4 : 6.8 %, C_2H_4 : 8.2 %, CO : 13.0 %, CO_2 : 41.2 %. A second mixture is added to observe the effect of gases with higher LHV and flame speed: LCO/NMC. LCO/NMC writes as: H_2 : 30.0 %, CH_4 : 8.6 %, C_2H_4 : 7.7 %, C_2H_6 : 1.2 %, CO : 27.6 %, CO_2 : 24.9 %.

Figure 12.2.1 schematically explains how mass flow and gas/wall temperature are obtained to mimic a real ignition sequence. During the overheat-to-TR experiment, inner reactions start to produce gases. The pressure builds up until the safety vent opens and triggers the first venting. For the cell selected in [96], as reactivity goes up, a second venting occurs which can be decomposed in three sequences: 1) a rapid ejection, 2) a slow sustained ejection and 3) ejection stops and gases condense on colder walls. In this study, a reproduction of the slow sustained ejection is targeted, as the low mass-flow appears to be suitable for flame anchoring. The total cell mass-flow \dot{m} during this phase is approximated with the value of $0.506 \text{ g}\cdot\text{s}^{-1}$ and both flow and wall temperatures are found equal to 956 K. For this scenario, the cell vents into the atmosphere where $T_{air} = 300 \text{ K}$ and $P_{air} = 101\,325.0 \text{ Pa}$, representing conditions close to the ones presented in Chap. 10.

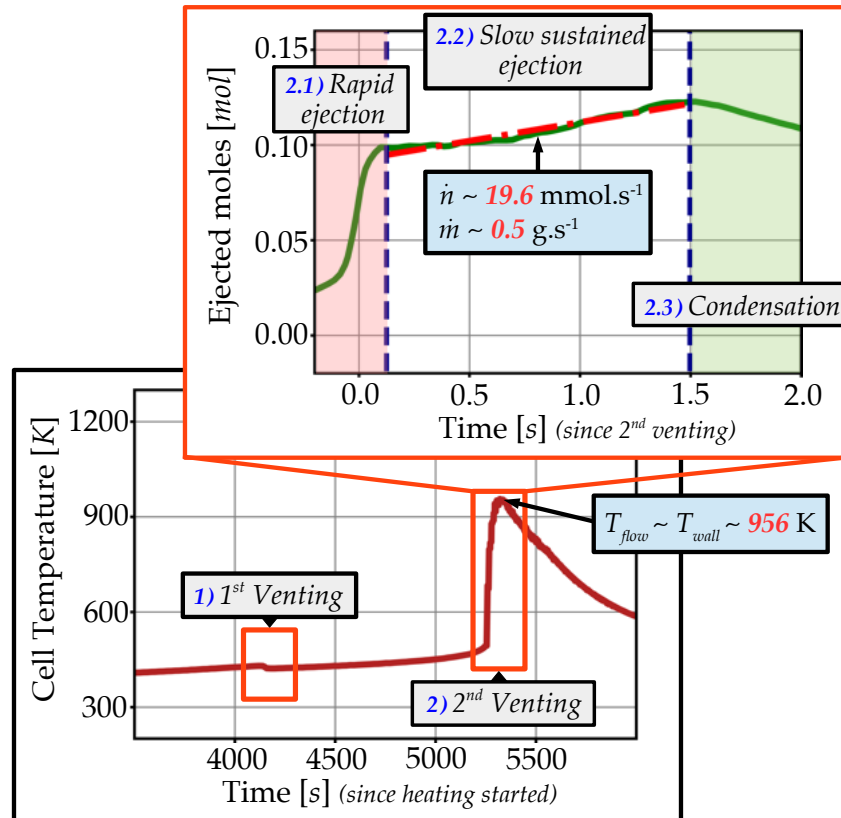


Figure 12.2.1: Schematic representation of the extraction of representative operating conditions from the work of Golubkov et al. [96].

12.2.2 Presentation of the structure

To complete the scenario, a generic geometry of a 18650 cell is chosen. The structure of the targeted reference 18650 cell is depicted in Fig. 12.2.2. It represents a simplified cell with five venting holes at a 45° tilt angle, enclosed in a 1 m diameter sphere playing the role of the surrounding atmosphere. To avoid modelling the details inside the cell at this preliminary step, vent gases are injected directly at the vent holes. The mass-flow of each hole is a fifth of the total mass-flow. The natural axi-periodicity of the cell is not used in this case to be able to compare to other designs and assert the feasibility and cost of a full cell computation.

In this study, the mesh precision is constrained by the necessity to resolve adequately a diffusion flame that is predicted to appear under the targeted venting conditions (see Chapter 7 Section 7.4). The unstructured tetrahedral mesh is refined around the ejection zone with a minimal cell spacing of $200\ \mu\text{m}$. At holes lips, a $100\ \mu\text{m}$ cell spacing is applied. The mesh accounts for 26.4 M tetrahedrons for a total volume of $0.31\ \text{m}^3$.

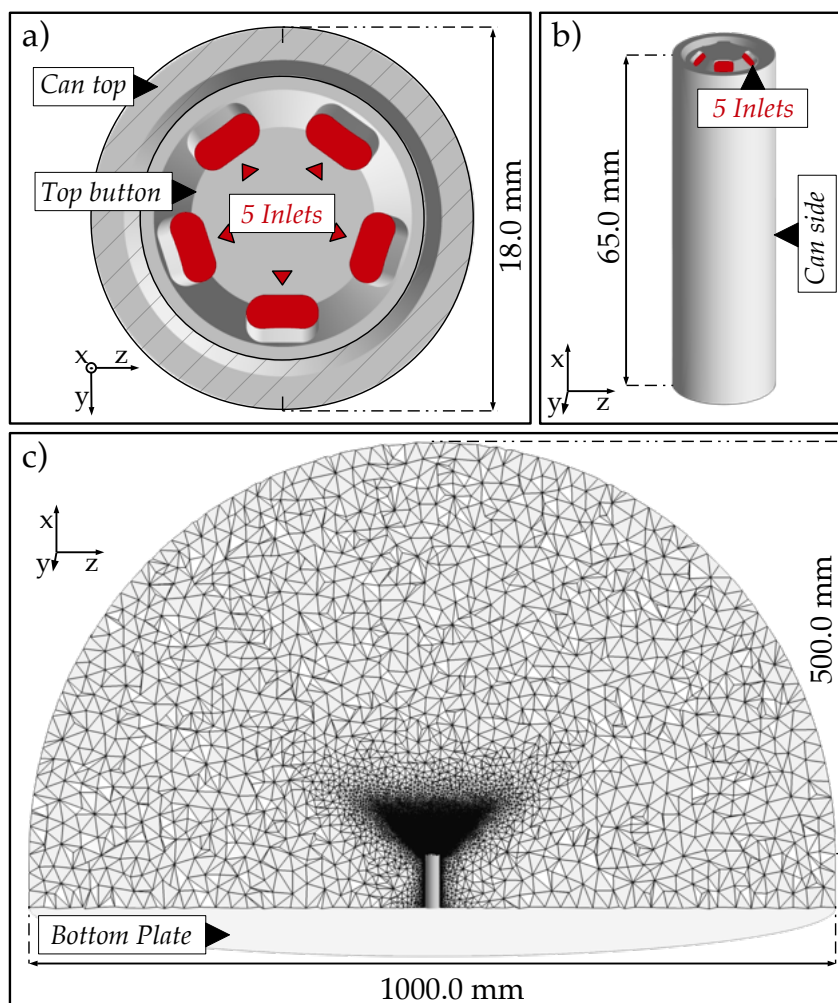


Figure 12.2.2: View of the structure and mesh of the 18650 generic case: a) view of the top button with the 5 holes, b) side view of the cell, c) cut view of the mesh with domain sizes.

12.2.3 Numerical setup

The Lax Wendroff convection scheme [152] is chosen to solve the discretized form of the filtered Navier-Stokes reactive flow equations. The subgrid scale model is the Smagorinsky turbulence model [245]², along with turbulent Prandtl and Schmidt number both equal to 0.6. The global CFL number is 0.7 and the Fourier number is 0.1. Second and fourth order artificial viscosity terms are added to stabilize the computation [125]. Inlets and outlets are treated with NSCBC [260, 214, 198].

To model the fact that the flow inside the cell encounters multiple flow restric-

²For this scenario that aims at proposing an affordable benchmark when designing cells, a turbulence closure and a numerical scheme generally available in all CFD frameworks is preferred. Using TTGC [50] with WALE [199] is expected to ensure better turbulence definition.

tions and deviations (under the form of the crimp plate, the vent disk holder, the mandrel, ... [79]), homogeneous isotropic turbulence is injected through the five inlets following the method described in the work of Guézennec and Poinso [102]. The most energetic turbulent length scale is set to half the width of one hole ($L_e = 1.7$ mm) and the level of turbulence is chosen to be such that $U_{RMS}/U_{bulk} = 0.20$. Li *et al.* [161] computed detached eddy simulation of cold, high pressure venting of air through a reproduction of an 18650 vent cap. They measured turbulence intensities reaching 50%. In the case considered in the present chapter, the second venting at lower mass-flow and higher temperature is targeted with real Li-ion vent gases. The turbulence level is estimated to be lower and an arbitrary trade-off of 20% is chosen. A cold flow simulation of the cell with internal obstacles is proposed in Appendix F, to nuance the choice of synthetic turbulence as an injection strategy. The outlet pressure is $P = 101\,325.0$ Pa and both the bottom plate of the domain and the side of the cylindrical can are using classical adiabatic wall log-laws. The top of the cell is however supposed to play a role in flame anchoring, no-slip conditions using heat transfers are thus used. The wall temperature is set to $T_{wall} = 956$ K and the thermal resistance is set to 3.3×10^{-5} K.m².W⁻¹ for the top button and 2.4×10^{-5} K.m².W⁻¹ for the top part of the can (see Fig. 12.2.3). These values are computed using wall thickness measurement in the work of Finegan *et al.* [79] and the thermal conductivity of materials commonly used for cell cans [105]. Adiabatic wall law is chosen for the walls at inlet ('Wall inlet'). The initial condition of the simulation consists in filling the entire domain with air at rest ($V = 0$ m.s⁻¹). $T_{air} = 300$ K and $P_{air} = 101\,325.0$ Pa.

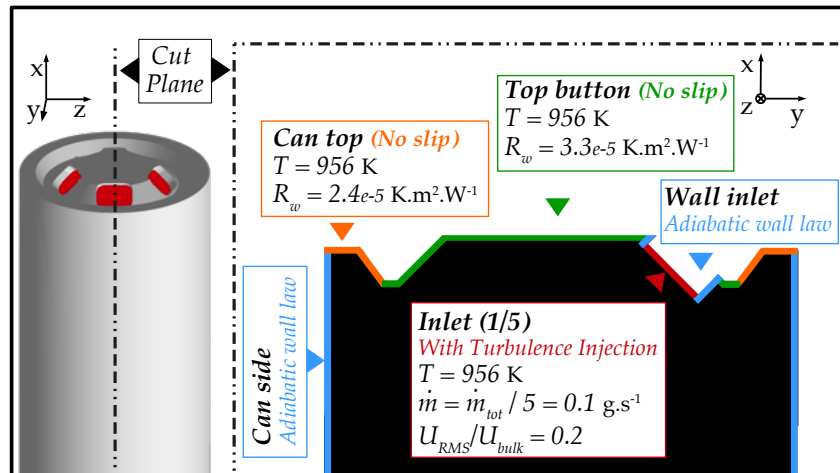


Figure 12.2.3: Schematic representation of the boundary conditions close to the cell on a cut view displaying one of the five holes.

12.3 Non-reactive flow characterization

First, a non-reactive simulation of the jet mixing is used as an initial condition for the spark ignition tests. The simulation runs for 50 ms until the flow is established. Figure 12.3.1 a) depicts a cut of the velocity field.

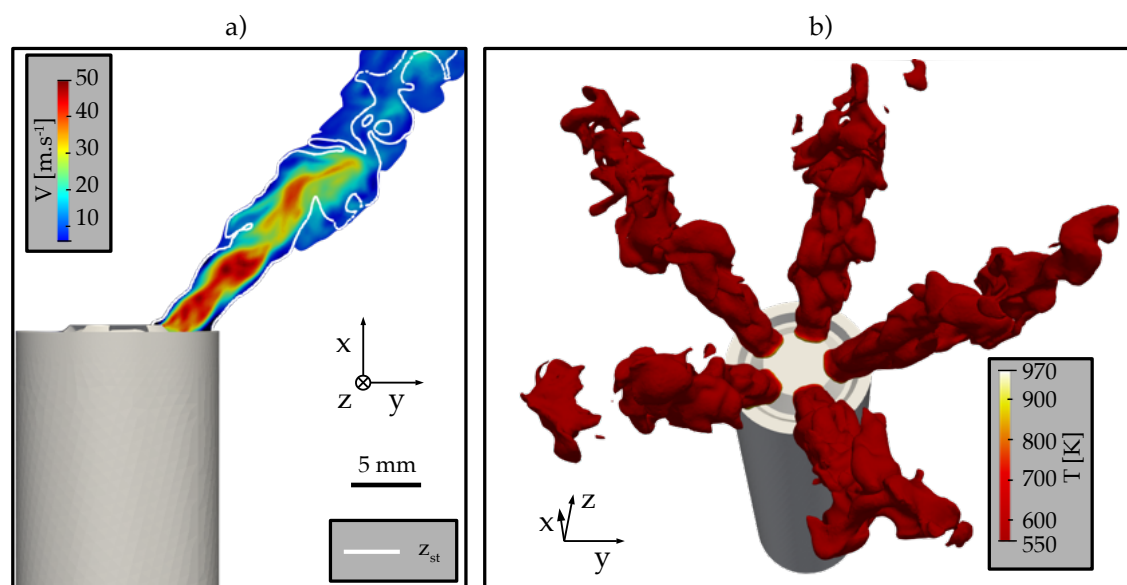


Figure 12.3.1: Non-reactive flow simulation of the five holes geometry, at $t = 50$ ms: a) cut view of the velocity field with the iso-line representing the stoichiometric mixture fraction, b) iso-contour of mixture fraction at stoichiometric conditions colored by the temperature.

Due to turbulence injection, the maximum velocity magnitude reaches 49.0 m.s^{-1} for a bulk velocity of 35.8 m.s^{-1} . Stoichiometric conditions are reached up to 40.0 mm away from the cell. However, Fig. 12.3.1 b) shows that the temperature where stoichiometry is reached is low, making auto-ignition events unlikely. Based on these results, a forced ignition test is conducted in the next section.

12.4 Forced ignition

To observe the effect of sudden ignition of the flammable gases vented out by the cell, a forced ignition sequence is set, echoing to the experimental jet flame section (Chap. 10). In practice, forced ignition during TR is possible due to e.g. short-circuit induced sparks, incandescent matter suddenly ejected, interaction with another failing cell, ... Ignition is triggered by a sphere of hot gases (see Appendix B Section B.2) at the ignition point (Fig. 12.4.1). The sphere temperature profile is Gaussian in time and space and the maximum temperature is set to $T_{ig} = 2452 \text{ K}$,

the adiabatic flame temperature for fresh gases at 1000 K and stoichiometric condition. The diameter of the deposition sphere is 5.0 mm. The ignition sequence lasts 4.0 ms. The five ignition spots (one for each jet) are placed 15.0 mm away from the inlet patches. Because, during ignition phases, diffusion and premixing cohabit and free premixed flames can be observed, the thickening model that accounts for flame-turbulence interaction and diffusion-premixing differentiation is set, based on the framework introduced in Chapter 7 Section 7.3.2 and 7.4.3. A static Charlette efficiency function with a constant equal to 0.5 completes the thickening model (See Chap. 4 Sec. 4.17).

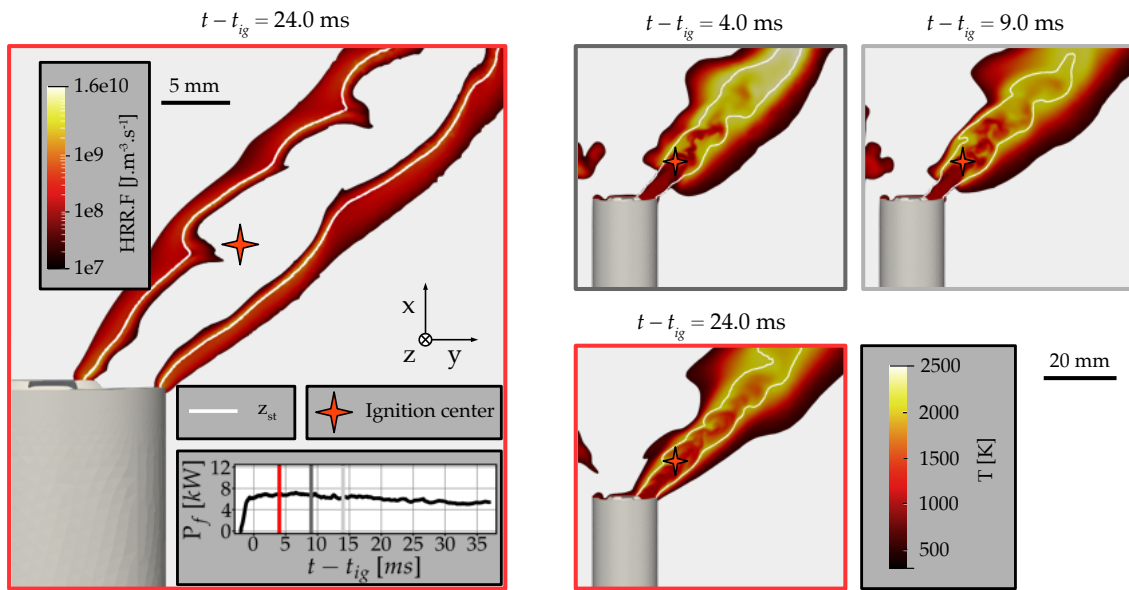


Figure 12.4.1: Reactive flow simulation of the five holes geometry venting NMC1: *left*, cut view of the heat release rate field after anchoring at $t = t_{ig} + 24$ ms, with a plot of the flame power in the domain P_f versus time, *right*, snapshots of the temperature field. The color of the frames for temperature and HRR are matched to instants depicted as vertical lines on flame power time plot.

Figure 12.4.1 shows a cut view of heat release rate, 24 ms after ignition. Under the operating conditions extracted in the previous section, a stable diffusion flame attaches to the lips of the cell at $t - t_{ig} = 14.4$ ms. Once anchoring is done, the thickening model is consistently deactivated by the Takeno sensor (see Chapter 7 and 7.4.3). The total power of the burning cell P_f reaches 5.3 kW^3 . The simulation proposed here is the default case (or reference), namely, the venting of NMC1 through five holes. From this reference, design choices can be moved to observe their effects on flame dynamics.

³average taken for the last 10 ms of stable flame computation

12.5 Effect of design choices

To highlight the usefulness of reactive flow simulation for simple design questions, the impact of two parameters is asserted: 1. A geometry change is made by testing a cell with only three venting holes, 2. The effect of internal chemistry is depicted by venting the LCO/NMC vent gas (see Chap. 6 Tab. 6.3.1). For completion the four combinations are tested:

1. Five Holes and NMC1 mixture (reference case).
2. Three Holes and NMC1 mixture.
3. Five Holes and LCO/NMC mixture.
4. Three Holes and LCO/NMC mixture.

To remain consistent, the quantity conserved in all the cases is the molar flow extracted in [96] and presented in Fig. 12.2.1.

12.5.1 Vent design

For the three-holes-case with the NMC1 mixture, the operating conditions being kept the same, the bulk velocity for each hole is increased in comparison with the reference case and reaches 59.7 m.s^{-1} . Under these conditions a totally different flame behavior is observed 4 ms after ignition. Figure 12.5.1 depicts a free premixed flame structure which is blowing off. At $t - t_{ig} = 22 \text{ ms}$, the flame is extinguished, as shown by the flame power curve given in Fig. 12.5.1 a).

In view of these results, a Li-ion cell designer can then choose *a priori* whether it is preferable to have an attached flame and no residual flammable gases in the venting space but a substantial amount of heat (five holes case), or a flame blown away and unburnt flammable gases accumulating in the venting space with no supplemental heat due to combustion (three holes case). Such a comparison also allows to study clogging effects [161] when the safety disk fails to open totally and blocks several holes, potentially shifting the behavior of the cell from the attached diffusion flame to the blown-off premixed flame. Adding auxiliary components surrounding the cell in the simulation setup is also to consider, to obtain more information on their interaction with the jet flame.

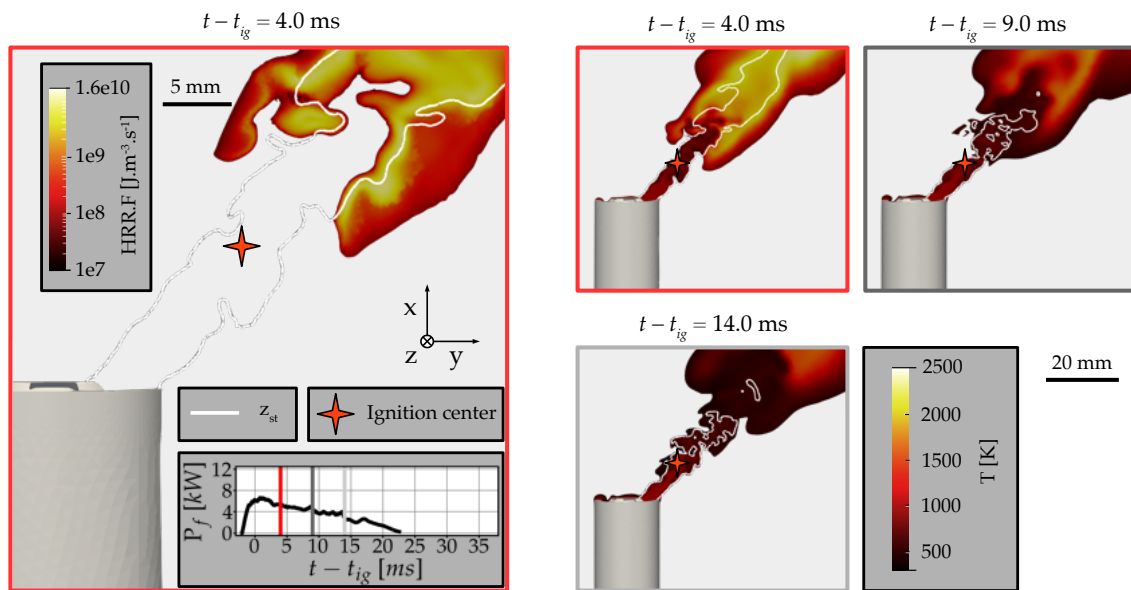


Figure 12.5.1: Reactive flow simulation of the three holes geometry venting NMC1: *left*, cut view of the heat release rate field before complete blow-off at $t = t_{ig} + 4$ ms, with a plot of the flame power in the domain P_f versus time, *right*, snapshots of the temperature field. The color of the frames for temperature and HRR are matched to instants depicted as vertical lines on flame power time plot.

12.5.2 Cell internal chemistry

A second parameter is tested: the vent gas mixture. In practice, a change in internal chemistry or in the SoC has a direct influence on vent gases combustion properties. The LCO/NMC mixture (Chap. 6 Tab. 6.3.1) depicts higher flame speed and LHV than NMC1, due to a lower dilution into CO_2 . For the five-holes-case, as expected, the anchoring of the flame happens 1.9 times faster than with NMC1 at $t - t_{ig} = 7.7$ ms, and the flame power is higher at 7.7 kW (see Fig. 12.5.2).

For the three holes case, the blow-off sequence is largely extended, and the overall higher consumption speed is close to allow the presence of a steady lifted flame (see Fig. 12.5.3). The power of the flame decays slowly, and is predicted to extinguish in 60 ms. As expected, higher flame speeds and LHV tend towards more intense fires and blow-off limits pushed to higher mass-flow/smaller venting surface. When designing a cell, simulations with multiple flow conditions, and gaseous mixtures may help to assert the robustness of a design, and estimate power outputs and characteristic flame times (anchoring, blow-off, ...).

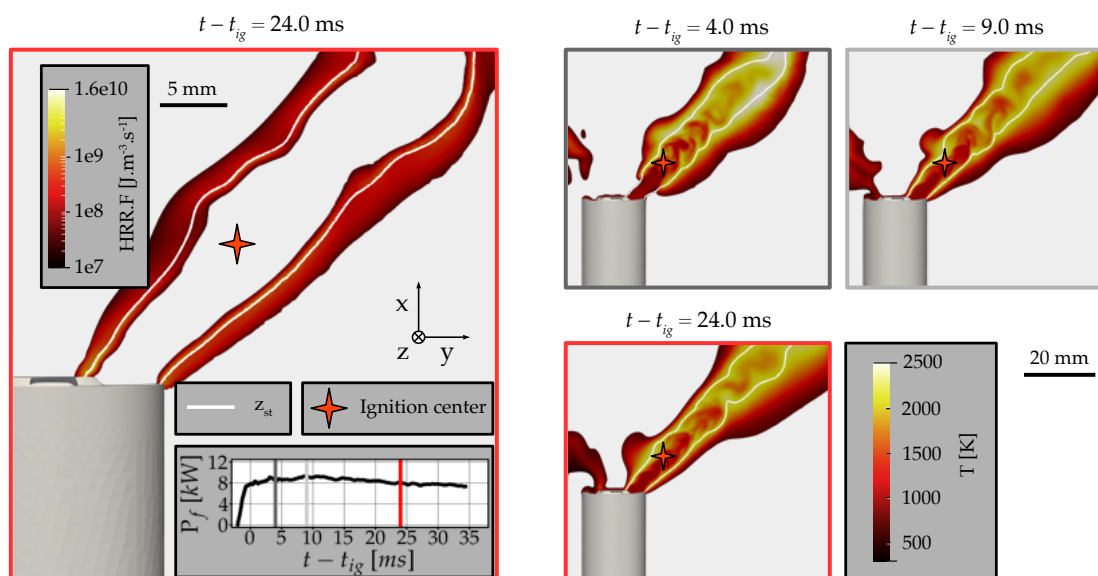


Figure 12.5.2: Reactive flow simulation of the five holes geometry venting LCO/NMC: *left*, cut view of the heat release rate after anchoring at $t = t_{ig} + 24$ ms, with a plot of the flame power in the domain P_f versus time, *right*, snapshots of the temperature field.

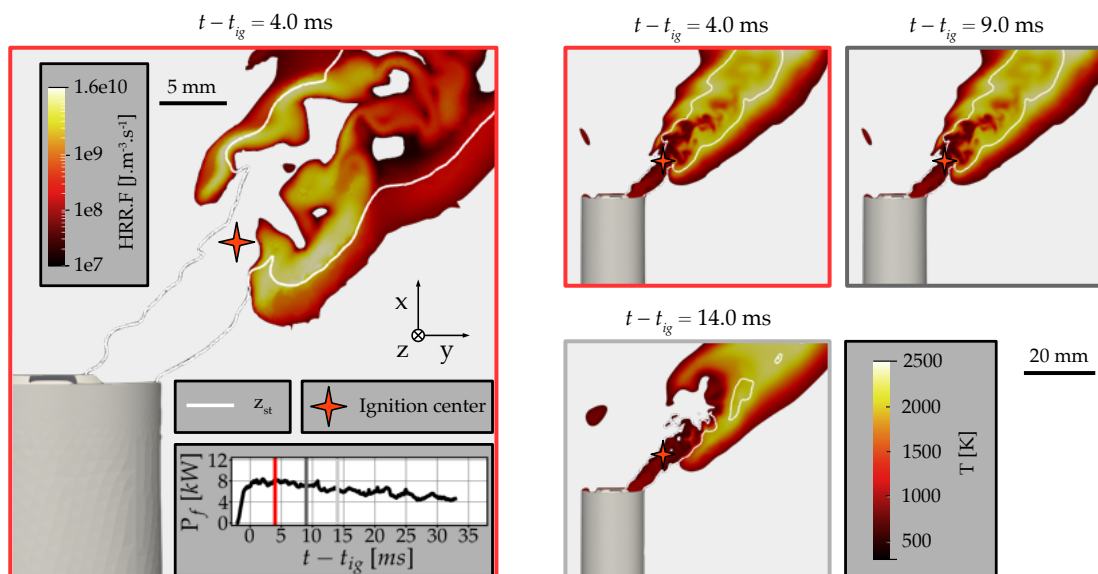


Figure 12.5.3: Reactive flow simulation of the three holes geometry venting LCO/NMC: *left*, cut view of the heat release rate field before complete blow-off at $t = t_{ig} + 4$ ms, with a plot of the flame power in the domain P_f versus time, *right*, snapshots of the temperature field.

12.5.3 Summary of the effect of design choices

Table 12.5.1 sums up the influence of each design choice on the fire main parameters, showing the trends that a cell designer could follow when preparing the prototyping step.

Table 12.5.1: Summary of the influence of design choices on 18650 flame dynamics.

	NMC1	LCO/NMC
5 Holes	- Status: Anchored - Anchoring time: 14.4 ms - Fire power: 5.3 kW	- Status: Anchored - Anchoring time: 7.7 ms - Fire power: 7.7 kW
3 Holes	- Status: Blown-off - Blow-off delay: 22 ms	- Status: Blown-off - Blow-off delay: 60 ms (est.)

12.6 Comparison to experimental observations

In their work, Fu *et al.* [85] measured the heat released by a fully charged failing 18650 cell with a six hole top cap using LCO chemistry and obtained a peak value of 6.8 kW. The order of magnitude obtained for a comparable case using simulation (case LCO/NMC - 5 holes: 7.7 kW) holds in comparison to the cited experiment and is an encouraging result to improve the confidence in the prediction ability of the simulation. Furthermore, García *et al.* [88] proposed Schlieren, natural luminosity and OH^* visualisations for burning 18650 cells with LCO cathodes. The flame structures are depicted as distinctive jets which qualitatively corresponds to the observations made using 3D simulation. However, the ejection of liquid electrolyte is predicted to play a crucial role in flame dynamics and ignition in early phases. Such observations pave the way to more advanced simulations that consider liquid phase and real electrolyte combustion.

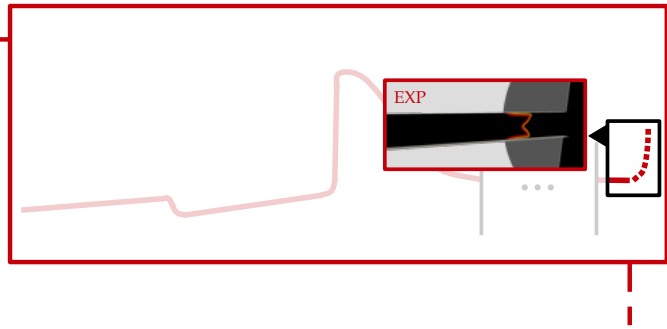
12.7 Conclusion on sustained venting simulation

This part of the work highlights potential use of simulation to assert several simple design choices on flame dynamics during Li-ion fires. In the scenarios presented here, cells appear as simplified structures venting into the atmosphere. However, as it was introduced in the previous chapter (Chap. 11) and further detailed in Appendix. F, accounting for cell internal designs, vent holes surface and shape, storage constraints, or cooling systems, is also possible and serves as perspectives. For example, exploring the difference in heat rendered with and without a flame, with and without obstacles, ... are essential for questions of cell-to-cell thermal runaway propagation, including radiation and conduction. Also, pollutant emission and gas harmfulness are bricks that can be added, starting from this basis.

Part V

Flame acceleration and explosions for Li-ion vent gases in confined environments

Chapter 13



Flame acceleration in a rectangular channel

Contents

13.1 The challenge of explosion simulations and batteries	198
13.2 Tulip flame simulation	199
13.3 Experimental and numerical setup	199
13.3.1 Source of the experimental data	199
13.3.2 Simulation framework and models	200
13.4 Validation of the simulation framework	203
13.4.1 A problem of wall boundary conditions	203
13.4.2 A procedure to better define boundary conditions	207
13.4.3 Effect of mesh refinement	211
13.4.4 Final experimental/simulation validation	214
13.5 Concluding remarks	218

After the characterization of vent opening and fire events during TR, a last sequence must be asserted. In case of delayed ignition, and after accumulation inside enclosed spaces, explosions¹ have been observed and is a major source of concern for battery designers (See Sec. 1.2 of the Introduction). Asserting effects of design choices on explosion parameters, along with the prototyping of mitigation strategies are key subjects for simulation. Being able to numerically predict flame propagation and overpressure is an important scientific and engineering challenge.

¹See Chap. 7 Sec. 7.5 for the complete list of scenarios in the timeline of TR.

13.1 The challenge of explosion simulations and batteries

On the way to predict the explosion behavior due to failing Lithium-ion batteries in confined spaces (storage, large scale power modules, ...), multiple interrogations can be highlighted concerning capability of computational fluid dynamics (CFD) solvers to accurately reproduce all the phenomena involved:

1. **Scale:** One first key problem is the scale of the system studied. Battery modules may have large dead volumes in which vent gases can expand until rest conditions are reached making simulation costly. A simulation platform adapted to large scale free fires must be chosen, implying the verification of the good agreement between experimental considerations and dynamic flame thickening methods applied to vent gas mixtures.
2. **Initial condition:** Due to the strong variability in the venting process, based on the type of cell, the TR trigger, ... the composition of the gases at rest vary along with the global equivalence ratio. Being able to compare different mixtures under similar numerical setups guarantees qualitative understanding of the influence of this initial condition on the explosion phenomenon.
3. **Boundary conditions:** There is a large panel of material used for the construction of battery modules, from metallic surfaces to plastic surfaces, the flame may encounter variable heat resistances on its way. But most importantly, in a failing electrical system, heating may become uncontrollable, certain hot surfaces can promote combustion, hence accelerating the free flame. Asserting the influence of boundary conditions on flame acceleration is necessary to obtain information on how a design impacts the explosion scenario.
4. **Effect of turbulence:** Inside the dead volume, obstacles are predicted to play a crucial role on the turbulence which impacts flame propagation speed. These obstruction may be due to the cable management, the structure of the cells, and electrical devices housing and cases. Flame-turbulence interactions must be evaluated, in addition to the flame thickening procedure.

As an attempt to reproduce a Li-ion vent-gases-related explosion, it has been decided to isolate items in two chapters. In this first chapter, the focus is on the simulation of tulip flames obtained experimentally by Henriksen *et al.* [111] using a smooth rectangular channel filled with synthetic vent gases. Extensive data is available allowing a proper calibration and validation of the numerical setup. In the following sections, the validation of the simulation framework against experimental data is given. Influences of boundary conditions and mesh refinement are asserted on the way to this validation. Overall, this study sets a milestone towards the

simulation of more complex explosions of Li-Ion vent gases, with a familiarization to the phenomena at hand in a simple academic case, already used for experimental *versus* simulation comparisons.

In the next chapter, a similar simulation setup is used to obtain qualitative results on the addition of obstacles, creating flame turbulence interactions (see Chap. 14).

13.2 Tulip flame simulation

The phenomenon of tulip flame formation in smooth tubes is commonly observed with multiple gaseous mixtures under various tubes cross-section shapes. It has been identified as early as the beginning of the XXth century [72], and continues to be experimentally studied, with an emphasis on the underlying mechanisms that are still under lively discussion [47, 215, 45]. Simulations play a crucial role in the identification of the mechanisms in place, which are reproduced easily with varying hypotheses [215]. The approximation of 2D domains allows to obtain first results at reasonable costs [98], helping to test theoretical correlations and depict finger flame to tulip flame transitions [6, 31, 32]. 3D tulip flame simulations validated versus experimental have then emerged [288, 163], including the test of the thickened flame model for such an application [302]. In this context, the simulation of the tulip flames obtained experimentally by Henriksen *et al.* [111] is proposed as an application of the thickened flame model to tulip flames propagating in Li-ion vent gases. This step serves as preliminary work for the next chapter (Chap. 14).

13.3 Experimental and numerical setup

13.3.1 Source of the experimental data

The experimental dataset is shared by Henriksen and Bjerketvedt [108, 111]. A description of the experimental setup used to produce the data is recalled here: the configuration consists in a rectangular tube (length 1000 mm, width 65 mm, height 116.5 mm), closed at the ignition end and opened at the venting end. The tube is filled at atmospheric conditions ($T_0 = 293.0$ K, $P_0 = 1.0$ atm) with a mixture of vent gases and air with predefined equivalence ratio. A 20 ms ignition sequence, consisting in two successive sparks, is triggered after a 1.0 min resting time. The system is equipped with four pressure sensors (Kistler 7001), and a high speed camera (Photron SA1) captures flame displacement through an optical access. A schematic description of the experimental setup is given in Figure 13.3.1.

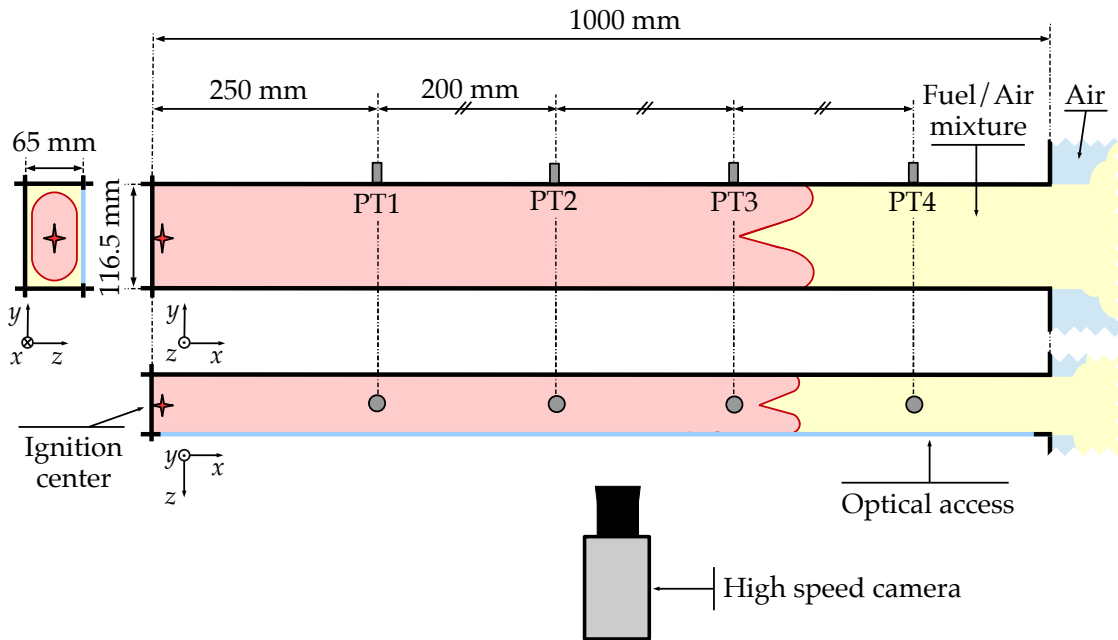


Figure 13.3.1: Schematic representation of the experimental setup proposed by Henriksen *et al.* [111] to assess Li-Ion vent gases explosions. The four pressure transducers are noted PT1-4.

The gaseous mixture considered in the study of Henriksen *et al.* results from vent gas analysis of commercial LFP cells. The molar composition is as follows: H_2 : 34.9 %, CH_4 : 15.0 %, C_2H_4 : 5.0 %, CO : 25.0 %, CO_2 : 20.1 %. More details are available in Chapter 6, as the mixture is part of the generalization test performed on the analytically reduced scheme.

13.3.2 Simulation framework and models

The approach to simulate the free flame proposed in this section serves two main objectives. On the one hand, it is a direct opportunity to validate further the choices made earlier in the manuscript, in terms of chemical kinetics modelling and flame modelling. On the other hand, it is a first calibration step to go further with cases including obstacles producing turbulence. For the first objective, the analytically reduced chemistry scheme (ARC) is setup in Chapter 5. Figure 13.3.2 shows the good agreement between the detailed San Diego scheme (SD) and ARC when computing a 1D premixed laminar flame at $T = 300$ K, ensuring the validity of this latter scheme for the cases to be computed in the following sections. Concerning the flame thickening model, the dynamic relaxation sensor is chosen [126]. It ensures five points in the flame front thickness by detecting methane consumption and artificially thickening the flame (see Chap. 4 Sec. 4.2.2 and Chap. 7 Sec. 7.3.2). For the second objective, meshes using unstructured tetrahedrons are successively tested to observe the influence of mesh refinement on 1. the flame structure, and 2. the flow

at the walls. The choice of an unstructured mesh in a case where a structured mesh would also perform properly is motivated by the fact that in cases where obstacles of arbitrary shapes are placed in the channel, this mesh topology will be mandatory. The calibration in this step concerns the way the walls are treated, which can be transposed further in turbulent cases. Three meshes are tested, Table 13.3.1 and Figure 13.3.3 summarize the key information about the structure of the case and the corresponding meshes. The reference mesh will be Mesh 1.0/1.0.

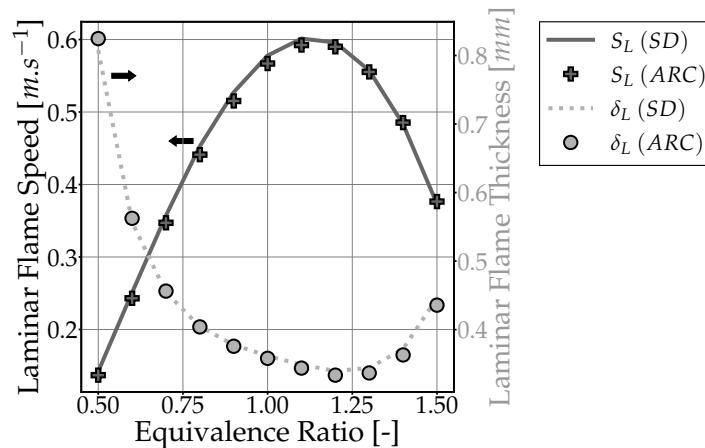


Figure 13.3.2: Simulation of a 1D premixed laminar flame using the Analytically Reduced Chemistry computed in Chapter 5 at $T = 300$ K. Comparison of the laminar flame speed S_L and the thermal flame thickness δ_L .

Table 13.3.1: Specification of the meshes used in the study, with corresponding sizes and refinement criteria.

Mesh name	Mesh 1.0/1.0	Mesh 2.0/2.0	Mesh 1.0/0.5
Mesh desc.	Fine	Coarse	Wall refined
N_{nodes}	8.13 M	1.07 M	10.82 M
N_{cells}	46.32 M	5.95 M	59.23 M
Δx (channel)	1.0 mm	2.0 mm	1.0 mm
Δx (walls)	1.0 mm	2.0 mm	0.5 mm
V_{cell}^{min}	$3.01 \times 10^{-2} \text{ mm}^3$	$4.36 \times 10^{-1} \text{ mm}^3$	$3.06 \times 10^{-3} \text{ mm}^3$

In the framework of AVBP [37], the convection scheme proposed by Lax and Wendroff [152] is chosen along with WALE as a subgrid scale turbulence model [199] for the turbulent open end of the channel. Turbulent Prandtl and Schmidt number are equal to 0.6. The CFL and Fourier numbers are set to 0.7 and 0.1 respectively. The computation is stabilized by second and fourth order artificial viscosity terms [125].

To mimic experimental conditions, the channel is initially filled with a mixture at rest corresponding to the stoichiometric condition targeted (experimental equivalence ratios are $\phi = 0.77$, $\phi = 1.03$ and $\phi = 1.19$). The outlet plenum is filled with air. The temperature of the gases is set to $T = 293.0$ K. Ignition is forced by imposing a hot temperature sphere at the closed end of the channel over a fixed duration.

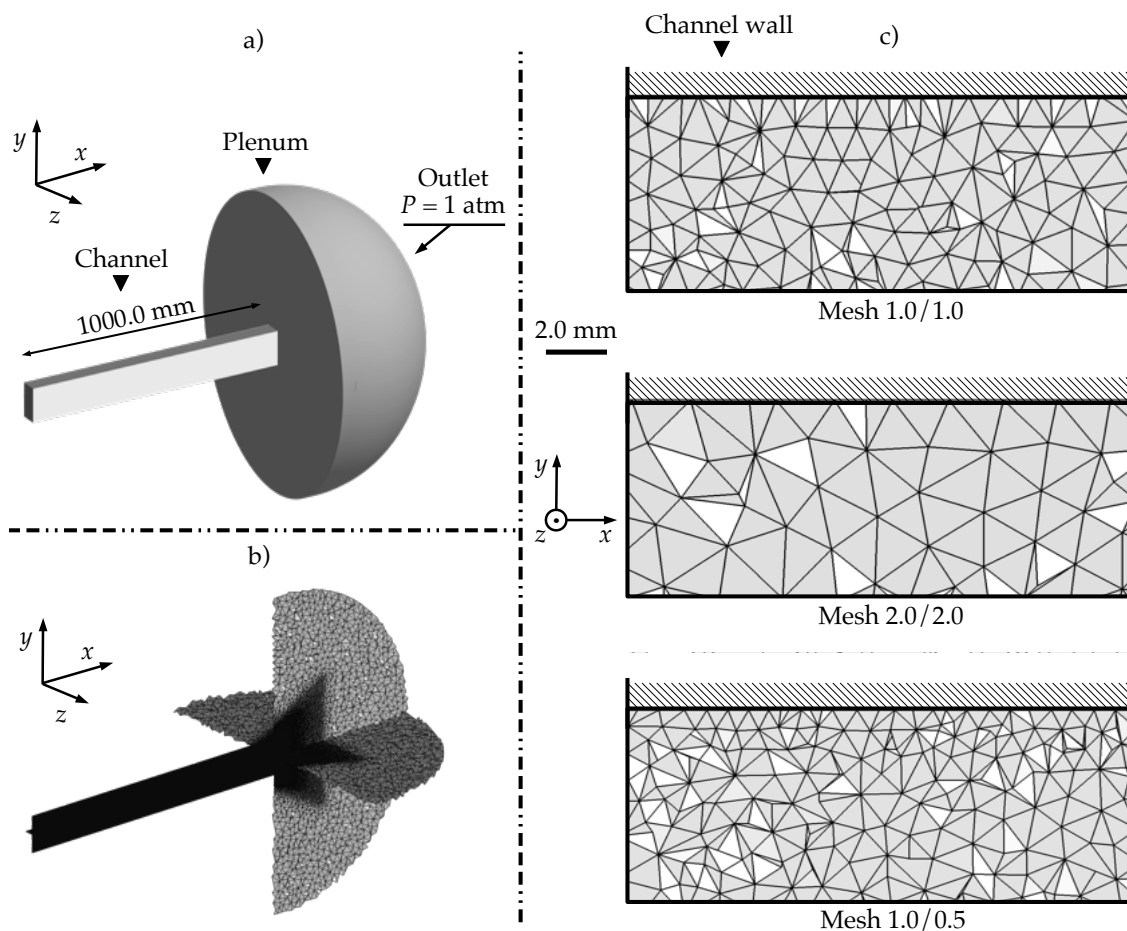


Figure 13.3.3: Description of the simulation case and the corresponding meshes: a) view of the case, b) z and y cuts of the typical mesh used, c) zoom on the resolution of the meshes at the channel wall. Mesh names are as follows: "Mesh A/B" where A corresponds to the homogeneous resolution used in the channel, B the resolution at the wall, in mm (see Table 13.3.1).

The sphere temperature profile is Gaussian in time and space, and the maximum temperature is set to $T_{ig} = 3000 \text{ K}$ (App. B). The ignition sequence lasts 20 ms and is enclosed in a diameter of 2.0 mm. The NSCBC formalism is used for the outlet [260, 214, 198]. The outlet relaxes to the atmospheric pressure $P = 101\,325.0 \text{ Pa}$. Wall treatments are the subject of the following section, and can be set to all conditions, from adiabatic to isothermal, passing by heat-loss modeling, with velocity laws.

13.4 Validation of the simulation framework

13.4.1 A problem of wall boundary conditions

The first step towards the validation of the simulation setup is the definition of boundary conditions able to properly reproduce the experimental setup. In large explosion cases, the common accepted strategy is to consider that the flame does not have the time to heat up the walls, hence the use of isothermal boundary conditions [220, 269]. A second strategy, often chosen in finger flame theory and simulations is the adiabatic boundary condition [6, 31, 32]. In practice, the influence of cold walls on flame acceleration is critical if the flame is reasonably slow: considering adiabatic will tend to promote this acceleration as it suppresses the heat necessarily lost by the flame, and isothermal conditions are only valid under the assumption that the flame is too fast to pre-heat the walls and when thermal resistance is low. It tends to underestimate the acceleration. Due to the large difference in thermal conductivity between metallic and acrylic surfaces in this experimental scenario, heat fluxes are neither zero (adiabatic), nor the one of the isothermal case. They lie in between and must be modelled. Two approaches are available. The first one consists in coupling fluid simulation to solid simulation in order to resolve unsteady temperature gradients inside the thickness of the walls. The second approach neglects transversal conduction and models walls with constant thermal resistance. The resistance depends on the material of the wall and its thickness, and the problem at hand becomes a 1D conduction problem [118]. In order to obtain preliminary results, the second approach is selected. The first approach is kept for future iterations.

Before elaborating a strategy to determine proper constant thermal resistances in this case, a first estimation of the conduction convection balance is proposed. The Biot number Bi is introduced to compare convection fluxes to conduction fluxes at the walls, inside the channel:

$$Bi = \frac{h\delta_w}{C_{th}} \quad (13.1)$$

where h is the convective heat transfer coefficient between the fluid and the wall, δ_w is the wall thickness and C_{th} is the material's thermal conductivity. To estimate h in the present application, the flow at one wall is considered to be burnt gases at $\phi = 1.03$ moving at the average experimental flame front speed $V = 16.8 \text{ m}\cdot\text{s}^{-1}$ over a flat plate. Introducing the Nusselt number Nu , the average of h can be approximated by $Nu\frac{\lambda}{L}$, where $L = 1.0 \text{ m}$ is the length of plate and $\lambda = 0.156 \text{ W}\cdot\text{m}^{-1}\cdot\text{K}^{-1}$ is the thermal conductivity of the burnt gases. As recalled by [175], Nusselt number correlations have been empirically derived, and for a laminar flow parallel to a plane surface it is defined as:

$$Nu \simeq 0.664 Re_L^{\frac{1}{2}} Pr^{\frac{1}{3}} \quad (13.2)$$

where $Re_L \simeq 6.6 \times 10^4$ is the Reynolds number associated to the length of the tube, and $Pr \simeq 0.68$ is the Prandtl number in the burnt gases ($Re_L < 5.0 \times 10^5$ and $Pr > 0.6$ are in the validity limits). The numerical application gives $h \simeq 17.6 \text{ W.m}^{-2}.\text{K}^{-1}$. By assuming wall thicknesses of the order of $\delta_w = 2.0 \text{ mm}$, more than an order of magnitude can separate the Biot number at metallic surfaces from the Biot number for optical accesses such that, for example, for stainless steel $C_{th} \simeq 14 \text{ W.m}^{-1}.\text{K}^{-1}$ gives $Bi_{steel} \simeq 0.0025$ and for acrylic glass $C_{th} \simeq 0.2 \text{ W.m}^{-1}.\text{K}^{-1}$ gives $Bi_{acrylic} \simeq 0.18$. Two conclusions arise:

1. The low value $Bi_{steel} = 0.0025 \ll 1$ means that metallic surfaces will tend to reproduce conditions close to isothermal at the atmospheric temperature.
2. The value $Bi_{acrylic} = 0.18$ means that acrylic surfaces may pose more problems as higher resistance coupled with the inherent transience of the phenomenon at hand may justify the use of a solid/gas coupled approach. Asserting the errors introduced by this first approach consisting in working with classical thermal resistances is part of future works where code coupling will be used to solve temperature gradients inside the wall. Similarly, radiation through the optical access may play a role, neglected for this first step.

In this chapter, constant thermal resistance write as $R_{th} = \delta_w / C_{th}$. It is proposed to evaluate the effect of this thermal resistance on the flame acceleration by changing the thickness δ_w . Asymptotically, an infinite thickness represents an adiabatic wall, a thickness equal to zero, an isothermal wall. To take into account the difference in materials used for the walls experimentally, it is chosen to model upper and lower channel walls by stainless steel ($C_{th} \simeq 14.0 \text{ W.m}^{-1}.\text{K}^{-1}$) and the optical access window with acrylic resin ($C_{th} \simeq 0.2 \text{ W.m}^{-1}.\text{K}^{-1}$). To ensure symmetry, the hanging wall in front of the window is modeled with the same material (See Fig. 13.4.1). The same thickness is used for the four channel walls. Changing this parameter could also be a perspective in further studies. The atmospheric temperature $T_{atm} = 293 \text{ K}$ is taken as the external wall temperature, considering the short timing of the experiment letting no time for heating.

First, to test the extremes, two simulations are performed and compared to the experimental results using the reference mesh Mesh 1.0/1.0: the first one uses adiabatic boundary ($\delta_w \rightarrow \infty$), the second one is close to isothermal ($\delta_w = 1.0 \text{ mm}$) for the an equivalence ratio of $\phi = 1.03$. Figure 13.4.2 gives visualizations of the flame propagation until the transition to a tulip flame. As it was observed in many other cases [72, 47, 215], the classical mechanism of tulip flame formation takes place. After the ignition, the spherical flame propagates slowly until confinement acts to form a finger flame, where the skirt of the flame extends from the tip to the

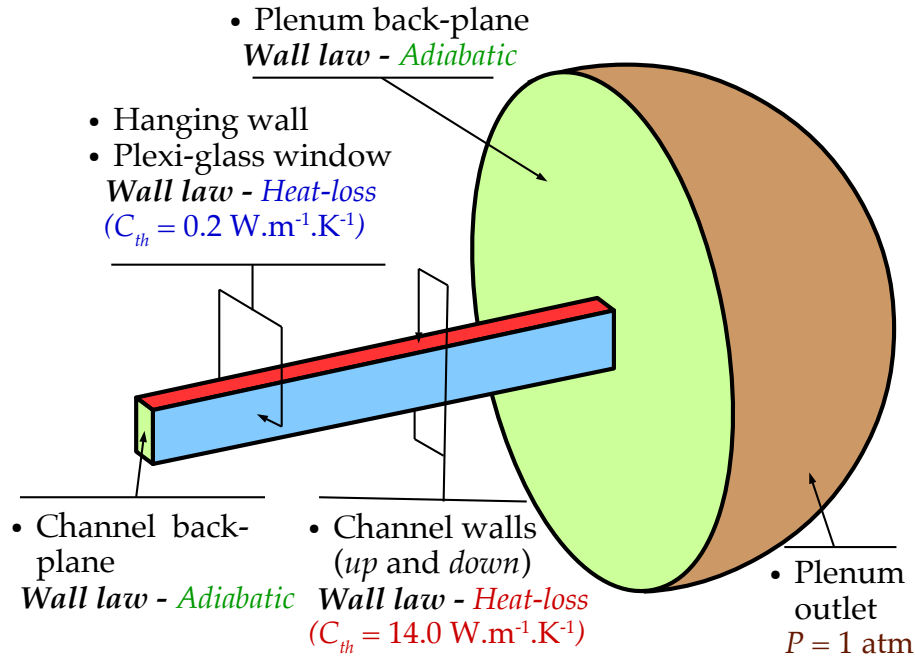


Figure 13.4.1: Choice of boundary conditions to experiment the effect of thermal resistance on flame acceleration.

back-plane. At $t = 36 \text{ ms}$, the flame extinguishes at the wall starting from the back-plane, reducing drastically the flame surface, and hence its speed, and the flame flattens. A tulip flame appears after the tip is drawn backward by an hydrodynamic unbalance between the flow in the burnt gases and the inertia of fresh gases pushed forward. Once formed, the flame continues to propagate under this form.

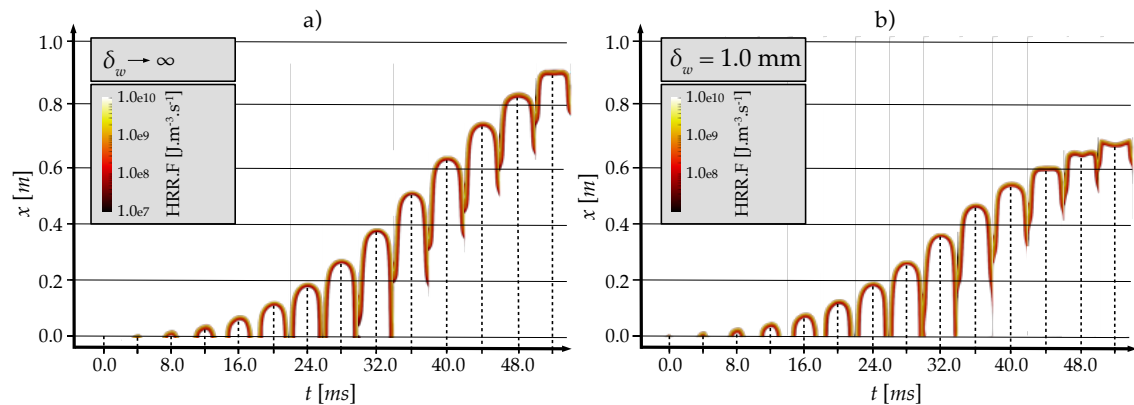


Figure 13.4.2: Flame propagation depicted as a z-normal cut of the heat release rate multiplied by thickening: a) adiabatic case $\delta_w \rightarrow \infty$, b) $\delta_w = 1.0 \text{ mm}$.

The effect of boundary conditions can already be seen in Fig. 13.4.2 and is confirmed in Fig. 13.4.3, where flame tip positions and velocity are depicted. In simulations, this position is obtained by tracking the x -position of the leading point of the heat release rate iso-contour level $1.0 \times 10^7 \text{ J.m}^{-3}.\text{s}^{-1}$. In comparison to the experimental results, the adiabatic case tends to promote flame acceleration such

that the transition to the slow tulip flame appears later. It induces errors directly on the peak velocity. On the contrary, the low thermal resistance case transitions early with a low peak velocity and slow propagation afterwards. Concerning overpressure prediction (see Fig. 13.4.4), as it is directly linked to flow velocity, the tendency is well retrieved until $t = 36$ ms with the succession of two positive peaks. The adiabatic case tends to over-predict peaks, a tendency corrected in the low thermal resistance case. The negative peak that follows is well captured by this latter case, but largely dampened with adiabatic boundary conditions. The phase that follows is characterized by strong pressure oscillation in the experimental results which are only partly retrieved by simulations (something already observed by Henriksen *et al.* [111] in the original publication). One principal reason advanced could be the fact that waves reflect on the walls in the laboratory, which is not acting as a perfect relaxing plenum, inducing resonance inside the channel. The pressure oscillations also influence the flame tip velocity, hence the large jumps observed in the final stage of the flame propagation (see Fig. 13.4.3).

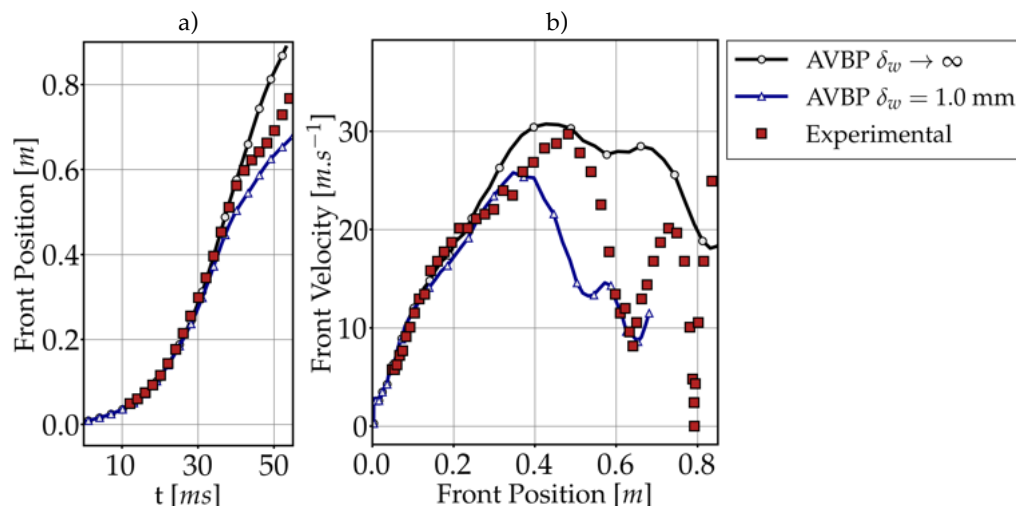


Figure 13.4.3: Experimental/simulation comparison of flame tip position and velocity for $\delta_w \rightarrow \infty$ and $\delta_w = 1.0$ mm: a) Flame front position *versus* time, b) Flame front velocity *versus* the flame front position.

Conclusions on this first familiarization with simulation are:

1. In the first finger flame stage, the agreement between experimental and simulation is good, both in terms of flame tip position/velocity and overpressure measurements, and this conclusion is largely independent from the boundary conditions.
2. Tulip flame transition is delayed with adiabatic walls, overpredicting flame tip velocity and overpressure in the channel
3. Tulip flame transition happens too early with low resistive walls, underpredicting flame tip velocity.

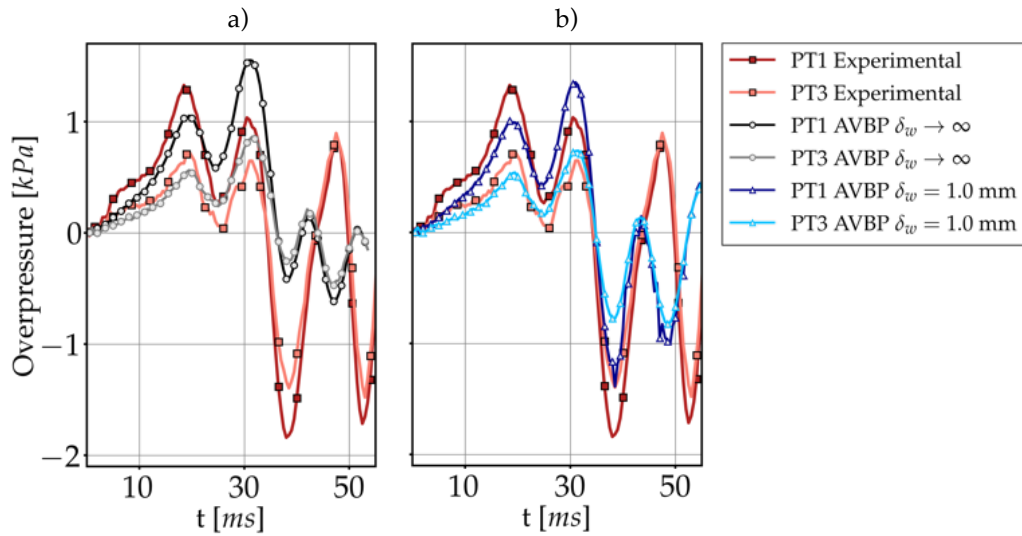


Figure 13.4.4: Experimental/simulation comparison of PT1 and PT3 overpressure (see Fig. 13.3.1 for sensor positions): a) $\delta_w \rightarrow \infty$, b) $\delta_w = 1.0$ mm.

4. After a certain time, pressure oscillations inducing large velocity changes are observed experimentally and only partly retrieved by means of simulation.

Heat losses at the wall can have a strong influence on a rather slow flame, where the finger-flame stage can heat walls. In view of the results presented here, an optimal thickness should be found to better model the flame propagation in the channel, correcting most of the flaws of the simulation. To avoid costly wild guesses, a procedure to link a macroscopic measure that can be obtained in both simulations and experiments to the wall thickness is proposed further, helping to fit heat losses at the wall. This fitted case will be transposed in other conditions (equivalence ratio, other gaseous mixtures, turbulent cases), leading to a better confidence in predictions regarding flame propagation speeds and overpressures.

Concerning the pressure oscillations, it is decided to first discard the phenomenon, mainly induced by uncontrolled laboratory-scale parameters. A perspective to test the hypothesis of wall bouncing waves would be to add the walls in simulations, which would increase drastically the cost of a simulation due to the size of the mesh.

13.4.2 A procedure to better define boundary conditions

The objective of this section is to use a minimal number of simulations to 1. obtain a finer understanding of the influence of heat losses at the walls and 2. propose a fitted wall thickness that can be further used in configurations where mixtures are changed or obstacles are added. Such an optimization to better render wall losses has been performed for a combustion chamber in [3, 2]. In addition to the two

simulations proposed in the previous section, two simulations with $\delta_w = 2.0$ mm and $\delta_w = 4.0$ mm are computed. To compare cases, a macroscopic measure is made on each case by proposing the "error to adiabatic" $\bar{\epsilon}$, so that for one *case*:

$$\epsilon(t) = x_{adiab}^{tip}(t) - x_{case}^{tip}(t) \quad (13.3)$$

$$\bar{\epsilon}_N = \frac{1}{N} \sum_{n=0}^{N-1} \epsilon(n\Delta t) \quad (13.4)$$

where x^{tip} is the position of the flame tip, Δt is the constant time-step separating two flame tip position evaluations, $[0, N\Delta t]$ is the interval on which the average is performed. $N\Delta t$ is chosen to correspond to the onset of the tulip flame in the adiabatic case ($t = 52.0$ ms). $\bar{\epsilon}$ is defined for both simulation cases and experimental cases, such that it is made easy to compare one computation result to the experimental reference and the adiabatic simulation.

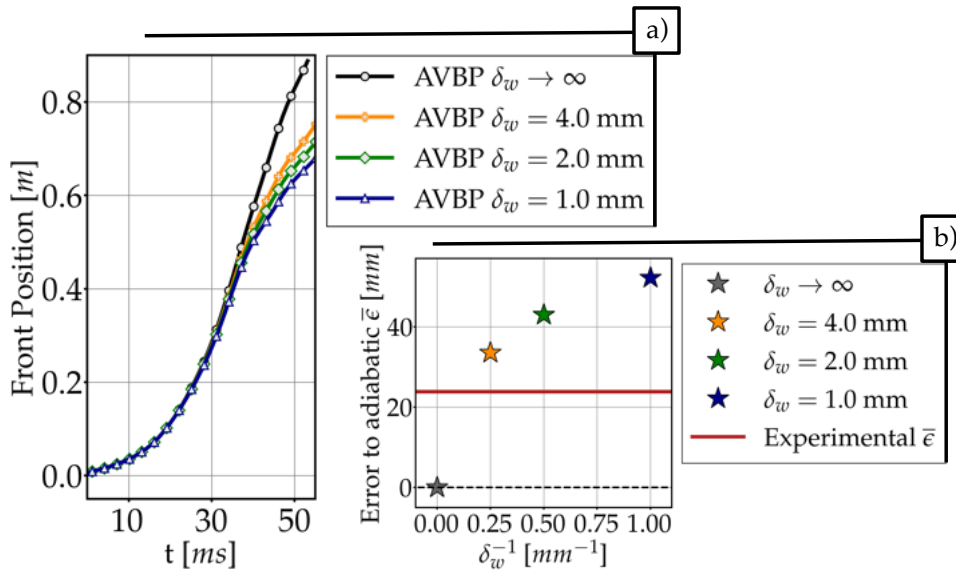


Figure 13.4.5: Comparison of flame tip position for varying δ_w : a) Flame front position versus time, b) error to adiabatic $\bar{\epsilon}$.

Figure 13.4.5 depicts that the error to adiabatic $\bar{\epsilon}$ decreases with the thickness δ_w , and crosses the error to adiabatic computed for the experimental acquisition. Therefore, there is an optimal thickness δ_w^* to search such that the error to adiabatic of the simulation matches the experiment. However, a very simple question arises: what is a proper fitting procedure to link $\bar{\epsilon}$ to δ_w^{-1} ? One first initiative could be to produce a linear fit, and correct it successively by adding simulations until convergence is reached. As this is costly, a more convenient approach could be to propose a fitting function that inherits from the physics of the problem, even if a perfect theoretical relation is not obtainable. To start with, let us model the flame by a finger flame, using the theory of Bychkov *et al.* [31]:

$$\frac{d}{dt}x^{tip} = \frac{\rho_f}{\rho_b} \frac{2}{r_{eq}} U x^{tip} \quad (13.5)$$

where ρ_f (resp. ρ_b) is the fresh (resp. burnt) gas density, r_{eq} is the equivalent radius of the flame: $r_{eq} = ab/(a+b)$, with a , b as height and width of the channel. U is the flame propagation speed. In the adiabatic case, $U = U_{adiab}$ (in the theory, $U_{adiab} = S_L$, the laminar flame speed). In order to model the effect of non-adiabatic conditions, a correction is searched to reduce the flame propagation speed so that with losses $U = U_{loss} = U_{adiab} - \alpha$. To find α , the integral of the energy conservation for the non-adiabatic flame is approximated by:

$$c_p(T_b - T_f)\rho_f A U_{loss} = c_p(T_b - T_f)\rho_f A U_{adiab} - (T_b - T_w) \frac{A}{R_{th}} \quad (13.6)$$

where c_p is the specific heat, T_f (resp. T_b) is the fresh (resp. burnt) gas temperature, A is the flame surface, T_w is the wall temperature, and R_{th} is the wall thermal resistance. For simplification purposes, $T_w = T_f$, and $R_{th} = \delta_w/C_{th}$. Equation 13.6 gives:

$$U_{loss} = U_{adiab} - \frac{C_{th}}{\rho_f c_p} \delta_w^{-1} \quad (13.7)$$

which leads to $\alpha = \frac{C_{th}}{\rho_f c_p} \delta_w^{-1}$. The influence of the thickness δ_w on flame propagation appears as a corrective term on its propagation velocity. Using the definition of ϵ given in Eq. 13.3, an order one differential equation in time is obtained:

$$\frac{d}{dt}\epsilon = -\frac{2C_{th}}{\rho_b c_p r_{eq}} \delta_w^{-1} \epsilon \quad (13.8)$$

With $\sigma = \frac{2C_{th}}{\rho_b c_p r_{eq}}$, and because $\epsilon(0) = 0$, a constant $B > 0$ exists such that, for $t > 0$:

$$\epsilon(t) = B \left(1 - \exp(-\sigma \delta_w^{-1} t)\right) \quad (13.9)$$

Over the interval $[0, N\Delta t]$, the error to adiabatic writes as:

$$\begin{aligned} \bar{\epsilon}_N &= \frac{1}{N} \sum_{n=0}^{N-1} B \left(1 - \exp(-\sigma \Delta t \delta_w^{-1} n)\right) \\ &= B \left(1 - \frac{1}{N} \frac{1 - \exp(-\sigma \Delta t \delta_w^{-1} N)}{1 - \exp(-\sigma \Delta t \delta_w^{-1})}\right) \end{aligned} \quad (13.10)$$

Asymptotically, the relation is coherent with the fact that when going closer to adiabatic, δ_w tends towards infinity, the ratio containing the exponential terms is equivalent to N/N , thus leading to $\lim_{\delta_w \rightarrow +\infty} \bar{\epsilon}_N = 0$. Similarly, when reaching isothermal boundary, δ_w tends towards 0, leading to $\lim_{\delta_w \rightarrow 0} \bar{\epsilon}_N = B(1 - 1/N)$, a positive constant depending on the width of the averaging interval.

It is important to notice that the relation obtained in Eq. 13.10 is only valid for a very restrained area (early finger flame) and *a priori*, it does not apply to the problem at hand. Therefore, it is not necessary to try to search directly numerical values of B and σ . However, it gives information on the type of function that could lead to a proper fitting of $\bar{\epsilon}$ as a function of δ_w^{-1} . It guides towards searching a function under the form:

$$f_{fit}(\delta_w^{-1}, N) = B' \left(1 - \frac{1}{N} \frac{1 - \exp(-\sigma' \delta_w^{-1} N)}{1 - \exp(-\sigma' \delta_w^{-1})} \right) \quad (13.11)$$

where B' and σ' are the parameters to fit. Under this assumption, a simple fitting procedure can be performed on the results depicted in Fig. 13.4.5 which leads to the constants $B' = 60.24 \text{ mm}$ and $\sigma' = 0.19 \text{ mm}$, for $N = 40$ steps. The model is shown in Fig. 13.4.6. Thanks to this very simple model, it is possible to obtain the optimal δ_w^* which corresponds to a thickness of 6.73 mm. A simulation is performed with this value and added to Fig. 13.4.6. Its value of $\bar{\epsilon}$ is 15 % higher relative to the experimental target. *A posteriori*, a model can be fitted again (see Fig. 13.4.6) and the process could be repeated with to update the value of δ_w^* for even better convergence.

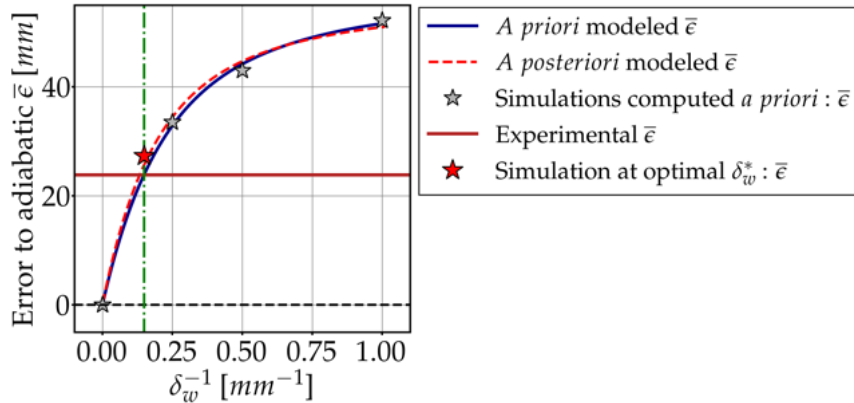


Figure 13.4.6: Model of the error to adiabatic as a function of δ_w^{-1} , simulation results *a priori* and *a posteriori*.

In the next sections, and with $\delta_w^* = 6.73 \text{ mm}$, a complete validation of the simulation setup *versus* experimental results can be done, including mesh refinement effects and comparisons to cases with different equivalence ratios.

13.4.3 Effect of mesh refinement

Once an optimal wall thickness δ_w^* is found, it is possible to observe the effect of mesh refinement on flame propagation. It serves two main objectives: 1. evaluate what finer cells at the walls change in terms of prediction precision, 2. Identify the limit of the thickened flame model in narrow channels with a coarser grid.

The reference simulation using the optimal wall thickness is computed using Mesh 1.0/1.0, refinement at the wall is asserted using Mesh 1.0/0.5, and the coarse simulation uses Mesh 2.0/2.0 (see Table 13.3.1). Figure 13.4.7 depicts the flame propagation in the reference case and can be easily compared to the other cases. It is completed by Fig. 13.4.8 for experimental *versus* simulation. To help comparisons, the flame propagation is divided into three phases: finger flame acceleration, tulip flame formation, constant speed tulip flame propagation (see Fig. 13.4.8 b).

Refining at the walls

The simulation using Mesh 1.0/0.5 includes cells of size 0.5 mm at the channel walls, helping to refine gradients. Figure 13.4.8 gives flame tip propagation properties. During the first phase (finger flame acceleration), both Mesh 1.0/1.0 and Mesh 1.0/0.5 give similar values of velocity and fit properly experimental flame tip position. The shape of the flame at the end of this phase are also very similar (see Fig. 13.4.9 at $t = 34.0$ ms). Concerning the second phase, it appears that the transition toward the tulip flame occurs faster experimentally than in the simulation.

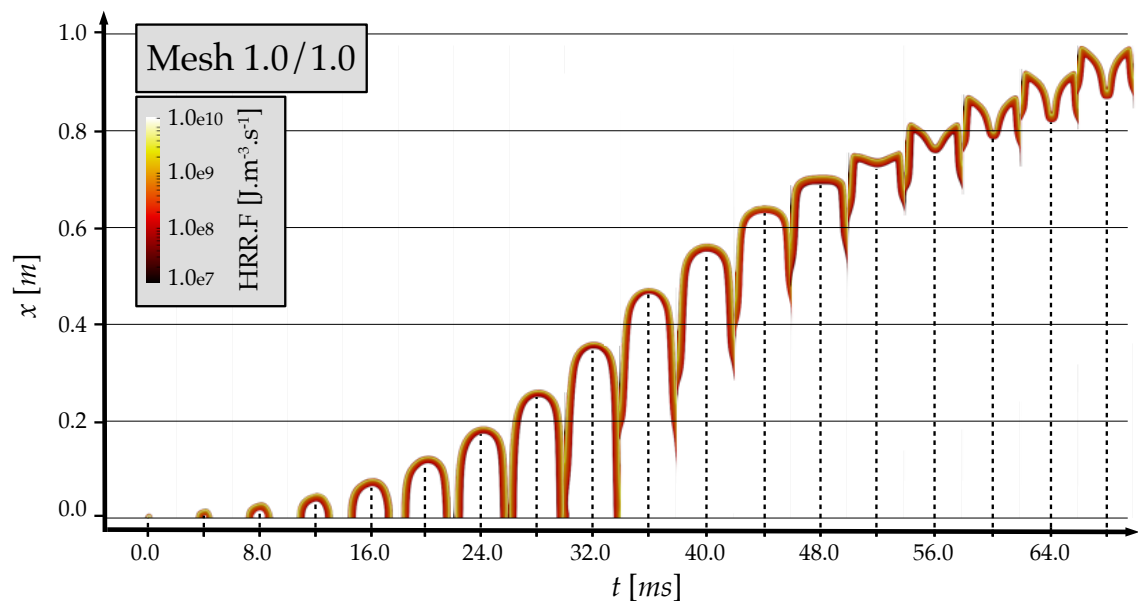


Figure 13.4.7: Flame propagation depicted as a z-normal cut of the heat release rate multiplied by thickening at $\phi = 1.03$, with the optimal δ_w^* for Mesh 1.0/1.0.

Furthermore, this transition is faster for the mesh refined at the walls. In their work, Ponizy *et al.* [215] have identified that the flow of unburnt gases close to walls pulling the flame in the axial direction is one of the crucial mechanisms of tulip flame formation. A poor resolution at the wall must have a direct influence on the quality of the prediction of this mechanism. Furthermore, the shape of the tulip flame in the last phase is different between the two meshes: the wall refined mesh produces a deeper tulip (see Fig. 13.4.9 at $t = 68.0$ ms).

Three first conclusions concerning mesh refinement can be made. First of all, flame position and velocity are well retrieved by both Mesh 1.0/1.0 and Mesh 1.0/0.5, ensuring that the general dynamics of the flame is correctly simulated. The fitted δ_w^* holds in the refined case, giving overall similar results. Then, wall mesh refinement has an influence on the tulip flame formation and final tulip flame shape meaning that a wall resolved simulation would produce more precise results. Lastly, the cost of the wall refined simulation is already 2.56 times higher ² due to the increase in mesh size and decrease in simulation time step. Even if further refinement would help to conclude on the exactitude of the mechanisms involved, the cost becomes a direct limitation.

Coarse mesh

There is a strong interest in testing coarser meshes as it would ensure faster results. However, limitations are directly observed with Mesh 2.0/2.0. Figure 13.4.8, shows

²An average of $859.8 \text{ hCPU.ms}_{phys}^{-1}$ versus $336.2 \text{ hCPU.ms}_{phys}^{-1}$ on 25×2 Intel Cascade Lake CPU (1000 cores).

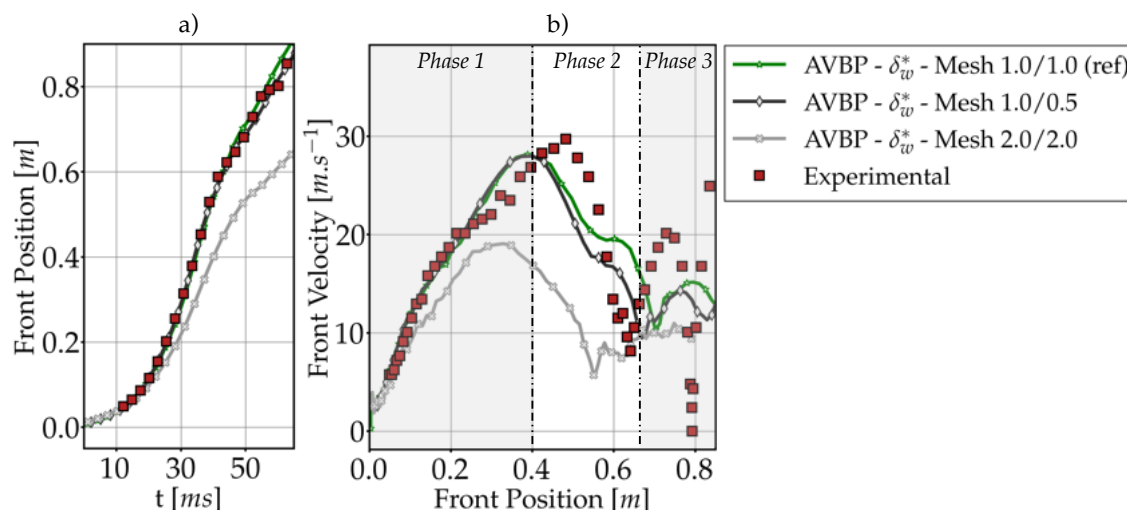


Figure 13.4.8: Experimental/simulation comparison of flame tip position and velocity at $\phi = 1.03$, with the optimal δ_w^* : a) Flame front position *versus* time, b) Flame front velocity *versus* the flame front position.

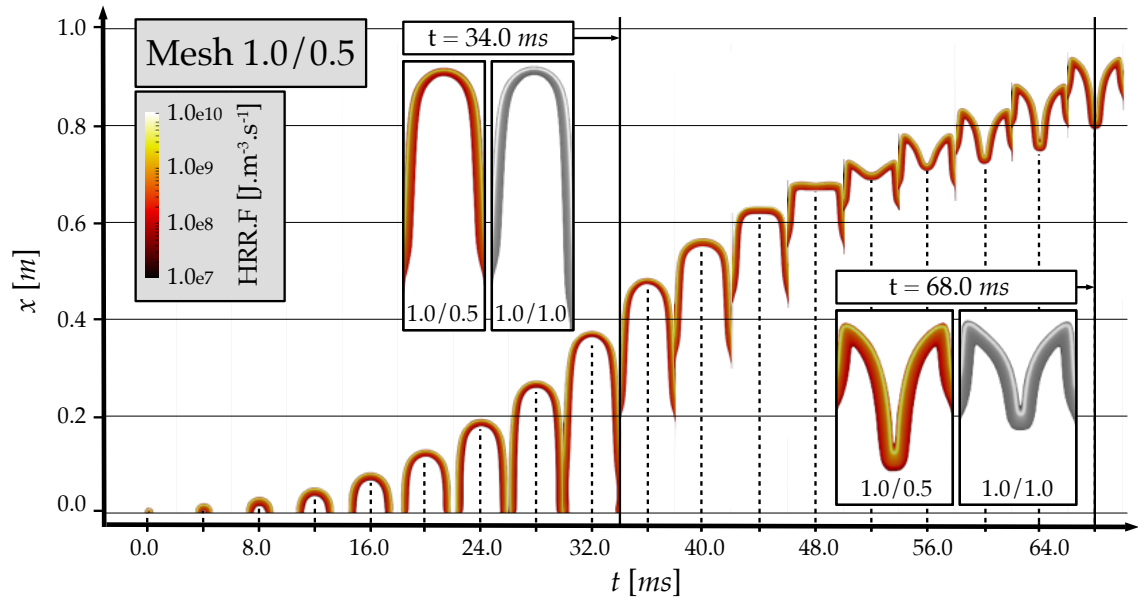


Figure 13.4.9: Flame propagation depicted as a z-normal cut of the heat release rate multiplied by thickening at $\phi = 1.03$, with the optimal δ_w^* for Mesh 1.0/0.5.

that the coarse simulation agrees well with experiment and finer simulations during the first 20 ms of flame propagation. However, as the flame gets closer to the walls, the acceleration rate reduces slightly, creating a drift in the solution. The maximum speed of the flame is reached sooner, and at a value 30 % lower than expected. A tulip is formed, but due to the thickening ($F \simeq 38.0$), its shape including the entire reaction zone (see Fig.13.4.10) is broad, and barely fits inside the channel. It is also important to recall that the width of the channel is 65 mm making it nearly impossible to fit correctly a flame folded multiple times to form a tulip, without inducing blockage, and therefore slow-down.

A coarse mesh becomes a limitation when considering narrow channels and phenomena involving complex-shaped flames with strongly dynamic transition behaviors, using the thickened flame model. A sufficient number of points is to be targeted to meet the experimental results. However, the phenomenon of tulip flame appears to be easily reproduced, even with largely under-refined conditions, which, as suggested by Ponizy *et al.*, the sign of simple flow patterns.

Conclusion on mesh refinement

When refining the mesh at the walls, positive effects are observed on the transition time between finger and tulip flames. The tulip flame appears to be deeper in this case than with the reference Mesh 1.0/1.0. Effects are however minimal on the overall flame propagation with coherent flame tip position and velocity profiles. Inversely, a very coarse mesh will reduce drastically the acceleration rate of the

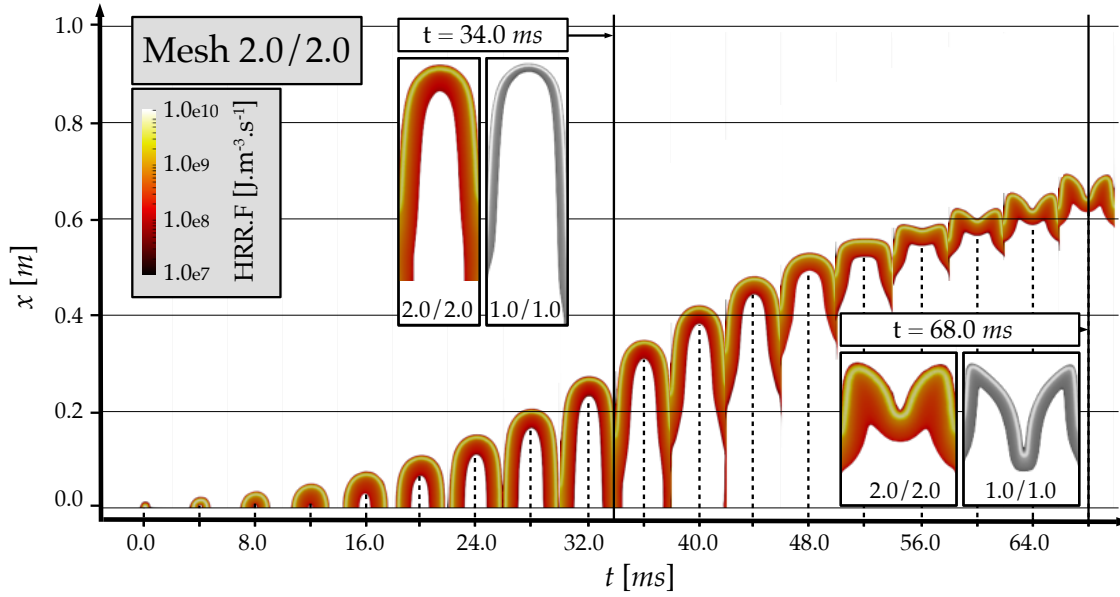


Figure 13.4.10: Flame propagation depicted as a z-normal cut of the heat release rate multiplied by thickening at $\phi = 1.03$, with the optimal δ_w^* for Mesh 2.0/2.0.

flame after it reaches the wall, inducing a lag between experimental and simulation. Based on these results, it is decided to continue the study with Mesh 1.0/1.0 as it accommodates more advantages. Tests with intermediate meshes between the coarse and the reference could be a perspective to this work. Also, Adaptive Mesh Refinement (AMR) would be a good candidate to continue with this study, both for laminar and turbulent cases [19, 190].

13.4.4 Final experimental/simulation validation

Eventually, using Mesh 1.0/1.0 and δ_w^* , a full validation of the simulation setup can be performed for three equivalence ratios: $\phi = 1.03$, $\phi = 1.19$, and $\phi = 0.77$ (see Fig. 13.4.13 p. 217). Figure 13.4.11 compares flame front position and velocity for simulation and experimental cases. Concerning flame tip position, a good agreement is reached for the three equivalence ratios targeted. To measure the drift of the simulation in comparison to the experiment, the average error with respect to the experimental results $\bar{\epsilon}_{exp}$ is computed:

$$\bar{\epsilon}_{exp} = \frac{1}{N} \sum_{n=0}^{N-1} (x_{sim}^{tip}(n\Delta t) - x_{exp}^{tip}(n\Delta t)) \quad (13.12)$$

where $[0, N\Delta t]$ is the interval where experimental results exist. For $\phi = 1.03$ (resp. $\phi = 1.19$ and $\phi = 0.77$), this average drift reaches +2.7 mm (resp. -16.8 mm and +26.2 mm). The low absolute value for $\phi = 1.03$ is reassuring as it confirms that the fitting procedure allows to successfully capture the flame displacement.

For $\phi = 1.19$ the negative value means that, on average, the simulated flame lags behind the experimental flame, but this lag remains low for a flame propagating in a 1.0 m-long tube, and an explosion event that lasts more than 70.0 ms. The conclusion is similar for $\phi = 0.77$, where the positive drift is of the order of magnitude of the hundredth of the tube length. In addition, the relative error on the peak velocity $|V_{sim}^{peak} - V_{ref}^{peak}|/V_{ref}^{peak}$ is computed, and reaches 5.3 % at $\phi = 1.03$, 10.9 % at $\phi = 1.19$, and 4.1 % at $\phi = 0.77$. Additionally, the transition position defined as the flame front position at which the simulated peak velocity is reached is 83.9 mm behind experimental (too early) at $\phi = 1.03$, 101.9 mm behind at $\phi = 1.19$, and 23.6 mm behind at $\phi = 0.77$ which represents errors of the order of 10 % of the tube length. Thus, finger-tulip transition position is only reasonably well predicted by simulation for the three equivalence ratios considered, and it remains a subject of improvement for future works.

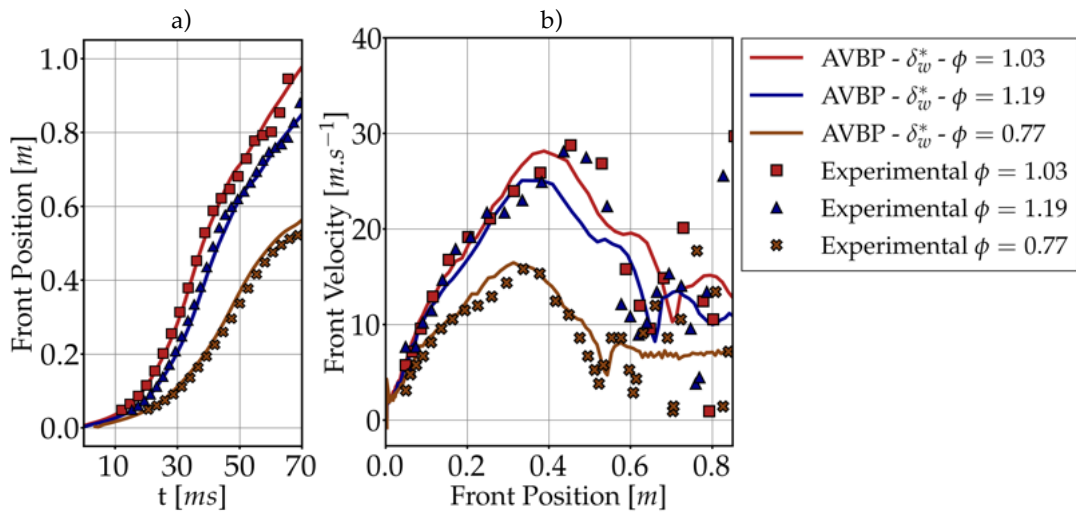


Figure 13.4.11: Experimental/simulation comparison of flame tip position and velocity for δ_w^* : a) Flame front position *versus* time, b) Flame front velocity *versus* the flame front position.

The comparison of overpressure sensor data to computed overpressure gives further information on the quality of the simulation (see Fig. 13.4.12). Maximum overpressure levels for the first sensor (PT1) are well retrieved by simulations (with relative errors lower than 10 % for all the equivalence ratios). The temporal succession of pressure peaks is predicted consistently, with two positive impulses followed by a negative one. However, when looking into details, a peak-to-peak comparison reveals that there are discrepancies. Experimentally, the first peak is higher than the second one, and it is inverted in the simulation. Also, the negative peak that follows is underpredicted by simulation. Finally, the effect of large oscillations assumed to be due to acoustic resonance of the tube are not perfectly recovered by simulation. In general, concerning pressure measurements, global levels and temporal responses are satisfactorily predicted. Differences are observed, and there are multiple ways to try to reduce them such as computing the acoustics at a laboratory scale to see its influence on tube resonance or improving the mesh refinement inside the channel.

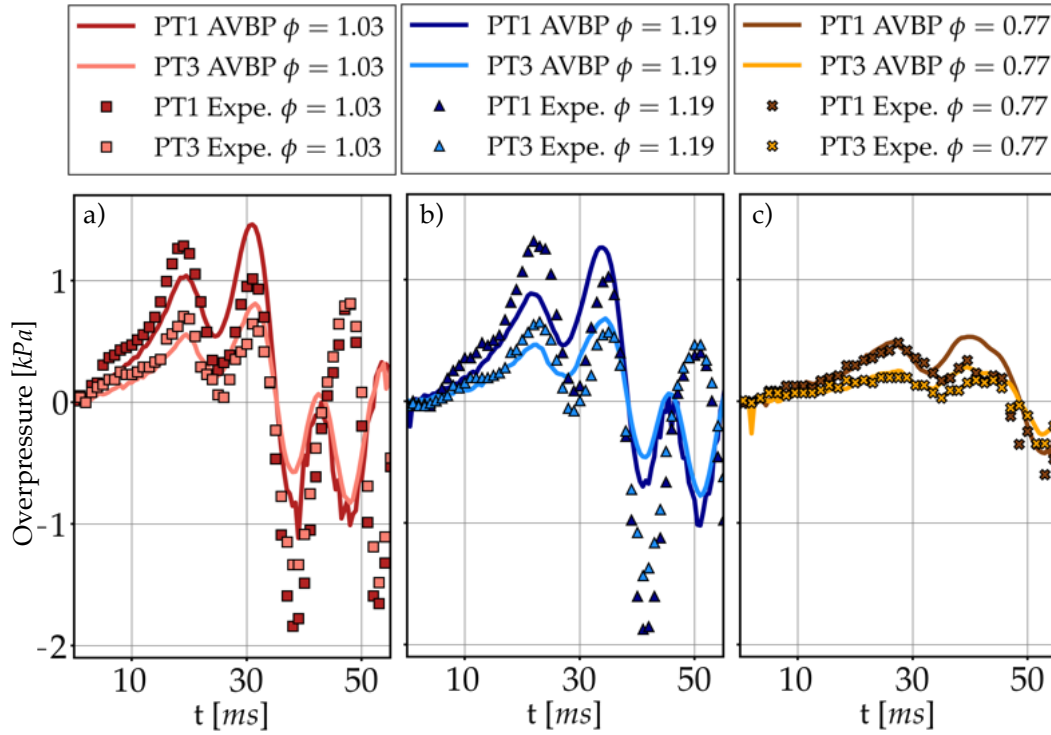


Figure 13.4.12: Experimental/simulation comparison of PT1 and PT3 sensors overpressure for δ_w^* : a) at $\phi = 1.03$, b) at $\phi = 1.19$, c) at $\phi = 0.77$.

Table 13.4.1 summarizes the magnitudes compared between experimental and simulation for the three equivalence ratios considered.

Table 13.4.1: Summary of the comparison between experimental and simulation for $\phi \in \{0.77, 1.03, 1.19\}$, and the optimal δ_w^* simulation case.

	$\phi = 1.03$	$\phi = 1.19$	$\phi = 0.77$
Average drift $\bar{\epsilon}_{exp}$ (Eq. 13.12)	2.7 mm	-16.8 mm	26.2 mm
Peak velocity error $ V_{sim}^{peak} - V_{ref}^{peak} / V_{ref}^{peak}$	5.3 %	10.9 %	4.1 %
Transition position $x_{sim}^{V^{peak}} - x_{ref}^{V^{peak}}$	-83.9 mm	-101.9 mm	-23.6 mm
PT1 Peak pressure error $ P_{sim}^{PT1,peak} - P_{ref}^{PT1,peak} / P_{ref}^{PT1,peak}$	10.0 %	4.1 %	6.4 %

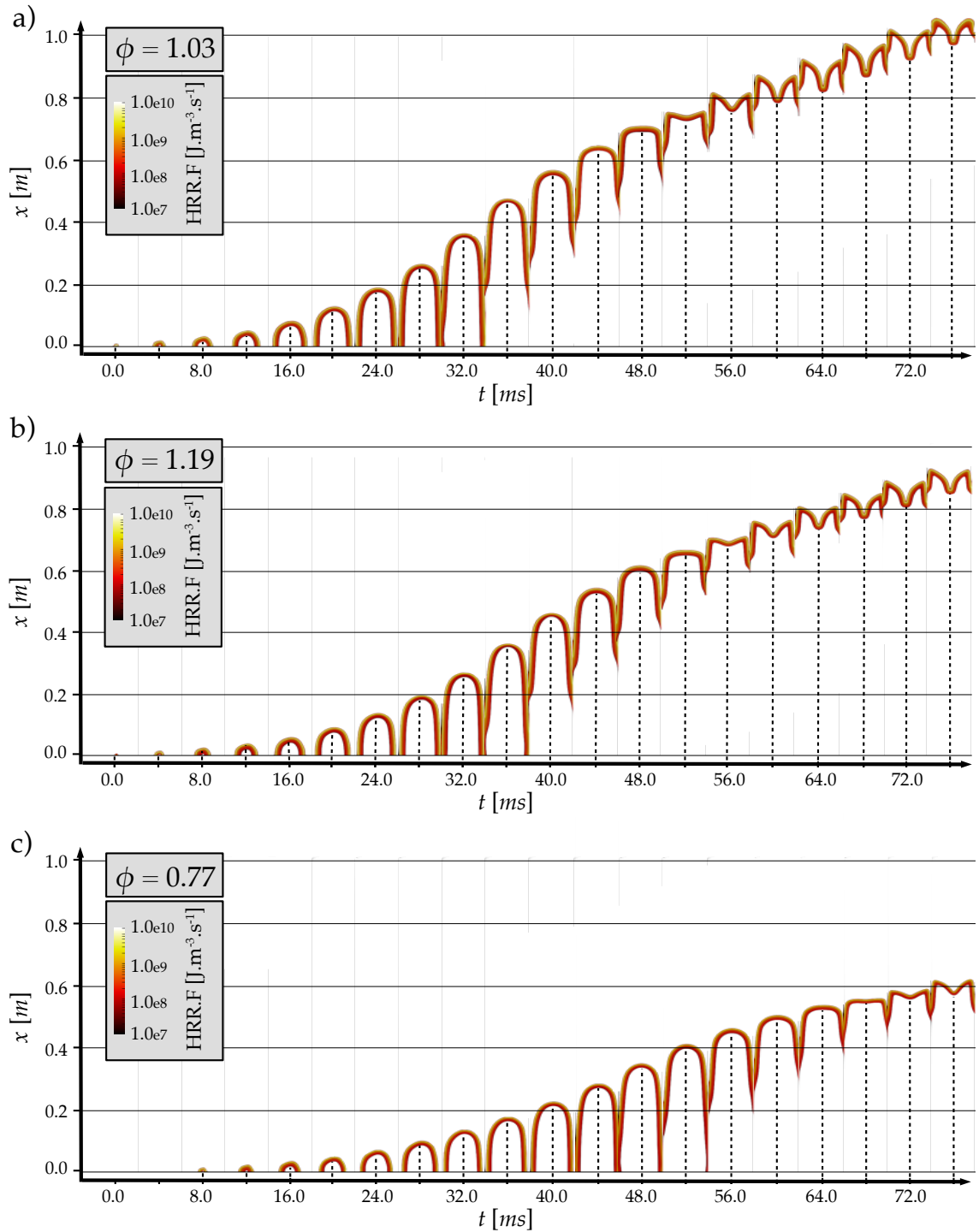


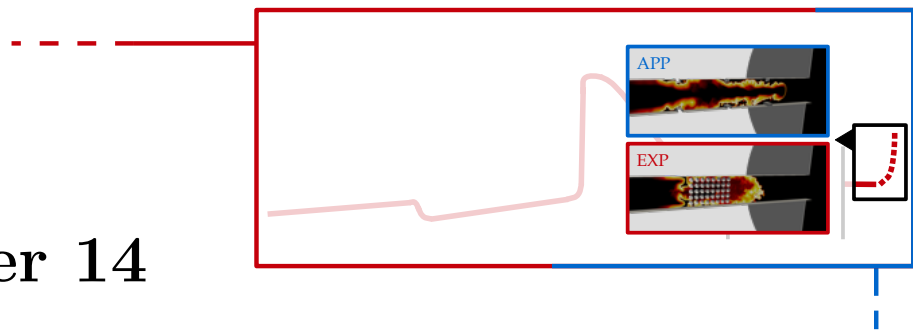
Figure 13.4.13: Flame propagation depicted as a z-normal cut of the heat release rate multiplied by thickening, with the optimal δ_w^* : a) at $\phi = 1.03$ b) at $\phi = 1.19$, c) at $\phi = 0.77$.

13.5 Concluding remarks

Through experimental *versus* simulation comparisons of flame front position/velocity and overpressure measurements, it is possible to validate the use of the simulation setup proposed here for the reproduction of finger-to-tulip flame transitions inside a rectangular channel with Li-ion vent gases at three different equivalence ratios. The effect of wall heat losses is observed, and a simple fitting procedure helps to close the gap between experimental and simulation by computing an optimal wall thickness δ_w^* .

Thanks to this first familiarization with the problem of explosion of Li-ion vent gases, it is possible to continue with qualitative comparisons of the effect of some parameters on explosion parameters. In the next chapter the test of configurations where turbulence interacts with the flame and preliminary comparisons on models are proposed.

Chapter 14



Towards more realistic explosion simulation applied to Li-ion

Contents

14.1 Turbulent explosion simulation	219
14.2 Experimental and numerical setup	220
14.2.1 Experimental setup	220
14.2.2 Numerical setup	221
14.3 Results and discussions	223
14.3.1 Profiles for the entire event	223
14.3.2 Laminar phase	225
14.3.3 Obstacle crossing	227
14.4 Perspectives for explosion scenarios	229

This chapter opens the perspective to the simulation of realistic explosion events inside battery modules, including the presence of obstacles, leading to flame turbulence interactions. The reproduction of an experimental explosion is proposed. The discussion helps to draw the plan for future works to expand on battery explosion.

14.1 Turbulent explosion simulation

Obstacle induced flame acceleration is a main topic of study for the combustion community concerned with explosion scenarios. Experimental studies have delivered state-of-the-art comparisons for CFD platforms. For example, the experimental works of Masri *et al.* [179, 133] or Boeck *et al.* [23] led to the validation of the use of

LES applied to explosion scenarios in presence of obstacles [100, 116, 101, 178, 220, 1, 272, 269, 24]. Application to the Li-ion battery explosion is however more recent, where the combination of vent gas composition and highly obstructed geometries render new complex scenarios. Henriksen *et al.* [112] proposed an experiment to combine these specificities, and offered first simulation results. In this chapter, the test rig is selected as a benchmark of the simulation framework prepared throughout the thesis, in complement of what has been presented in Chap. 13. This opens the perspectives to an application to larger scale batteries [205] where reduced explosion models are for now the only reasonable solutions [193, 265].

14.2 Experimental and numerical setup

14.2.1 Experimental setup

The experimental system is a continuation of the one presented in Chapter 13. It is proposed by Henriksen *et al.* [112, 109] to study the effect of obstacles on explosion parameters in the context of Li-ion.

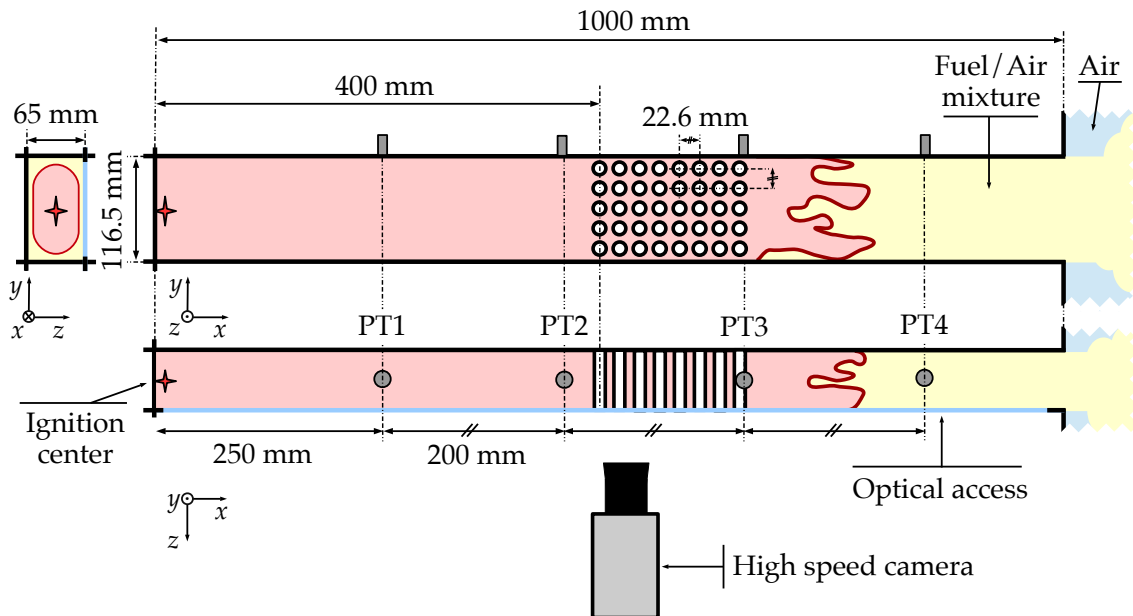


Figure 14.2.1: Schematic representation of the experimental setup proposed by Henriksen *et al.* [112] to assess Li-Ion vent gases explosions in presence of obstacles.

In addition to the laminar setup, forty 18650-cells-like obstacles are placed inside the channel. Figure 14.2.1 outlines the setup and its specificity. Multiple mixtures are tested in the original publication. A focus is made on one composition and one equivalence ratio in particular, where simulation results were presented and can be compared easily to the simulation results proposed in this manuscript. The

composition differs from the previous chapter. In volume fraction it is: H_2 : 42.8 %, CH_4 : 7.1 %, C_2H_4 : 3.0 %, CO : 37.1 %, CO_2 : 10.0 %. And the equivalence ratio is $\phi = 0.98$.

14.2.2 Numerical setup

The case proposed is an opportunity to continue the validation of the choices already made throughout the manuscript. The presence of a free turbulent flame accelerating through numerous obstacles creating a substantial blockage ratio (77 %), generates high levels of turbulence. Flow speed can be locally supersonic (obstacles exit plane). It is a complete scenario needing numerous models mentioned earlier: chemical kinetic scheme, flame modelling with flame-turbulence interaction, and shock modelling:

1. **Chemical kinetics:** The chemical kinetic scheme deployed in Chapter 6 is used. Figure 14.2.2 compares the detailed San Diego scheme (SD) and ARC when computing a 1D premixed laminar flame at $T = 300$ K with the mixture considered in this chapter. It consolidates the generalization capability of the scheme, already mentioned in Chap. 6 Sec.6.5. The overall larger flame speed due to a high level of hydrogen and low level of dilution in CO_2 enhances the potential of acceleration in comparison to the mixture of the previous chapter.

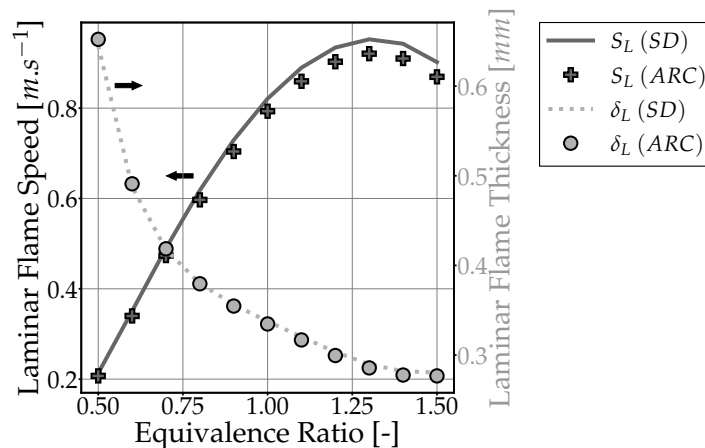


Figure 14.2.2: Simulation of a 1D premixed laminar flame using the Analytically Reduced Chemistry computed in Chapter 6 at $T = 300$ K. Comparison of the laminar flame speed S_L and the thermal flame thickness δ_L .

2. **Flame modelling:** The DTFLES approach presented in Chap. 4 Sec. 4.2.2 is selected. Concerning flame-turbulence interactions, it is proposed to assert three declinations of the Charlette model [39] (Eq. 4.17): 1. Constant parameter $\beta = 0.5$ (CC - 0.5), 2. Constant parameter $\beta = 0.8$ (CC - 0.8), 3.

Dynamically evaluated parameter (Charlette Dynamic with Saturated Mouri-
aux corrections - CDSM [40, 191]). For all cases, the efficiency is forced to one
during the laminar phase, before obstacles are encountered.

3. **Shock handling:** Due to the locally large velocity at the exit plane of the
obstacles, normal shocks are expected and must be handled. For its good
performance in presence of weak shocks, the LAD filtering sensor is preferred
in this case (see Chap. 4 Sec. 4.2.3 and Chap. 9).

The mesh is composed of 87.3 M tetrahedra, so that the refinement reaches
 $\Delta x = 0.5$ mm around the obstacles and $\Delta x = 1.0$ mm in the rest of the channel.
Figure 14.2.3 shows views of the mesh.

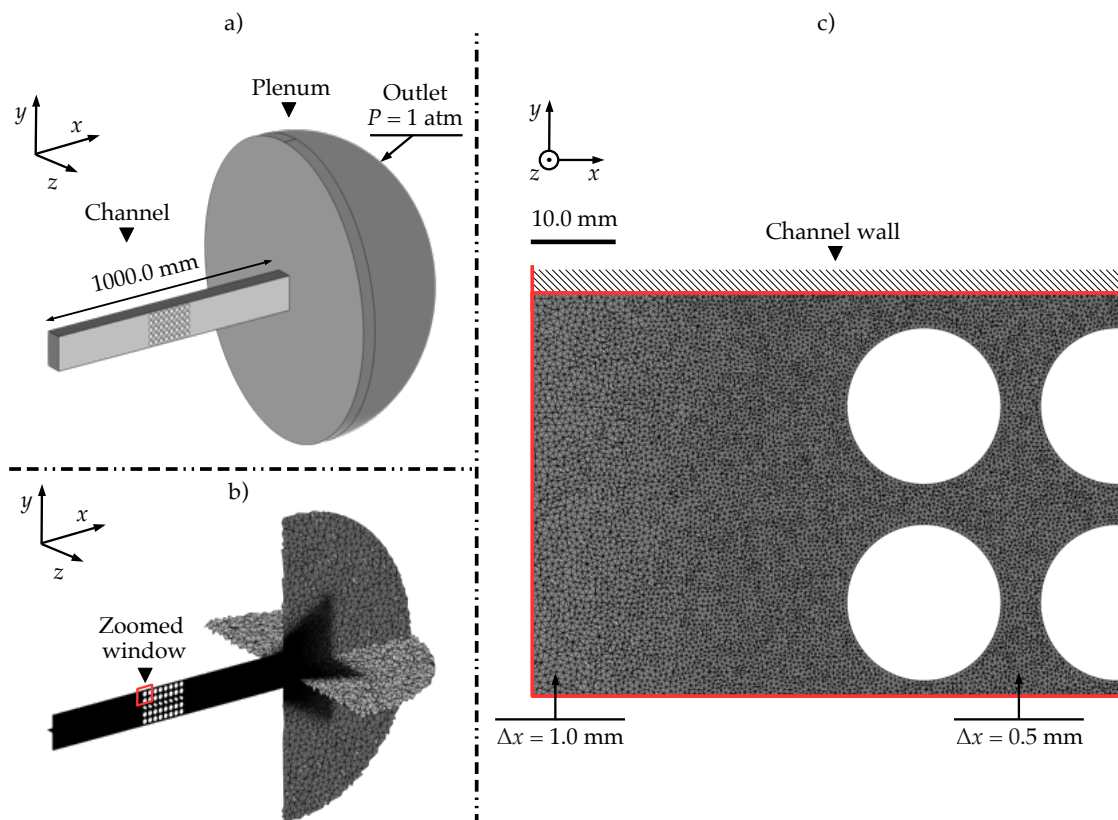


Figure 14.2.3: Description of the simulation case and the corresponding mesh: a) view of the case, b) z and y cuts of the mesh, c) zoom on the refined area containing obstacles.

The convection scheme is the one of Lax and Wendroff [152] with WALE as a subgrid scale turbulence model [199] to render wall-turbulence interaction. Turbulent Prandtl and Schmidt number are equal to 0.6. The CFL and Fourier numbers are 0.7 and 0.1 respectively. Second and fourth order artificial viscosity terms [125] are used to stabilize the computation.

Similarly to the Chapter 13, after the filling of the channel, ignition is triggered by imposing a hot temperature sphere at the closed end of the channel over a fixed

duration. The sphere temperature profile is Gaussian in time and space, and the maximum temperature is set to $T_{ig} = 3000$ K (App. B). The ignition sequence lasts 20 ms and is enclosed in a diameter of 2.0 mm. The NSCBC formalism is used for the outlet [260, 214, 198]. The outlet relaxes to the atmospheric pressure $P = 101\,325.0$ Pa. The heat loss modelling at the walls, necessary to retrieve properly the laminar phase is taken from the developments of Chapter 13 corresponding to a wall temperature of 293.0 K and a thermal resistance of 3.36×10^{-2} K.m².W⁻¹ for acrylic side surfaces (resp. 4.81×10^{-4} K.m².W⁻¹ for the upper and lower metallic surfaces).

14.3 Results and discussions

First, the focus is on showing the pressure and flame front position profiles obtained with simulation and comparing to experimental results. It is followed by more details on the different phases of the event, starting with the laminar phase and concluding by the obstacle crossing.

14.3.1 Profiles for the entire event

To begin with, overpressure measurements are compared with the experimental. Figure 14.3.1 gives the comparison between the three efficiency models and the experimental results. It appears right away that the high level of obstruction and inherent turbulent levels are the order one parameter to choose an efficiency parameter constant. The often cited parameter $\beta = 0.5$ (CC - 0.5) fails to properly find the overpressure level. The parameter $\beta = 0.8$ (CC - 0.8) gives better match between experimental and simulation with low errors for PT2, PT3, PT4 (resp. 17.1 %, 6.6 %, and 5.2 %). The error is larger for PT1 (51.5 %), located upstream in the burnt gases and receiving a pressure wave when the flame passes the obstacles. Sadly, the dynamic model CDSM fails in this case, despite the fact that it leverages values of β as high as 0.85 locally. Three main reasons can be advanced: 1. The number of obstacles and the thin passages makes the filtering procedure of the model difficult, 2. interactions between flame fronts are omnipresent due to the high level of turbulence and the saturation plays its role, and 3. The mesh refinement across this region (approximately 10 points in-between obstacles) is too coarse to perform a proper evaluation of the efficiency function.

Concerning the flame front position, Fig. 14.3.2 shows that the laminar phase is well retrieved by simulation, thanks to the fitting presented in the previous chapter. Case CC - 0.8 shows a good agreement with experimental. The average velocity after the first obstacle are crossed reaches 306.1 m.s⁻¹ in the simulation, and 261.4 m.s⁻¹ experimentally.

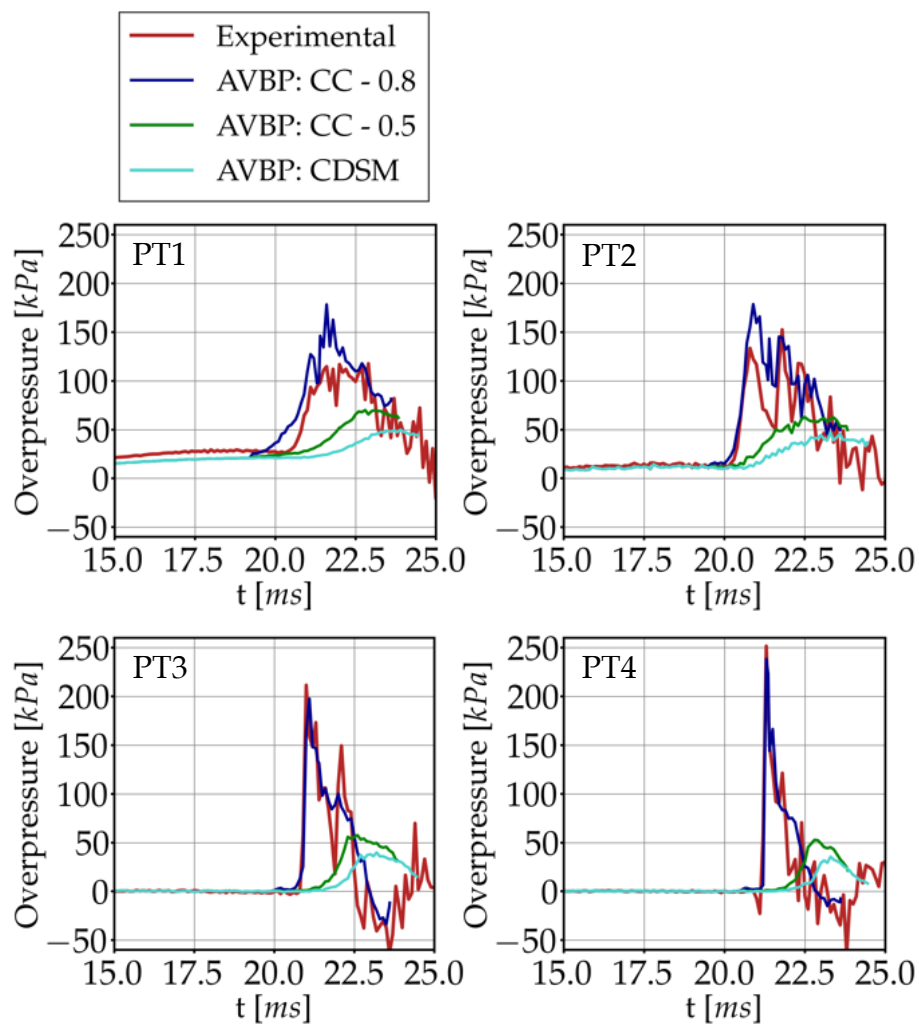


Figure 14.3.1: Over pressure measurements for the simulation with different efficiency models *versus* experimental. The timeline is fitted so that case CC - 0.8 matches the PT4 pressure impulse.

For this preliminary comparison, the best fitted model is taken (CC - 0.8). It should be noted that a finer analysis of the CDSM model is part of future works exclusively focused on Li-ion explosion, including a further refinement of the mesh to be able to compare the performance of the model based on the scale of the resolved structures. The two main phases of the explosion are presented in the next paragraphs.

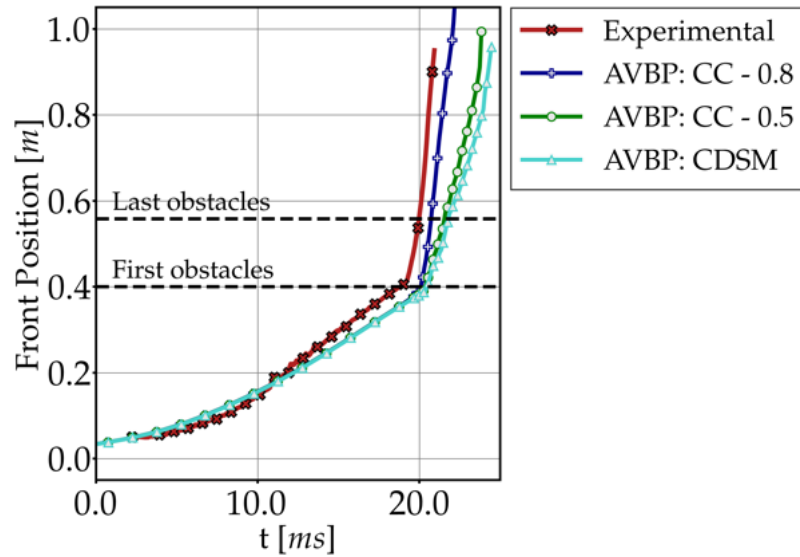


Figure 14.3.2: Comparison of simulation flame front position *versus* experimental. The timeline is fitted so that case CC - 0.8 matches the PT4 pressure impulse.

14.3.2 Laminar phase

The finger flame slowly forming and propagating creates a piston effect pushing fresh gases through the obstacles, creating turbulence. This phase is referred to as the laminar phase. In Fig. 14.3.3 the profiles of pressure and flame tip position are given.

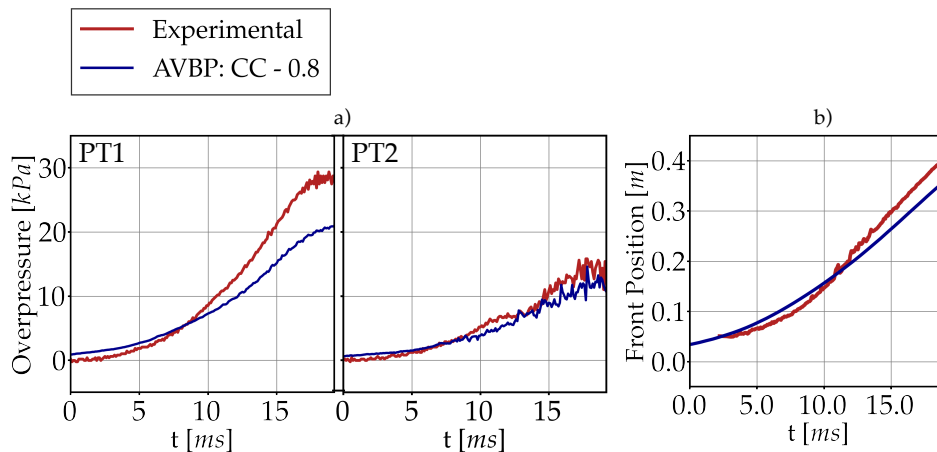


Figure 14.3.3: Laminar phase pressure and flame front position in comparison to experimental: a) Pressure sensors PT1 and PT2, b) Flame front position.

The simulation agrees reasonably with experimental, and the drift between flame tip positions at $t = 19$ ms is maintained under 10 %. The peak overpressure during this phase is well recovered at PT2, but under-predicted at PT1 by 24 %, which sets space for improvement. Profiles of Mach number just before the flame enters the obstacle zone, at $t = 19.8$ ms (flame tip position $x_{tip} = 0.38$ m, Fig. 14.3.4) are presented in Fig. 14.3.5. A zoom inside the obstacle zone shows that the Mach number is already elevated due to the flow constriction. Locally, the space between cylinders acts as a nozzle first converging then diverging. With a further acceleration of the flow, sonic conditions are expected at the artificial nozzle throat. The level of turbulence is elevated, and the vorticity ($\nabla \times \mathbf{u}$) peaks at $2.3 \times 10^5 \text{ s}^{-1}$ producing a quasi-homogeneous turbulent flow, creating the perfect conditions for an efficient flame acceleration, once the flame enters the obstacle zone (see Fig. 14.3.6).

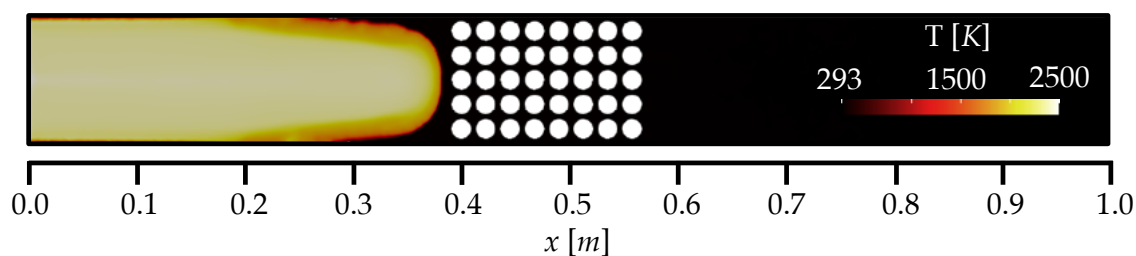


Figure 14.3.4: z-normal cut views of the flow field at $t = 19.8$ ms: Temperature profile for the entire channel.

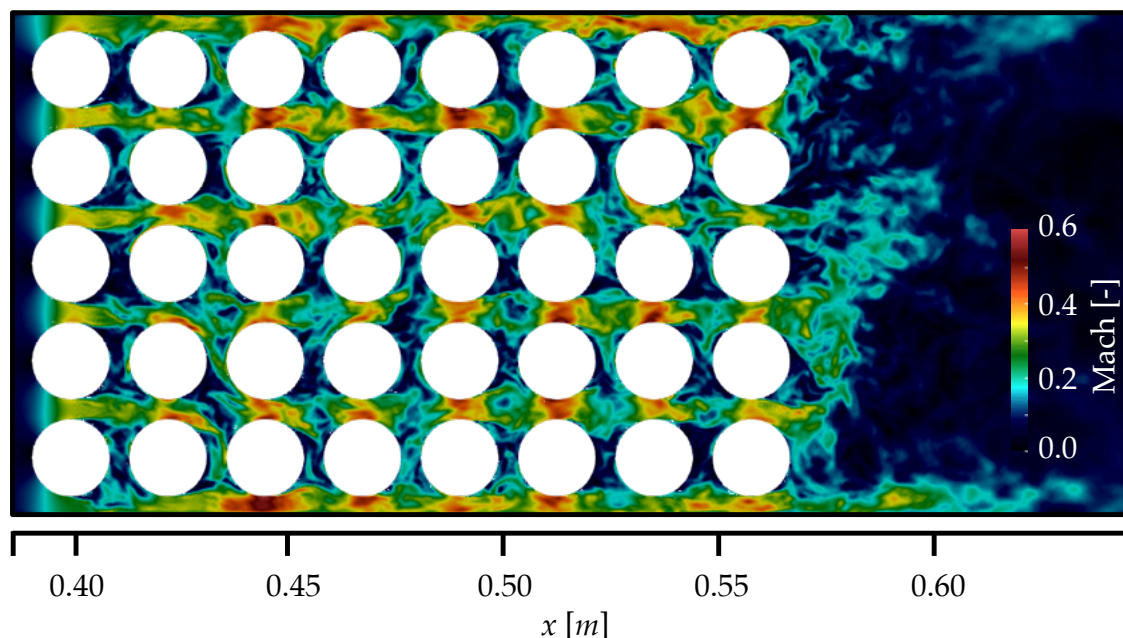


Figure 14.3.5: z-normal cut views of the flow field at $t = 19.8$ ms: Mach profile in the obstacle zone.

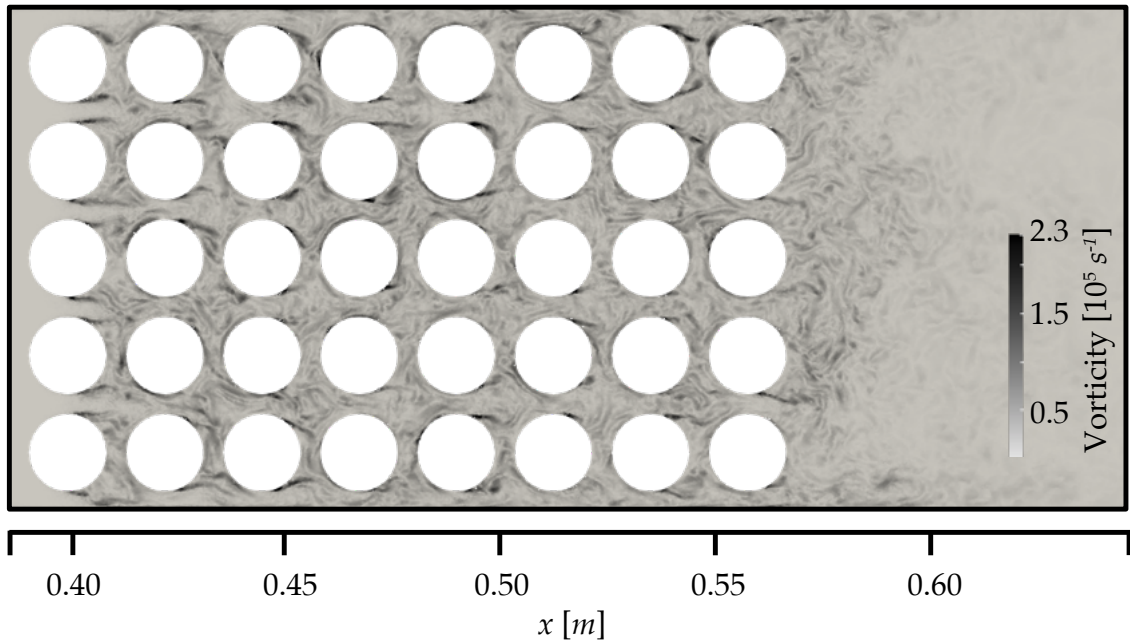


Figure 14.3.6: z-normal cut views of the flow field at $t = 19.8$ ms: Vorticity profile in the obstacle zone.

14.3.3 Obstacle crossing

As the flame encounters obstacles, the high level of turbulence already established behind the cylinders wrinkles the flame and drastically enhances its efficiency. Figure 14.3.7 shows profiles of temperature, Mach and heat release for four instants ($t \in \{20.3, 20.5, 20.7, 20.9\}$ ms). It depicts how flame wrinkling evolves through the rows of obstacles.

At $t = 20.3$ ms, sonic conditions start to appear in front of the flame. The flame creates fingers that pass longitudinally (x -direction) through the obstacles. Part of the flame is still anchored at the first row. At $t = 20.5$ ms, the flow becomes locally sonic as the flame enters entirely the obstacle zone, preparing choking. The flame fills spaces in the y -direction and its intensity is increased by the interaction with local turbulence conditions. Once the flame has reached the last row ($t = 20.7$ ms), a typical nozzle flow structure is observed, where a subsonic flow is accelerated until reaching $\text{Mach} = 1.0$ at the throat, which gives space to a further acceleration to $\text{Mach} > 2.0$, and the creation of a normal shock at the obstacles exit plane, responsible for a thin negative Heat release. The flame crosses the shock and reaches the post-obstacles zone where turbulence is fully developed and a peak of efficiency, correlated with the maximum pressure inside the domain is observed ($t = 21.0$ ms). A strong pressure wave propagates backward, creating a back-flow strong enough to reach sonic conditions at the first row of obstacles (see Fig. 14.3.7, at $t = 20.9$ ms).

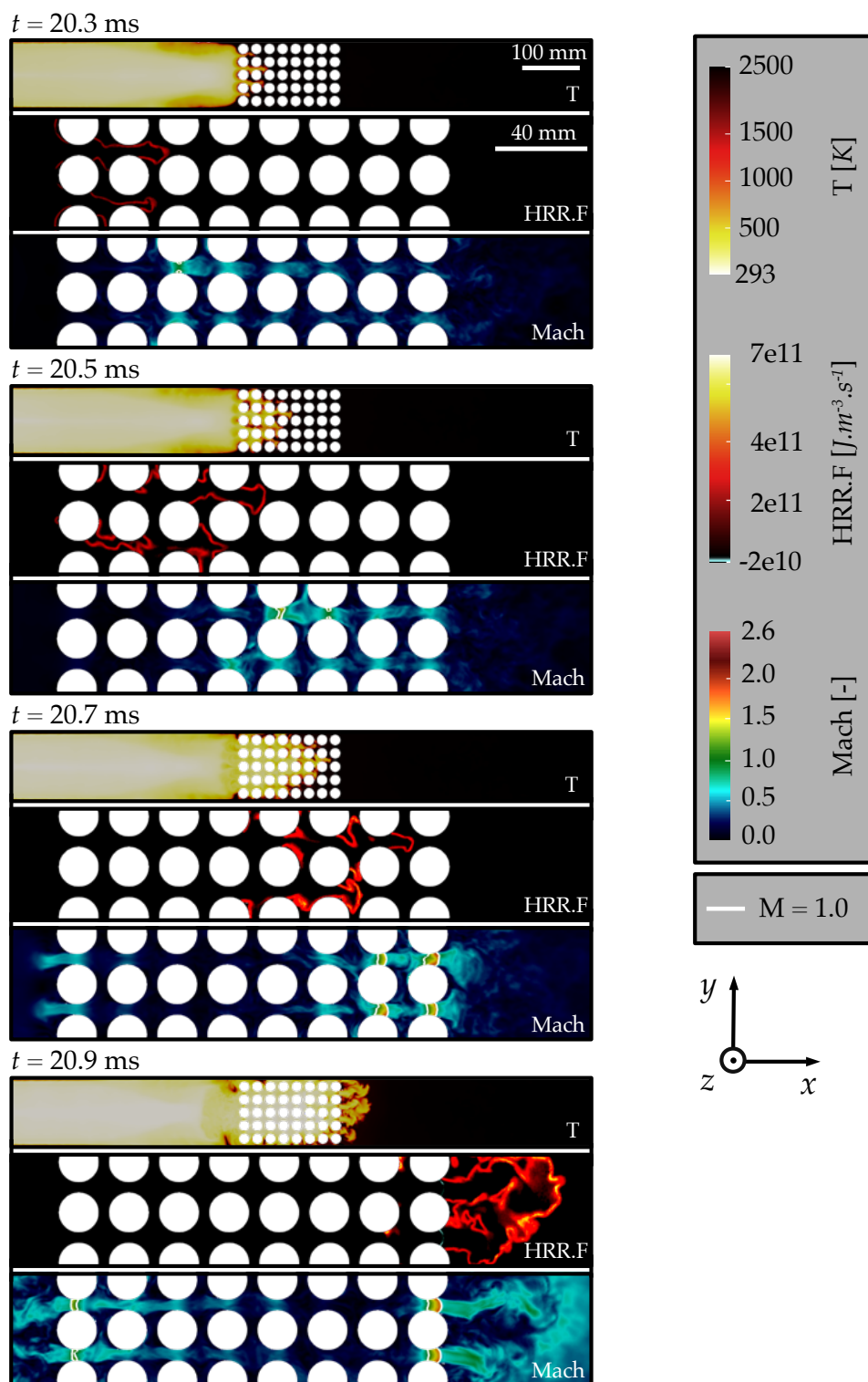


Figure 14.3.7: z-normal cut views of flow field during obstacle crossing for $t \in \{20.3, 20.5, 20.7, 20.9\}$ ms. Temperature profiles are given for the entire channel, Heat release and Mach profiles are zoomed on the central obstacle row.

The LAD sensor in conjunction with Lax Wendroff smooths the crucial exit-plane zone where two strong competing gradients encounter, the flame and the shock. Tests using the default Cook and Cabot hyperviscosity set up in Chap. 4 Sec. 4.2.3 invariably led to a failing simulation. Non-default parameters could still be used with the risk of impinging on the flame modelling and slowing down the simulation, while over-dissipating the structure of the shock. LAD remains therefore recommended for such a scenario.

With the superposition of complex flame-turbulence interactions and the creation of shocks, the case at hand is a stiff problem where nearly all the choices made throughout the manuscript contribute to the result. The experimental setup consists in a complete source of validation for the numerical setup introduced, from chemical modelling, to flame modelling and shock handling. Following these preliminary results, perspectives arise to drive further studies on Li-ion-related explosion.

14.4 Perspectives for explosion scenarios

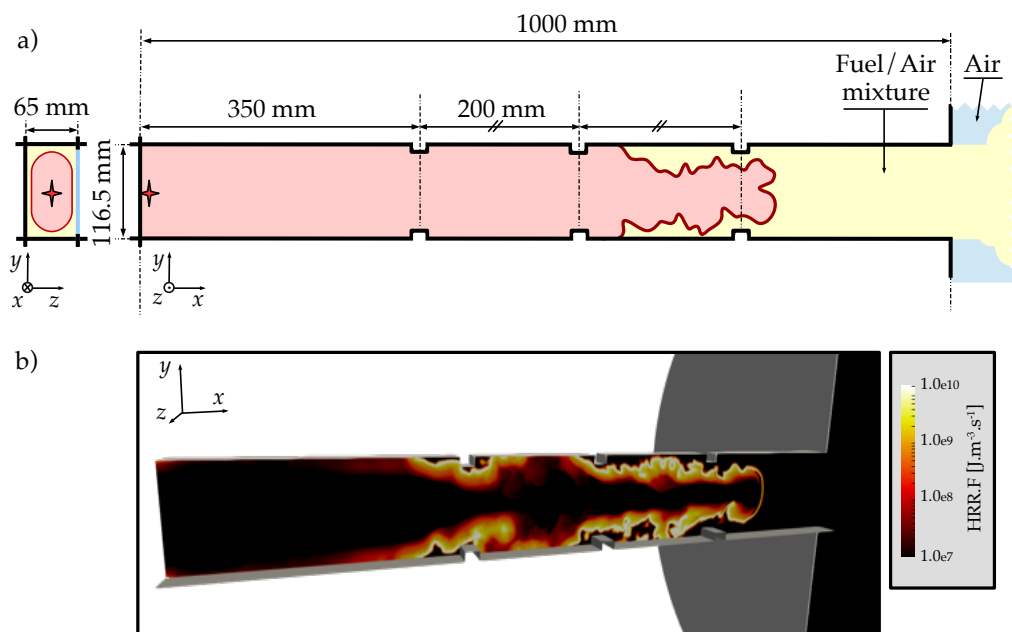


Figure 14.4.1: Effect of different types of obstacles on flow conditions and flame acceleration, a perspective to develop other databases inspired by Graent-like structures [271]: a) structure of the case, b) View of a cut of the Heat release rate of a preliminary simulation of the case.

In this chapter, a step towards realistic battery explosion scenarios is taken. Two main areas for improvement can be drawn. On the one hand, the experimental data to reproduce are a proper basis to iterate on model versions and enhance the capability of the solver to generalize to multiple conditions. Various equivalence

ratios, initial mixture and obstacle positioning are available to benchmark a solver. In the previous section, it appeared that a confident reproduction could be done at the cost of modifying efficiency constant parameters. A more robust approach is the dynamically evaluated efficiency constant. Investigations must be conducted to understand the source of the limited performance of the model in the case presented here. On the other hand, moving closer to real explosion scenarios in large scale storage devices means finding ways to scale up from a 1-module-problem to a many-modules-problem, and containers [205]. Representative sub-parts of these batteries must be studied thoroughly to predict large scale Li-ion related explosions, including new sets of obstacles and configurations (e.g. Fig. 14.4.1)

Chapter 15

Conclusions and Perspectives

This work aims at proposing a methodology to simulate failing Lithium-ion batteries-related combustion scenarios. With the increase in production of such energy storage systems, being able to look deeper in the mechanisms leading to combustion can help to mitigate critical events such as battery fires, or battery-related explosions. The diversity of applications targeted by Li-ion being wide, a strategy the most generic possible is to be chosen, avoiding bias of over confidently reproducing one phenomenon by neglecting the others. During the typical course of Thermal Runaway for Li-ion batteries, three main events are identified to be of first interest regarding interactions between the flow, the structure and the venting conditions at cell and module levels:

1. **Opening:** Following the initialization of Thermal Runaway and the beginning of gas production, the pressure building up inside the cell imposes the use of a coping strategy such as venting. To avoid an uncontrolled destruction of the casing, a pre-constrained surface is often added. At opening, shocks first propagate followed by under-expanded jets of hot flammable gases.
2. **Sustained venting:** Once the cell is opened to the atmosphere, decomposition reactions are not necessarily stopped. Gas production and temperature may increase exponentially reaching a climax where sustained venting followed by ignition creates a fire.
3. **Explosion:** In the event of a delayed ignition, the gases accumulate in the free space (storage, module casing, ...) offering conditions suitable for an explosion. The presence of congestion due to multiple obstacles increases the impact of the deflagration through flame acceleration, resulting in higher overpressures and rate of pressure rise.

Using Large Eddy Simulation, these three key events from a flow perspective can be observed, and effects of design may be predicted to accompany prototyping

steps. To guarantee a level of confidence between simulated scenarios and realistic cases, numerical and experimental results join.

First of all, in Chapter 5, the relation between components, and how they react to produce gases is presented and helps to identify the species of interest when considering battery fires. A focus on electrolyte oxidation is added. Simplifying hypotheses are presented to explain the use of vent gas analyzes obtained after Thermal Runaway (TR), available in the literature, as a basis for the rest of the study. To ensure affordable costs when targeting 3D simulation cases, an Analytically Reduced Chemistry [35] kinetic scheme is derived and validated, in Chapter 6, for TR-representative combustion cases. The capability to generalize to multiple vent gas mixtures is tested successfully. Using this scheme, canonical cases are prepared to set and adapt the numerical setup for the 3D scenarios, ensuring a smooth transition from simplified chemical considerations to more complex 3D geometries (Chap. 7). With these models prepared, the main events during TR are tackled, helping to discuss on models and strategies for Li-ion specific 3D applications.

Experimental results are then proposed to offer a validation of the numerical setup in a controlled environment, for conditions close to Li-ion venting. The events targeted are 1. Under-expanded jets (representing cell opening, Chap. 9), and 2. Jet ignition (for cell sustained venting and fire, Chap. 10). The experimental setup developed and operated at the Pprime institute delivers relevant operating points, and will continue to be used to characterize simulation tools for hot gases leaks. LES reproduces satisfactorily both under-expanded jets and jet ignition. The study is also an opportunity to refine the choices of models, delivering a consistent methodology for both opening and sustained venting simulation in realistic cases.

The methodology is applied to the generic 18650 Li-ion cell, starting by the sudden opening of a cell in Chapter 11. First, an axi-periodic cut of a detailed cell is used to reproduce high-pressure high-temperature gases suddenly venting into the atmosphere. Shock structures and under-expanded jet topology are depicted and compared when the cell is confined close to a wall. A second scenario is proposed in Chapter 12, involving a simplified 18650 cell is used to assert the effect of design on cell ignition during the sustained venting phase. Under similar conditions, the number of holes and the type of vented mixture are tested. Modifications of the geometry and vented mixture lead to changes in anchoring/blow-off limits, and corresponding timing, which gives information on the type of scenario expected when selecting a design. It shows the potential of such a method to establish guidelines, following manufacturer specifications, prior to any prototyping step.

Eventually, the question of delayed ignition and explosion is explored in Chapter 13 and 14. Using experimental results [111, 108], laminar tulip flame formation and propagation is reproduced with simulation. The case allows to study effects of boundary conditions to better prepare more complex turbulent cases. The addition of 18650-like obstacles [112, 109] allows to test flame-turbulence models and feeds perspectives to continue with this study.

Perspectives

This manuscript shows ways to make links between a problem definition and the multiple ways simulation can help to solve engineering questions. The place for improvement is wide, and consists in either deepening the analysis or continuing to build above this first brick.

The first topic of interest concerns vent gases. The hypotheses made to work with homogeneous mixtures averaged on entire TR procedures should be alleviated by considering temporally varying mixtures, where corresponding experiments are rare [232]. Also, considering liquid electrolyte ejection, leading to spray, evaporation and combustion is a path to follow to better the representativeness of cell fires reproductions [88].

The experimental depiction of jet ignition behavior is also a study to continue. Future iterations are planned to improve the characterization of the ignition sequence, helping to better determine blow off/anchoring limits of typical vent gases. More quantitative diagnostics and repeatability are also targeted. The influence of the composition on ignition conditions, including the test of auto-ignition of pure H_2 are already performed offering insights on worst case scenarios, and new operating points to reproduce using simulation.

The study of fires around generic 18650 cells serves a larger purpose which includes the consideration of fires inside small modules. The effect of heat propagation with and without combustion is to be targeted. The use of multi-physics coupled simulation frameworks with conduction, convection and radiation will allow quantitative and qualitative comparisons between different mitigation techniques. The coupling to a thermo-chemical model adapted to cell Thermal Runaway may help to understand the status of each cell of a module when submitted to the thermal load imposed by one or more failing cell [105, 52, 51, 135, 248, 74, 256]. Such a study would benefit from findings at the scale of one cell, and directs towards the scale of the module, more generally used in real applications.

Eventually, the critical battery-related explosion scenario raises questions. The multiplication of such events, forces to prioritize the study of confident simulation frameworks. The cases presented in this study offer multiple ways to improve flame-turbulence models to ensure a better transposition to large cases. This is to be accompanied by even simpler chemical schemes (1-2 steps) still relevant for one specific vent gas. Scaling-up to larger cases, with an efficient LES framework is key considering the size of certain applications [62]. Moreover, the comparison with simplified phenomenological models often used in the industry is necessary [193, 265, 241, 244, 201]. Simulations could offer better insights and feed such models to improve their representativeness in Li-ion related explosions.

Appendix A

Reduced kinetic scheme for Li-ion vent gases

The kinetic scheme used in this study is obtained following the reduction process of ARCANE [34], proposed in Chapter 6, from the UC San Diego scheme [41]. It is validated for 0D (isochoric auto-ignition) and 1D laminar flames (premixed and counter-flow diffusion). The scheme is composed of 18 transported species, 6 quasi-steady state species, and 93 reactions.

- The transported species are: N_2 , H , O_2 , OH , O , H_2 , H_2O , HO_2 , H_2O_2 , CO , CO_2 , CH_3 , CH_4 , CH_2O , C_2H_4 , C_2H_6 , C_2H_4O , C_3H_6 .
- The quasi-steady state species are: HCO , $T - CH_2$, $S - CH_2$, C_2H_5 , C_2H_3 , CH_2CHO .

The reactions are listed in Tab. A.0.1.

Table A.0.1: List of reactions: A is the pre-exponential factor in $\text{m}^{3(n-1)}.\text{kmol}^{-(n-1)}.\text{s}^{-1}$ where n is the order of the reaction, b is the temperature exponent and E_a is the activation energy in J.kmol^{-1} . In the case of fall-off reactions, two sets of Arrhenius coefficients are specified, the first one being the low temperature set and the second one the high temperature set.

No.	Reaction	A	b	E_a
1	$\text{H} + \text{O}_2 \longleftrightarrow \text{O} + \text{OH}$	3.520000E+13	-7.000000E-01	7.142000E+07
2	$\text{H}_2 + \text{O} \longleftrightarrow \text{H} + \text{OH}$	5.060000E+01	2.670000E+00	2.632000E+07
3	$\text{H}_2 + \text{OH} \longleftrightarrow \text{H} + \text{H}_2\text{O}$	1.170000E+06	1.300000E+00	1.521001E+07
4	$\text{H}_2\text{O} + \text{O} \longleftrightarrow 2 \text{OH}$	7.000000E+02	2.330000E+00	6.087000E+07
5	$2 \text{H} + \text{M} \longleftrightarrow \text{H}_2 + \text{M}$	1.300000E+12	-1.000000E+00	0.000000E+00
	CO:1.90E+00 CO2:3.80E+00 H2:2.50E+00 H2O:1.20E+01			
6	$\text{H} + \text{OH} + \text{M} \longleftrightarrow \text{H}_2\text{O} + \text{M}$	4.000000E+16	-2.000000E+00	0.000000E+00
	CO:1.90E+00 CO2:3.80E+00 H2:2.50E+00 H2O:1.20E+01			
7	$2 \text{O} + \text{M} \longleftrightarrow \text{O}_2 + \text{M}$	6.170000E+09	-5.000000E-01	0.000000E+00
	CO:1.90E+00 CO2:3.80E+00 H2:2.50E+00 H2O:1.20E+01			
8	$\text{H} + \text{O} + \text{M} \longleftrightarrow \text{OH} + \text{M}$	4.710000E+12	-1.000000E+00	0.000000E+00
	CO:1.90E+00 CO2:3.80E+00 H2:2.50E+00 H2O:1.20E+01			
9	$\text{H} + \text{O}_2 (+\text{M}) \longleftrightarrow \text{HO}_2 (+\text{M})$	5.750000E+13	-1.400000E+00	0.000000E+00
	5.00E-01 1.00E-30 1.00E+30 0.00E+00	4.650000E+09	4.400000E-01	0.000000E+00
	C2H6:1.5E+00 CO:1.2E+00 CO2:2.4E+00 H2:2.5E+00 H2O:1.6E+01			
10	$\text{H} + \text{HO}_2 \longleftrightarrow 2 \text{OH}$	7.080000E+10	0.000000E+00	1.233987E+06
11	$\text{H} + \text{HO}_2 \longleftrightarrow \text{H}_2 + \text{O}_2$	1.660000E+10	0.000000E+00	3.443014E+06
12	$\text{H} + \text{HO}_2 \longleftrightarrow \text{H}_2\text{O} + \text{O}$	3.100000E+10	0.000000E+00	7.199995E+06
13	$\text{HO}_2 + \text{O} \longleftrightarrow \text{O}_2 + \text{OH}$	2.000000E+10	0.000000E+00	0.000000E+00
14	$\text{HO}_2 + \text{OH} \longleftrightarrow \text{H}_2\text{O} + \text{O}_2$	7.000000E+09	0.000000E+00	-4.580016E+06
15	$\text{HO}_2 + \text{OH} \longleftrightarrow \text{H}_2\text{O} + \text{O}_2$	4.500000E+11	0.000000E+00	4.572999E+07
16	$2 \text{OH} (+\text{M}) \longleftrightarrow \text{H}_2\text{O}_2 (+\text{M})$	2.760000E+19	-3.200000E+00	0.000000E+00
	5.70E-01 1.00E+30 1.00E-30 0.00E+00	9.550000E+10	-2.700000E-01	0.000000E+00
	CO:1.5E+00 CO2:2.0E+00 H2:2.5E+00 H2O:6.0E+00			
17	$2 \text{HO}_2 \longleftrightarrow \text{H}_2\text{O}_2 + \text{O}_2$	1.030000E+11	0.000000E+00	4.620002E+07
18	$2 \text{HO}_2 \longleftrightarrow \text{H}_2\text{O}_2 + \text{O}_2$	1.940000E+08	0.000000E+00	-5.895005E+06
19	$\text{H} + \text{H}_2\text{O}_2 \longleftrightarrow \text{H}_2 + \text{HO}_2$	2.300000E+10	0.000000E+00	3.326301E+07
20	$\text{H} + \text{H}_2\text{O}_2 \longleftrightarrow \text{H}_2\text{O} + \text{OH}$	1.000000E+10	0.000000E+00	1.500002E+07
21	$\text{H}_2\text{O}_2 + \text{OH} \longleftrightarrow \text{H}_2\text{O} + \text{HO}_2$	1.740000E+09	0.000000E+00	5.999982E+06
22	$\text{H}_2\text{O}_2 + \text{OH} \longleftrightarrow \text{H}_2\text{O} + \text{HO}_2$	7.590000E+10	0.000000E+00	3.042998E+07
23	$\text{H}_2\text{O}_2 + \text{O} \longleftrightarrow \text{HO}_2 + \text{OH}$	9.630000E+03	2.000000E+00	1.670002E+07

No.	Reaction	<i>A</i>	<i>b</i>	<i>E_a</i>
24	CO + O (+M) \longleftrightarrow CO2 (+M) 1.00E+00 1.00E+00 1.00E+07 1.00E+07 CO:2.0E+00 CO2:4.0E+00 H2:2.5E+00 H2O:1.2E+01	1.550000E+18 1.800000E+08	-2.790000E+00 0.000000E+00	1.753502E+07 9.974991E+06
25	CO + OH \longleftrightarrow CO2 + H	4.400000E+03	1.500000E+00	-3.100009E+06
26	CO + HO2 \longleftrightarrow CO2 + OH	2.000000E+10	0.000000E+00	9.600000E+07
27	CO + O2 \longleftrightarrow CO2 + O	1.000000E+09	0.000000E+00	1.995770E+08
28	HCO + M \longleftrightarrow CO + H + M CO:2.50E+00 CO2:2.50E+00 H2:1.90E+00 H2O:1.20E+01	1.860000E+14	-1.000000E+00	7.113001E+07
29	H + HCO \longleftrightarrow CO + H2	5.000000E+10	0.000000E+00	0.000000E+00
30	HCO + O \longleftrightarrow CO + OH	3.000000E+10	0.000000E+00	0.000000E+00
31	HCO + O \longleftrightarrow CO2 + H	3.000000E+10	0.000000E+00	0.000000E+00
32	HCO + OH \longleftrightarrow CO + H2O	3.000000E+10	0.000000E+00	0.000000E+00
33	HCO + O2 \longleftrightarrow CO + HO2	7.580000E+09	0.000000E+00	1.714980E+06
34	CH3 + HCO \longleftrightarrow CH4 + CO	5.000000E+10	0.000000E+00	0.000000E+00
35	H + HCO (+M) \longleftrightarrow CH2O (+M) 7.82E-01 2.71E+02 2.76E+03 6.57E+03 C2H6:3.0E+00 CH4:2.0E+00 CO:1.5E+00 CO2:2.0E+00 H2:2.0E+00 H2O:6.0E+00	1.350000E+18 1.090000E+09	-2.570000E+00 4.800000E-01	1.777991E+06 -1.088007E+06
36	CH2O + H \longleftrightarrow H2 + HCO	5.740000E+04	1.900000E+00	1.150002E+07
37	CH2O + O \longleftrightarrow HCO + OH	3.500000E+10	0.000000E+00	1.469998E+07
38	CH2O + OH \longleftrightarrow H2O + HCO	3.900000E+07	8.900000E-01	1.700001E+06
39	CH2O + O2 \longleftrightarrow HCO + HO2	6.000000E+10	0.000000E+00	1.701800E+08
40	CH2O + HO2 \longleftrightarrow H2O2 + HCO	4.110000E+01	2.500000E+00	4.272002E+07
41	CH4 + H \longleftrightarrow CH3 + H2	1.300000E+01	3.000000E+00	3.362999E+07
42	CH4 + OH \longleftrightarrow CH3 + H2O	1.600000E+04	1.830000E+00	1.164001E+07
43	CH4 + O \longleftrightarrow CH3 + OH	1.900000E+06	1.440000E+00	3.630001E+07
44	CH4 + O2 \longleftrightarrow CH3 + HO2	3.980000E+10	0.000000E+00	2.380300E+08
45	CH4 + HO2 \longleftrightarrow CH3 + H2O2	9.030000E+09	0.000000E+00	1.031000E+08
46	CH3 + H \longleftrightarrow H2 + T-CH2	1.800000E+11	0.000000E+00	6.319999E+07
47	CH3 + H \longleftrightarrow H2 + S-CH2	1.550000E+11	0.000000E+00	5.639999E+07
48	CH3 + OH \longleftrightarrow H2O + S-CH2	4.000000E+10	0.000000E+00	1.047000E+07
49	CH3 + O \longleftrightarrow CH2O + H	8.430000E+10	0.000000E+00	0.000000E+00
50	CH3 + T-CH2 \longleftrightarrow C2H4 + H	4.220000E+10	0.000000E+00	0.000000E+00
51	CH3 + O2 \longleftrightarrow CH2O + OH	3.300000E+08	0.000000E+00	3.740998E+07
52	2 CH3 \longleftrightarrow C2H4 + H2	1.000000E+11	0.000000E+00	1.339000E+08

No.	Reaction	A	b	E_a
53	2 CH3 \longleftrightarrow C2H5 + H	3.160000E+10	0.000000E+00	6.149999E+07
54	CH3 + H (+M) \longleftrightarrow CH4 (+M)	2.470000E+27	-4.760000E+00	1.020900E+07
	7.83E-01 7.40E+01 2.94E+03 6.96E+03	1.270000E+13	-6.300000E-01	1.602012E+06
	CH4:2.0E+00 CO:1.5E+00 CO2:2.0E+00 H2:2.0E+00 H2O:1.6E+01			
55	2 CH3 (+M) \longleftrightarrow C2H6 (+M)	1.270000E+35	-7.000000E+00	1.156002E+07
	6.20E-01 7.30E+01 1.20E+03 0.00E+00	1.810000E+10	0.000000E+00	0.000000E+00
	C2H6:3.0E+00 CH4:2.0E+00 CO:1.5E+00 CO2:2.0E+00 H2:2.0E+00 H2O:6.0E+00			
56	OH + S-CH2 \longleftrightarrow CH2O + H	3.000000E+10	0.000000E+00	0.000000E+00
57	O2 + S-CH2 \longleftrightarrow CO + H + OH	3.130000E+10	0.000000E+00	0.000000E+00
58	CO2 + S-CH2 \longleftrightarrow CH2O + CO	3.000000E+09	0.000000E+00	0.000000E+00
59	S-CH2 + M \longleftrightarrow T-CH2 + M	6.000000E+09	0.000000E+00	0.000000E+00
	CO:1.80E+00 CO2:3.60E+00 H2:2.40E+00 H2O:1.54E+01			
60	OH + T-CH2 \longleftrightarrow CH2O + H	2.500000E+10	0.000000E+00	0.000000E+00
61	O + T-CH2 \longleftrightarrow CO + 2 H	8.000000E+10	0.000000E+00	0.000000E+00
62	O + T-CH2 \longleftrightarrow CO + H2	4.000000E+10	0.000000E+00	0.000000E+00
63	O2 + T-CH2 \longleftrightarrow CO2 + H2	2.630000E+09	0.000000E+00	6.240018E+06
64	O2 + T-CH2 \longleftrightarrow CO + H + OH	6.580000E+09	0.000000E+00	6.240018E+06
65	C2H6 + H \longleftrightarrow C2H5 + H2	5.400000E-01	3.500000E+00	2.180002E+07
66	C2H6 + O \longleftrightarrow C2H5 + OH	1.400000E-03	4.300000E+00	1.160001E+07
67	C2H6 + OH \longleftrightarrow C2H5 + H2O	2.200000E+04	1.900000E+00	4.700013E+06
68	C2H6 + CH3 \longleftrightarrow C2H5 + CH4	5.500000E-04	4.000000E+00	3.470000E+07
69	C2H6 (+M) \longleftrightarrow C2H5 + H (+M)	4.900000E+39	-6.430000E+00	4.483989E+08
	8.40E-01 1.25E+02 2.22E+03 6.88E+03	8.850000E+20	-1.230000E+00	4.277002E+08
	C2H6:3.0E+00 CH4:2.0E+00 CO:1.5E+00 CO2:2.0E+00 H2:2.0E+00 H2O:6.0E+00			
70	C2H6 + HO2 \longleftrightarrow C2H5 + H2O2	1.320000E+10	0.000000E+00	8.564602E+07
71	C2H5 + H \longleftrightarrow C2H4 + H2	3.000000E+10	0.000000E+00	0.000000E+00
72	C2H5 + O \longleftrightarrow C2H4 + OH	3.060000E+10	0.000000E+00	0.000000E+00
73	C2H5 + O \longleftrightarrow CH2O + CH3	4.240000E+10	0.000000E+00	0.000000E+00
74	C2H5 + O2 \longleftrightarrow C2H4 + HO2	7.500000E+11	-1.000000E+00	2.008299E+07
75	C2H5 (+M) \longleftrightarrow C2H4 + H (+M)	3.990000E+30	-4.990000E+00	1.673600E+08
	1.68E-01 1.20E+03 1.00E-30 0.00E+00	1.110000E+10	1.037000E+00	1.538400E+08
	CH4:2.0E+00 CO:1.5E+00 CO2:2.0E+00 H2:2.0E+00 H2O:6.0E+00			
76	C2H4 + H \longleftrightarrow C2H3 + H2	4.490000E+04	2.120000E+00	5.590000E+07
77	C2H4 + OH \longleftrightarrow C2H3 + H2O	5.530000E+02	2.310000E+00	1.240000E+07

No.	Reaction	<i>A</i>	<i>b</i>	<i>E_a</i>
78	C2H4 + O \longleftrightarrow CH3 + HCO	2.250000E+03	2.080000E+00	0.000000E+00
79	C2H4 + O \longleftrightarrow CH2CHO + H	1.210000E+03	2.080000E+00	0.000000E+00
80	C2H4 + O2 \longleftrightarrow C2H3 + HO2	4.220000E+10	0.000000E+00	2.410950E+08
81	C2H4 + HO2 \longleftrightarrow C2H4O + OH	2.230000E+09	0.000000E+00	7.191999E+07
82	C2H4O + HO2 \longleftrightarrow CH3 + CO + H2O2	4.000000E+09	0.000000E+00	7.116001E+07
83	C2H4 + M \longleftrightarrow C2H3 + H + M CH4:2.00E+00 CO:1.50E+00 CO2:2.00E+00 H2:2.00E+00 H2O:6.00E+00	2.600000E+14	0.000000E+00	4.040410E+08
84	C2H3 + O2 \longleftrightarrow CH2O + HCO	1.700000E+26	-5.312000E+00	2.720901E+07
85	C2H3 + O2 \longleftrightarrow CH2CHO + O	7.000000E+11	-6.110000E-01	2.201801E+07
86	CH2CHO + H \longleftrightarrow CH3 + HCO	5.000000E+10	0.000000E+00	0.000000E+00
87	CH2CHO + O \longleftrightarrow CH2O + HCO	1.000000E+11	0.000000E+00	0.000000E+00
88	CH2CHO + O2 \longleftrightarrow CH2O + CO + OH	3.000000E+07	0.000000E+00	0.000000E+00
89	CH2CHO + CH3 \longleftrightarrow C2H5 + CO + H	4.900000E+11	-5.000000E-01	0.000000E+00
90	CH2CHO + HO2 \longleftrightarrow CH2O + HCO + OH	7.000000E+09	0.000000E+00	0.000000E+00
91	CH2CHO \longleftrightarrow CH3 + CO	1.170000E+43	-9.800000E+00	1.832590E+08
92	C2H3 + CH3 (+M) \longleftrightarrow C3H6 (+M) 1.75E-01 1.34E+03 6.00E+04 1.01E+04 C2H6:3.0E+00 CH4:2.0E+00 CO:1.5E+00 CO2:2.0E+00 H2:2.0E+00 H2O:6.0E+00	4.270000E+52 2.500000E+10	-1.194000E+01 0.000000E+00	4.087998E+07 0.000000E+00
93	C3H6 + H \longleftrightarrow C2H4 + CH3	1.600000E+19	-2.390000E+00	4.680001E+07

Appendix B

Models for spark ignition procedures

When targeting the forced ignition of a mixture, several solutions are available. Depending on the choice made, the realism of the procedure can be impacted. In this study two main techniques are considered: the Energy Deposition model (ED) [148, 147], and the Soft Ignition with Relaxed Temperature (SIRT) [37]. The models, and their use cases are described in the next sections.

B.1 Energy Deposition model

The Energy Deposition (ED) model consists in applying a an energy source term locally to trigger the chemical runaway of the mixture. It reproduces the behavior of a spark ignition (pin-pin electrodes), or a laser ignition. For numerical applications using CFD solvers, an implementation was proposed by Lacaze *et al.* [148], consisting in modelling the energy source term \dot{Q} (in $\text{J.m}^{-3}.\text{s}^{-1}$) by a Gaussian function in time t and space $\mathbf{x} = (x, y, z)$ such that in 3D:

$$\begin{aligned} \dot{Q}(\mathbf{x}, t) = \frac{\varepsilon_i}{4\pi^2\sigma_t\sigma_s^3} \times \exp\left(-\frac{(t-t_0)^2}{2\sigma_t^2}\right) \\ \times \exp\left(-\frac{(x-x_0)^2 + (y-y_0)^2 + (z-z_0)^2}{2\sigma_s^2}\right) \end{aligned} \quad (\text{B.1})$$

where ε_i is the total deposited energy in J, t_0 is the deposition center time, and $\mathbf{x}_0 = (x_0, y_0, z_0)$ is the deposition center position in the domain. The Gaussian function is parametrized by the deposit duration Δ_t and deposit characteristic size Δ_s (e.g. electrode distance) so that the standard deviations σ_t and σ_s impose that,

1. for all point \mathbf{x} , the amplitude of the source term is 1 % of its peak value $\dot{Q}(\mathbf{x}, t_0)$ at the time $t_0 \pm \frac{1}{2}\Delta_t$, and 2. at all time t , the source term is 1 % of its peak value $\dot{Q}(\mathbf{x}_0, t)$ at a distance $\frac{1}{2}\Delta_s$ from \mathbf{x}_0 . To put it into equations:

$$\frac{\dot{Q}(\mathbf{x}, t_0 \pm \frac{1}{2}\Delta_t)}{\dot{Q}(\mathbf{x}, t_0)} = 10^{-2} \text{ and } \frac{\dot{Q}(\mathbf{x}_{\frac{1}{2}\Delta_s}, t)}{\dot{Q}(\mathbf{x}_0, t)} = 10^{-2} \implies \sigma_s = \frac{\Delta_s}{4\sqrt{\ln(10)}} \quad (\text{B.2})$$

$$\text{and } \sigma_t = \frac{\Delta_t}{4\sqrt{\ln(10)}}$$

where $\mathbf{x}_{\frac{1}{2}\Delta_s}$ represents the points at the surface of the sphere of center \mathbf{x}_0 and of radius $\frac{1}{2}\Delta_s$. For the rest of the study $a = 4\sqrt{\ln(10)}$.

The key parameters of the ED are thus ε_i , Δ_t , and Δ_s [172, 259].

1. ε_i : It is defined as the total deposited energy, which must not be confused with the device energy consumption ε_{tot} . Due to the formation of shock-waves and because radiative and conductive heat are lost in the domain and the solid, a significant proportion of the energy commanded is lost and cannot be transmitted to the mixture to ignite. It is generally considered that ε_i represents 10-30 % of ε_{tot} .
2. Δ_t : The spark duration is an experimental parameter, that depends strongly on the system evaluated. Typical values range in [50, 5000] μs .
3. Δ_s : After ionization phase, a sphere of hot glowing gases is created. The order of magnitude of the diameter is close to the one of the gap of the electrode gap for a spark plug. It ranges in [0.5, 3] mm.

One could be tempted to impose those parameters directly in the model. However, as mentioned before, the ignition phase is characterized by a phase of ionization where temperatures as high as 2×10^4 K can be reached. In practice this extremely stiff phase is out of reach for most CFD solvers. To limit the maximum temperature inside the kernel during the deposition, it is decided to artificially broaden spatially the Gaussian-shaped source term by adapting Δ_s . To do so, a relation for the maximum temperature reached at the center of the kernel T_{max} is found by assuming no heat losses:

$$T_{max} \simeq T_0 + \frac{\varepsilon_i}{\rho C_p (\sqrt{2\pi}\sigma_s)^3} \quad (\text{B.3})$$

where ρ , T_0 , C_p are the density, the temperature and the constant pressure heat capacity of the unburnt gases, and $(\sqrt{2\pi}\sigma_s)^3$ is the Gaussian volume of the deposit. It leads to:

$$\Delta_s \simeq \frac{a}{\sqrt{2\pi}} \sqrt[3]{\frac{\varepsilon_i}{\rho C_p (T_{max} - T_0)}} \quad (\text{B.4})$$

The order of magnitude of Δ_s is of the order of 3 to 5 times the electrode gap, depending on the other parameters and the acceptable T_{max} chosen. In this thesis, $T_{max} = 3500$ K is selected to ensure a comfortable margin (thermodynamic tables are generally extended to 5000 K, as values higher are generally poorly representative when working with perfect gases).

An example of numerical application is given for the ignition of a jet diffusion flame of hot vent gases, assuming that the mixture to ignite is badly mixed and thermo-dynamically close to pure fuel (see Chapter 10). With $\varepsilon_i = 50$ mJ, $\Delta_t = 100$ μ s, $\Delta_s \simeq 8.09$ mm should be imposed. Fig. B.1.1 depicts ignition profiles along with estimated kernel temperatures.

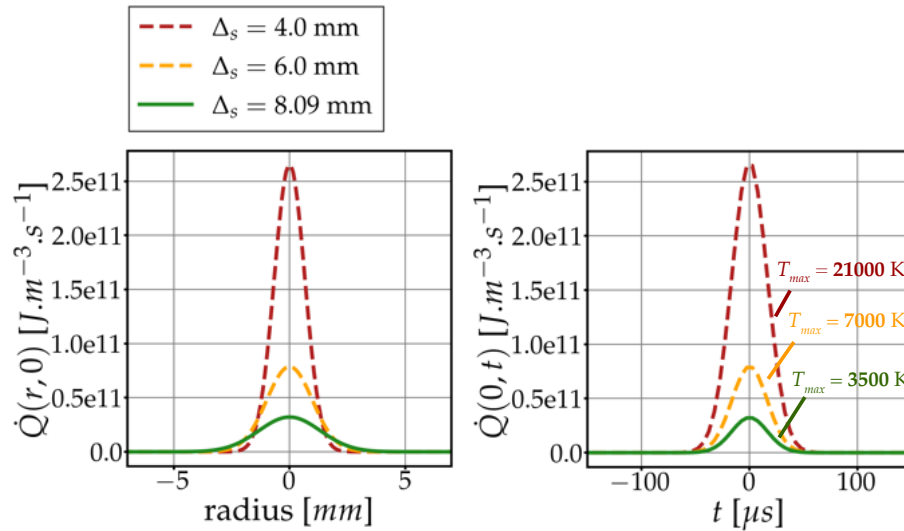


Figure B.1.1: Profile of energy deposition for varying deposition characteristic size Δ_s : *left*, energy source as a function of the radius from the center of deposition at the center time (here $t_0 = 0$); *right*, energy source as a function of the time for the deposition center position.

B.2 Soft Ignition with Relaxed Temperature

In numerous cases, the ignition procedure is not well documented and obtaining information on the ignition energy or on characteristic times is either not relevant, or impossible. A robust and simple way to form a kernel is therefore to impose a sufficiently high temperature locally and for a short time period, so that chemical runaway is ensured and a flame propagates. This strategy mimics the previous one but imposes a Gaussian profile of temperature relaxing toward the target temperature T_{max} :

$$\dot{Q}(\mathbf{x}, t) = \max \left[0, \alpha \frac{T_{max} - T}{4\pi^2 \sigma_t \sigma_s^3} \times \exp \left(\left(-\frac{(t - t_0)^2}{2\sigma_t^2} \right) \right) \times \exp \left(\left(-\frac{(x - x_0)^2 + (y - y_0)^2 + (z - z_0)^2}{2\sigma_s^2} \right) \right) \right] \quad (\text{B.5})$$

where α (J.K⁻¹) is the relaxation factor. Thanks to the Gaussian masks in time and space, the source term enforces progressively the target temperature, until the chemical runaway is triggered. A kernel is formed, and can propagate freely.

B.3 Conclusion on ignition models

When access to igniter specifications is given, ED is preferred and helps to ensure a better representation of the physics of an ignition. However, this method requires a sufficient grid refinement, and can be stiff to use. It relies on an adequate strategy to smooth the deposition to avoid large temperatures. The second approach (SIRT) is better fitted to cases where ignition conditions are less well specified, or when temperature overshoots cannot be avoided without producing a non-physical large kernel (large energy deposition).

Appendix C

Under-expanded jet of pure N_2

To complete the study validating the use of simulation for 3D under-expanded, pre-heated jets, a second mixture is added to the *inert* NMC1 surrogate: N_2 . The figures that follow depicts experimental to simulation comparison elements. It gives similar qualitative and quantitative results as the cases shown in Chapter 9.

Table C.0.1: Experimental and simulation conditions at venting climax for N_2 .

Case Name		T5 [K]	P5 [bar]	T6 [K]	P6 [bar]
N_2 -800	Exp.	1075.4	4.77	1037.9	4.52
	Sim.	"	"	1089.8	4.55
N_2 -400	Exp.	685.6	4.49	685.4	4.28
	Sim.	"	"	696.0	4.29
N_2 -035	Exp.	308.2	3.59	307.8	3.52
	Sim.	"	"	313.0	3.42

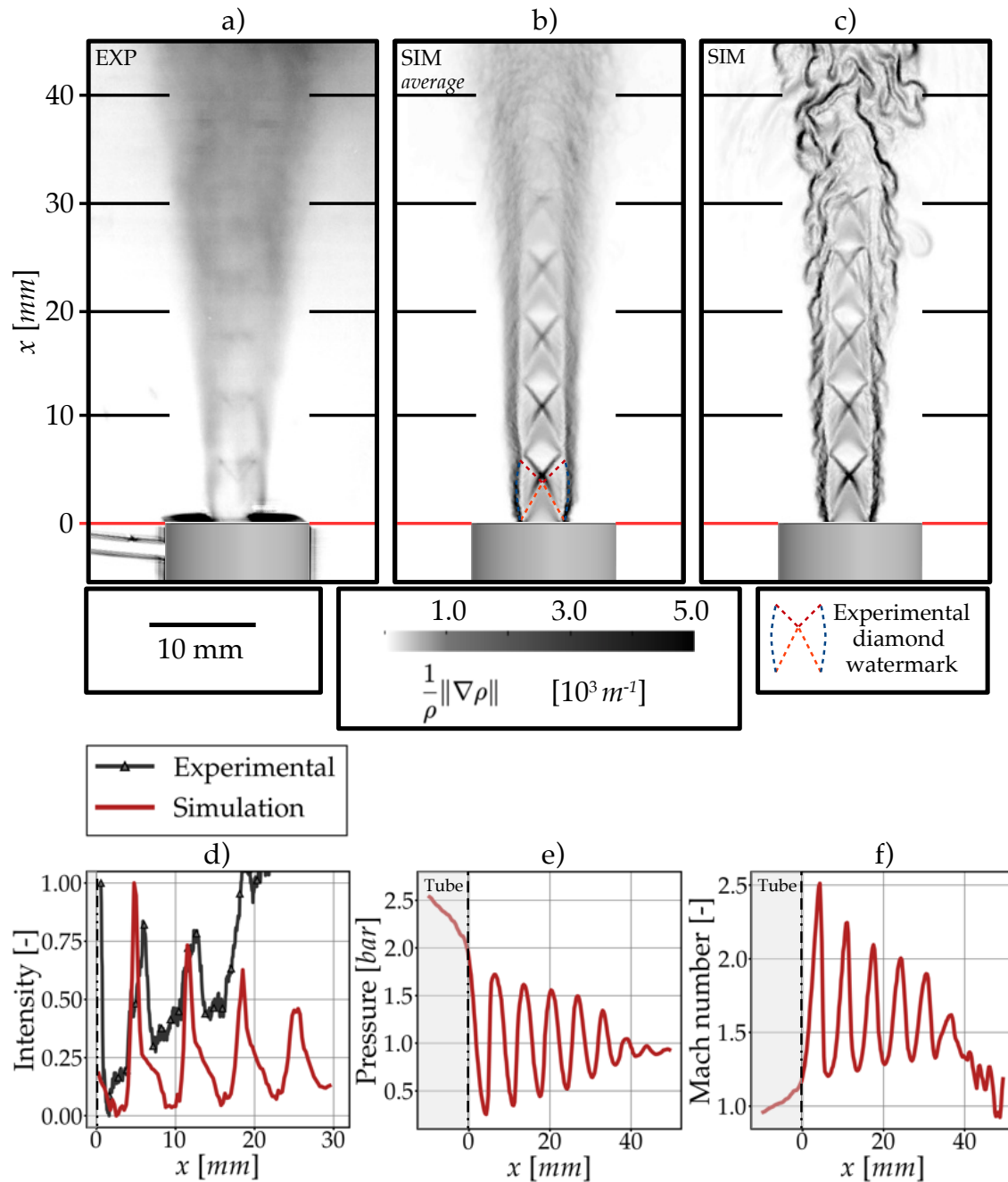


Figure C.0.1: N_2 pre-heated at $800^\circ C$, comparing experimental to simulations: a) Experimental shadowgraph imaging, b) 5.0 ms averaging of numerical Schlieren z -normal cut, c) Instantaneous numerical Schlieren z -normal cut, d) Comparison of intensity from shadowgraph (exp.) and numerical schlieren (sim.), e) Pressure profile, f) Mach profile.

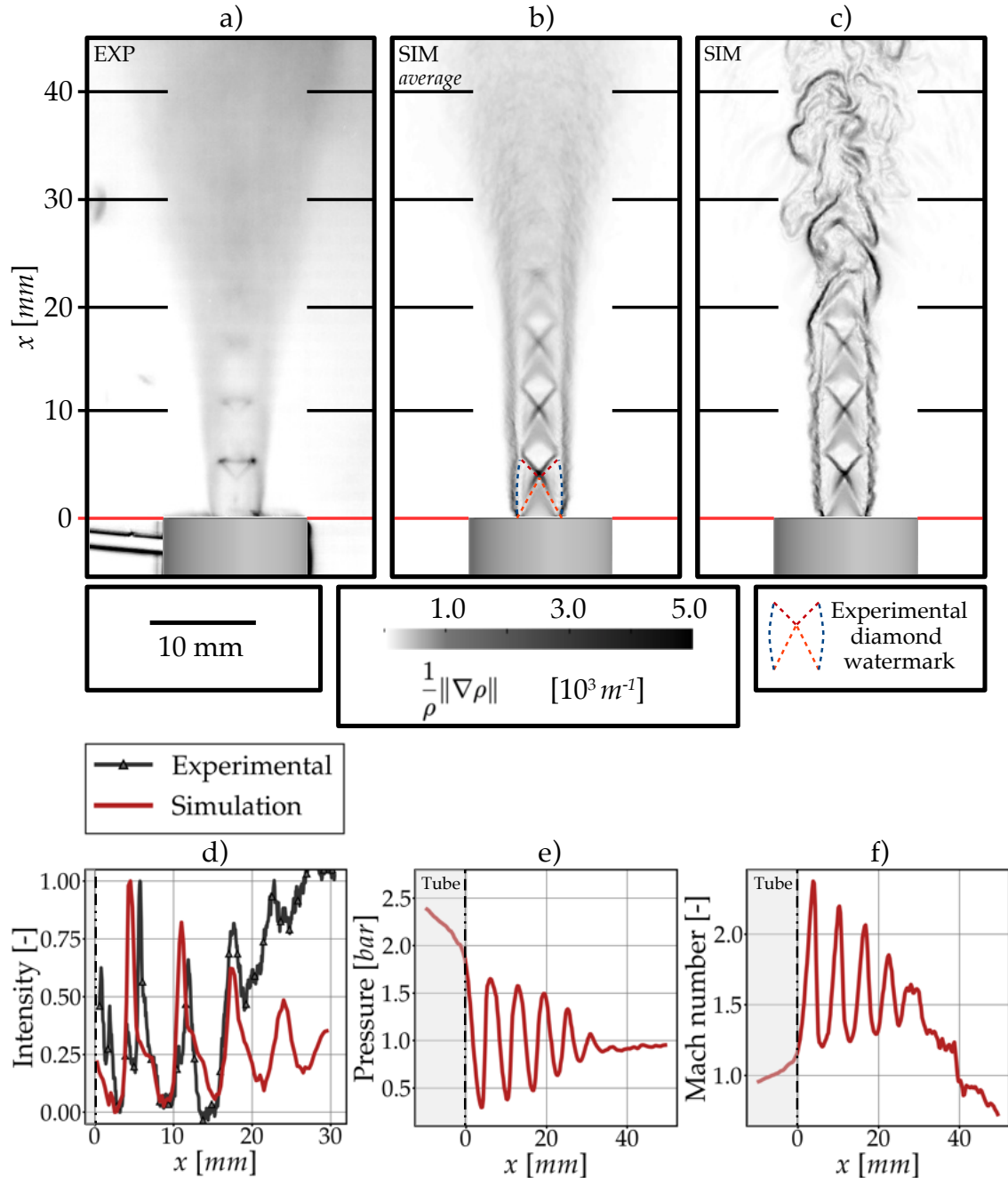


Figure C.0.2: N_2 pre-heated at 400°C , comparing experimental to simulations: a) Experimental shadowgraph imaging, b) 5.0 ms averaging of numerical Schlieren z -normal cut, c) Instantaneous numerical Schlieren z -normal cut, d) Comparison of intensity from shadowgraph (exp.) and numerical schlieren (sim.), e) Pressure profile, f) Mach profile.

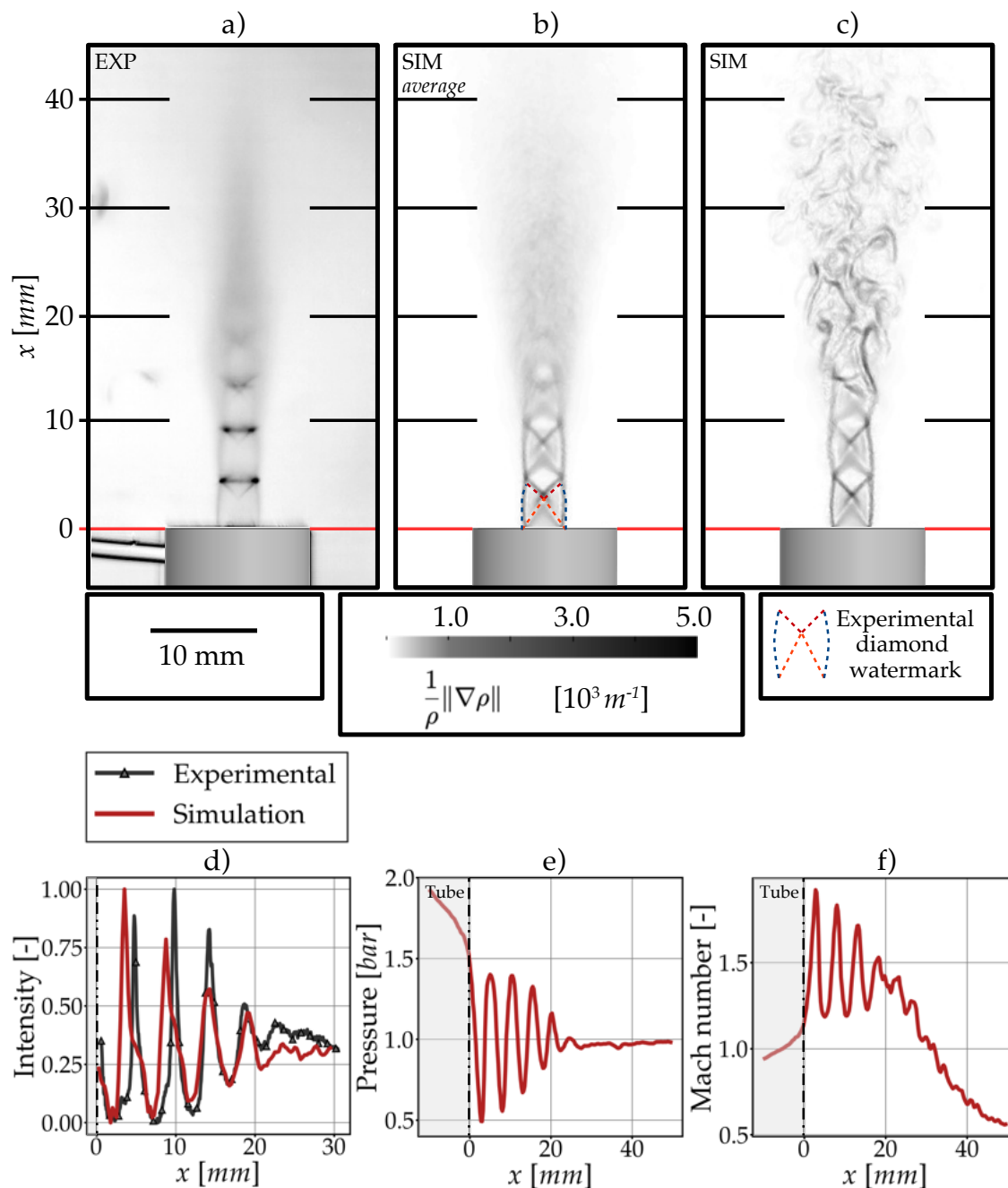


Figure C.0.3: N_2 pre-heated at 400°C , comparing experimental to simulations: a) Experimental shadowgraph imaging, b) 5.0 ms averaging of numerical Schlieren z -normal cut, c) Instantaneous numerical Schlieren z -normal cut, d) Comparison of intensity from shadowgraph (exp.) and numerical schlieren (sim.), e) Pressure profile, f) Mach profile.

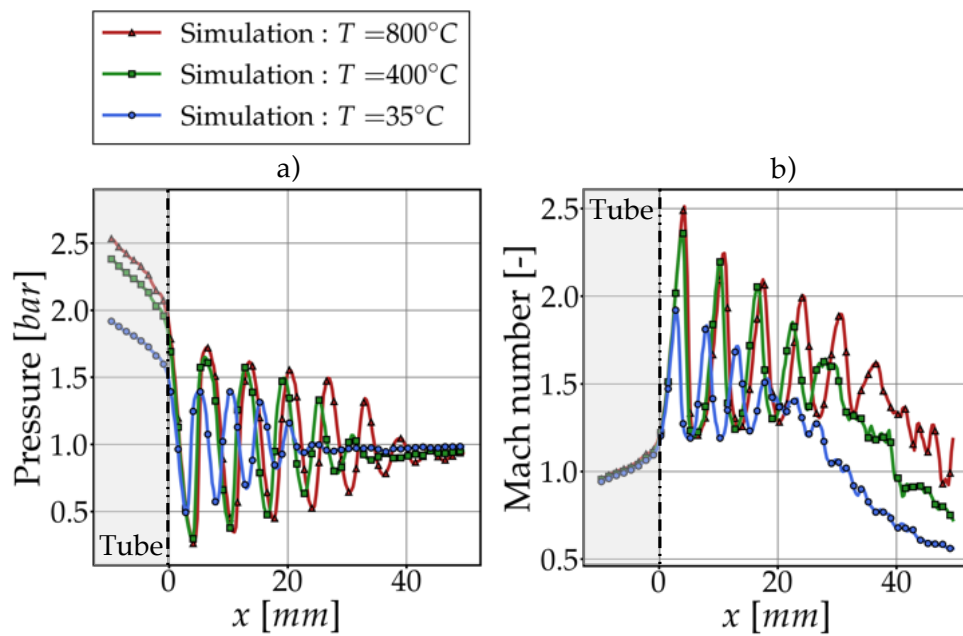


Figure C.0.4: Comparison of profiles for N_2 and the three pre-heating temperatures: a) Pressure profile, b) Mach profile.

Appendix D

Heat release rate visualization

In this manuscript, the only flame model used in 3D is the DTFLES model. The model is suited for premixed flames and adapts to mesh distortions. It is amended to deactivate in regions of diffusion. The parameter controlling the effect of the model is the thickening field F . When visualizing flames, the Heat Released Rate field is primordial. However, the application of DTFLES tends to bias the rendering when compared to experimental for two reasons:

1. **Partial premixing:** In presence of both premixed and diffusion flames, the application of thickening in regions of premixing only, tends to undermine the intensity of the premixed regions. Experimentally, premixed flames generally peak higher in terms of heat released and temperature, glowing more intensely. By plotting, $HRR.F$, the artificially dampened premixed regions are re-intensified, better rendering the strength of such flames with respect to diffusion sections (see Fig. [D.0.1 a](#))).
2. **Mesh refinement/de-refinement:** DTFLES is also adapted to mesh inhomogeneities and higher values of thickening are applied in coarser regions at iso-fresh-gas-conditions, dampening the peak values while the flame is experimentally at the same intensity. $HRR.F$ corrects this bias and allows a constant intensity even if mesh de-refines, better recovering experimental observations (see Fig. [D.0.1 b](#))).

For better visualizations, the field $HRR.F$ will be preferred throughout the thesis. The HRR field still remains mandatory when asserting integral values in the domain (such as flame total power).

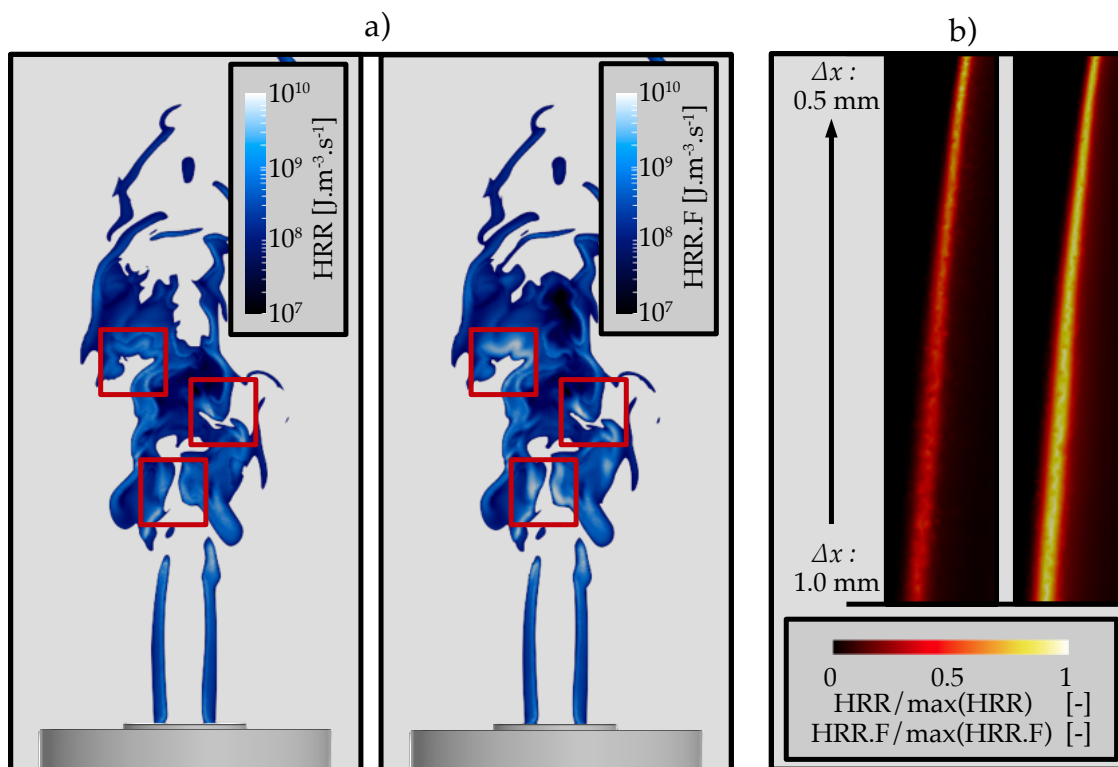


Figure D.0.1: HRR versus HRR.F visualization: a) cases with diffusion and premixed flames, b) cases with mesh distortion.

Appendix E

Jet ignition using TTGC

In addition to Lax Wendroff, a second computation of a full ignition sequence is performed using TTGC. The intention is to evaluate the potential loss of precision due to lower order. Similarly to LW, the full sequence is described versus experimental in Fig. E.0.4. The anchoring is also predicted using TTGC, and timescales are close to the ones observed with LW, especially for the lip anchoring sequence (see Fig. E.0.1 and E.0.3).

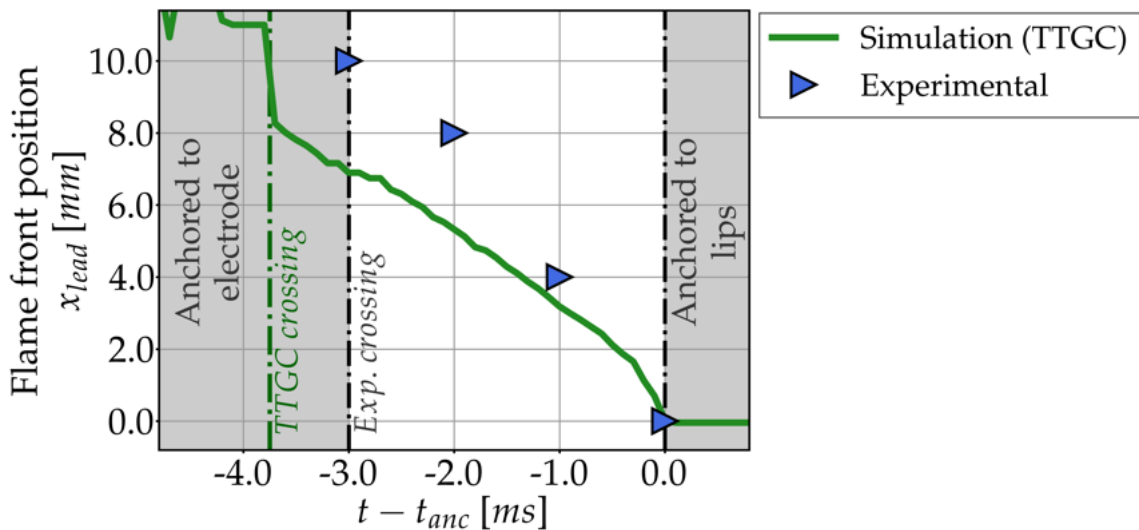


Figure E.0.1: Flame positions with respect to the lips during the anchoring phase using TTGC.

However, with TTGC, the flame is nearly cylindrical when touching the lips, while with LW, a laps of time is needed for the flame to anchor completely once the leading triple flame has reached the lips. This difference plays a role on the timing of the whole anchoring procedure (2.0 ms with LW, resp. 3.9 ms with TTGC, when considering the triple flame leading point displacement from electrode to lips). The triple flame propagation speed is lower on average for TTGC, but it is unclear

whether it is related to numerics or to the stochastic dimension of the flow at ignition. More effort is to be put into determining the set of parameters playing the biggest role in such differences.

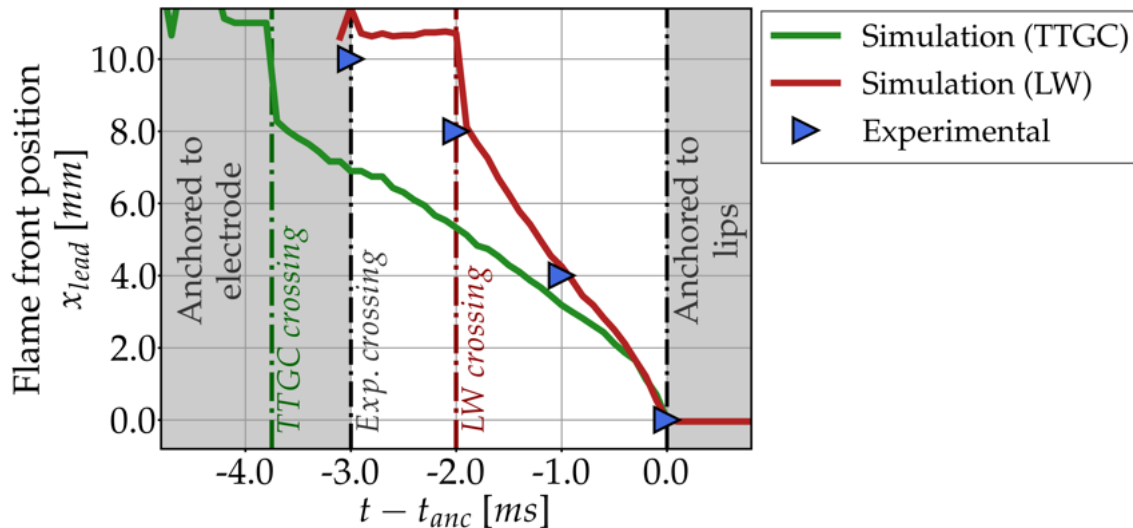


Figure E.0.2: Comparison of flame front positions with respect to the lips during the anchoring phase using TTGC and LW.

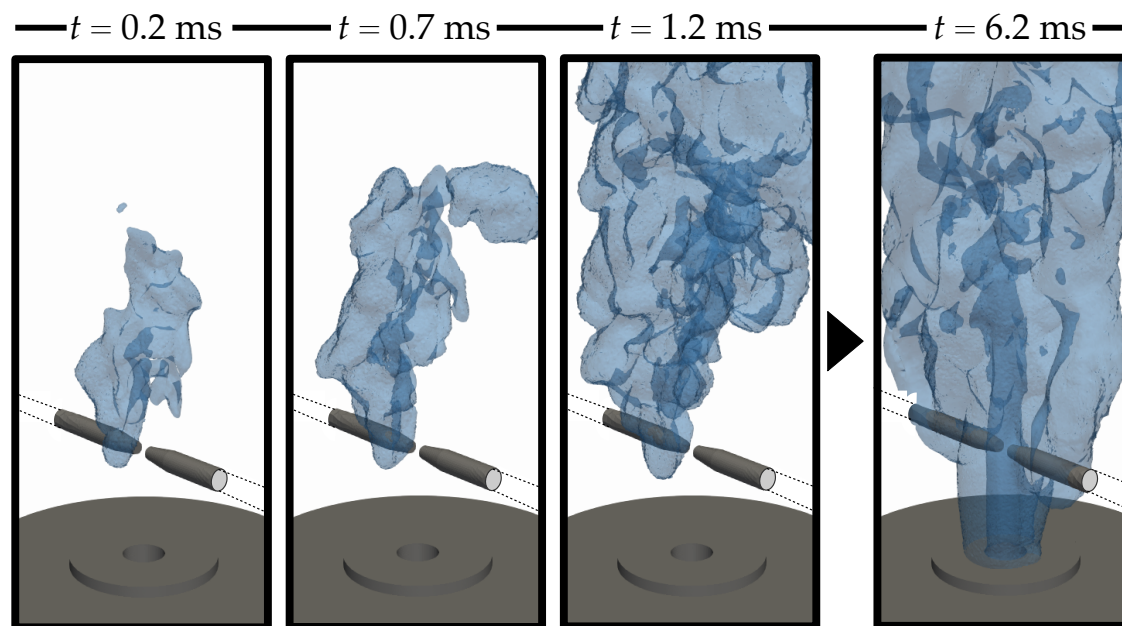


Figure E.0.3: Effect of mass-flow on the ignition procedure outlined as 3D contour of HRR (iso-level $\text{HRR.F} = 1 \times 10^7 \text{ J.m}^{-3}.\text{s}^{-1}$): a) $\dot{m}^{sim} = 0.31 \text{ g.s}^{-1}$, b) $\dot{m}^{sim} = 0.326 \text{ g.s}^{-1}$.

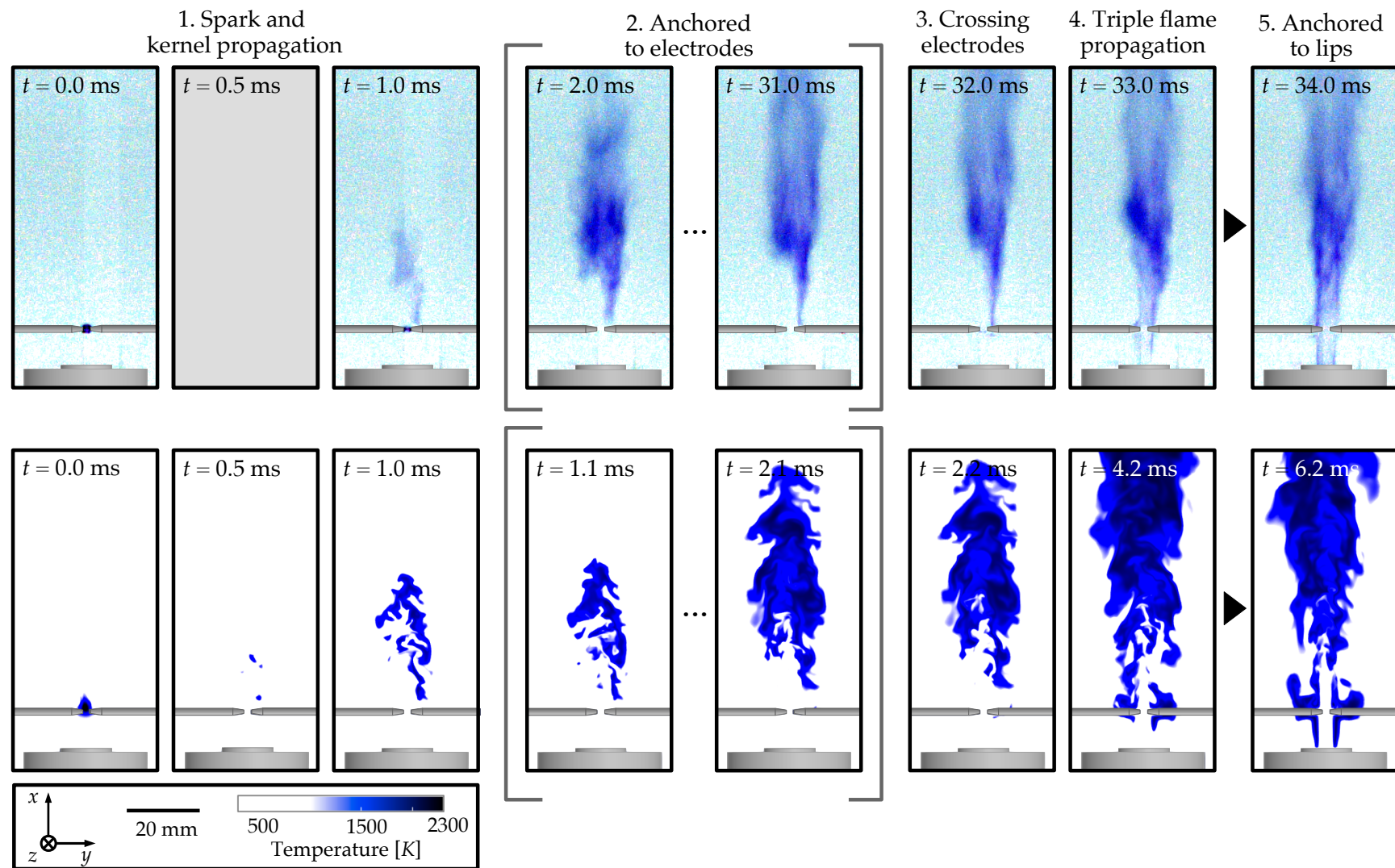


Figure E.0.4: Experimental versus simulation comparison of the three phases of the ignition-to-anchoring procedure (TTGC). Experimental visualization corresponds to contrasted photography of the flame, simulation shows z -normal cuts of the temperature field.

Overall, both schemes compare, knowing that uncertainties are strong in the timing of such an event experimentally, making LW a good alternative to obtain reasonable results at lower CPU costs, explaining its choices when iterating on other numerical aspects¹.

¹LW represents $125.9 \text{ hCPU.ms}_{phys}^{-1}$, whereas TTGC costs $248.9 \text{ hCPU.ms}_{phys}^{-1}$

Appendix F

18650 venting cell: internal details and turbulence

To observe the influence of cell internal layout against the choice of turbulence modelling for the generic cell, an opportunity to produce a detailed reference flow is proposed using the structure of the previous Chapter (Chap. 11 Sec. 11.2.1). The venting from a section of a cell including its internal obstacles, producing a natural turbulence is simulated under similar mass-flow and temperature conditions. Figure F.0.1 describes the case and the corresponding mesh. For completion, the hole shapes match the generic case and probe location is the same, at a place where mesh refinement is identical.

Using the numerical scheme TTGC [50] with the WALE [199] turbulence model for a precise turbulence description, fluctuation kinetic energy spectrum in the jet (see probe location in Fig. F.0.1 c)) and turbulent kinetic energy fields can be compared to the generic case introduced in this chapter. A cut of the turbulent kinetic energy field proposed in Fig. F.0.2 gives a comparison between the jet topologies. On the one hand, the level of turbulence is much more elevated for the complete case, leading to a more efficient mixing, thus a shorter $Z > Z_{st}$ zone. On the other hand, blocking devices such as the opened breaking disk modify the jet angle and symmetry. The probe, identically located for both case, is placed in a region with similar levels of TKE in both cases, but due to the modification of the angle, is not well centered in the detailed cell case. Comparisons must be taken with a grain of salt. In Fig. F.0.3, the comparison of the Power Spectrum Density (PSD) of the fluctuation kinetic energy on a 10 ms time window is proposed. The good agreement between spectra from the generic case and the detailed case shows that the scales of the turbulent structures artificially introduced match the natural ones created by the flow restriction, at the probe location¹.

¹Given that the hole is close to rectangular, its hydraulic diameter gives $D_h \simeq 3.0$ mm, the distance is approximately 5.0 hydraulic diameters.

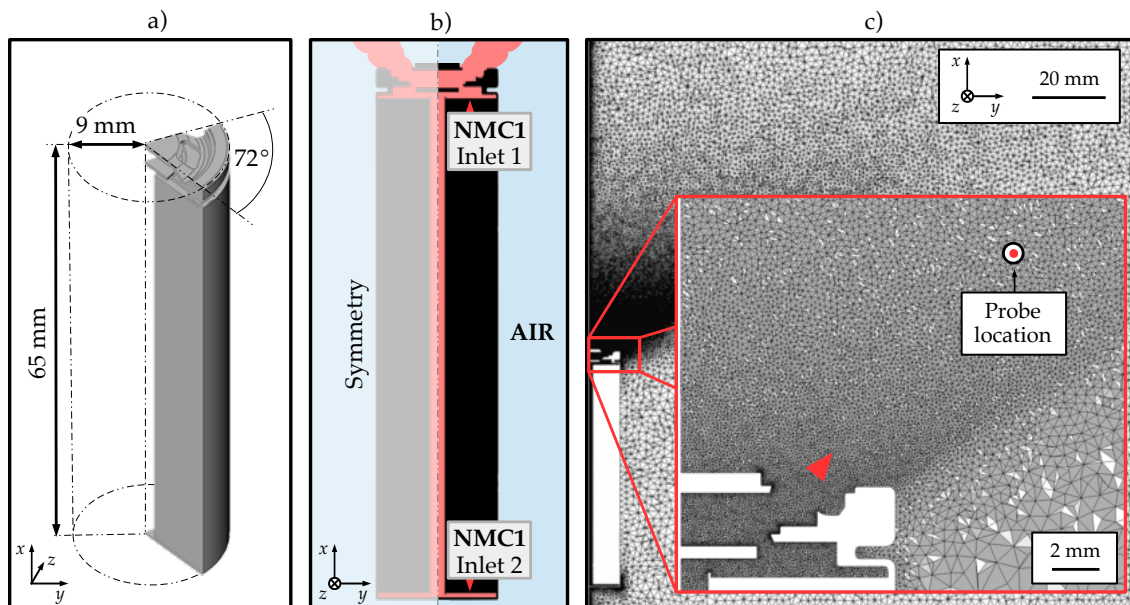


Figure F.0.1: View of the case used to validate turbulence level: a) Structure of the section of the 18650 cell, b) Cut view of the cell and principle, c) Cuts of the mesh, refinement reaches $100\ \mu\text{m}$ at the cell exit and in dead volumes, and up to $50\ \mu\text{m}$ close to the walls. It consists in 8.2 M tetrahedra.

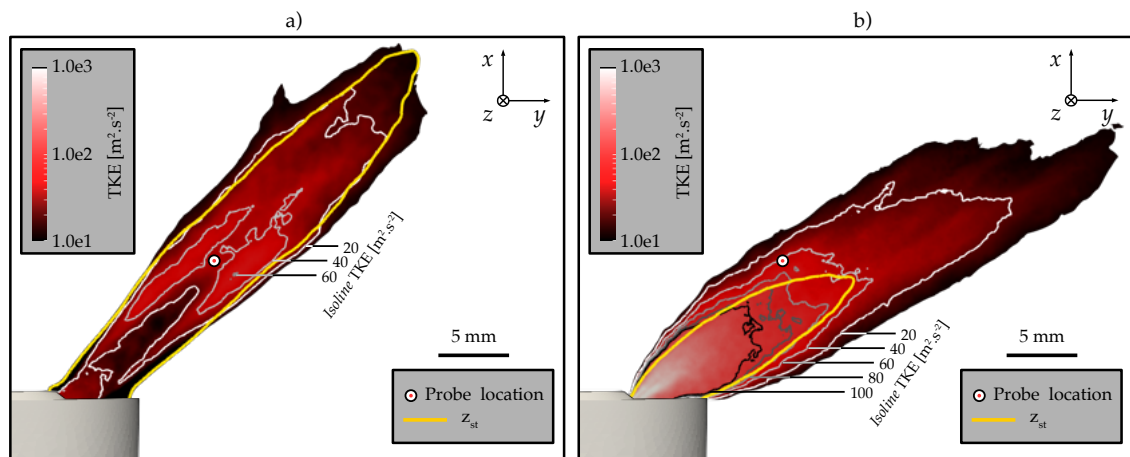


Figure F.0.2: Comparison of the Turbulent Kinetic Energy (TKE) for the detailed and simplified generic cases: a) Simplified geometry, b) Detailed geometry.

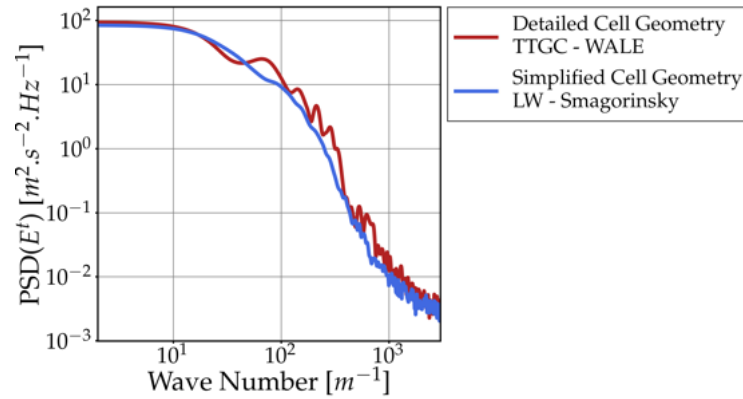


Figure F.0.3: Spectrum of the fluctuation kinetic energy E^t at the probe location over 10 ms of computation.

These mixed results concerning generic *versus* detailed turbulence evaluation leads to the conclusion that, in addition to the test of simple design choices with a generic structure at early prototyping steps, the simulation of a complete cell with all flow constrictions is advised once a design has been selected. However, the feasibility of such a detailed simulation is constrained by its cost due to low time-stepping and chemical kinetics when ignition is to be tested. Cost is estimated to be $\sim 2.8 \text{ khCPU} \cdot \text{ms}_{phys}^{-1}$ for the non-reactive jet formation and $\sim 7.5 \text{ khCPU} \cdot \text{ms}_{phys}^{-1}$ for the ignition sequence (on a 900 cores Skylake CPU architecture). A full sequence represents approximately 50 ms of jet formation and 40 ms of ignition, leading to a total cost of 440 khCPU. Costs must be multiplied by 5 when targeting a full cell and not an axi-periodic slice. In comparison, the simplified cell proposed in Chap. 12 represents a total cost of 72 khCPU on a comparable 1000 cores Intel Cascade Lake architecture. Nonetheless, it remains an option for critical applications, in parallel with experimental preparations, to ensure a proper representativeness of the simulated design.

Bibliography

- [1] M. A. Abdel-Raheem, S. S. Ibrahim, W. Malalasekera, and A. R. Masri. Large Eddy simulation of hydrogen-air premixed flames in a small scale combustion chamber. *International Journal of Hydrogen Energy*, 40(7):3098–3109, 2015. [220](#)
- [2] P. W. Agostinelli. *Assessment of Large Eddy Simulation in the Conjugate Heat Transfer context for engine operability: application to Hydrogen enrichment and Spinning Combustion Technology*. PhD thesis, 2022. [207](#)
- [3] P. W. Agostinelli, D. Laera, I. Boxx, L. Gicquel, and T. Poinsot. Impact of wall heat transfer in Large Eddy Simulation of flame dynamics in a swirled combustion chamber. *Combustion and Flame*, 234:111728, 2021. [207](#)
- [4] R. S. Ahima. Global warming threatens human thermoregulation and survival. *Journal of Clinical Investigation*, 130(2):559–561, 2020. [2](#)
- [5] S. F. Ahmed and E. Mastorakos. Spark ignition of lifted turbulent jet flames. *Combustion and Flame*, 146(1-2):215–231, 2006. [124](#), [144](#), [151](#), [161](#)
- [6] V. Akkerman, V. Bychkov, A. Petchenko, and L. E. Eriksson. Accelerating flames in cylindrical tubes with nonslip at the walls. *Combustion and Flame*, 145(1-2):206–219, 2006. [199](#), [203](#)
- [7] K. Alexandrino, M. U. Alzueta, and H. J. Curran. An experimental and modeling study of the ignition of dimethyl carbonate in shock tubes and rapid compression machine. *Combustion and Flame*, 188:212–226, 2018. [64](#)
- [8] J. Andersson and S. Grönkvist. Large-scale storage of hydrogen. *International Journal of Hydrogen Energy*, 44(23):11901–11919, 2019. [3](#)
- [9] M. Armand and J. Tarascon. Building better batteries. *Nature*, 451, 2008. [3](#)
- [10] D. Aurbach, Y. Talyosef, B. Markovsky, E. Markevich, E. Zinigrad, L. Asraf, J. S. Gnanaraj, and H. J. Kim. Design of electrolyte solutions for Li and Li-ion batteries: A review. *Electrochimica Acta*, 50(2-3 SPEC. ISS.):247–254, 2004. [58](#)
- [11] F. Austin Mier, M. J. Hargather, and S. R. Ferreira. Experimental Quantification of Vent Mechanism Flow Parameters in 18650 Format Lithium Ion Batteries. *Journal of Fluids Engineering, Transactions of the ASME*, 141(6):1–11, 2019. [11](#), [12](#), [91](#), [92](#), [119](#), [170](#)

- [12] A. R. Baird, E. J. Archibald, K. C. Marr, and O. A. Ezekoye. Explosion hazards from lithium-ion battery vent gas. *Journal of Power Sources*, 446:227257, 2020. [60](#), [75](#), [85](#)
- [13] R. S. Barlow and J. Frank. Effects on Turbulence on Species Mass Fractions in Methane/Air Jet Flames. *Proceedings of the Twenty-Seventh Symposium (International) on Combustion*, pages 1087–1095, 1998. [144](#)
- [14] H. A. Behabtu, M. Messagie, T. Coosemans, M. Berecibar, K. A. Fante, A. A. Kebede, and J. Van Mierlo. A review of energy storage technologies' application potentials in renewable energy sources grid integration. *Sustainability (Switzerland)*, 12(24):1–20, 2020. [3](#)
- [15] I. Belharouak, W. Lu, D. Vissers, and K. Amine. Safety characteristics of $\text{Li}(\text{Ni}_{0.8}\text{Co}_{0.15}\text{Al}_{0.05})\text{O}_2$ and $\text{Li}(\text{Ni}_{1/3}\text{Co}_{1/3}\text{Mn}_{1/3})\text{O}_2$. *Electrochemistry Communications*, 8(2):329–335, 2006. [57](#), [63](#), [78](#)
- [16] C. J. Benito Parejo. *Experimental Characterization of Electrical Discharges and Formation of the Ignition Kernel. Application to the Study of Performances of Aeronautical Igniters*. PhD thesis, 2019. [151](#), [152](#)
- [17] L. Berger, A. Attili, and H. Pitsch. Intrinsic instabilities in premixed hydrogen flames: Parametric variation of pressure, equivalence ratio, and temperature. Part 1 - Dispersion relations in the linear regime. *Combustion and Flame*, 240(xxxx):111935, 2022. [100](#)
- [18] L. Berger, A. Attili, and H. Pitsch. Intrinsic instabilities in premixed hydrogen flames: parametric variation of pressure, equivalence ratio, and temperature. Part 2 – Non-linear regime and flame speed enhancement. *Combustion and Flame*, 240(xxxx):111936, 2022. [100](#)
- [19] M. J. Berger. Local adaptive mesh refinement for shock hydrodynamics. *Journal of Computational Physics*, 82:64–84, 1989. [214](#)
- [20] A. Bhagatwala and S. K. Lele. A modified artificial viscosity approach for compressible turbulence simulations. *Journal of Computational Physics*, 228:4965–4969, 2009. [48](#)
- [21] R. W. Bilger. The structure of turbulent nonpremixed flames. *Symposium (International) on Combustion*, pages 475–488, 1988. [103](#)
- [22] R. W. Bilger and S. H. Stårner. On reduced mechanisms for Methane-Air combustion in non-premixed flames. *Combustion and Flame*, 80:135–149, 1990. [102](#), [103](#), [107](#)
- [23] L. R. Boeck, M. Kellenberger, G. Rainsford, and G. Ciccarelli. Simultaneous OH-PLIF and schlieren imaging of flame acceleration in an obstacle-laden channel. *Proceedings of the Combustion Institute*, 36(2):2807–2814, 2017. [219](#)
- [24] L. R. Boeck, S. Lapointe, J. Melguizo-Gavilanes, and G. Ciccarelli. Flame propagation across an obstacle: OH-PLIF and 2-D simulations with detailed chemistry. *Proceedings of the Combustion Institute*, 36(2):2799–2806, 2017. [220](#)

- [25] A. Bordes, D. Danilov, P. Desprez, A. Lecocq, G. Marlair, B. Truchot, M. Dahmani, C. Siret, S. Laurent, S. Herreyre, A. Dominget, L. Hamelin, G. Rigobert, S. Benjamin, N. Legrand, M. Belerrajoul, W. Maurer, Z. Chen, L. Rajmakers, D. Li, J. Zhou, P. Notten, P. Perlo, M. Biasiotto, R. Introzzi, M. Petit, J. Martin, J. Bernard, S. Koffel, V. Lonrentz, E. Durling, S. Korali, Z. Wang, M. Massazza, and S. Lamontarana. A holistic contribution to fast innovation in electric vehicles: An overview of the DEMOBASE research project. *eTransportation*, 11:100144, 2021. [3](#)
- [26] A. Börger, J. Mertens, and H. Wenzl. Thermal runaway and thermal runaway propagation in batteries: What do we talk about? *Journal of Energy Storage*, 24(August 2018):100649, 2019. [9](#)
- [27] M. V. Bragin and V. V. Molkov. Physics of spontaneous ignition of high-pressure hydrogen release and transition to jet fire. *International Journal of Hydrogen Energy*, 36(3):2589–2596, 2011. [128](#)
- [28] C. Brand and B. Boardman. Taming of the few-The unequal distribution of greenhouse gas emissions from personal travel in the UK. *Energy Policy*, 36(1):224–238, 2008. [2](#)
- [29] K. N. Bray and J. B. Moss. A closure model for the turbulent premixed flame with sequential chemistry. *Combustion and Flame*, 30(C):125–131, 1977. [42](#)
- [30] J. Buckmaster. Edge-flames. *Progress in Energy and Combustion Science*, 28(5):435–475, 2002. [144](#)
- [31] V. Bychkov, V. Akkerman, G. Fru, A. Petchenko, and L. E. Eriksson. Flame acceleration in the early stages of burning in tubes. *Combustion and Flame*, 150(4):263–276, 2007. [199](#), [203](#), [208](#)
- [32] V. Bychkov, V. Akkerman, D. Valiev, and C. K. Law. Influence of gas compression on flame acceleration in channels with obstacles. *Combustion and Flame*, 157(10):2008–2011, 2010. [199](#), [203](#)
- [33] Q. Cazères. *Analysis and reduction of chemical kinetics for combustion applications*. PhD thesis, 2021. [23](#), [73](#), [74](#), [102](#)
- [34] Q. Cazères and P. Pepiot. ARCANÉ - Analytical Reduction of Chemistry : Automatic, Nice and Efficient. [73](#), [74](#), [235](#)
- [35] Q. Cazères, P. Pepiot, E. Riber, and B. Cuenot. A fully automatic procedure for the analytical reduction of chemical kinetics mechanisms for Computational Fluid Dynamics applications. *Fuel*, 303(December 2020), 2021. [73](#), [74](#), [232](#)
- [36] A. Cellier, F. Duchaine, T. Poinso, G. Okyay, M. Leyko, and M. Pallud. An analytically reduced chemistry scheme for large eddy simulation of lithium-ion battery fires. *Combustion and Flame*, 250:112648, 2023. [87](#)
- [37] Cerfacs. AVBP CFD solver. [12](#), [22](#), [50](#), [201](#), [241](#)

- [38] M. Chaos and F. L. Dryer. Chemical-Kinetic Modeling of Ignition Delay: Considerations in Interpreting Shock Tube Data. *International Journal of Chemical Kinetics*, 2009. 36
- [39] F. Charlette, C. Meneveau, and D. Veynante. A power-law flame wrinkling model for LES of premixed turbulent combustion Part I: Non-dynamic formulation and initial tests. *Combustion and Flame*, 131(1-2):159–180, 2002. 47, 221
- [40] F. Charlette, C. Meneveau, and D. Veynante. A power-law flame wrinkling model for LES of premixed turbulent combustion Part II: Dynamic formulation. *Combustion and Flame*, 131(1-2):181–197, 2002. 47, 222
- [41] Chemical-Kinetic Mechanisms for Combustion Applications, UC San Diego Mechanism web page. <http://combustion.ucsd.edu>. 72, 76, 235
- [42] F. Chen, A. Allou, Q. Douasbin, L. Selle, and J. D. Parisse. Influence of straight nozzle geometry on the supersonic under-expanded gas jets. *Nuclear Engineering and Design*, 339(September):92–104, 2018. 128
- [43] S. Chen, Z. Wang, J. Wang, X. Tong, and W. Yan. Lower explosion limit of the vented gases from Li-ion batteries thermal runaway in high temperature condition. *Journal of Loss Prevention in the Process Industries*, 63:103992, 2020. 76
- [44] Y. Chen, Y. Kang, Y. Zhao, L. Wang, J. Liu, Y. Li, Z. Liang, X. He, X. Li, N. Tavajohi, and B. Li. A review of lithium-ion battery safety concerns: The issues, strategies, and testing standards. *Journal of Energy Chemistry*, 59:83–99, 2021. 9, 10, 12
- [45] S. P. Choudhury and R. Joarder. High-speed photography and background oriented schlieren techniques for characterizing tulip flame. *Combustion and Flame*, 245:112304, 2022. 199
- [46] S. H. Chung. Stabilization, propagation and instability of tribrachial triple flames. *Proceedings of the Combustion Institute*, 31 I(1):877–892, 2007. 144
- [47] C. Clanet and G. Searby. On the "Tulip flame" phenomenon. *Combustion and Flame*, 105(1-2):225–238, 1996. 199, 204
- [48] P. Clavin and P. Searby. *Combustion Waves and Fronts in Flows*. Cambridge University Press, 2016. 33
- [49] O. Colin, F. Ducros, D. Veynante, and T. Poinsot. A thickened flame model for large eddy simulations of turbulent premixed combustion. *Physics of Fluids*, 12(7):1843–1863, 2000. 42, 46
- [50] O. Colin and M. Rudgyard. Development of High-Order Taylor-Galerkin Schemes for LES. *Journal of Computational Physics*, 162(2):338–371, 2000. 51, 93, 128, 135, 147, 186, 257

- [51] P. T. Coman, E. C. Darcy, C. T. Veje, and R. E. White. Numerical analysis of heat propagation in a battery pack using a novel technology for triggering thermal runaway. *Applied Energy*, 203:189–200, 2017. 9, 233
- [52] P. T. Coman, S. Rayman, and R. E. White. A lumped model of venting during thermal runaway in a cylindrical Lithium Cobalt Oxide lithium-ion cell. *Journal of Power Sources*, 307:56–62, 2016. 233
- [53] A. W. Cook and W. H. Cabot. A high-wavenumber viscosity for high-resolution numerical methods. *Journal of Computational Physics*, 195(2):594–601, 2004. 48
- [54] A. W. Cook and W. H. Cabot. Hyperviscosity for shock-turbulence interactions. *Journal of Computational Physics*, 203(2):379–385, 2005. 43, 48
- [55] A. W. Cook and J. J. Riley. A subgrid model for equilibrium chemistry in turbulent flows. *Physics of Fluids*, 6(8):2868–2870, 1994. 42
- [56] R. Courant, K. Friedrichs, and H. Lewy. On the partial difference equations of mathematical physics. Technical report, New York University, 1956. 40
- [57] Creck Modeling Group. <http://creckmodeling.chem.polimi.it/menu-kinetics/menu-kinetics-detailed-mechanisms>. 72, 76
- [58] F. Cucchiella, I. D’Adamo, and M. Gastaldi. Future trajectories of renewable energy consumption in the European Union. *Resources*, 7(1), 2018. 2
- [59] B. Cuenot, F. Shum-Kivan, and S. Blanchard. The thickened flame approach for non-premixed combustion: Principles and implications for turbulent combustion modeling. *Combustion and Flame*, 239:111702, 2022. 30, 42, 108
- [60] D. F. Davidson and R. K. Hanson. Interpreting shock tube ignition data. *International Journal of Chemical Kinetics*, 36(9):510–523, 2004. 36
- [61] R. M. DeConto and D. Pollard. Contribution of Antarctica to past and future sea-level rise. *Nature*, 531(7596):591–597, 2016. 2
- [62] DNV GL - Energy. McMicken Battery Energy Storage System Event Technical Analysis and Recommendations. page 78, 2020. 12, 233
- [63] J. W. Dold. Flame Propagation in a Nonuniform Mixture: Analysis of a Propagating Triple-Flame. *Combustion and Flame*, 76:71–88, 1989. 31, 161
- [64] O. Dounia. *Etudes des phénomènes d’accélération de flammes, transition à la détonation et d’inhibition de flammes*. PhD thesis, 2018. 132
- [65] A. Du Pasquier, F. Disma, T. Bowmer, A. S. Gozdz, G. Amatucci, and J. Tarascon. Differential Scanning Calorimetry Study of the Reactivity of Carbon Anodes in Plastic Li-Ion Batteries. *Journal of The Electrochemical Society*, 145(4):1413–1413, 1998. 59, 63
- [66] J. Duan, X. Tang, H. Dai, Y. Yang, W. Wu, X. Wei, and Y. Huang. *Building Safe Lithium - Ion Batteries for Electric Vehicles : A Review*, volume 3. Springer Singapore, 2020. 3

- [67] F. Ducros, V. Ferrand, F. Nicoud, F. Weber, D. Darracq, C. Gacherieu, and T. Poinsot. Large-Eddy Simulation of the Shock/ Turbulence Interaction. *Journal of Computational Physics*, 152:517–549, 1999. 48
- [68] R. Dufo-Lopez, J. Bernal-Agustin, and J. A. Dominguez-Navarro. Generation management using batteries in wind farms : Economical and technical analysis for Spain. *Energy Policy*, 37:126–139, 2009. 3
- [69] S. Dühnen, J. Betz, M. Kolek, R. Schmuch, M. Winter, and T. Placke. Toward Green Battery Cells: Perspective on Materials and Technologies. *Small Methods*, 4(7), 2020. 3, 57
- [70] A. M. Elbaz, S. Wang, T. F. Guiberti, and W. L. Roberts. Review on the recent advances on ammonia combustion from the fundamentals to the applications. *Fuel Communications*, 10(December 2021):100053, 2022. 3
- [71] A. M. Elberry, J. Thakur, A. Santasalo-Aarnio, and M. Larimi. Large-scale compressed hydrogen storage as part of renewable electricity storage systems. *International Journal of Hydrogen Energy*, 46(29):15671–15690, 2021. 3
- [72] O. C. d. C. Ellis, W. A. Kirkby, and V. R. Wheeler. Explosions in Closed Cylinders. Part I: Methane-Air Explosions in a Long Cylinder, Part II: The Effect of the Length of the Cylinder, and Part III: The Manner of Movement of Flame. *Journal of the American Chemical Society*, 7:3203–3218, 1928. 199, 204
- [73] FAA. Risks of Fire or Explosion when Transporting Lithium Ion or Lithium Metal Batteries as Cargo on Passenger and Cargo Aircraft. Technical report, 2016. 6
- [74] X. Feng, L. Lu, M. Ouyang, J. Li, and X. He. A 3D thermal runaway propagation model for a large format lithium ion battery module. *Energy*, 115:194–208, 2016. 9, 233
- [75] X. Feng, M. Ouyang, X. Liu, L. Lu, Y. Xia, and X. He. Thermal runaway mechanism of lithium ion battery for electric vehicles: A review. *Energy Storage Materials*, 10(May 2017):246–267, 2018. 9, 10, 11, 12, 61
- [76] X. Feng, S. Zheng, D. Ren, X. He, L. Wang, X. Liu, M. Li, and M. Ouyang. Key characteristics for thermal runaway of Li-ion batteries. *Energy Procedia*, 158:4684–4689, 2019. 10
- [77] E. Fernández-Tarrazo, M. Vera, and A. Liñán. Liftoff and blowoff of a diffusion flame between parallel streams of fuel and air. *Combustion and Flame*, 144(1-2):261–276, 2006. 144
- [78] D. P. Finegan, E. Darcy, M. Keyser, B. Tjaden, T. M. Heenan, R. Jarvis, J. J. Bailey, R. Malik, N. T. Vo, O. V. Magdysyuk, R. Atwood, M. Drakopoulos, M. DiMichiel, A. Rack, G. Hinds, D. J. Brett, and P. R. Shearing. Characterising thermal runaway within lithium-ion cells by inducing and monitoring internal short circuits. *Energy and Environmental Science*, 10(6):1377–1388, 2017. 10

- [79] D. P. Finegan, E. Darcy, M. Keyser, B. Tjaden, T. M. Heenan, R. Jervis, J. J. Bailey, N. T. Vo, O. V. Magdysyuk, M. Drakopoulos, M. D. Michiel, A. Rack, G. Hinds, D. J. Brett, and P. R. Shearing. Identifying the Cause of Rupture of Li-Ion Batteries during Thermal Runaway. *Advanced Science*, 5(2018), 2018. [7](#), [12](#), [119](#), [170](#), [177](#), [187](#)
- [80] D. P. Finegan, M. Scheel, J. B. Robinson, B. Tjaden, I. Hunt, T. J. Mason, J. Millichamp, M. Di Michiel, G. J. Offer, G. Hinds, D. J. Brett, and P. R. Shearing. In-operando high-speed tomography of lithium-ion batteries during thermal runaway. *Nature Communications*, 6:1–10, 2015. [12](#), [170](#)
- [81] B. Fiorina, R. Vicquelin, P. Auzillon, N. Darabiha, O. Gicquel, and D. Veynante. A filtered tabulated chemistry model for LES of premixed combustion. *Combustion and Flame*, 157(3):465–475, 2010. [42](#), [73](#)
- [82] D. A. Fordham, H. Resit Akçakaya, M. B. Araújo, J. Elith, D. A. Keith, R. Pearson, T. D. Auld, C. Mellin, J. W. Morgan, T. J. Regan, M. Tozer, M. J. Watts, M. White, B. A. Wintle, C. Yates, and B. W. Brook. Plant extinction risk under climate change: Are forecast range shifts alone a good indicator of species vulnerability to global warming? *Global Change Biology*, 18(4):1357–1371, 2012. [2](#)
- [83] E. Franquet, V. Perrier, S. Gibout, and P. Bruel. Free underexpanded jets in a quiescent medium: A review. *Progress in Aerospace Sciences*, 77:25–53, 2015. [128](#), [130](#), [131](#)
- [84] B. Franzelli, E. Riber, M. Sanjosé, and T. Poinso. A two-step chemical scheme for kerosene-air premixed flames. *Combustion and Flame*, 157(7):1364–1373, 2010. [73](#)
- [85] Y. Fu, S. Lu, K. Li, C. Liu, X. Cheng, and H. Zhang. An experimental study on burning behaviors of 18650 lithium ion batteries using a cone calorimeter. *Journal of Power Sources*, 273:216–222, 2015. [12](#), [184](#), [193](#)
- [86] N. E. Galushkin, N. N. Yazvinskaya, and D. N. Galushkin. Mechanism of Thermal Runaway in Lithium-Ion Cells. *Journal of The Electrochemical Society*, 165(7):A1303–A1308, 2018. [9](#)
- [87] S. Gao, L. Lu, M. Ouyang, Y. Duan, X. Zhu, C. Xu, B. Ng, N. Kamyab, R. E. White, and P. T. Coman. Experimental Study on Module-to-Module Thermal Runaway-Propagation in a Battery Pack. *Journal of The Electrochemical Society*, 166(10):A2065–A2073, 2019. [12](#)
- [88] A. García, J. Monsalve-Serrano, R. Lago Sari, and S. Martinez-Boggio. An optical investigation of thermal runaway phenomenon under thermal abuse conditions. *Energy Conversion and Management*, 246:114663, 2021. [12](#), [63](#), [104](#), [179](#), [184](#), [193](#), [233](#)
- [89] D. J. Gardner, D. R. Reynolds, C. S. Woodward, and C. J. Balos. Enabling new flexibility in the {SUNDIALS} suite of nonlinear and differential/algebraic equation solvers. *ACM Transactions on Mathematical Software (TOMS)*, 2022. [50](#)

- [90] GENCI website. <https://www.genci.fr>. 14
- [91] O. Gicquel, N. Darabiha, and D. Thévenin. Laminar premixed hydrogen/air counterflow flame simulations using flame prolongation of ILDM with differential diffusion. *Proceedings of the Combustion Institute*, 28(2):1901–1908, 2000. 73
- [92] V. Giovangigli. *Multicomponent Flow Modelling*. Birkhäuser, Boston, 1999. 19
- [93] V. Giovangigli. Multicomponent transport in laminar flames. *Proceedings of the Combustion Institute*, 35(1):625–637, 2015. 19
- [94] J. S. Gnanaraj, E. Zinigrad, L. Asraf, H. E. Gottlieb, M. Sprecher, D. Aurbach, and M. Schmidt. The use of accelerating rate calorimetry (ARC) for the study of the thermal reactions of Li-ion battery electrolyte solutions. *Journal of Power Sources*, 119-121:794–798, 2003. 63
- [95] V. V. Golub, D. I. Baklanov, T. V. Bazhenova, M. V. Bragin, S. V. Golovastov, M. F. Ivanov, and V. V. Volodin. Shock-induced ignition of hydrogen gas during accidental or technical opening of high-pressure tanks. *Journal of Loss Prevention in the Process Industries*, 20(4-6):439–446, 2007. 36
- [96] A. W. Golubkov, D. Fuchs, J. Wagner, H. Wiltsche, C. Stangl, G. Fauler, G. Voitic, A. Thaler, and V. Hacker. Thermal-runaway experiments on consumer Li-ion batteries with metal-oxide and olivin-type cathodes. *RSC Advances*, 4(7):3633–3642, 2014. 11, 12, 59, 60, 61, 63, 64, 67, 78, 80, 92, 118, 170, 172, 173, 178, 184, 185, 190
- [97] A. W. Golubkov, S. Scheikl, R. Planteu, G. Voitic, H. Wiltsche, C. Stangl, G. Fauler, A. Thaler, and V. Hacker. Thermal runaway of commercial 18650 Li-ion batteries with LFP and NCA cathodes - Impact of state of charge and overcharge. *RSC Advances*, 5(70):57171–57186, 2015. 12, 60, 61, 64, 67, 78, 80, 118, 170
- [98] M. Gonzalez, R. Borghi, and A. Saouab. Interaction of a flame front with its self-generated flow in an enclosure: The "tulip flame" phenomenon. *Combustion and Flame*, 88(2):201–220, 1992. 199
- [99] D. G. Goodwin, R. L. Speth, H. K. Moffat, and B. W. Weber. Cantera: An Object-oriented Software Toolkit for Chemical Kinetics, Thermodynamics, and Transport Processes, 2.3.0, 2017. 19, 22, 50, 65, 72, 76, 164
- [100] S. R. Gubba, S. S. Ibrahim, W. Malalasekera, and A. R. Masri. An assessment of large eddy simulations of premixed flames propagating past repeated obstacles. *Combustion Theory and Modelling*, 13(3):513–540, 2009. 220
- [101] S. R. Gubba, S. S. Ibrahim, W. Malalasekera, and A. R. Masri. Measurements and LES calculations of turbulent premixed flame propagation past repeated obstacles. *Combustion and Flame*, 158(12):2465–2481, 2011. 220

- [102] N. Guézennec and T. Poinso. Acoustically nonreflecting and reflecting boundary conditions for vorticity injection in compressible solvers. *AIAA Journal*, 47(7):1709–1722, 2009. 187
- [103] A. Hamzehloo and P. G. Aleiferis. Numerical modelling of transient under-expanded jets under different ambient thermodynamic conditions with adaptive mesh refinement. *International Journal of Heat and Fluid Flow*, 61:711–729, 2016. 128
- [104] A. Hamzehloo and P. G. Aleiferis. LES and RANS modelling of under-expanded jets with application to gaseous fuel direct injection for advanced propulsion systems. *International Journal of Heat and Fluid Flow*, 76(March):309–334, 2019. 128
- [105] T. D. Hatchard, D. D. MacNeil, A. Basu, and J. R. Dahn. Thermal Model of Cylindrical and Prismatic Lithium-Ion Cells. *Journal of The Electrochemical Society*, 148(7):A755, 2001. 187, 233
- [106] M. E. Hauer, E. Fussell, V. Mueller, M. Burkett, M. Call, K. Abel, R. McLeman, and D. Wrathall. Sea-level rise and human migration. *Nature Reviews Earth and Environment*, 1(1):28–39, 2020. 2
- [107] G. He, J. Lin, F. Sifuentes, X. Liu, N. Abhyankar, and A. Phadke. Rapid cost decrease of renewables and storage accelerates the decarbonization of China’s power system. *Nature Communications*, 11(1):1–9, 2020. 3
- [108] M. Henriksen and D. Bjerketved. Experimental data of gas explosions in a 1-meter open-ended channel. University of South-Eastern Norway. Dataset, <https://doi.org/10.23642/usn.13796108.v2>, 2021. 114, 199, 232
- [109] M. Henriksen and D. Bjerketved. Experiments of Premixed Gas Explosion in a 1-meter Channel Partly Filled with 18650 Cell Geometry. Dataset, <https://doi.org/10.23642/USN.15134442.V1>, 2021. 114, 220, 232
- [110] M. Henriksen, K. Vaagsaether, J. Lundberg, S. Forseth, and D. Bjerketvedt. Laminar burning velocity of gases vented from failed Li-ion batteries. *Journal of Power Sources*, 506(March):230141, 2021. 61, 64, 72, 78, 88
- [111] M. Henriksen, K. Vaagsaether, J. Lundberg, S. Forseth, and D. Bjerketvedt. Simulation of a premixed explosion of gas vented during Li-ion battery failure. *Fire Safety Journal*, 126(April):103478, 2021. 12, 114, 198, 199, 200, 206, 232
- [112] M. Henriksen, K. Vaagsaether, J. Lundberg, S. Forseth, and D. Bjerketvedt. Numerical study of premixed gas explosion in a 1-m channel partly filled with 18650 cell-like cylinders with experiments. *Journal of Loss Prevention in the Process Industries*, 77(August 2021):104761, 2022. 12, 114, 220, 232
- [113] J. O. Hirschfelder. *Molecular theory of gases and liquids*. John Wiley, New York, 1969. 19
- [114] J. Houghton. Global warming. *Reports on Progress in Physics*, 68(6):1343–1403, 2005. 2

- [115] H. Hugoniot. Sur la propagation du mouvement dans les corps, Partie 2. *Journal de l'Ecole Polytechnique*, 1889. 33
- [116] S. S. Ibrahim, S. R. Gubba, A. R. Masri, and W. Malalasekera. Calculations of explosion deflagrating flames using a dynamic flame surface density model. *Journal of Loss Prevention in the Process Industries*, 22(3):258–264, 2009. 220
- [117] IDRIS website. <http://www.idris.fr>. 14
- [118] F. P. Incropera, D. P. Dewitt, T. L. Bergman, and A. S. Lavine. *Fundamentals of Heat and Mass Transfer*. John Wiley & Sons, 2007. 203
- [119] Intergovernmental Panel on Climate Change. Global warming of 1.5°C. Technical report, 2018. 2
- [120] Intergovernmental Panel on Climate Change. Synthesis Report of the IPCC Sixth Assessment Report. Technical report, 2021. 2
- [121] Intergovernmental Panel on Climate Change. Climate Change 2022 : Mitigation of Climate Change. Technical report, 2022. 2
- [122] International Energy Agency. Key World Energy Statistics 2021 – Statistics Report. Technical report, 2021. 1, 2
- [123] International Energy Agency. Global Supply Chains of EV Batteries. Technical report, 2022. 2, 3
- [124] J. Jaguemont, L. Boulon, and Y. Dubé. A comprehensive review of lithium-ion batteries used in hybrid and electric vehicles at cold temperatures. *Applied Energy*, 164:99–114, 2016. 3
- [125] A. Jameson, W. Schmidt, and E. Turkel. Numerical solution of the Euler equations by finite volume methods using Runge Kutta time stepping schemes. *AIAA Fluid and Plasma Dynamics Conference*, (1981), 1981. 43, 128, 147, 174, 186, 201, 222
- [126] T. Jaravel. *Prediction of Pollutants in Gas Turbines Using Large Eddy Simulation*. PhD thesis, 2016. 101, 200
- [127] C. Jiménez and B. Cuenot. DNS study of stabilization of turbulent triple flames by hot gases. *Proceedings of the Combustion Institute*, 31 I(1):1649–1656, 2007. 144
- [128] R. V. Kaenel and L. Kleiser. Large-Eddy Simulation of Shock-Turbulence Interaction. *AIAA Journal*, 42, 2004. 43, 49
- [129] G. T. Kalghatgi. Blow-Out Stability of Gaseous Jet Diffusion Flames. Part I In Still Air. *Combustion Science and Technology*, 26(5-6):233–239, 1981. 144
- [130] G. T. Kalghatgi. Blow-Out Stability of Gaseous Jet Diffusion Flames Part II: Effect of Cross Wind. *Combustion Science and Technology*, 26(5-6):241–244, 1981. 144

- [131] G. T. Kalghatgi. Blow-out stability of gaseous jet diffusion flames: Part III - effect of burner orientation to wind direction. *Combustion Science and Technology*, 28(5-6):241–245, 1982. [144](#)
- [132] K. Kanayama, S. Takahashi, S. Morikura, H. Nakamura, T. Tezuka, and K. Maruta. Study on oxidation and pyrolysis of carbonate esters using a micro flow reactor with a controlled temperature profile. Part I: Reactivities of dimethyl carbonate, ethyl methyl carbonate and diethyl carbonate. *Combustion and Flame*, 237:111810, 2022. [61](#), [64](#)
- [133] J. Kent, A. Masri, S. Starner, and S. Ibrahim. A new chamber to study premixed flame propagation past repeated obstacles,. In *5th Asia-Pacific Conference on Combustion*, 2005. [219](#)
- [134] A. A. Khasnis and M. D. Nettleman. Global Warming and Infectious Disease. *Archives of Medical Research*, 36:689–696, 2005. [2](#)
- [135] G. H. Kim, A. Pesaran, and R. Spotnitz. A three-dimensional thermal abuse model for lithium-ion cells. *Journal of Power Sources*, 170(2):476–489, 2007. [12](#), [233](#)
- [136] J. Kim, A. Mallarapu, D. P. Finegan, and S. Santhanagopalan. Modeling cell venting and gas-phase reactions in 18650 lithium ion batteries during thermal runaway. *Journal of Power Sources*, 489(October 2020):229496, 2021. [12](#)
- [137] S. Kim, J. Chen, T. Cheng, A. Gindulyte, J. He, S. He, Q. Li, B. A. Shoemaker, P. A. Thiessen, B. Yu, L. Zaslavsky, J. Zhang, and E. E. Bolton. PubChem in 2021: New data content and improved web interfaces. *Nucleic Acids Research*, 49(D1):D1388–D1395, 2021. [59](#)
- [138] P. N. Kioni, B. Rogg, K. N. Bray, and A. Liñán. Flame spread in laminar mixing layers: The triple flame. *Combustion and Flame*, 95(3):276–290, 1993. [144](#), [147](#), [152](#), [161](#)
- [139] K. Kitoh and H. Nemoto. 100 Wh large size Li-ion batteries and safety tests. *Journal of Power Sources*, 81-82:887–890, 1999. [10](#)
- [140] Y. S. Ko and S. H. Chung. Propagation of unsteady tribrachial flames in laminar non-premixed jets. *Combustion and Flame*, 118(1-2):151–163, 1999. [144](#)
- [141] S. Koch, A. Fill, and K. P. Birke. Comprehensive gas analysis on large scale automotive lithium-ion cells in thermal runaway. *Journal of Power Sources*, 398(June):106–112, 2018. [60](#), [61](#), [64](#), [80](#)
- [142] A. N. Kolmogorov. The local structure of turbulence in incompressible viscous fluid for very large Reynolds numbers. *Proceedings of the Royal Society of London. Series A: Mathematical and Physical Sciences*, 434:9–13, 1991. [26](#)
- [143] D. Kong, G. Wang, P. Ping, and J. Wen. A coupled conjugate heat transfer and CFD model for the thermal runaway evolution and jet fire of 18650 lithium-ion battery under thermal abuse. *eTransportation*, 12:100157, 2022. [12](#), [184](#)

- [144] L. Kong, C. Li, J. Jiang, and M. G. Pecht. Li-ion battery fire hazards and safety strategies. *Energies*, 11(9):1–11, 2018. [9](#), [170](#)
- [145] K. K.-Y. Kuo. *Principles of Combustion*. John Wiley, second edition, 2005. [22](#), [23](#), [26](#), [27](#), [29](#), [30](#)
- [146] G. Lacaze. Simulation aux grandes échelles de l’allumage de moteurs de fusées cryotechniques. 2009. [124](#)
- [147] G. Lacaze, B. Cuenot, T. Poinso, and M. Oswald. Large eddy simulation of laser ignition and compressible reacting flow in a rocket-like configuration. *Combustion and Flame*, 156(6):1166–1180, 2009. [128](#), [241](#)
- [148] G. Lacaze, E. Richardson, and T. Poinso. Large eddy simulation of spark ignition in a turbulent methane jet. *Combustion and Flame*, 156(10):1993–2009, 2009. [124](#), [144](#), [151](#), [152](#), [161](#), [241](#)
- [149] M. Lammer, A. Königseder, and V. Hacker. Holistic methodology for characterisation of the thermally induced failure of commercially available 18650 lithium ion cells. *RSC Advances*, 7(39):24425–24429, 2017. [61](#), [64](#), [85](#), [88](#)
- [150] F. Larsson, J. Anderson, P. Andersson, and B.-E. Mellander. Thermal Modelling of Cell-to-Cell Fire Propagation and Cascading Thermal Runaway Failure Effects for Lithium-Ion Battery Cells and Modules Using Fire Walls. *Journal of The Electrochemical Society*, 163(14):A2854–A2865, 2016. [9](#), [12](#)
- [151] F. Larsson, P. Andersson, and B. E. Mellander. Lithium-ion battery aspects on fires in electrified vehicles on the basis of experimental abuse tests. *Batteries*, 2(2):1–13, 2016. [12](#), [170](#)
- [152] P. Lax and B. Wendroff. Systems of conservation laws. Technical report, 1959. [51](#), [93](#), [128](#), [135](#), [147](#), [174](#), [186](#), [201](#), [222](#)
- [153] J. Lee, S. H. Won, S. H. Jin, S. H. Chung, O. Fujita, and K. Ito. Propagation speed of tribrachial (triple) flame of propane in laminar jets under normal and micro gravity conditions. *Combustion and Flame*, 134(4):411–420, 2003. [144](#)
- [154] J. H. Lee. *The Detonation Phenomenon*. Cambridge University Press, 2008. [33](#)
- [155] J. P. Legier, T. Poinso, and D. Veynante. Dynamically thickened flame LES model for premixed and non-premixed turbulent combustion. *Proceedings of the Summer Program, Centre for Turbulence Research*, pages 157–168, 2000. [47](#)
- [156] T. Lehtola and A. Zahedi. Solar energy and wind power supply supported by storage technology : A review. *Sustainable Energy Technologies and Assessments*, 35(May):25–31, 2019. [3](#)
- [157] H. Li, Q. Duan, C. Zhao, Z. Huang, and Q. Wang. Experimental investigation on the thermal runaway and its propagation in the large format battery module with Li(Ni_{1/3}Co_{1/3}Mn_{1/3})O₂ as cathode. *Journal of Hazardous Materials*, 375(January):241–254, 2019. [12](#)

- [158] M. Li, J. Lu, Z. Chen, and K. Amine. 30 Years of Lithium-Ion Batteries. *Advanced Materials*, 2018. 3
- [159] W. Li, K. Crompton, and J. K. Ostanek. Comparison of current interrupt device and vent design for 18650 format lithium-ion battery caps: New findings. *Journal of Energy Storage*, 46(July 2021):103841, 2022. 12, 170
- [160] W. Li, K. R. Crompton, C. Hacker, and J. K. Ostanek. Comparison of Current Interrupt Device and Vent Design for 18650 Format Lithium-ion Battery Caps. *Journal of Energy Storage*, 32(July):101890, 2020. 12, 170
- [161] W. Li, V. León Quiroga, K. R. Crompton, and J. K. Ostanek. High Resolution 3-D Simulations of Venting in 18650 Lithium-Ion Cells. *Frontiers in Energy Research*, 9(December):1–19, 2021. 12, 170, 175, 187, 190
- [162] X. Li, F. He, and L. Ma. Thermal management of cylindrical batteries investigated using wind tunnel testing and computational fluid dynamics simulation. *Journal of Power Sources*, 238:395–402, 2013. 12
- [163] M. A. Liberman, C. Qian, and C. Wang. Dynamics of flames in tubes with no-slip walls and the mechanism of tulip flame formation1. *Combustion Science and Technology*, 195(7):1637–1665, 2023. 199
- [164] X. Liu, S. I. Stoliarov, M. Denlinger, A. Masias, and K. Snyder. Comprehensive calorimetry of the thermally-induced failure of a lithium ion battery. *Journal of Power Sources*, 280:516–525, 2015. 9, 10, 12
- [165] S. C. Lo, K. M. Aikens, G. A. Blaisdell, and A. S. Lyrantzis. Numerical investigation of 3-D supersonic jet flows using large-eddy simulation. *International Journal of Aeroacoustics*, 11(7-8):783–812, 2012. 128
- [166] T. Lu and C. K. Law. A directed relation graph method for mechanism reduction. *Proceedings of the Combustion Institute*, 30(1):1333–1341, 2005. 74
- [167] T. Lu and C. K. Law. Systematic approach to obtain analytic solutions of quasi steady state species in reduced mechanisms. *Journal of Physical Chemistry A*, 110(49):13202–13208, 2006. 74
- [168] N. Lupoglazoff, A. Biancherin, F. Vuillot, and G. Rahier. Comprehensive 3D Unsteady simulations of subsonic and supersonic hot jet flow-fields. Part1: Aerodynamic Analysis. *8th AIAA/CEAS Aeroacoustics Conference*, pages 1–11, 2002. 128
- [169] K. M. Lyons. Toward an understanding of the stabilization mechanisms of lifted turbulent jet flames: Experiments. *Progress in Energy and Combustion Science*, 33(2):211–231, 2007. 144
- [170] J. R. Malcolm, C. Liu, R. P. Neilson, L. Hansen, and L. Hannah. Global warming and extinctions of endemic species from biodiversity hotspots. *Conservation Biology*, 20(2):538–548, 2006. 2

- [171] T. Maloney. Lithium Battery Thermal Runaway Vent Gas Analysis. Technical report, Federal Aviation Administration, Office of Hazardous Materials Safety, 2016. 60, 61, 64, 80
- [172] R. Maly and M. Vogel. Initiation and propagation of flame fronts in lean CH₄-air mixtures by the three modes of the ignition spark. *Symposium (International) on Combustion*, 17(1):821–831, 1979. 152, 242
- [173] A. Manthiram. Electrode materials for rechargeable lithium batteries. *Jom*, 49(3):43–46, 1997. 57
- [174] B. Mao, P. Huang, H. Chen, Q. Wang, and J. Sun. Self-heating reaction and thermal runaway criticality of the lithium ion battery. *International Journal of Heat and Mass Transfer*, 149:119178, 2020. 58, 59, 61
- [175] G. Maragkos and T. Beji. Review of convective heat transfer modelling in cfd simulations of fire-driven flows. *Applied Sciences (Switzerland)*, 11(11), 2021. 203
- [176] S. Marragou, H. Magnes, A. Aniello, L. Selle, T. Poinso, and T. Schuller. Experimental analysis and theoretical lift-off criterion for H₂/air flames stabilized on a dual swirl injector. *Proceedings of the Combustion Institute*, 000:1–10, 2022. 161, 163
- [177] A. Masias, J. Marcicki, and W. A. Paxton. Batteries in Automotive Applications. *ACS Energy Letters*, 2021. 3
- [178] A. R. Masri, A. AlHarbi, S. Meares, and S. S. Ibrahim. A Comparative Study of Turbulent Premixed Flames Propagating Past Repeated Obstacles. *Ind. Eng. Chem. Res.*, 51, 2012. 220
- [179] A. R. Masri, S. S. Ibrahim, and B. J. Cadwallader. Measurements and large eddy simulation of propagating premixed flames. *Experimental Thermal and Fluid Science*, 30(7):687–702, 2006. 219
- [180] E. Mastorakos. Ignition of turbulent non-premixed flames. *Progress in Energy and Combustion Science*, 35(1):57–97, 2009. 144
- [181] S. Mathur and S. C. Saxena. Viscosity of polar gas mixtures: Wilke’s method. *Applied Scientific Research*, 15:404–410, 1966. 20
- [182] S. Mathur and S. C. Saxena. Methods of calculating thermal conductivity of binary mixtures involving polyatomic gases. *Applied Scientific Research*, 17:155–168, 1967. 20
- [183] S. Mathur, P. K. Tondon, and S. C. Saxena. Thermal conductivity of binary, ternary and quaternary mixtures of rare gases. *Molecular Physics*, 12(6), 1967. 20
- [184] T. Matsuda, Y. Umeda, R. Ishii, A. Yasuda, and K. Sawada. Numerical and Experimental Studies on Choked Underexpanded Jets. *AlAA 19th Fluid Dynamics, Plasma Dynamics and Lasers Conference*, 1987. 128

- [185] W. Meier, R. S. Barlow, Y. L. Chen, and J. Y. Chen. Raman/Rayleigh/LIF measurements in a turbulent CH₄/H₂/N₂ jet diffusion flame: Experimental techniques and turbulence-chemistry interaction. *Combustion and Flame*, 123(3):326–343, 2000. 144
- [186] W. K. Metcalfe, S. M. Burke, S. S. Ahmed, and H. J. Curran. A hierarchical and comparative kinetic modeling study of C1 - C2 hydrocarbon and oxygenated fuels. *International Journal of Chemical Kinetics*, 45(10):638–675, 2013. 64
- [187] T. Meyer. *Über zweidimensionale Bewegungsvorgänge in einem Gas, das mit Überschallgeschwindigkeit strömt*. PhD thesis, Georg-August Universität, Göttingen, 1908. 35
- [188] F. A. Mier, M. Hargather, and S. Ferreira. Determining the Internal Pressure in 18650 Format Lithium Batteries Under Thermal Abuse. *Eesat 2017*, pages 1–12, 2017. 11, 127, 170
- [189] V. Moureau, B. Fiorina, and H. Pitsch. A level set formulation for premixed combustion LES considering the turbulent flame structure. *Combustion and Flame*, 156(4):801–812, 2009. 42
- [190] V. Moureau, G. Lartigue, P. Bénard, and R. Mercier. Parallel and dynamic mesh adaptation of tetrahedral-based meshes for propagating fronts and interfaces : application to premixed combustion. In *32nd International Conference on Parallel Computational Fluid Dynamics*, 2021. 214
- [191] S. Mouriaux, O. Colin, and D. Veynante. Adaptation of a dynamic wrinkling model to an engine configuration. *Proceedings of the Combustion Institute*, 36(3):3415–3422, 2017. 47, 222
- [192] V. Muenzel, A. F. Hollenkamp, A. I. Bhatt, J. de Hoog, M. Brazil, D. A. Thomas, and I. Mareels. A Comparative Testing Study of Commercial 18650-Format Lithium-Ion Battery Cells. *Journal of The Electrochemical Society*, 162(8):A1592–A1600, 2015. 8
- [193] S. R. Mulpuru and G. B. Wilkin. A model for vented deflagration of hydrogen in a volume. Technical Report 5975, 1978. 220, 233
- [194] L. Muñiz and M. G. Mungal. Instantaneous flame-stabilization velocities in lifted-jet diffusion flames. *Combustion and Flame*, 111(1-2):16–30, 1997. 144, 147, 152
- [195] NACA. Equations, tables, and charts for compressible flow, 1953. 33, 34, 35
- [196] H. Nakamura, H. J. Curran, A. Polo Córdoba, W. J. Pitz, P. Dagaut, C. Togbé, S. M. Sarathy, M. Mehl, J. R. Agudelo, and F. Bustamante. An experimental and modeling study of diethyl carbonate oxidation. *Combustion and Flame*, 162(4):1395–1405, 2015. 64
- [197] K. Nakayama, R. Ishikawa, S. Kobayashi, N. Shibata, and Y. Ikuhara. Dislocation and oxygen-release driven delithiation in Li₂MnO₃. *Nature Communications*, 11(1), 2020. 57, 63

- [198] F. Nicoud. Defining Wave Amplitude in Characteristic Boundary Conditions. *Journal of Computational Physics*, 149(2):418–422, 1999. [123](#), [174](#), [186](#), [202](#), [223](#)
- [199] F. Nicoud and F. Ducros. Subgrid-scale stress modelling based on the square of the velocity. *Flow Measurement and Instrumentation*, 62:183–200, 1999. [45](#), [128](#), [147](#), [174](#), [186](#), [201](#), [222](#), [257](#)
- [200] U. Niemann, K. Seshadri, and F. A. Williams. Accuracies of laminar counterflow flame experiments. *Combustion and Flame*, 162(4):1540–1549, 2015. [31](#)
- [201] S. Ogunfuye, H. Sezer, F. Kodakoglu, H. F. Farahani, A. S. Rangwala, and V. Akkerman. Dynamics of explosions in cylindrical vented enclosures: Validation of a computational model by experiments. *Fire*, 4(1):1–10, 2021. [233](#)
- [202] E. Oldenhof, M. J. Tummers, E. H. van Veen, and D. J. Roekaerts. Role of entrainment in the stabilisation of jet-in-hot-coflow flames. *Combustion and Flame*, 158(8):1553–1563, 2011. [144](#)
- [203] E. Oldenhof, M. J. Tummers, E. H. van Veen, and D. J. Roekaerts. Transient response of the Delft jet-in-hot coflow flames. *Combustion and Flame*, 159(2):697–706, 2012. [144](#)
- [204] M. Otto, K. L. Chagoya, R. G. Blair, S. M. Hick, and J. S. Kapat. Optimal hydrogen carrier: Holistic evaluation of hydrogen storage and transportation concepts for power generation, aviation, and transportation. *Journal of Energy Storage*, 55(PD):105714, 2022. [3](#)
- [205] R. Peng, P. Ping, G. Wang, X. He, D. Kong, and W. Gao. Numerical investigation on explosion hazards of lithium-ion battery vented gases and deflagration venting design in containerized energy storage system. *Fuel*, 351(June), 2023. [12](#), [220](#), [230](#)
- [206] P. Pepiot-Desjardins and H. Pitsch. An automatic chemical lumping method for the reduction of large chemical kinetic mechanisms. *Combustion Theory and Modelling*, 12(6):1089–1108, 2008. [74](#)
- [207] P. Pepiot-Desjardins and H. Pitsch. An efficient error-propagation-based reduction method for large chemical kinetic mechanisms. *Combustion and Flame*, 154(1-2):67–81, 2008. [74](#)
- [208] A. Pestre. *Simulations numériques d’allumages des moteurs aéronautiques en conditions réalistes de hautes altitudes*. PhD thesis, 2023. [151](#)
- [209] N. Peters. Laminar diffusion flamelet models in non-premixed turbulent combustion. *Progress in Energy and Combustion Science*, 10(3):319–339, 1984. [73](#)
- [210] N. Peters. *Turbulent Combustion*. Cambridge University Press, 2000. [26](#), [31](#), [32](#), [33](#), [42](#)

- [211] R. A. Pielke Jr., C. Landsea, M. Mayfield, J. Laver, and R. Pasch. Hurricanes and global warming. *American Meteorological Society*, 2005. [2](#)
- [212] H. Pitsch and H. Steiner. Large-eddy simulation of a turbulent piloted methane/air diffusion flame (Sandia flame D). *Physics of Fluids*, 12:2541–2554, 2000. [144](#)
- [213] T. Poinso and D. Veynante. *Theoretical and Numerical Combustion*. <https://elearning.cerfacs.fr>, third edition, 2012. [18](#), [21](#), [22](#), [26](#), [27](#), [28](#), [29](#), [30](#), [31](#), [32](#), [42](#), [43](#), [44](#), [46](#), [47](#), [103](#), [106](#)
- [214] T. J. Poinso and S. K. Lele. Boundary conditions for direct simulations of compressible viscous flows. *Journal of Computational Physics*, 101(1):104–129, 1992. [51](#), [123](#), [174](#), [186](#), [202](#), [223](#)
- [215] B. Ponizy, A. Claverie, and B. Veyssi re. Tulip flame - the mechanism of flame front inversion. *Combustion and Flame*, 161(12):3051–3062, 2014. [199](#), [204](#), [212](#)
- [216] S. B. Pope. *Turbulent Flows*. 2000. [26](#)
- [217] J. A. Pounds, M. R. Bustamante, L. A. Coloma, J. A. Consuegra, M. P. Fogden, P. N. Foster, E. La Marca, K. L. Masters, A. Merino-Viteri, R. Puschen-dorf, S. R. Ron, G. A. S nchez-Azofeifa, C. J. Still, and B. E. Young. Widespread amphibian extinctions from epidemic disease driven by global warming. *Nature*, 439(7073):161–167, 2006. [2](#)
- [218] Pprime website. <https://pprime.fr>. [14](#)
- [219] L. Prandtl. Neue Untersuchungen  ber die str mende Bewegung der Gase und D mpfe. *Physikalische Zeitschrift*, pages 23–30, 1907. [35](#)
- [220] P. Quillatre, O. Vermorel, T. Poinso, and P. Ricoux. Large eddy simulation of vented deflagration. *Industrial and Engineering Chemistry Research*, 52(33):11414–11423, 2013. [203](#), [220](#)
- [221] W. J. M. Rankine. On the thermodynamic theory of waves of finite longitudinal disturbance. *Philosophical Transactions of the Royal Society*, 1869. [33](#)
- [222] E. Ranzi, C. Cavallotti, A. Cuoci, A. Frassoldati, M. Pelucchi, and T. Faravelli. New reaction classes in the kinetic modeling of low temperature oxidation of n-alkanes. *Combustion and Flame*, 162(5):1679–1691, 2015. [72](#)
- [223] E. Ranzi, A. Frassoldati, R. Grana, A. Cuoci, T. Faravelli, A. P. Kelley, and C. K. Law. Hierarchical and comparative kinetic modeling of laminar flame speeds of hydrocarbon and oxygenated fuels. *Progress in Energy and Combustion Science*, 38(4):468–501, 2012. [72](#)
- [224] M. V. Reddy, A. Mauger, C. M. Julien, A. Paoletta, and K. Zagh b. Brief History of Early Lithium-Battery Development. *Materials*, 13:1884, 2020. [3](#)

- [225] B. Rochette, E. Riber, B. Cuenot, and O. Vermorel. A generic and self-adapting method for flame detection and thickening in the thickened flame model. *Combustion and Flame*, 212:448–458, 2020. 101
- [226] P. Rodrigues. *Modélisation multiphysique de flammes turbulentes suitées avec la prise en compte des transferts radiatifs et des transferts de chaleur pariétaux*. PhD thesis, 2018. 159
- [227] L. A. Román-Ramírez and J. Marco. Design of experiments applied to lithium-ion batteries: A literature review. *Applied Energy*, 320(May), 2022. 12
- [228] D. A. Rosenberg, P. M. Allison, and J. F. Driscoll. Flame index and its statistical properties measured to understand partially premixed turbulent combustion. *Combustion and Flame*, 162(7):2808–2822, 2015. 110
- [229] G. R. Ruetsch, L. Vervisch, and A. Liñán. Effects of heat release on triple flames. *Physics of Fluids*, 7(6):1447–1454, 1995. 144, 147, 152, 164
- [230] A. S. Sabau and W. D. Porter. Alloy shrinkage factors for the investment casting of 17-4PH stainless steel parts. *Metallurgical and Materials Transactions B: Process Metallurgy and Materials Processing Science*, 39(2):317–330, 2008. 146
- [231] SAFT batteries website. <https://www.saft.com>. 7, 9, 14
- [232] A. O. Said, C. Lee, S. I. Stoliarov, and A. W. Marshall. Comprehensive analysis of dynamics and hazards associated with cascading failure in 18650 lithium ion cell arrays. *Applied Energy*, 248(October 2018):415–428, 2019. 233
- [233] S. Santhanagopalan, K. Smith, J. Neubauer, G.-H. Kim, M. Keyser, and A. Pesarani. Chapter 1 : Types of Batteries. In *Design and Analysis of Large Lithium-ion Battery Systems*. Artech House, 2015. 8, 56
- [234] M. Saputra, A. Syuhada, and R. Sary. Study of Solar and Wind Energy Using As Water Pump Drive-Land For Agricultural Irrigation. *International Conference on Science and Technology*, pages 2018–2021, 2018. 3
- [235] A. Sartbaeva, V. L. Kuznetsov, S. A. Wells, and P. P. Edwards. Hydrogen nexus in a sustainable energy future. *Energy and Environmental Science*, 1(1):79–85, 2008. 3
- [236] C. Schneider, A. Dreizler, J. Janicka, and E. P. Hassel. Flow field measurements of stable and locally extinguishing hydrocarbon-fuelled jet flames. *Combustion and Flame*, 135(1-2):185–190, 2003. 144
- [237] T. Schönfeld and M. Rudgyard. Steady and unsteady flow simulations using the hybrid flow solver AVBP. *AIAA journal*, 37(11):1378–1385, 1999. 12, 50
- [238] R. Schröder, M. Aydemir, and G. Seliger. Comparatively Assessing different Shapes of Lithium-ion Battery Cells. *Procedia Manufacturing*, 8(October 2016):104–111, 2017. 6

- [239] B. Scrosati. History of lithium batteries. *Journal of Solid State Electrochemistry*, 15(7-8):1623–1630, 2011. [3](#)
- [240] K. Seshadri and F. A. Williams. Laminar flow between parallel plates with injection of a reactant at high reynolds number. *International Journal of Heat and Mass Transfer*, 21(2):251–253, 1978. [31](#)
- [241] H. Sezer, F. Kronz, V. Akkerman, and A. S. Rangwala. Methane-induced explosions in vented enclosures. *Journal of Loss Prevention in the Process Industries*, 48:199–206, 2017. [233](#)
- [242] S. Shahid and M. Agelin-chaab. Energy Conversion and Management : X A review of thermal runaway prevention and mitigation strategies for lithium-ion batteries. *Energy Conversion and Management: X*, 16(July):100310, 2022. [12](#)
- [243] J. S. Shin, C. H. Han, U. H. Jung, S. I. Lee, H. J. Kim, and K. Kim. Effect of Li₂CO₃ additive on gas generation in lithium-ion batteries. *Journal of Power Sources*, 109(1):47–52, 2002. [62](#), [63](#)
- [244] A. Sinha and J. X. Wen. A simple model for calculating peak pressure in vented explosions of hydrogen and hydrocarbons. *International Journal of Hydrogen Energy*, 44(40):22719–22732, 2019. [233](#)
- [245] J. Smagorinsky. General Circulation Experiments With the Primitive Equations. *Monthly Weather Review*, 91(3):99–164, 1963. [45](#), [186](#)
- [246] G. A. Sod. A survey of several finite difference methods for systems of nonlinear hyperbolic conservation laws. *Journal of Computational Physics*, 27(1):1–31, 1978. [92](#)
- [247] V. Somandepalli, K. Marr, and Q. Horn. Quantification of combustion hazards of thermal runaway failures in lithium-ion batteries. *SAE International Journal of Alternative Powertrains*, 3(1):98–104, 2014. [86](#), [88](#)
- [248] R. Spotnitz. Analysis of Thermal Behaviors of Li-Ion Batteries Using Thermal Abuse Reaction Model: Cell Thermal Runaway and Module Propagation. *ECS Meeting Abstracts*, 2007. [9](#), [233](#)
- [249] R. Spotnitz and J. Franklin. Abuse behavior of high-power, lithium-ion cells. *Journal of Power Sources*, 113(1):81–100, 2003. [10](#), [57](#), [62](#), [63](#)
- [250] R. Srinivasan, M. E. Thomas, M. B. Airola, B. G. Carkhuff, L. J. Frizzell-Makowski, H. Alkandry, J. G. Reuster, H. N. Oguz, P. W. Green, J. La Favors, L. J. Currano, and P. A. Demirev. Preventing Cell-to-Cell Propagation of Thermal Runaway in Lithium-Ion Batteries. *Journal of The Electrochemical Society*, 167(2):020559, 2020. [12](#)
- [251] S. Stolz and N. A. Adams. An approximate deconvolution procedure for large-eddy simulation. *Physics of Fluids*, 11(7):1699–1701, 1999. [43](#), [48](#), [49](#)
- [252] P. Sun, R. Bisschop, H. Niu, and X. Huang. *A Review of Battery Fires in Electric Vehicles*, volume 56. Springer US, 2020. [12](#)

- [253] W. Sun, B. Yang, N. Hansen, C. K. Westbrook, F. Zhang, G. Wang, K. Moshhammer, and C. K. Law. An experimental and kinetic modeling study on dimethyl carbonate (DMC) pyrolysis and combustion. *Combustion and Flame*, 164:224–238, 2016. [64](#), [78](#)
- [254] J. Taine and J.-P. Petit. *Transferts thermiques*. Dunod, 2nd edition, 1995. [40](#)
- [255] S. Takahashi, K. Kanayama, S. Morikura, H. Nakamura, T. Tezuka, and K. Maruta. Study on oxidation and pyrolysis of carbonate esters using a micro flow reactor with a controlled temperature profile. Part II: Chemical kinetic modeling of ethyl methyl carbonate. *Combustion and Flame*, 2021. [61](#), [64](#)
- [256] Z. Tang, A. Song, S. Wang, J. Cheng, and C. Tao. Numerical analysis of heat transfer mechanism of thermal runaway propagation for cylindrical lithium-ion cells in battery module. *Energies*, 13(4), 2020. [233](#)
- [257] K. Tasaki, A. Goldberg, J.-J. Lian, M. Walker, A. Timmons, and S. J. Harris. Solubility of Lithium Salts Formed on the Lithium-Ion Battery Negative Electrode Surface in Organic Solvents. *Journal of The Electrochemical Society*, 156(12):A1019, 2009. [58](#), [59](#), [63](#)
- [258] R. G. Taylor, B. Scanlon, P. Döll, M. Rodell, R. Van Beek, Y. Wada, L. Longuevergne, M. Leblanc, J. S. Famiglietti, M. Edmunds, L. Konikow, T. R. Green, J. Chen, M. Taniguchi, M. F. Bierkens, A. Macdonald, Y. Fan, R. M. Maxwell, Y. Yechieli, J. J. Gurdak, D. M. Allen, M. Shamsudduha, K. Hiscock, P. J. Yeh, I. Holman, and H. Treidel. Ground water and climate change. *Nature Climate Change*, 3(4):322–329, 2013. [2](#)
- [259] R. E. Teets and J. A. Sell. Calorimetry of ignition sparks. *SAE Technical Papers*, 97:371–383, 1988. [152](#), [242](#)
- [260] K. Thompson. Time Dependent Boundary Conditions for Hyperbolic Systems, II. *Journal of Computational Physics*, 89:439–461, 1990. [123](#), [174](#), [186](#), [202](#), [223](#)
- [261] S. R. Tieszen, D. W. Stamps, and T. J. O’Hern. A heuristic model of turbulent mixing applied to blowout of turbulent jet diffusion flames. *Combustion and Flame*, 106(4):442–462, 1996. [124](#)
- [262] E. F. Toro. *Riemann solvers and numerical methods for fluid dynamics*. 2009. [35](#), [36](#)
- [263] TotalEnergies website. <https://careers.totalenergies.com/en>. [14](#)
- [264] H. Tsuji and I. Yamaoka. The structure of counterflow diffusion flames in the forward stagnation region of a porous cylinder. *Symposium (International) on Combustion*, 13(1):723–731, 1971. [82](#)
- [265] O. J. Ugarte, V. Akkerman, and A. S. Rangwala. A computational platform for gas explosion venting. *Process Safety and Environmental Protection*, 99:167–174, 2016. [220](#), [233](#)

- [266] M. R. Usman. Hydrogen storage methods: Review and current status. *Renewable and Sustainable Energy Reviews*, 167(July 2020):112743, 2022. [3](#)
- [267] A. Velikorodny and S. Kudriakov. Numerical study of the near-field of highly underexpanded turbulent gas jets. *International Journal of Hydrogen Energy*, 37(22):17390–17399, 2012. [128](#)
- [268] L. M. Verhoeven, W. J. Ramaekers, J. A. van Oijen, and L. P. De Goeij. Modeling non-premixed laminar co-flow flames using flamelet-generated manifolds. *Combustion and Flame*, 159(1):230–241, 2012. [144](#)
- [269] O. Vermorel, P. Quillatre, and T. Poinso. LES of explosions in venting chamber: A test case for premixed turbulent combustion models. *Combustion and Flame*, 183:207–223, 2017. [203](#), [220](#)
- [270] M. M. Vogel, J. Zscheischler, E. M. Fischer, and S. I. Seneviratne. Development of Future Heatwaves for Different Hazard Thresholds. *Journal of Geophysical Research: Atmospheres*, 125(9), 2020. [2](#)
- [271] K. G. Vollmer, F. Ettner, and T. Sattelmayer. Deflagration-to-detonation transition in hydrogen/air mixtures with a concentration gradient. *Combustion Science and Technology*, 184(10-11):1903–1915, 2012. [229](#)
- [272] P. S. Volpiani, T. Schmitt, O. Vermorel, P. Quillatre, and D. Veynante. Large eddy simulation of explosion deflagrating flames using a dynamic wrinkling formulation. *Combustion and Flame*, 186:17–31, 2017. [220](#)
- [273] J. VonNeumann and R. D. Richtmyer. A method for the numerical calculation of hydrodynamic shocks. *Journal of Applied Physics*, 21(3):232–237, 1950. [43](#)
- [274] A. W. Vreman, B. A. Albrecht, J. A. van Oijen, L. P. de Goeij, and R. J. Bastiaans. Premixed and nonpremixed generated manifolds in large-eddy simulation of Sandia flame D and F. *Combustion and Flame*, 153(3):394–416, 2008. [144](#)
- [275] K. J. Walsh, J. L. Mcbride, P. J. Klotzbach, S. Balachandran, S. J. Camargo, G. Holland, T. R. Knutson, J. P. Kossin, T. cheung Lee, A. Sobel, and M. Sugi. Tropical cyclones and climate change. *Wiley Interdisciplinary Reviews: Climate Change*, 7(1):65–89, 2016. [2](#)
- [276] K. Wan, L. Vervisch, J. Xia, P. Domingo, Z. Wang, Y. Liu, and K. Cen. Alkali metal emissions in an early-stage pulverized-coal flame: DNS analysis of reacting layers and chemistry tabulation. *Proceedings of the Combustion Institute*, 37(3):2791–2799, 2019. [109](#)
- [277] G. Wang, M. Boileau, and D. Veynante. Implementation of a dynamic thickened flame model for large eddy simulations of turbulent premixed combustion. *Combustion and Flame*, 158(11):2199–2213, 2011. [47](#)
- [278] G. Wang, D. Kong, P. Ping, X. He, H. Lv, H. Zhao, and W. Hong. Modeling venting behavior of lithium-ion batteries during thermal runaway propagation by coupling CFD and thermal resistance network. *Applied Energy*, 334(October 2022):120660, 2023. [12](#)

- [279] H. Wang, E. Rus, T. Sakuraba, J. Kikuchi, Y. Kiya, and H. D. Abruna. CO₂ and O₂ evolution at high voltage cathode materials of li-ion batteries: A differential electrochemical mass spectrometry study. *Analytical Chemistry*, 86(13):6197–6201, 2014. 57, 63
- [280] H. Wang, H. Xu, Z. Zhao, Q. Wang, C. Jin, Y. Li, J. Sheng, K. Li, Z. Du, C. Xu, and X. Feng. An experimental analysis on thermal runaway and its propagation in Cell-to-Pack lithium-ion batteries. *Applied Thermal Engineering*, 211(June 2021):118418, 2022. 12
- [281] Q. Wang, P. Ping, X. Zhao, G. Chu, J. Sun, and C. Chen. Thermal runaway caused fire and explosion of lithium ion battery. *Journal of Power Sources*, 208:210–224, 2012. 12
- [282] Z. Wang, N. Mao, and F. Jiang. Study on the effect of spacing on thermal runaway propagation for lithium-ion batteries. *Journal of Thermal Analysis and Calorimetry*, 140(6):2849–2863, 2020. 12
- [283] J. Warner. Chapter 7 : Lithium-Ion and Other Cell Chemistries. In *The Handbook of Lithium-Ion Battery Pack Design*. Elsevier, 2015. 6, 8, 56, 57
- [284] J. X. Wen, B. P. Xu, and V. H. Tam. Numerical study on spontaneous ignition of pressurized hydrogen release through a length of tube. *Combustion and Flame*, 156(11):2173–2189, 2009. 36
- [285] C. R. Wilke. A viscosity equation for gas mixtures. *The Journal of Chemical Physics*, 18(4):517–519, 1950. 20
- [286] F. A. Williams. *Combustion Theory*. Benjamin Cummings, Menlo Park, CA, 1985. 19, 26, 27, 32, 42
- [287] J. Wirtz. *Modelling the impact of fuel in aeronautical gas turbines*. PhD thesis, 2021. 42, 46, 109
- [288] H. Xiao, D. Makarov, J. Sun, and V. Molkov. Experimental and numerical investigation of premixed flame propagation with distorted tulip shape in a closed duct. *Combustion and Flame*, 159(4):1523–1538, 2012. 199
- [289] J. Xie and Y.-c. Lu. A retrospective on lithium-ion batteries. *Nature Communications*, pages 9–12, 2020. 3
- [290] B. P. Xu, L. El Hima, J. X. Wen, S. Dembele, V. H. Tam, and T. Donchev. Numerical study on the spontaneous ignition of pressurized hydrogen release through a tube into air. *Journal of Loss Prevention in the Process Industries*, 21(2):205–213, 2008. 36
- [291] B. P. Xu and J. X. Wen. Numerical study of spontaneous ignition in pressurized hydrogen release through a length of tube with local contraction. *International Journal of Hydrogen Energy*, 37(22):17571–17579, 2012. 128
- [292] B. P. Xu, J. X. Wen, S. Dembele, V. H. Tam, and S. J. Hawksworth. The effect of pressure boundary rupture rate on spontaneous ignition of pressurized hydrogen release. *Journal of Loss Prevention in the Process Industries*, 22(3):279–287, 2009. 128

- [293] E. Yamada, S. Watanabe, A. K. Hayashi, and N. Tsuboi. Numerical analysis on auto-ignition of a high pressure hydrogen jet spouting from a tube. *Proceedings of the Combustion Institute*, 32 II(2):2363–2369, 2009. 36
- [294] H. Yamashita, M. Shimada, and T. Takeno. A numerical study on flame stability at the transition point of jet diffusion flames. *Symposium (International) on Combustion*, 26(1):27–34, 1996. 31, 108
- [295] K. Y. Yap, H. H. Huin, and J. J. Klemes. Solar Energy-Powered Battery Electric Vehicle charging stations : Current development and future prospect review. *Renewable and Sustainable Energy Reviews*, 169(March), 2022. 3
- [296] H. Yoshida, T. Fukunaga, T. Hazama, M. Terasaki, M. Mizutani, and M. Yamachi. Degradation mechanism of alkyl carbonate solvents used in lithium-ion cells during initial charging. *Journal of Power Sources*, 68(2):311–315, 1997. 62, 63
- [297] S. Zadsirjan, S. Tabejamaat, E. Abtahizadeh, and J. van Oijen. Large eddy simulation of turbulent diffusion jet flames based on novel modifications of flamelet generated manifolds. *Combustion and Flame*, 216:398–411, 2020. 144
- [298] Q. Zeng, Q. Duan, K. Jin, M. Zhu, and J. Sun. Effects of nitrogen addition on the shock-induced ignition of high-pressure hydrogen release through a rectangular tube of 400 mm in length. *Fuel*, 308(July 2021):122016, 2022. 36
- [299] S. S. Zhang. A review on the separators of liquid electrolyte Li-ion batteries. *Journal of Power Sources*, 164(1):351–364, 2007. 58
- [300] X. Zhang, Z. Li, L. Luo, Y. Fan, and Z. Du. A review on thermal management of lithium-ion batteries for electric vehicles. *Energy*, 238:121652, 2022. 3
- [301] R. Zhao, J. Liu, and J. Gu. Simulation and experimental study on lithium ion battery short circuit. *Applied Energy*, 173:29–39, 2016. 10
- [302] K. Zheng, J. Jiang, Z. Xing, Y. M. Hao, M. Yu, X. Yang, and Y. Tao. Application of large eddy simulation in methane-air explosion prediction using thickening flame approach. *Process Safety and Environmental Protection*, 159:662–673, 2022. 199
- [303] C. W. Zhou, Y. Li, E. O’Connor, K. P. Somers, S. Thion, C. Keesee, O. Mathieu, E. L. Petersen, T. A. DeVerter, M. A. Oehlschlaeger, G. Kukkadapu, C. J. Sung, M. Alrefae, F. Khaled, A. Farooq, P. Dirrenberger, P. A. Glaude, F. Battin-Leclerc, J. Santner, Y. Ju, T. Held, F. M. Haas, F. L. Dryer, and H. J. Curran. A comprehensive experimental and modeling study of isobutene oxidation. *Combustion and Flame*, 167:353–379, 2016. 64
- [304] Y. Zhou. Transition towards carbon-neutral districts based on storage techniques and spatiotemporal energy sharing with electrification and hydrogenation. *Renewable and Sustainable Energy Reviews*, 162(February):112444, 2022. 3

-
- [305] T. Zirwes, F. Zhang, P. Habisreuther, M. Hansinger, H. Bockhorn, M. Pfitzner, and D. Trimis. *Identification of Flame Regimes in Partially Premixed Combustion from a Quasi-DNS Dataset*, volume 106. Springer Netherlands, 2021.
109